



University  
of Glasgow

Hamilton, Neil G. (2010) *The application of inelastic neutron scattering to the investigation of industrial heterogeneous catalysts*. PhD thesis.

<http://theses.gla.ac.uk/2164/>

Copyright and moral rights for this thesis are retained by the author

A copy can be downloaded for personal non-commercial research or study, without prior permission or charge

This thesis cannot be reproduced or quoted extensively from without first obtaining permission in writing from the Author

The content must not be changed in any way or sold commercially in any format or medium without the formal permission of the Author

When referring to this work, full bibliographic details including the author, title, awarding institution and date of the thesis must be given

# **The application of inelastic neutron scattering to the investigation of industrial heterogeneous catalysts**

**Neil George Hamilton**

**Thesis submitted in part fulfilment of the requirements for the  
Degree of Doctor of Philosophy**



**Department of Chemistry  
Faculty of Physical Sciences  
January 2010**

## **Author's Declaration**

This thesis is submitted in part fulfilment of the requirement for the degree of Doctor of Philosophy at the University of Glasgow. This thesis represents the original work carried out by Neil G. Hamilton unless otherwise stated in the text.

The research described herein was carried out at the University of Glasgow in the Department of Chemistry under the supervision of Dr. David Lennon during the period of October 2005 - October 2009.

Neil George Hamilton

## Acknowledgement

I would firstly like to give thanks to everyone who contributed to the work presented in this thesis. I'd like to thank Dr. Ian Silverwood for support, company during difficult trips to ISIS, and also for allowing me to pick his brain on many occasions. Niko Naredi-Rainer is also thanked for his friendship and help with preliminary studies relating to the CO hydrogenation project (Oh yeah, and for that time he cycled two bikes to help me get home when I got lost at Oktoberfest!). I'd like to thank Dr. Alastair McInroy, my academic predecessor for providing training and not getting angry when I inundated his email account with questions about alumina. I'd also like to thank Dr. rer. nat. Lutz Hecht, whose critical analysis, while verging on painful, has encouraged me to improve my academic writing skills. Finally, and most importantly, I thank Dr. David Lennon, my PhD supervisor, who over the last 5 years has provided a tremendous amount of support, guidance, and above all, infectious enthusiasm, without which I would not be in the position I am now.

Big thanks go to Prof. Bob Tooze and Dr. Paul Webb of SASOL Technology UK, who had patience and faith in the Fischer Tropsch project, for their constructive contributions during our progress meetings.

Dr. Stewart Parker is thanked for his significant contributions in helping me understand neutron scattering and aiding the interpretation of infrared and INS spectra. I'd also like to thank him for putting up with my, at times incessant, questions.

I thank Liam McMillan, Andrew McFarlane, June Callison, and Emma Gibson for putting up with me in the lab and also for their advice through the years.

A really big thank you goes to all my other friends who I met through Chemistry. There's not enough room to mention everyone here but I especially thank Mark Facchini, who has been a great friend since our undergraduate years. Big thanks also go to my buddies from Ayr, who at times helped me forget all about chemistry and kept me entertained throughout my years at Glasgow University.

Finally, Claire, who without chemistry I'd never have met: thanks for everything. Last, but certainly not least, thanks to my family. Your moral (and financial!) help over the years has meant a lot to me and has given me the drive to get through my, often arduous, education.

## Introductory remarks

Inelastic neutron scattering (INS) spectroscopy is applied in concert with other laboratory-based analysis techniques to the investigation of two distinct and different heterogeneous catalyst systems.

The first system investigated is an activated  $\eta$ - $\text{Al}_2\text{O}_3$  catalyst. The mechanism of activation was studied first. While it is commonly accepted that the activation of transition metal oxides proceeds via a dehydroxylation-dehydration process there is surprisingly little spectroscopic evidence within the literature that comprehensively proves this concept. This is partly due to the fact that transition metal oxides present an effective optical cut-off in infrared spectroscopy at energies  $<1100\text{ cm}^{-1}$ , which is due to intense lattice vibrations. This optical cut-off prevents observation of diagnostic hydroxyl deformation modes that can allow the differentiation of surface-bound hydroxyl groups and adsorbed water molecules. INS spectroscopy presents a unique opportunity to access these modes as the metal-oxygen lattice modes that often hinder the application of infrared spectroscopy do not negatively affect the INS measurement. In this manner, this investigation has provided spectroscopic evidence for desorption of both water molecules and surface-bound hydroxyl groups upon thermal activation of an  $\eta$ - $\text{Al}_2\text{O}_3$  catalyst.

Activation of an  $\eta$ - $\text{Al}_2\text{O}_3$  catalyst in this way results in the generation of Lewis acidic coordinatively unsaturated  $\text{Al}^{\text{III}}$  centres that promote Lewis acid mediated catalysis. Activated transition alumina catalysts typically present a range of  $\text{Al}^{\text{III}}$  centres with varying degrees of Lewis acidity. In some applications the Lewis acidity can be too strong resulting in a loss of selectivity to the desired product. Normally, these undesirably strong Lewis acid sites are ‘capped’ using alkali metals that physically block access to the site. This investigation has revealed that careful calcination of an  $\eta$ - $\text{Al}_2\text{O}_3$  catalyst prior to activation can result in a partial phase change towards  $\theta$ - $\text{Al}_2\text{O}_3$ , that consequently results in a redistribution of the Lewis acid sites exposed at the surface. This process constitutes a potentially cost-effective and novel method of modifying the selectivity profiles of industrial grade alumina catalysts that has hitherto been unreported.

Characterisation of the Lewis acidity presented by activated transition alumina catalysts is usually achieved by application of pyridine adsorption coupled with infrared spectroscopy. Energy shifts associated with the  $\nu_{8a}$  mode of adsorbed pyridine can reveal the Lewis acid

distribution of the activated catalyst. The dynamic range observed for the  $\nu_{8a}$  mode of pyridine adsorbed on activated alumina is *ca.*  $25 \text{ cm}^{-1}$ . This investigation has shown, via a combination of INS spectroscopy and ancillary periodic density functional theory (DFT) calculations that the  $\nu_{6a}$  mode of pyridine exhibits an unprecedented energy shift of  $165 \text{ cm}^{-1}$  upon adsorption to the activated alumina substrate. The implication of this result is considered.

The second part of this work applies INS spectroscopy to characterise the hydrocarbonaceous deposits present on the surface of iron-based catalysts for the Fischer-Tropsch synthesis (FTS) of higher hydrocarbons and also the ambient pressure hydrogenation of carbon monoxide towards methane. Surprisingly, the vibrational fingerprint of the hydrocarbonaceous deposits present on a post-reaction fused iron catalyst after exposure to high pressure FTS conditions for a full industrial cycle (*ca.* 12 months) was found to be very similar to that of a precipitated iron catalyst that had been exposed to ambient pressure CO methanation for a period of 6 h. This observation indicates a hydrocarbonaceous surface species that is common to both catalysts despite them being exposed to very different conditions. This hydrocarbonaceous overlayer is proposed to constitute at least part of the active site for both catalyst systems. A unique property of INS is that due to its underlying physical principles quantification of individual vibrational states is easily facilitated. In this manner it is possible to quantify the hydrogen content of the hydrocarbonaceous overlayer present on post-reaction catalyst samples. This data is combined with parallel temperature programmed oxidation (TPO) measurements to reveal the global C:H ratio for the post-reaction catalyst.

In this way, INS spectroscopy has been able to reveal properties of two very different heterogeneous catalyst systems that are difficult to obtain by other spectroscopic techniques.

## **Abstract**

Vibrational spectroscopy has been used to probe the surface chemistry of two heterogeneous catalysts. This has principally involved the application of infrared (IR) spectroscopy and inelastic neutron scattering (INS), with a much reduced role for Raman scattering.

Firstly, the activation of high surface area alumina catalysts has been investigated. IR spectroscopy is able to discern the presence of a recently postulated active site. Moreover, INS measurements indicate the potential of this technique to provide additional insight into the surface Lewis acidity of this substrate.

The second part of this project uses the reaction of carbon monoxide and hydrogen over an Fe-based catalysts to discern some of the fundamental processes that are likely to contribute to the more complex Fischer-Tropsch synthesis (FTS) process. Ancillary measurements on an industrial grade FTS catalyst validate the procedure adopted.

# Table of contents

<b>Chapter 1 Spectroscopy in catalysis</b> .....	<b>4</b>
1.1 Infrared Spectroscopy in Catalysis .....	5
1.1.1 Transmission Spectroscopy .....	6
1.1.2 Diffuse Reflectance Infrared Fourier Transform Spectroscopy (DRIFTS)....	6
1.2 Inelastic neutron scattering (INS) .....	8
1.2.1 INS and DFT .....	9
1.2.2 Instrumentation .....	10
1.2.2.2 TOSCA.....	10
1.2.2.3 MARI .....	11
1.2.2.4 MAPS.....	11
<b>Chapter 2 Experimental procedure</b> .....	<b>14</b>
2.1 Experimental apparatus.....	15
2.1.1 Small scale laboratory based experiments .....	15
2.1.2 Larger scale experiments for INS analysis.....	16
Alumina activation and pyridine adsorption .....	16
CO hydrogenation over iron-based samples .....	16
2.2 Catalyst Characterisation .....	20
2.3 Alumina activation .....	22
2.3.1 TGA .....	22
2.3.2 Infrared Spectroscopy .....	22
2.3.3 INS - MARI .....	23
2.3.4 XRD .....	23
2.4 Pyridine adsorption/desorption on activated alumina .....	25
2.4.1 Temperature Programmed Desorption (TPD).....	25
2.4.2 Infrared spectroscopy .....	25
2.4.3 INS spectroscopy - TOSCA .....	26
2.5 Calcination of $\eta$ -Al <sub>2</sub> O <sub>3</sub> .....	28
2.5.1 Infrared – pyridine .....	28
2.5.2 XRD .....	28
2.5.3 BET .....	28
2.6 Analysis of SASOL catalyst fines samples .....	29
2.6.1 Raman scattering spectroscopy .....	29
2.6.2 Infrared.....	29
2.6.3 INS – TOSCA .....	29
2.6.4 TPO .....	30
2.6.4.1 Calibration of the TPO apparatus.....	30
2.6.5 TEM .....	36
2.7 Analysis of post-reaction CO hydrogenation catalyst samples.....	36
2.7.1 Microreactor catalyst testing .....	36
2.7.2 Scale-up of microreactor .....	41
2.7.3 Raman spectroscopy .....	43
2.7.4 Infrared spectroscopy .....	43
2.7.5 INS spectroscopy .....	43
2.7.5.1 TOSCA.....	43
2.7.5.2 MAPS.....	43
2.7.6 Post-reaction Temperature Programmed Oxidation.....	43
2.7.7 XRD .....	44
2.7.8 TEM .....	44

<b>Chapter 3 Activation and surface Lewis acidity of transition alumina catalysts .....</b>	<b>45</b>
3.1 Activation of transition aluminas .....	47
3.2 Acidity of transition aluminas .....	48
3.2.1 Lewis acidity of transition aluminas .....	49
3.2.2 Brønsted acidity of transition aluminas .....	49
3.3 Vibrational spectroscopy to probe activation mechanism of transition aluminas .....	51
3.3.1 Infrared spectroscopy .....	51
3.3.2 Raman spectroscopy .....	52
3.3.3 Inelastic neutron scattering (INS) spectroscopy .....	53
3.4 Characterisation of transition alumina surface acidity by vibrational spectroscopy of adsorbed species .....	54
3.4.1 Adsorption of basic probe molecules .....	55
3.5 Modification of surface acidity .....	59
<b>Chapter 4 Activation of transition alumina catalysts .....</b>	<b>61</b>
4.1. Thermogravimetric Analysis (TGA) .....	62
4.2 X-ray Diffraction (XRD) .....	64
4.3 Infrared spectroscopy .....	66
4.4 Inelastic neutron Scattering spectroscopy (MAPS) .....	73
4.4.1 Vibrational spectra .....	73
4.4.2 Momentum transfer dependence .....	79
4.5 Evidence for the generation of Lewis acidity upon thermal activation .....	83
4.5.1 Pyridine adsorption – infrared spectroscopy .....	83
4.5.2 Temperature programmed desorption infrared spectroscopy .....	90
4.5.3 Mass selective temperature programmed desorption of methanol .....	95
4.6 Conclusions .....	98
<b>Chapter 5 Modification of surface Lewis acidity of transition alumina catalysts .....</b>	<b>100</b>
5.1 Thermal effects on Alumina structure .....	102
5.2 X-ray diffraction (XRD) analysis .....	103
5.3 Surface area analysis .....	110
5.4 Diffuse Reflectance Infrared Spectroscopy (DRIFTS) .....	113
5.4.1 Infrared spectra of the calcined alumina catalysts .....	113
5.4.2 Infrared difference spectra of adsorbed pyridine .....	117
5.5 Conclusions .....	122
<b>Chapter 6 A new vibrational probe for Lewis acidity .....</b>	<b>123</b>
6.1 Infrared spectroscopy – pyridine adsorption .....	124
6.2 Inelastic neutron scattering – pyridine adsorption .....	127
6.3 <i>Ab initio</i> methods to investigate pyridine adsorption .....	131
6.3.1 Optimisation of the $\alpha$ -Al <sub>2</sub> O <sub>3</sub> bulk and (0001) surface .....	132
6.3.2 Pyridine on $\alpha$ -Al <sub>2</sub> O <sub>3</sub> (0001) surface .....	133
6.3.3 Simulation of the INS spectrum of pyridine on $\alpha$ -Al <sub>2</sub> O <sub>3</sub> (0001) .....	136
6.4 Conclusions .....	144
<b>Chapter 7 Fischer-Tropsch Synthesis and CO hydrogenation over Fe-based catalysts .....</b>	<b>145</b>
<b>Chapter 8 .....</b>	<b>152</b>
<b>Analysis of a post-reaction fused iron Fischer-Tropsch catalyst .....</b>	<b>152</b>
8.1 Infrared spectroscopy .....	154
8.2 Raman scattering spectroscopy .....	158

8.3	Inelastic Neutron Scattering (INS) spectroscopy .....	160
8.4	Density Functional Theory calculations.....	164
8.5	X-ray diffraction of post-reaction catalyst fines .....	168
8.6	Transmission Electron Microscopy.....	172
8.7	Quantification of hydrocarbonaceous deposits by temperature programmed oxidation (TPO) .....	174
8.8	Conclusions .....	177
<b>Chapter 9 Carbon monoxide hydrogenation over an iron oxide precursor .....</b>		<b>179</b>
9.1	Temperature programmed reaction testing.....	181
9.1.1	Temperature programmed reduction.....	181
9.1.2	CO hydrogenation over iron samples at 623 K.....	181
9.1.3	CO hydrogenation over iron samples at 723 K.....	182
9.2	Scale-up of microreactor studies.....	198
9.3	X-ray diffraction (XRD) .....	198
9.4	Infrared and Raman vibrational spectroscopy .....	205
9.5	Inelastic neutron scattering (INS) spectroscopy .....	208
9.6	Quantification of hydrocarbonaceous overlayer .....	228
9.6.1	Hydrogen quantification by INS .....	228
9.7	Temperature programmed oxidation (TPO).....	239
9.8	Determination of the global C:H ratio of post-reaction samples .....	241
9.9	Transmission electron spectroscopy.....	247
9.10	Conclusions.....	254
<b>Chapter 10 Summary.....</b>		<b>257</b>
10.1	Activation of transition alumina catalysts.....	258
10.2	Modification of surface Lewis acidity of transition alumina catalysts .....	258
10.3	A new vibrational probe for Lewis acidity.....	259
10.4	Analysis of a post-reaction fused iron Fischer-Tropsch catalyst .....	260
10.5	Carbon monoxide hydrogenation over an iron oxide precursor .....	261
10.6	Future work.....	262
10.6.1	Alumina.....	262
10.6.2	Iron catalysts .....	262
<b>Chapter 11 References .....</b>		<b>263</b>

# 1

## Chapter 1 Spectroscopy in catalysis

Although this investigation utilises a number of different vibrational spectroscopic techniques, including infrared, Raman and inelastic neutron scattering (INS), along with parallel application of other standard laboratory-based analyses, the most heavily featured techniques are infrared spectroscopy and inelastic neutron scattering (INS) spectroscopy.

These techniques are combined to explore the activation of transition alumina catalysts and to characterise the Lewis acidity that is generated during the activation procedure. INS spectroscopy is also applied to the characterisation of hydrocarbonaceous deposits present on the surface of catalysts active in Fischer-Tropsch synthesis (FTS) and ambient pressure carbon monoxide hydrogenation. A brief description of these techniques and historical events in their application to the progression of the field of heterogeneous catalysis research is discussed in the following chapter.

## 1.1 Infrared Spectroscopy in Catalysis

Infrared spectroscopy was first applied to the characterisation of catalysts and adsorbed species in the 1940s and 50s by Terinin in Russia [1, 2]. The technique was then further developed by Eischens *et al.* [3] at Texaco Laboratories and by Sheppard at Cambridge University [4, 5]. Since then the use of IR spectroscopy has become very common in both academic and industrial laboratories. The most significant improvement of the technique in the last few decades was the development and commercialisation of the Fourier transform infrared spectrometer (FT-IR). The FT-IR spectrometer offered several advantages over dispersive spectrometers (previously used), including improved signal to noise and lower acquisition times [6, 7].

Infrared spectroscopy does however have some limitations when examining alumina or alumina supported catalysts. One of these limitations is that below  $1100\text{ cm}^{-1}$  fundamental vibrations of the solid alumina are of such a high intensity that they represent a complete spectral cut-off [8]. This means that any vibrational modes of adsorbed molecules below  $1100\text{ cm}^{-1}$  are inaccessible. Although this cut-off represents a limitation, the spectral range ( $4000\text{--}1100\text{ cm}^{-1}$ ) is still adequate for detailed investigations to be performed.

### **1.1.1 Transmission Spectroscopy**

Transmission IR spectroscopy was the technique first used for the application of IR spectroscopy to study catalysis and is probably still the most popular technique used today [9]. In order to use this technique, the catalyst sample must be pressed into a self-supporting wafer, ideally with no binding material. The catalyst disk should also be sufficiently thin so as to minimise absorption of the IR radiation by the catalyst and also to limit the amount of scattering of the incident photons. To carry out experiments the disk is usually held in an environmental cell perpendicular to the infrared beam. Spectra are then recorded by observing the transmitted beam.

### **1.1.2 Diffuse Reflectance Infrared Fourier Transform Spectroscopy (DRIFTS)**

Diffuse reflectance infrared spectroscopy has been used less commonly than transmission spectroscopy in catalysis [10]. Up until recently this had been mainly due to the more complex optical arrangements required and the absence of simple, easy to use cell designs [10]. However, this is no longer the case and the commercialisation of suitable attachments and cells has led to an increase in the use of this technique [11]. The major advantage of DRIFTS is that, unlike transmission spectroscopy, samples do not have to be pressed into self-supporting disks. This leads to simplified sample preparation and also allows analysis of materials normally difficult to compress [10]. Another advantage of the technique is that samples which give rise to substantial amounts of scattered radiation can be analysed, unlike with the transmission technique [11].

The technique involves placing a powdered sample in a shallow sample cup and exposing it to infrared radiation. Incident radiation passes into the bulk and undergoes reflection, refraction, and absorption before re-emerging at the sample surface [10]. Diffusely reflected radiation from the sample is collected by a spherical or elliptical mirror and focussed onto the detector of the spectrometer. Figure 1.1.1 shows a schematic representation of a typical diffuse reflectance arrangement.

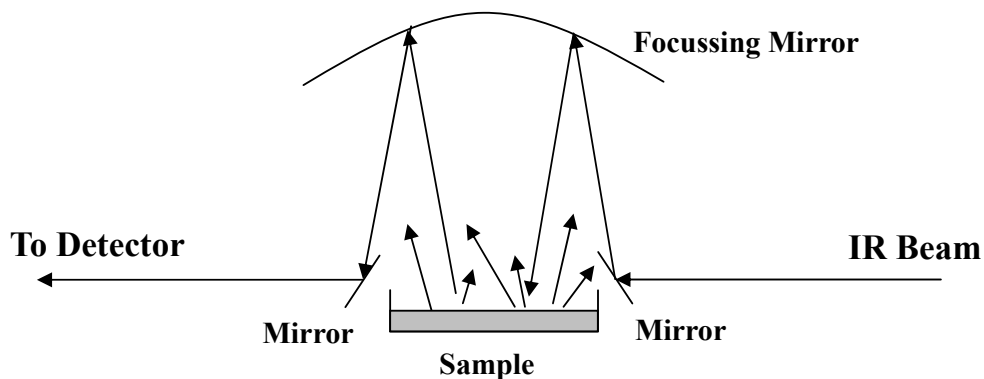


Figure 1.1.1: Optical diagram of a typical diffuse reflectance (DRIFTS) assembly.

Interpretation of the results is often based on the phenomenological theory of Kubelka and Munk, who defined a function known as the Kubelka-Munk function (Equation 1) [12]. This approach assumes that all the radiation within a sample can be resolved into two fluxes. These fluxes propagate in the negative x direction and the positive x direction respectively. Fluxes in all other directions of the infinitely extended sample are assumed to return to the  $\pm x$  direction by scattering without adsorption [10].

$$f(R_{\infty}) = (1 - R_{\infty})^2 / 2R_{\infty} = k / s \quad (1)$$

Where  $R_{\infty}$  is the reflectance of an ‘infinitely thick’ layer. The Kubelka-Munk function has a linear dependency from the absorption coefficient  $k$  ( $k = 2.303 \varepsilon c$ , where  $\varepsilon$  is the molar adsorption coefficient and  $c$  is the molar concentration) and an inverse dependency with the scattering factor  $s$ . The latter quantity is dependent on the particle size distribution, particle shape distribution, and packing density. These variables are difficult to control, and are the main reason why quantitative analysis using DRIFTS can be difficult [13]. A Kubelka-Munk spectrum is generated by treating background and sample single-beam spectra according to the following expression:

$$Kubelka - Munk = \frac{\left(1 - \left(\frac{sample}{background}\right)\right)^2}{2 * \left(\frac{sample}{background}\right)} \quad (2)$$

## 1.2 Inelastic neutron scattering (INS)

As discussed above, the application of infrared spectroscopy for the examination of heterogeneous catalysts can be hindered by the lattice modes associated with the support material, which can present an effective optical cut-off at energies up to *ca.*  $1100\text{ cm}^{-1}$ . In addition, infrared spectroscopy can be an unsuitable technique for the characterisation of heavily coked or unsupported heterogeneous catalysts due to the high optical absorbance of such samples, which can prevent the acquisition of a usable vibrational spectrum. One technique that can be used to overcome this problem is inelastic neutron scattering (INS) spectroscopy. A reason for this is that the intensity of a signal in INS spectroscopy is dependent upon the inelastic incoherent neutron scattering cross section ( $\sigma_{\text{inc}}$ ), which is characteristic of each element and does not depend on its chemical environment, of the atoms involved in the vibrational mode [14]. Hydrogen presents an anomalously high cross section of 82.2 barns, while almost every other element presents a cross section of less than 5 barns [14]. Consequently, vibrational modes involving motion of hydrogen dominate the INS spectrum, whereas those that do not contribute very little to the spectrum. This means that metal oxide supports, such as alumina, contribute very little to the INS spectrum while adsorbed species can have significant intensity, provided that they contain a suitable proportion of hydrogen-containing vibrational modes. In practise this means that the optical cut-off that blights infrared spectroscopic measurements of alumina support materials is not observed in INS spectroscopic measurements. In addition, INS is a scattering process involving the nucleus of the atoms involved in the vibration, which means that the opacity of the sample is not important. This means that the vibrational spectra of very dark samples, which are not amenable to infrared spectroscopy, can be readily attained using INS spectroscopy. An example of this is activated carbon supports for heterogeneous catalysts that are so opaque that acquisition of an infrared spectrum is impossible. Albers *et al.* [15] employed INS spectroscopy to reveal a number of well-defined vibrational modes in the energy region  $5\text{-}4000\text{ cm}^{-1}$  for a series of carbon support materials.

Another property of INS spectroscopy is that it is not subject to the electro-optical selection rules that govern the applicability of infrared and Raman scattering spectroscopic techniques. Instead, the observed intensity of an INS signal,  $S$ , is a function of both the energy,  $\omega$  ( $\text{cm}^{-1}$ ) and momentum,  $Q$  ( $\text{\AA}$ ), exchanged during the scattering process and is defined by the scattering law (Equation 3):

$$S(Q, \omega_i) \propto (QU_i)^2 \exp(-(QU_{Tot})^2) \sigma \quad (3)$$

Where  $\omega_i$  is the  $i^{\text{th}}$  mode at wavenumber  $\omega$ ,  $U_i$  is the root mean square displacement of the atoms in the mode,  $U_{Tot}$  is the total root mean square displacement of all the atoms in all the modes, and  $\sigma$  is the inelastic neutron scattering cross section of the atom. Momentum transfer,  $Q$ , is an experimental variable, and the inelastic neutron scattering cross section,  $\sigma$  (barn), is a fundamental property so only the amplitude of motion is a molecular property. In principle, both infrared active and Raman active vibrational modes are observable. However, as seen from the scattering law, the INS intensities are dependent upon the inelastic neutron scattering cross section,  $\sigma$ , whereas in infrared and Raman spectroscopy the intensity is derived from changes in the electronic properties of the molecule, *i.e.* the dynamic dipole moment for infrared measurements and the polarisation sphere for Raman measurements [16].

The fact that both Raman active and infrared active modes can be observed within a single measurement is obviously advantageous; however it does bring about a serious disadvantage. In the INS measurement all vibrational modes are active including overtones and other non-fundamental modes. This means that at room temperature there are such a high number of contributions to the spectrum that individual and diagnostic vibrational features cannot be discerned. To counteract this problem samples are usually cooled to below 20 K in order to minimise thermal population of non-fundamental modes. While this is not a serious issue for the acquisition of INS spectra of samples in an *ex situ* environment it seriously impedes the acquisition of the vibrational spectrum of catalyst samples in an *in situ* or *operando* environment.

### 1.2.1 INS and DFT

*Ab initio* methods have been increasingly applied to the calculation of molecular structures and dynamics over the past twenty years. The application of *ab initio* methods to the interpretation of INS spectra is particularly relevant due to the fact that the intensity of INS signals are not subject to the photon selection rules that complicate the calculation of infrared and Raman spectral intensities [14, 17, 18]. Simulated infrared and Raman spectra are calculated by determining the response of the electron cloud upon nuclear displacement during each normal mode of vibration [17, 18]. Inconsistencies in the calculation of electron density can therefore result in inaccurate intensities of simulated infrared and

Raman spectra. INS spectroscopy measures nuclear displacement *directly* and due to the fact that INS intensity is directly proportional to nuclear displacement, as seen in Equation 3, the calculation of the INS intensity of each normal mode of vibration is therefore comparatively simple. This property of INS spectroscopy improves the certainty of spectral assignments made with the assistance of theoretical calculations and can therefore provide a rigorous test of the veracity of the theoretical model.

## 1.2.2 Instrumentation

In order to perform INS experiments a neutron source is required. There are two types of neutron source currently in general use for spectroscopy: a polychromatic continuous neutron source from a nuclear fission reactor; or a pulsed neutron beam associated with a spallation source. In the UK INS measurements can be performed using the pulsed spallation neutron source at the ISIS Facility, located at the Rutherford Appleton Laboratory (Didcot, Chilton, Oxfordshire). In this environment, INS experiments are conducted using two types of instrument: indirect geometry spectrometers or direct geometry spectrometers [14]. The TOSCA instrument at ISIS, which features in this investigation, is an example of an indirect geometry spectrometer and determines the incident energy of inelastically scattered neutrons by time-of-flight techniques [14, 19]. The MARI and MAPS instruments, which also feature in this investigation, are direct geometry instruments, in which a single incident neutron energy is selected and the final energy and momentum transfer of the scattered neutrons is analysed by scattering angle and time-of-flight measurements.

### 1.2.2.2 TOSCA

TOSCA [19] is an INS spectrometer optimised for vibrational spectroscopy in the energy range 5-4000  $\text{cm}^{-1}$ . A schematic diagram of the spectrometer is presented in Figure 1.2.1. The spectrometer uses time-of-flight methodology to determine the energy loss of the inelastically scattered neutrons. This is made possible by the fact that scattered neutrons are reflected onto a highly ordered pyrolytic graphite crystal, which reflects scattered neutrons of a specific final energy onto the detectors. By accurately measuring the time taken for the neutrons to arrive at the detectors, the incident energy of each scattered neutron can be determined. The energy loss of each scattered neutron may then be easily calculated. The resolution of the spectrometer is around 2% of the energy transfer and although, in theory, TOSCA can record spectra from 5-8000  $\text{cm}^{-1}$ , the best results are at

energies  $< 2000 \text{ cm}^{-1}$  [14]. Another property of this instrument is that higher energy modes, *i.e.*  $\nu > 2500 \text{ cm}^{-1}$ , are dominated by neutrons with a high momentum transfer *e.g.* overtones.

### **1.2.2.3 MARI**

MARI [20] is a direct geometry instrument. It uses a Fermi chopper to monochromate the incident neutron beam to allow incident energies in the range 9-1000 meV. A schematic diagram describing a direct geometry INS spectrometer is presented in Figure 1.2.2. In an INS experiment conducted on a direct geometry chopper instrument, the neutrons arrive at the sample in pulses of known energy. After scattering from the sample the neutrons are detected by fixed arrays of detector banks as a function of their total time-of-flight. The final energies of the scattered neutrons are determined using the time-of-flight of each neutron and the distance of each detected neutron from the sample. As MARI is equipped with detector banks at various angles, the scattering angle of each scattered neutron can be measured, which allows the momentum transfer,  $Q$ , of each neutron to be determined. Fundamental modes involving hydrogen typically scatter at low values of  $Q$ , whereas modes involving heavier atoms, *e.g.* such as metal oxide phonon modes, scatter at higher values of  $Q$ . Analysing the momentum transfer dependence of a given INS signal then allows it to be assigned as a fundamental or a phonon mode.

### **1.2.2.4 MAPS**

MAPS [21] is a direct geometry chopper spectrometer that is conceptually very similar to MARI. Designed for the detection of high energy magnetic excitations in single crystals, it is highly sensitive by virtue of an exceptionally large array of position sensitive detector banks (*ca.*  $16 \text{ m}^2$ ). This property of the MAPS instrument makes it amenable to the acquisition of the vibrational spectra of samples that contain very small quantities of hydrogen.

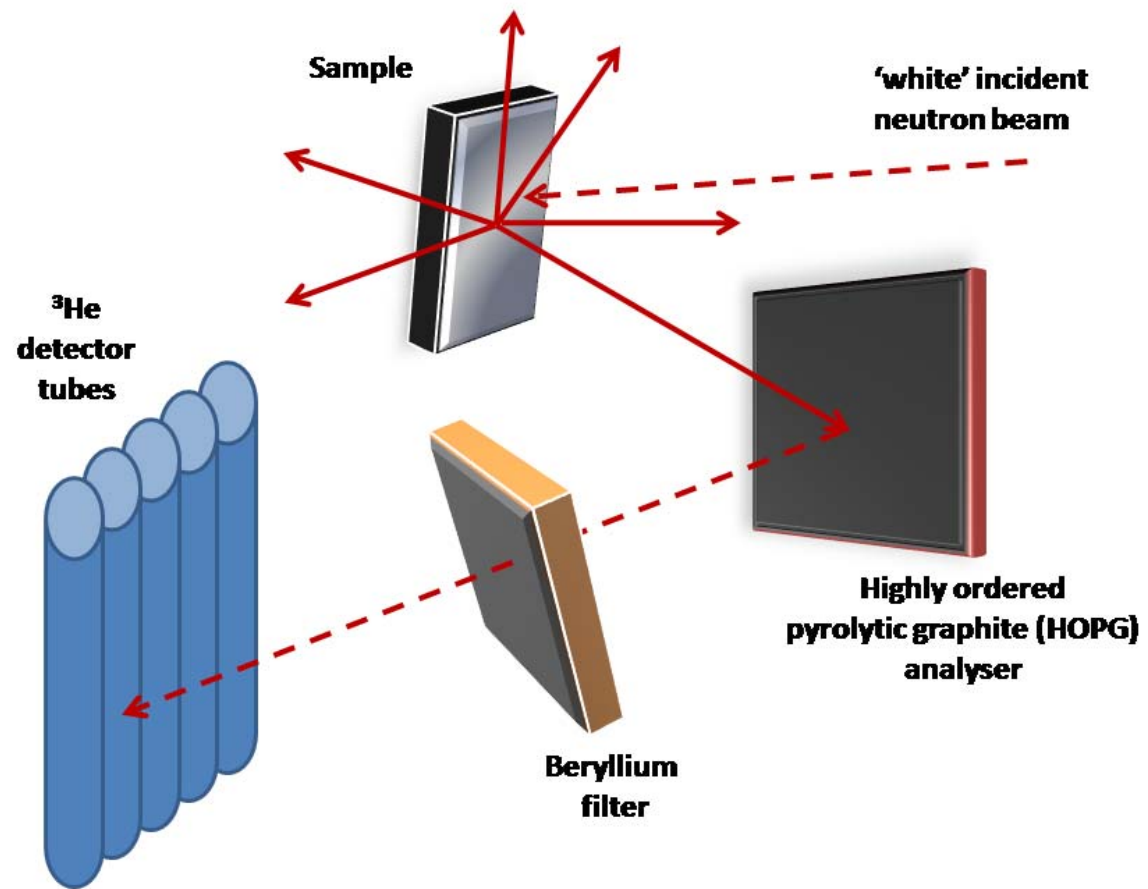


Figure 1.2.1: Schematic diagram of the TOSCA INS spectrometer.

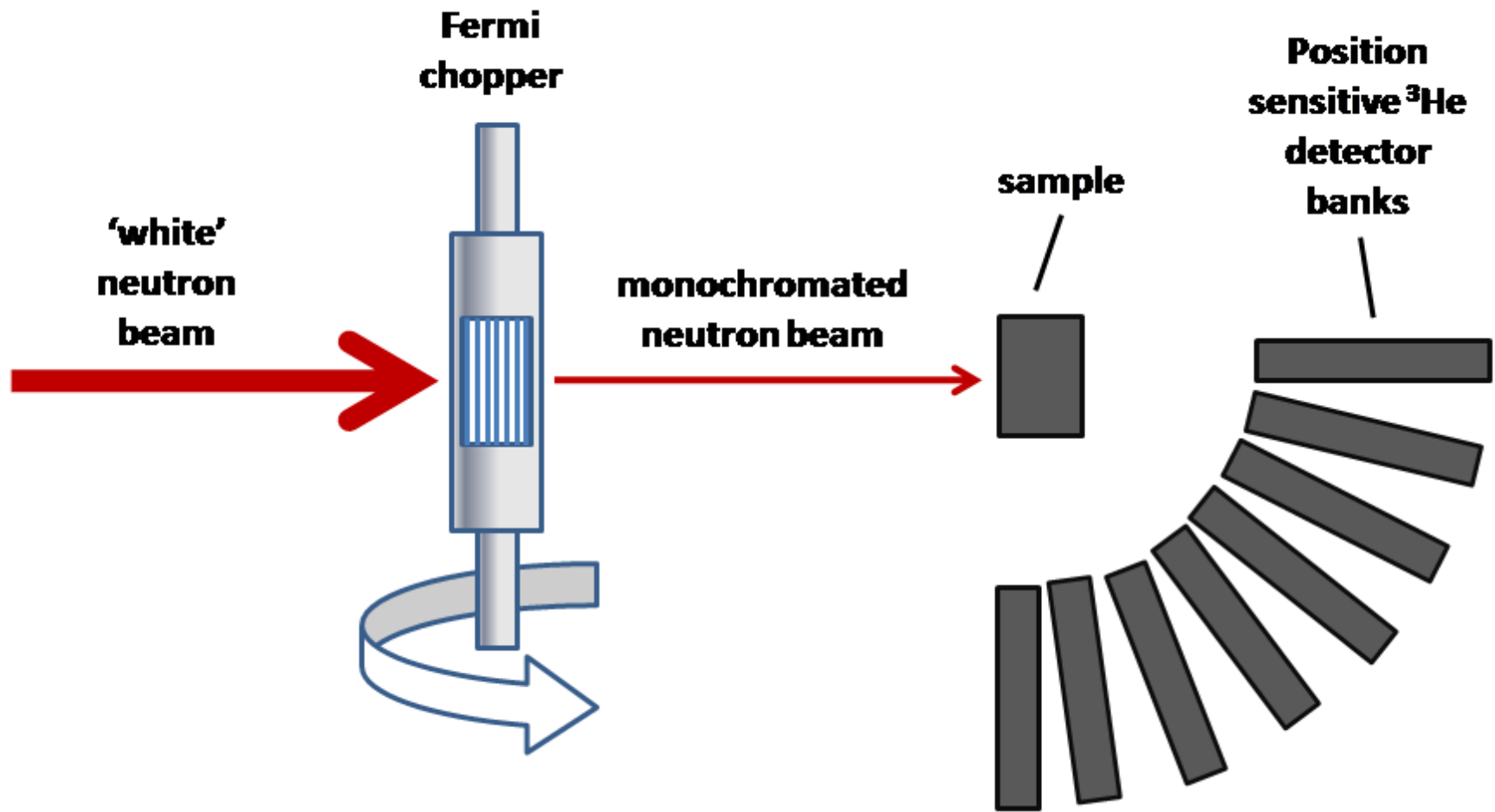


Figure 1.2.2: Schematic diagram of a direct geometry INS spectrometer, e.g. MARI or MAPS.

# 2

## Chapter 2 Experimental procedure

## 2.1 Experimental apparatus

### 2.1.1 Small scale laboratory based experiments

In order to probe both the active sites on activated  $\eta$ - $\text{Al}_2\text{O}_3$  catalysts and the reaction chemistry of  $\alpha$ - $\text{Fe}_2\text{O}_3$  catalysts in CO hydrogenation, a catalyst characterisation facility capable of both continuous and pulsed flow modes was used. This set up, shown schematically in Figure 2.1.1, permitted samples to be analysed *in situ* by the following techniques: infrared spectroscopy (transmission and diffuse reflectance), temperature programmed desorption (TPD), and mass spectrometry. It also facilitated temperature programmed oxidation (TPO) and the collection of infrared spectra of catalyst samples prepared *ex situ*.

The catalyst characterisation facility allowed catalyst samples to be analysed using three different reactor configurations. These were: (a) an environmental cell located within an infrared spectrometer operating in diffuse reflectance mode; (b) a packed bed tubular reactor (1/4" Swagelok Tubing) located within a temperature programmable oven (Neytech 25 PAF); and (c) a quartz U-shaped reactor fitted with a ground quartz sinter. The IR cell was used to examine the species on the catalyst surface after the adsorption of probe and reactant molecules and after thermal desorption at elevated temperatures. The tubular reactor allowed studies such as temperature programmed desorption and temperature programmed reaction spectroscopy as well as relative coverage experiments to be performed. The U-shaped quartz reactor was used for the CO hydrogenation experiments due to the fact that the stainless steel tubular reactor contains iron, which is reactive towards CO. Exit streams under all operating conditions could be continuously monitored via a mass spectrometer (Leda Mass, Residual Gas Analyser, LM22). The mass spectrometer sampled the elutant gas stream via a differentially pumped capillary leak that fed directly into a closed ionisation source. The arrangement was configured to confer short residence times and enhanced sensitivity. The vacuum in the mass spectrometer was maintained by a water cooled oil diffusion pump, (Edwards Diffstak, Model No. 63) backed by two rotary pumps. One rotary pump (Edwards E2M5) evacuated the jet separator, whilst the other rotary pump backed the diffusion pump (Edwards, E2M8).

### 2.1.2 Larger scale experiments for INS analysis

As a consequence of the relative insensitivity of the INS technique, INS measurements of the surface species present on the surface of heterogeneous catalysts, *e.g.* hydroxyl groups and/or adsorbed probe molecules, require very much larger samples (*ca.* 20 g) than are required for analogous infrared or Raman measurements (*ca.* 50 mg). In order to produce such large quantities of material the apparatus used had to be upscaled.

#### ***Alumina activation and pyridine adsorption***

Activation and pyridine dosing of alumina catalysts were performed *in situ* in stainless steel INS cells. Heating of the cells was achieved using collar heaters controlled by Eurotherm temperature controllers. For alumina activation experiments the cell was connected directly to a controlled helium (BOC, 99.999%) flow, while for pyridine (Sigma, *ReagentPlus*  $\geq 99\%$ ) adsorption experiments a bubbler arrangement was inserted in the gas flow as shown in Figure 2.1.2.

#### ***CO hydrogenation over iron-based samples***

Acquisition of acceptable vibrational spectra of the surface species present on heterogeneous catalysts by INS spectroscopy usually requires a large mass of sample (*ca.* 20g). In order to produce such large quantities of catalyst a facility was required that could allow the heating of a large U-shaped quartz reactor under an accurately controllable flow of reactant gases. The gas handling system used to achieve this is described in the schematic diagram presented in Figure 2.1.3. Carbon monoxide (CK, 99.5 %) and hydrogen (BOC 99.995 %) reactants and helium (BOC 99.999 %) carrier gas were supplied via a series of rotameters fed into a mixing volume located before the reactor. The manifold was equipped with pressure relief valves and a back pressure regulator fitted in order to control the pressure of the system. The eluting gases were continuously sampled via a differentially pumped quadrupole mass spectrometer (Spectra Microvision Plus).

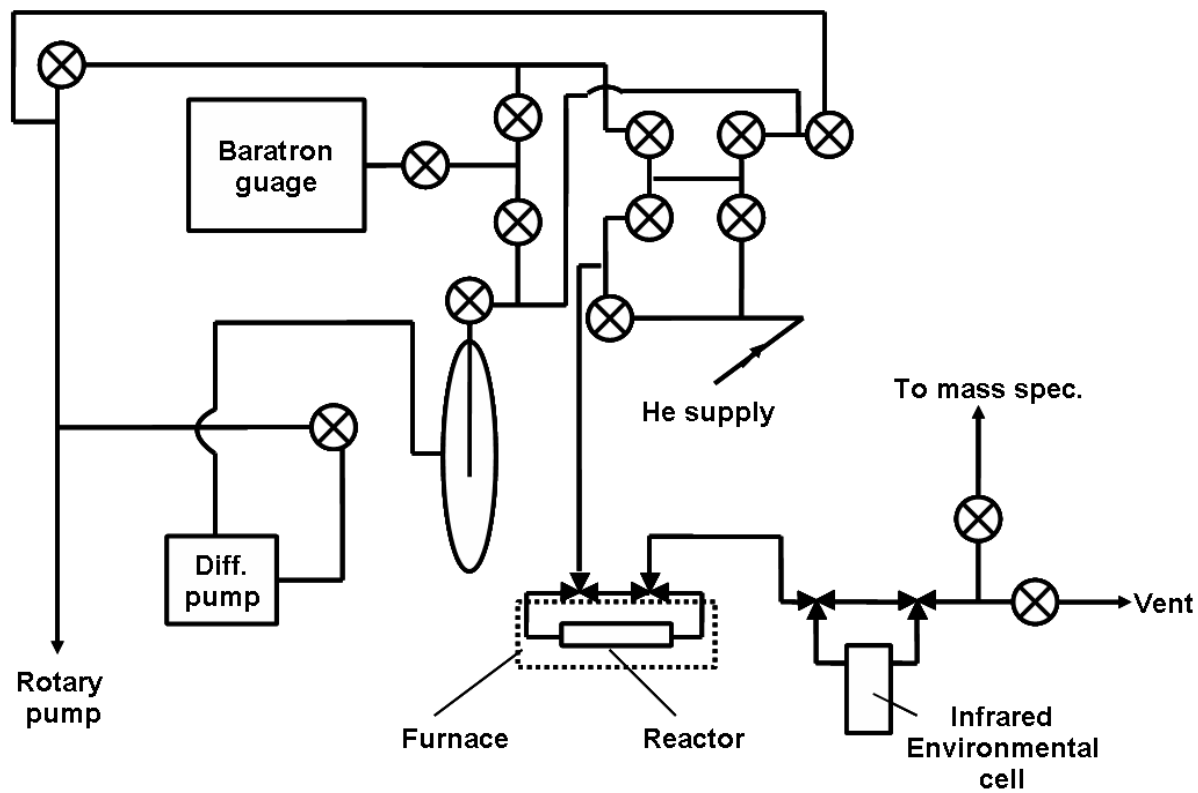


Figure 2.1.1: Schematic diagram describing the gas handling system, microreactor environment, and analytic capabilities of the laboratory set-up.

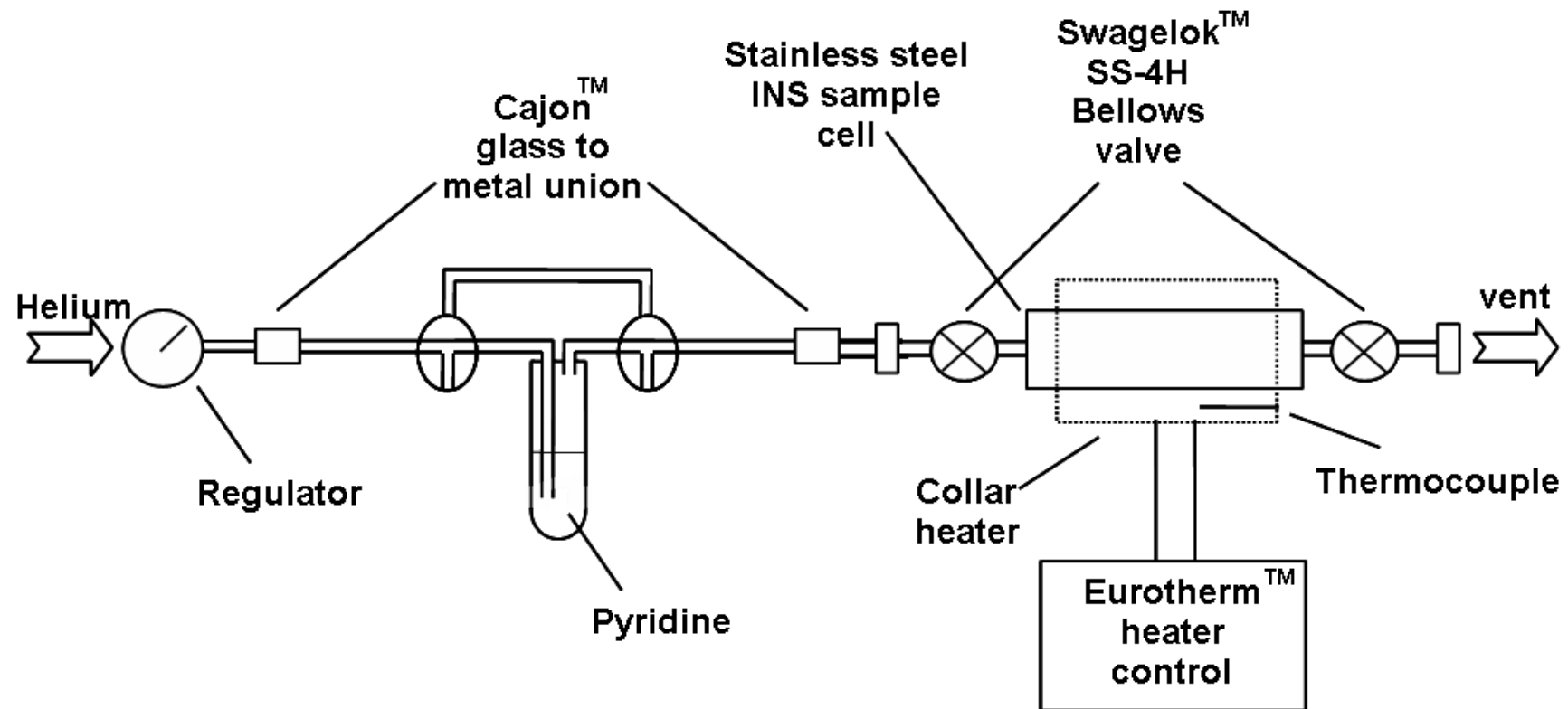


Figure 2.1.2: Schematic diagram showing the experimental apparatus used for large scale pyridine adsorption on activated  $\eta$ -Al<sub>2</sub>O<sub>3</sub>.

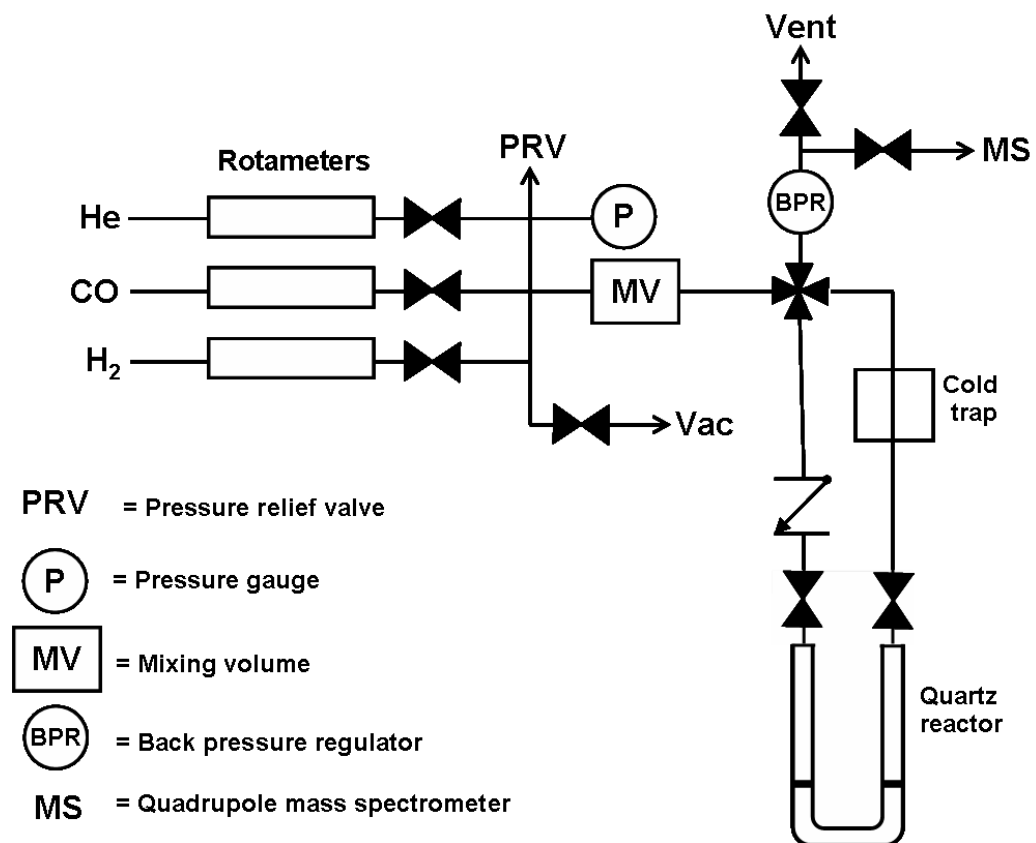


Figure 2.1.3: Schematic diagram describing the gas handling facility used for the large scale reactions conducted at the ISIS Facility.

## 2.2 Catalyst Characterisation

### **Alumina (Chapters 4-6):**

The alumina surface Lewis acidity investigations reported in this study were conducted on two different commercial grade alumina catalysts. Although both samples were recorded as being in the  $\eta$ -phase, slight variations in structure and activity between samples cannot be ruled out. Therefore, although a consistent alumina sample is used for each suite of experimental procedures, direct comparisons between experiments performed on different  $\eta$ -Al<sub>2</sub>O<sub>3</sub> samples will not necessarily yield identical results. Any differences encountered when using the two samples are likely to be a result of inconsistency in the thermal pre-treatment process. The following sections identify which series of experiments relate to which batch of catalyst.

### **Al5636 (Chapters 4 and 6)**

This is a high purity commercial-grade catalyst. Nitrogen BET chemisorption measurements were performed and revealed a surface area of  $269 \pm 9 \text{ m}^2 \text{ g}^{-1}$  and an average pore volume of  $0.29 \pm 0.02 \text{ cm}^3 \text{ g}^{-1}$ . Errors quoted represent the standard deviation in three replicate measurements. XRD analysis showed a pattern consistent with the alumina existing in the  $\eta$ -phase. This batch of  $\eta$ -Al<sub>2</sub>O<sub>3</sub> was used for the activation, pyridine adsorption and thermal desorption, and methanol TPD experiments.

### **Al5636G (Chapter 5)**

This specially prepared batch of  $\eta$ -Al<sub>2</sub>O<sub>3</sub> was used to investigate the effects of varying calcination temperature on the Lewis acid site distribution of activated  $\eta$ -Al<sub>2</sub>O<sub>3</sub> catalysts. This specially prepared batch of Al5636 had not previously been exposed to temperatures greater than 773 K.

### **Iron-based catalyst samples (Chapters 8 and 9):**

Two types of iron-based catalyst are investigated in Chapter 8 and 9. Chapter 8 concentrates on fused iron catalyst fines that were removed from a SASOL fluidised bed reactor during an industrial catalytic production cycle. Section 9 considers the atmospheric pressure hydrogenation of carbon monoxide over a precipitated haematite (Fe<sub>2</sub>O<sub>3</sub>) precursor. Further details of the source and preparation of the catalyst samples are given below:

### **SASOL catalyst fines samples (Chapter 8)**

Chapter 7 of this thesis investigates the composition and surface species present on samples of catalyst fines extracted from a fluidised bed reactor used in the Fischer-Tropsch synthesis (FTS) process. These catalysts fines are iron based particles that have degraded such that they are of dimensions too small to maintain bed fluidity; they are still intrinsically active in FTS but can no longer be fluidised. SASOL Technology UK provided two samples of these fines, which were taken from the Secunda reactor complex at Sasolburg, S.A.: one of which had undergone standard toluene Soxhlet extraction, while the other had undergone additional Soxhlet extraction in dichloromethane. These extraction processes are commonplace and are employed in order to remove heavy wax residues from the surface and pores of the catalyst [22, 23]. Although it has been shown that Soxhlet extraction can negatively affect the composition of the catalyst by encouraging the formation of  $\gamma$ -Fe<sub>5</sub>C<sub>2</sub> and Fe<sub>3</sub>O<sub>4</sub> phases [24], this extraction procedure is deemed necessary for this investigation as the high molecular weight wax residues that would otherwise occupy the surface and pores of the catalyst would dominate subsequent INS measurements and other analyses, whereas it is the properties of the underlying catalyst and strongly bound hydrocarbonaceous residue that are of primary interest to this investigation.

### **Precipitated Fe<sub>2</sub>O<sub>3</sub> catalyst (Chapter 9)**

The haematite (Fe<sub>2</sub>O<sub>3</sub>) used as the starting material in the investigations reported in Chapter 8 of this thesis was prepared by precipitation according to a procedure described elsewhere [25]. Briefly, solutions of iron nitrate (Sigma-Aldrich ≥98%, 1 mol/L) and aqueous ammonia (Sigma-Aldrich 28% in double-distilled H<sub>2</sub>O, 5.6 mol/L) were co-added to a precipitating bath containing 1L of deionised water at a rate such that the pH of the liquor was maintained at pH 8. A temperature of 343 K was maintained using a stirrer hot plate. After precipitation was complete the mixture was allowed to age at temperature for 12 h. The resultant slurry was then filtered, washed with deionised water and then calcined at 673 K for a period of 8 hours. The solid was then ground in a mortar and pestle and sieved to a fraction of 170-500 μm.

## 2.3 Alumina activation

Identical activation procedures were adopted for both alumina catalysts. Knözinger and Ratnasamy [26] report that temperatures in excess of 573 K are required to induce catalytic activity in transition aluminas. The  $\eta$ -Al<sub>2</sub>O<sub>3</sub> samples were activated by heating, *in situ*, to 623 K under flowing helium (99.999 %, BOC) for 150 min and then allowed to cool to reaction temperature. For the majority of the experimental procedures, the samples were continuously flushed with helium gas, fed to the catalyst via an in line gas purification facility (MG Oxisorb).

### 2.3.1 TGA-DSC

Simultaneous thermogravimetric analysis (TGA) and differential scanning calorimetry (DSC) was applied in order to gain an understanding of the transformations occurring to the  $\eta$ -Al<sub>2</sub>O<sub>3</sub> catalysts under the activation conditions employed throughout this investigation. For these measurements approximately 10 mg of  $\eta$ -Al<sub>2</sub>O<sub>3</sub> was used to fill the sample cup of the TGA instrument (TA Instruments SDT Q600). A temperature ramp of 10 K/min was applied to the room temperature sample until a temperature of 373 K was attained, which was maintained for a period of 1 hour. The temperature of the sample was then increased from 373 K to 623 K at a rate of 10 K/min and maintained for a period of 150 mins. The weight change and heat flow during this procedure was continuously monitored.

### 2.3.2 Infrared Spectroscopy

Infrared experiments were performed using a Nicolet Nexus FTIR spectrometer fitted with a high D\* MCT detector (128 scans, resolution 2 cm<sup>-1</sup>). Experiments were performed in diffuse reflectance mode, using a SpectraTech Smart diffuse reflectance cell and environmental chamber, using a typical sample size of *ca.* 50 mg. This arrangement is shown schematically in Figure 2.3.1. The sample cell was connected to a dual purpose vacuum manifold-gas flow apparatus that provides control of flow gases into the infrared cell. The catalyst sample was placed in a ceramic cup connected to a temperature controller in order to conduct variable temperature experiments. Catalyst samples were activated *in situ* within the environmental chamber of the infrared cell. A spectrum of KBr dried *in situ* at 373 K in high purity helium (BOC, 99.999%) served as a background spectrum. All spectra are presented as background subtractions, in which a spectrum of dried KBr has been removed from that of the activated catalyst according to the popular Kubelka-Munk

transform method [12]. No baseline or offset corrections were made.

### 2.3.3 INS - MARI

A stainless steel INS cell, described in Figure 2.3.1, was filled with  $\eta$ -Al<sub>2</sub>O<sub>3</sub> pellets (*ca.* 20g) and connected to flowing helium. A collar heater (Watlow) was used to heat the cell to 373 K in order to remove physisorbed water from the alumina contained within the cell. The temperature was maintained for a period of 150 mins. The cell was allowed to cool to room temperature before being isolated under helium, removed from the gas supply, and weighed. The cell containing the sample was cooled in liquid nitrogen and placed into the spectrometer and the INS spectrum was acquired using a number of incident neutron energies. After acquisition of the INS spectra the cell was removed from the spectrometer and allowed to return to room temperature before being reconnected to the heater and helium supply. The temperature of the cell was increased to 623 K for a period of 150 mins in order to activate the alumina catalyst. The cell was allowed to return to room temperature under helium flow before being isolated and weighed. The cell was then reintroduced to the spectrometer where INS spectra were recorded at several incident energies.

### 2.3.4 XRD

XRD patterns of the catalyst after being dried at 373 K and after being activated at 623 K were carried out in order to determine if the activation procedure was sufficient to provoke structural changes in the bulk crystal structure of the alumina catalyst. A quantity of the catalyst (Al5636) was deposited into the sample cup of an *in situ* XRD reaction cell (Anton Paar XRK 900 reactor chamber). The temperature of the cell was increased to 373 K for a period of 10 h under flowing argon using a dedicated temperature controller unit (Anton Paar TCU 750), and allowed to return to room temperature before the XRD pattern was acquired. The temperature of the cell was then increased to 623 K for a period of 150 mins and allowed to return to room temperature before the XRD pattern was acquired. Both diffractograms were recorded using a Siemens D5000 powder diffractometer using Cu K $\alpha$  radiation in Bragg-Brentano geometry in the range 10-70° 2 $\theta$ .

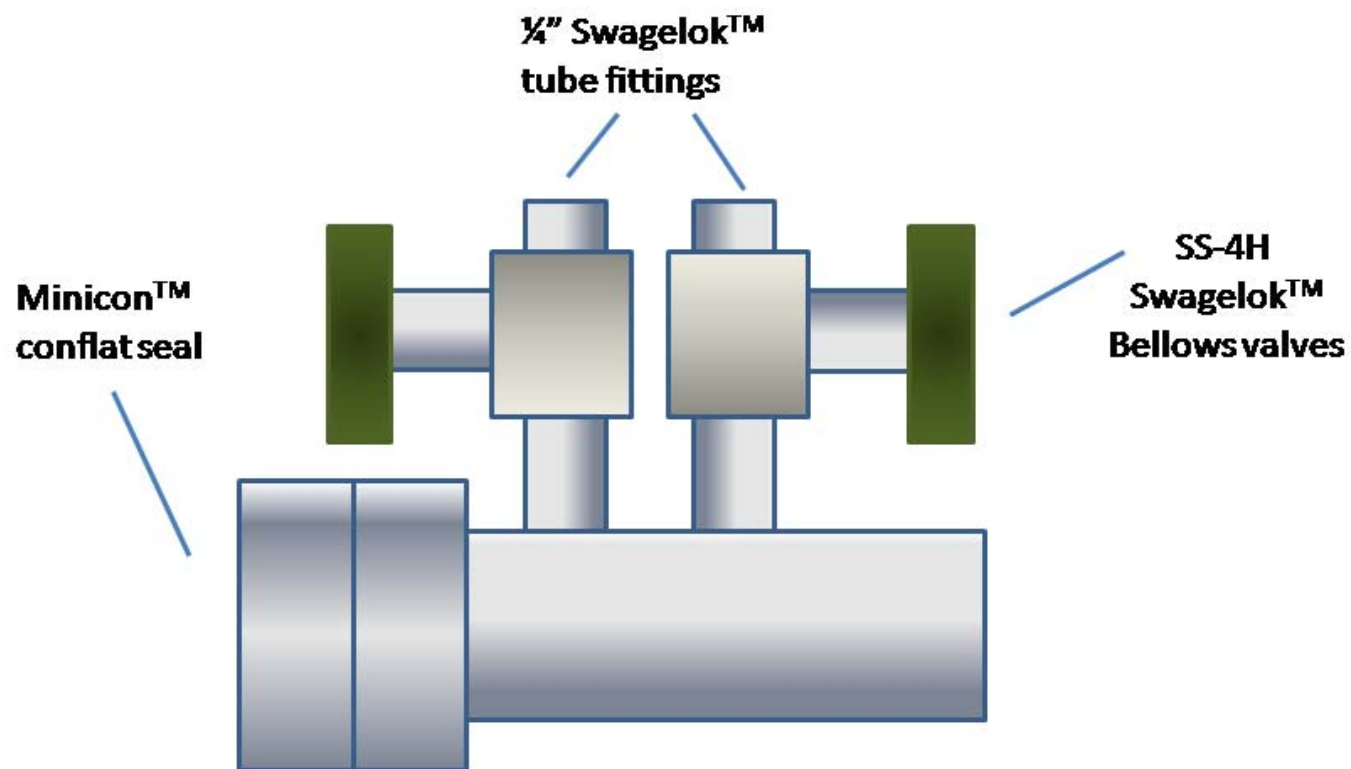


Figure 2.3.1: Schematic diagram of the stainless steel reaction cell used for sample preparation in the MARI INS measurements.

## 2.4 Pyridine adsorption/desorption on activated alumina

### 2.4.1 Temperature Programmed Desorption (TPD)

TPD measurements were performed for methanol on activated  $\eta$ -Al<sub>2</sub>O<sub>3</sub>. The results are presented in Section 3.5.2. These experiments were performed with the catalyst sample (*ca.* 0.1 g) contained within a packed bed tubular reactor (1/4" stainless steel tubing) located within a temperature programmable oven (Neytech 25 PAF). A mass spectrometer (Leda Mass Gas Analyser, LM22, closed ion source) sampled the eluting gases via a differentially pumped capillary line and a precision leak. The alumina sample was activated and subsequently dosed with pulses of methanol (Sigma-Aldrich 99.8%) vapour (as outlined previously for pyridine (Section 2.0.1)), using high purity helium (99.999%, BOC) as a carrier gas. Saturation of the sample was observed by monitoring the eluent stream on the mass spectrometer. TPD measurements were carried out using the temperature programmable oven set at a heating rate of 8 K min<sup>-1</sup>. The eluent stream from the reactor was monitored by the mass spectrometer at all times during the TPD experiment. The following masses were recorded during experiments:  $m/z$  18 (H<sub>2</sub>O);  $m/z$ : 45 (dimethyl ether);  $m/z$  31 (methanol).

### 2.4.2 Infrared spectroscopy

As with the alumina activation studies (Section 2.2.2), infrared measurements were performed using a Nicolet Nexus FTIR spectrometer fitted with a high D\* MCT detector (128 scans, resolution 2 cm<sup>-1</sup>). Catalyst samples were activated *in situ* within the environmental chamber of the infrared cell. In this case, a spectrum of the activated catalyst served as a background spectrum. Pyridine (Aldrich, 99.9+ %) vapour, purified by vacuum distillation and freeze-pump-thaw procedures, was dosed onto the catalyst contained within the environmental cell using pulse flow techniques [27, 28] at 373 K. The elevated temperature used for pyridine adsorption prevented retention of physisorbed material and is expected to yield a chemisorbed adlayer on alumina [8]. The geometric arrangement of the cell meant that dosing was associated with a substantial degree of gas by-pass. Ancillary experiments confirmed that a 10 min delay after each dosing pulse was sufficient for the adsorbent to be completely removed from the environmental chamber. Spectra were recorded (128 scans, resolution 2 cm<sup>-1</sup>) at 293 K, requiring cooling after dosing during pyridine experiments.

For desorption experiments, the cell containing alumina previously dosed with pyridine was heated under flowing He (BOC, 99.999%). The cell was maintained at each

temperature for 10 min before being cooled to room temperature where a spectrum was recorded. Subsequent XRD experiments (Chapter 4) indicated the alumina to retain its  $\eta$ -phase throughout the temperature range applied in these experiments. Where recorded, infrared band areas were determined using a Gaussian fitting function available within the Origin (Version 6.1) graphical software package [29].

### **2.4.3 INS spectroscopy - TOSCA**

A stainless steel INS cell, described in Figure 2.4.1, was filled with  $\eta$ -Al<sub>2</sub>O<sub>3</sub> pellets (*ca.* 20 g) with a quartz wool plug at both ends and connected to flowing helium. A collar heater (Watlow) was used to heat the cell to 623 K in order to activate the alumina contained within the cell. The temperature was maintained for a period of 150 mins. After activation the cell was allowed to cool to room temperature before being isolated under helium, removed from the gas supply, and weighed. The cell containing the sample was cooled in liquid nitrogen and placed into the spectrometer. The INS spectrum of the activated alumina was collected and used as a background spectrum that could be subtracted from subsequent spectra containing adsorbed pyridine to provide the INS spectrum of adsorbed pyridine.

After collection of the INS spectrum the stainless steel INS cell was removed from the spectrometer and allowed to return to room temperature before being reconnected to the helium supply with an in line pyridine bubbler, as previously shown in Figure 2.1.2. The heater was reconnected and the temperature of the cell increased to 373 K. The helium flow was then diverted through the pyridine bubbler to allow pyridine vapour to flow through the INS cell containing activated alumina. The flow was then switched back to helium only for a period of 30 mins before the cell was isolated and reweighed. The cell was then cooled in liquid nitrogen and returned to the spectrometer where a second spectrum was acquired.

The INS cell containing activated alumina saturated with pyridine vapour was then returned to the helium supply and heater, where the temperature of the cell was increased to 473 K for a period of 30 mins. The cell was then isolated, weighed, and returned to the spectrometer where a final spectrum was recorded.

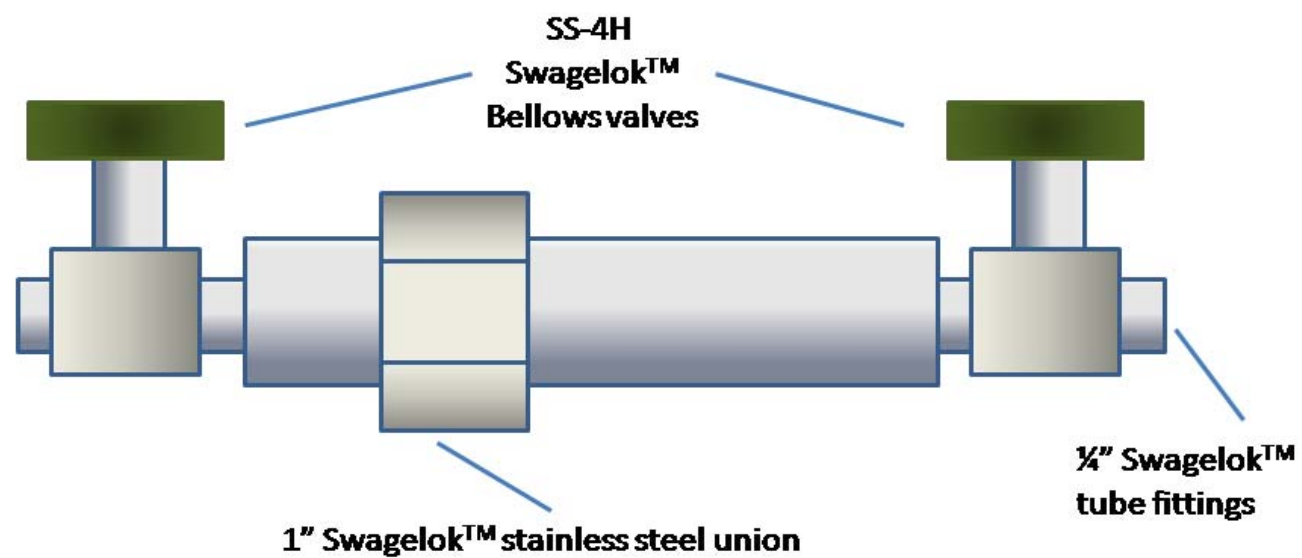


Figure 2.4.1: Schematic diagram of the stainless steel reaction cell used for sample preparation in the TOSCA INS measurements.

## 2.5 Calcination of $\eta$ -Al<sub>2</sub>O<sub>3</sub>

Samples of the as received Al5636G were calcined in alumina boats held within a temperature programmable tube furnace (Carbolite, Eurotherm 2416) for a period of 60 mins at 773 K, 923 K, 1073 K, and 1173 K. A combination of x-ray diffraction (XRD), nitrogen adsorption isotherms (BET), and infrared spectroscopic measurements was employed in order to investigate the physical changes occurring within the structure of an  $\eta$ -Al<sub>2</sub>O<sub>3</sub> catalyst under these different thermal pre-treatment conditions and the effect this has on the identity and relative populations of the Lewis acid sites expressed at the catalyst surface.

### 2.5.1 Infrared – pyridine

Each of the differently calcined  $\eta$ -Al<sub>2</sub>O<sub>3</sub> catalyst samples was activated at 623 K in flowing helium for a period of 150 mins using the environmental reaction cell. The sample was allowed to cool to room temperature before the spectrum of the activated catalyst was acquired, which was used as a background spectrum. The catalysts were then dosed with pyridine vapours at 373 K using pulse flow techniques [27, 28] until saturation was achieved. The cell was allowed to return to room temperature and the infrared spectrum of a saturated overlayer of pyridine on each of the differently calcined alumina catalysts was then acquired as outlined in Section 2.3.2.

### 2.5.2 XRD

Samples (*ca.* 1 g) of the calcined alumina catalysts were ground in a mortar and pestle and then pressed into a silicon sample holder before XRD patterns were acquired using a Siemens D5000 powder diffractometer using Cu K<sub>α</sub> radiation in Bragg-Brentano geometry in the range 10-90° 2 $\theta$ .

### 2.5.3 BET

A Miromeritics Gemini 2370 instrument was used to measure the surface area and pore size distribution of the range of differently calcined  $\eta$ -Al<sub>2</sub>O<sub>3</sub> catalysts. A small quantity of sample (*ca.* 0.06 g) was placed into a test tube, the weight of which was accurately known. The sample and test tube were placed in a heating block at 384 K for 48 h under a nitrogen

atmosphere. This procedure ensured that the catalyst was perfectly dry before measurements were made to ensure that adsorbed water did not impede the experiment. The sample was then weighed before being automatically analysed by the instrument using the BET method [30] using nitrogen adsorption at liquid nitrogen temperatures (77 K). The pore size distribution was analysed using the BJH technique [31].

## **2.6 Analysis of SASOL catalyst fines samples**

### **2.6.1 Raman scattering spectroscopy**

Raman spectra of the SASOL catalysts fines and a sample of  $\text{Fe}_2\text{O}_3$  that had previously been subjected to methanation conditions were acquired. A sample of each catalyst was diluted at a 1:10 ratio in a KBr matrix before being pressed into a disc. Raman spectra of each sample were acquired using a custom built Raman spectrometer equipped with a holographic Notch filter, a spectrograph with a holographic grating and a back-thinned CCD detector. A continuous wave diode-pumped solid state laser emitting at 532 nm was used at a power of 20 mW for all measurements.

### **2.6.2 Infrared spectroscopy**

Infrared spectra of the SASOL catalyst fines were acquired by first diluting the sample in a 1:10 ratio with dry KBr. The powder was then ground in a mortar and pestle before being deposited in the sample cup of the environmental cell. Spectra were recorded with a resolution of  $1\text{ cm}^{-1}$  for 512 scans. All spectra are presented as difference spectra, where the spectrum of KBr dried *in situ* at 373 K has been removed from that of the catalyst sample.

### **2.6.3 INS – TOSCA**

For each sample, approximately 25g of catalyst was weighed into aluminium sachets and placed into an aluminium INS cell sealed with indium wire. The sample was cooled in liquid nitrogen before being introduced to the spectrometer. The INS spectra were then acquired over a period of *ca.* 16 h.

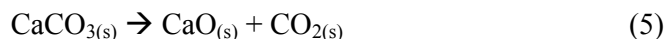
## 2.6.4 TPO

Temperature programmed oxidation (TPO) measurements were used in order to detect and quantify the carbonaceous deposits present in the catalyst fines samples. For each sample, a small quantity (*ca.* 50 mg) was deposited in a quartz U-shaped reactor cell fitted with a quartz sinter (Figure 2.6.1) and subjected to flowing oxygen (5% O<sub>2</sub>/He, 50 mL/min) while a linear heating ramp (10 K/min) up to 1200 K was applied. The eluting gases were sampled via an online differentially pumped quadrupole mass spectrometer. Online quadrupole mass spectrometry presents an ideal method for application of TPO measurements due to the fact that CO<sub>2</sub> evolution can be selectively analyzed by measuring the *m/z* 44 fragment.

The amount of carbon oxidised from each sample was determined by quantification of the CO<sub>2</sub> produced via the *m/z* 44 signal. In order to quantify the evolved CO<sub>2</sub> the TPO apparatus was first calibrated using reference standards of graphite (Sigma-Aldrich, purum, powder) and calcium carbonate (BDH, 98%).

### 2.6.4.1 Calibration of the TPO apparatus

The temperature programmed oxidation of graphite (Equation 4) and the temperature programmed decomposition of calcium carbonate (Equation 5) were each used in order to quantify the response of the mass spectrometer to evolved CO<sub>2</sub>. For graphite oxidation, the fact that no graphite residue was observed in the reaction chamber of the TPO apparatus after each measurement and that the ratio of the *m/z* 44 and *m/z* 28 signals was of the correct value for the cracking pattern of CO<sub>2</sub> (*m/z* 44 = 100%, *m/z* 28 = 8%), indicated that complete oxidation of the graphite samples had taken place. Stacked plots of the TPO profiles for graphite and CaCO<sub>3</sub> samples are presented in Figures 2.6.2 and 2.6.3, respectively.



The integrated area under the CO<sub>2</sub> peak produced in each case was determined using the calculus function within the Origin<sup>TM</sup> graphing program [29]. In this manner, the mass spectrometer response was found to be linear with respect to the number of moles of

carbon dioxide expected to be evolved from complete oxidation of graphite and complete decomposition of  $\text{CaCO}_3$ . The calibration curve produced from correlation of the area under the  $\text{CO}_2$  peak yielded by each sample and the number of moles of carbon contained in each sample is presented in Figure 2.6.4. Data associated with graphite oxidation measurements are represented by black squares while data associated with  $\text{CaCO}_3$  decomposition measurements are represented by red circles. The response factor yielded from this calibration curve ( $2.5113 \times 10^{-3}$  a.u./mol<sub>carbon</sub>) was used to quantify the TPO (temperature programmed oxidation) profile of each of the extracted catalyst fines samples.

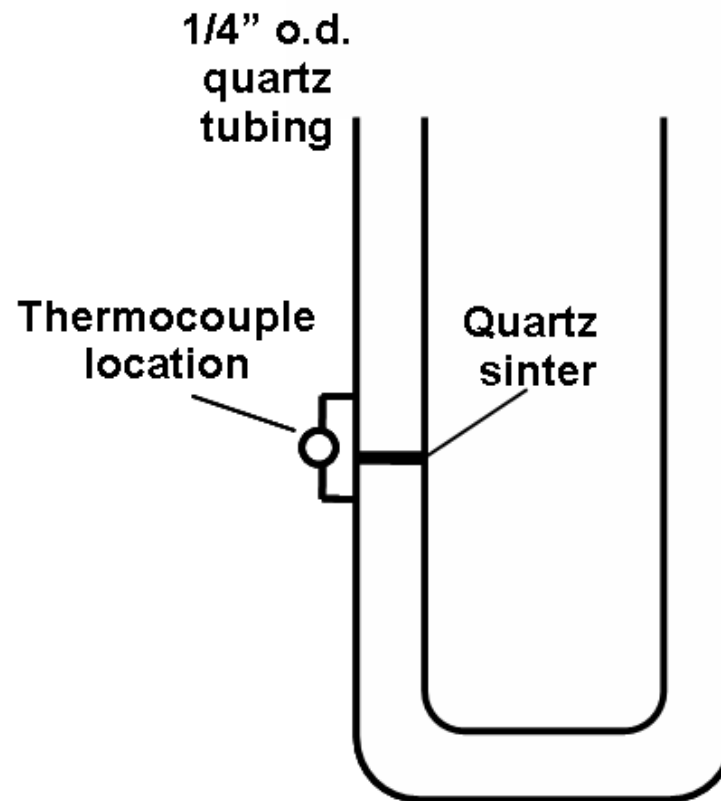


Figure 2.6.1: Schematic diagram of quartz reactor used for microreactor reaction testing and temperature programmed oxidation (TPO) measurements.

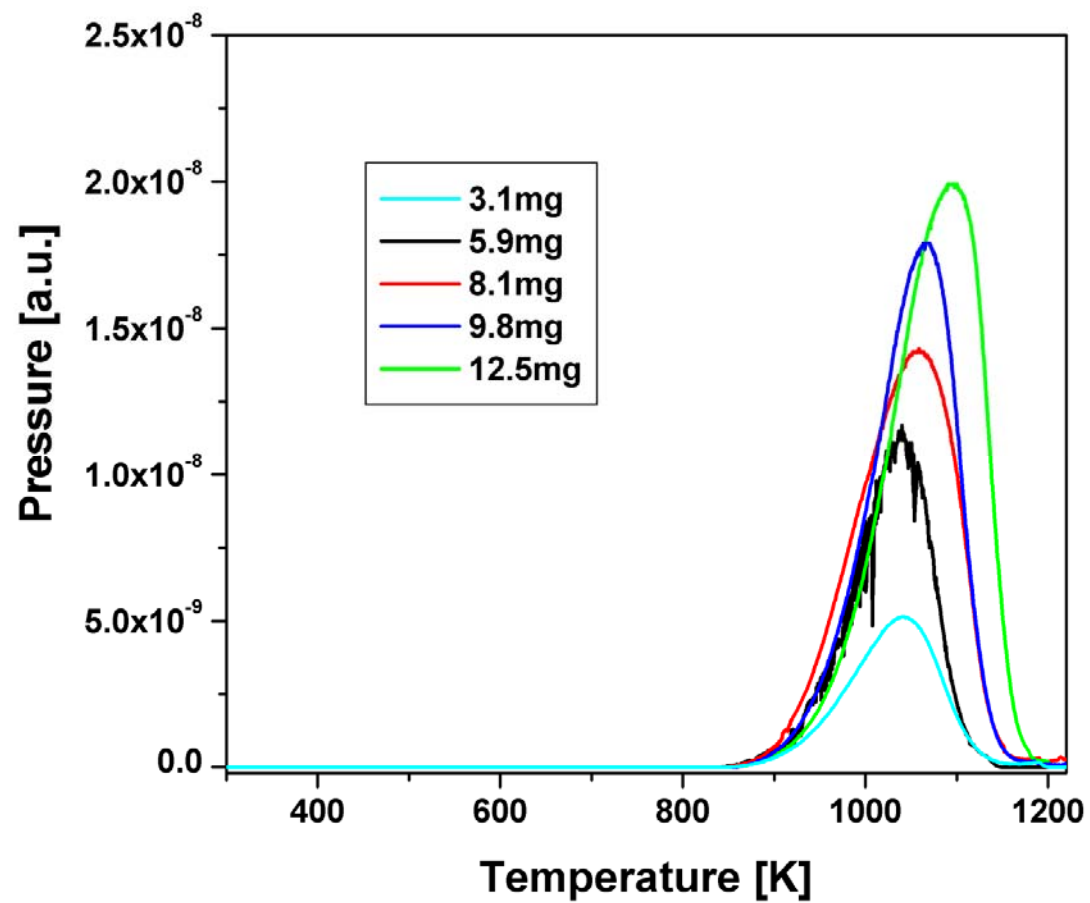


Figure 2.6.2: Stacked plot of temperature programmed oxidation profiles for various masses of graphite powder.

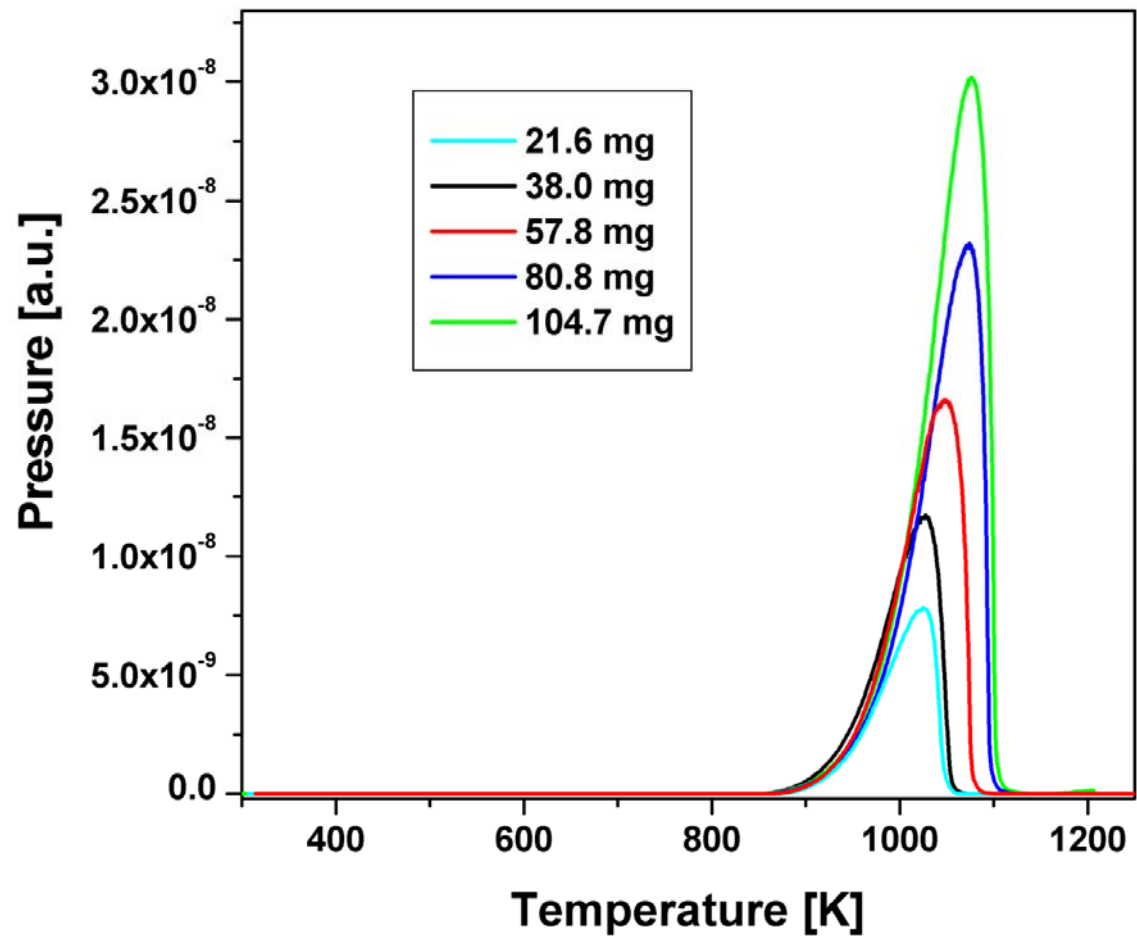


Figure 2.6.3: Stacked plot of temperature programmed decomposition (TPO) profiles for various masses of  $\text{CaCO}_3$ .

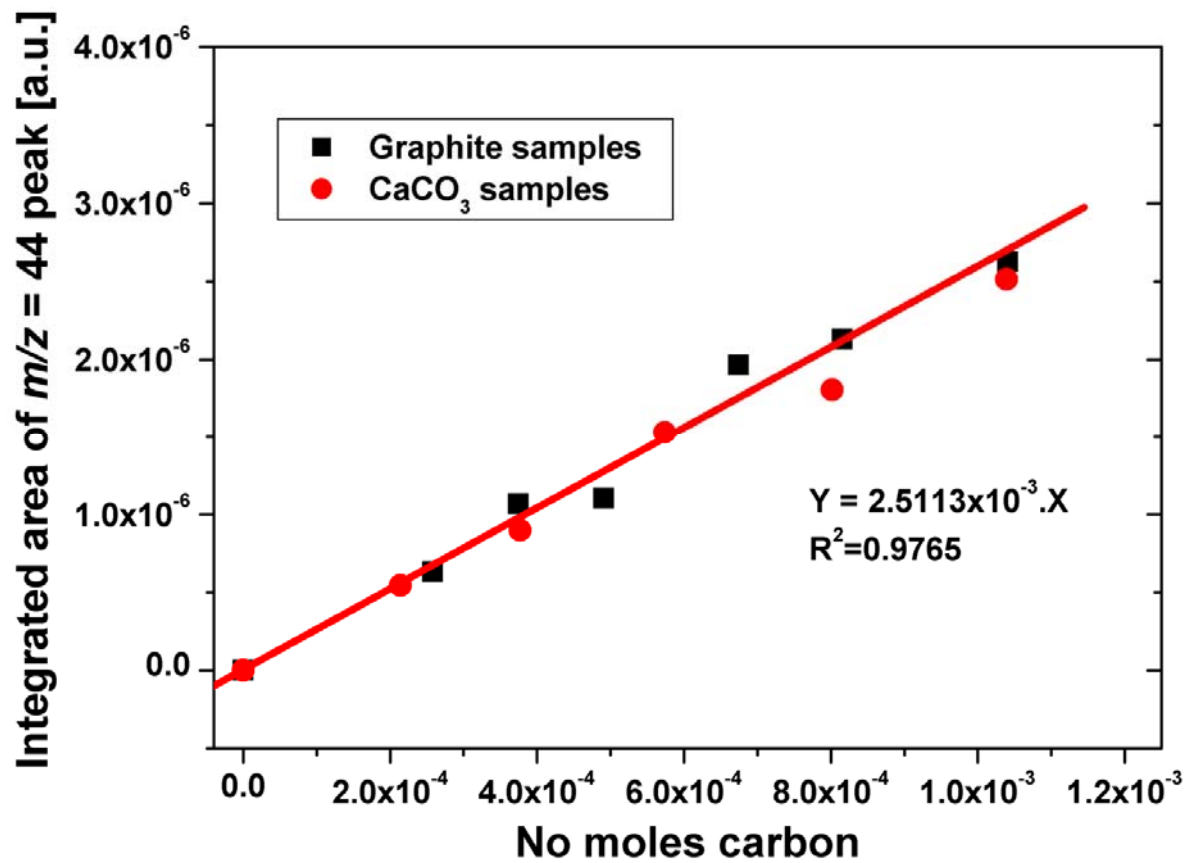


Figure 2.6.4: Calibration curved for integrated area under  $m/z = 44$  curve after oxidation of graphite and decomposition of calcium carbonate against the number of moles of carbon in each of the samples.

### 2.6.5 TEM

The microstructure of the catalyst fines samples was studied by transmission electron microscopy (TEM) using a Tecnai T20 microscope, with an accelerating voltage of 200 keV, fitted with a Gatan image filter. Samples were dispersed in methanol before being deposited on carbon film (300  $\mu\text{m}$  mesh grid, Agar scientific).

## 2.7 Analysis of post-reaction CO hydrogenation catalyst samples

The hydrogenation of carbon monoxide was performed over an iron oxide precursor at atmospheric pressure at two different temperatures. Post reaction catalyst samples were analysed by a combination of various techniques.

### 2.7.1 Microreactor catalyst testing

For each of the reaction testing experiments a sample of the precipitated  $\text{Fe}_2\text{O}_3$  precursor was loaded into a U-shaped quartz microreactor, previously described in Figure 2.6.1, which was housed within a thermostatically controlled furnace (Neytech 25PAF). Samples were treated with a 2:1  $\text{H}_2/\text{CO}$  mixture diluted in helium ( $\text{CO}$ , 3.35 mL/min;  $\text{H}_2$ , 6.75 mL/min; He, 21.25 mL/min). These conditions provide a total weight hourly space velocity (WHSV), which is defined as the weight of feed flowing per unit weight of the catalyst per hour [32], of  $10.4 \text{ h}^{-1}$ . A linear heating program of 5 K/min was applied up to the stated reaction temperature, where the temperature of the system was maintained for a period of 6 h. The heating program was then terminated and the catalyst sample was allowed to cool to room temperature under a flow of the reactant gases. The eluting gases were continuously monitored by online quadrupole mass spectrometry.

In cases where the catalyst was reduced prior to syngas exposure, a sample (*ca.* 50 mg) of  $\text{Fe}_2\text{O}_3$  was loaded into the quartz microreactor and subjected to flowing diluted  $\text{H}_2$  (30% $\text{H}_2/\text{He}$ , 30 mL/min). A heating program of 10 K/min was applied until the temperature of the sample reached 773 K, where the temperature was maintained for a period of 60 mins.

For the temperature programmed reaction measurements, the response of the online quadrupole mass spectrometer was first calibrated for the main reactant and product gases in the carbon monoxide hydrogenation reaction. The calibration curves for each of CO, H<sub>2</sub>, and CH<sub>4</sub> are presented in Figures 2.7.2-2.7.4. Calibration of the mass spectrometer in this manner allowed the gases evolved during the reaction to be quantified, which is essential for the determination of accurate values for methane selectivity and yield. Selectivity to a reaction product is the quotient of the amount of reaction product  $Q_R$  and the amount of a converted feedstock component  $Q_C$ , as described in Equation 6 [33]:

$$Selectivity (\%) = \frac{Q_R}{Q_C} \times 100 \quad (6)$$

The conversion of a reaction component is the quotient of the amount reacted  $Q_C$  and the initial quantity of the reactant  $Q_F$ , as described in Equation 7 [33]:

$$Conversion (\%) = \frac{Q_C}{Q_F} \times 100 \quad (7)$$

Conversion, selectivity and yield are interrelated by Equation 8 [33]:

$$\frac{Conversion \times Selectivity}{100} = Yield \quad (8)$$

Quadrupole mass spectrometers exhibit different response factors for each mass analysed. Thus, using the mass spectrometer response to determine product selectivity and yield, where the measurement of mass spectrometer signals of potentially different relative sensitivities is required, could therefore lead to inaccurate measurements unless the instrument is calibrated.

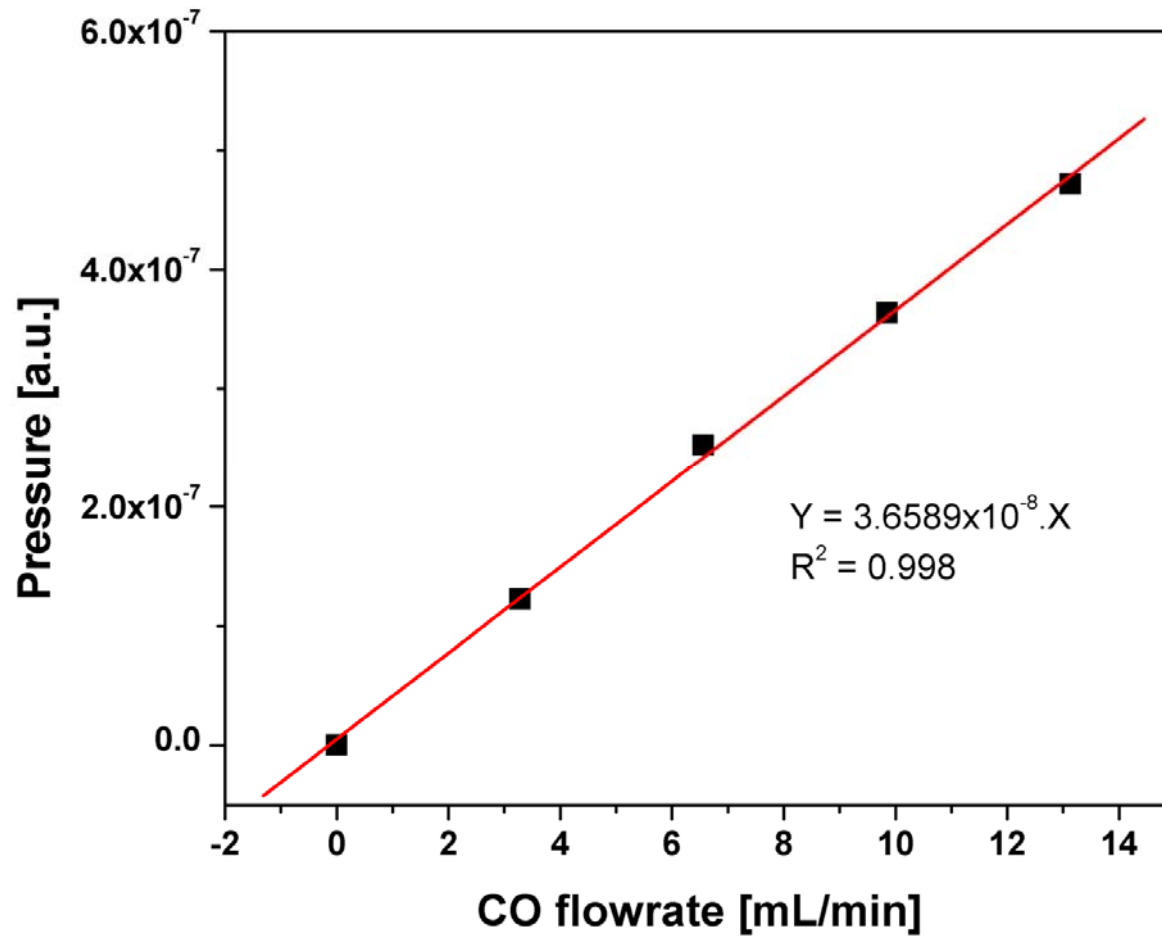


Figure 2.7.2: Calibration curve for mass spectrometer response to various flowrates of CO.

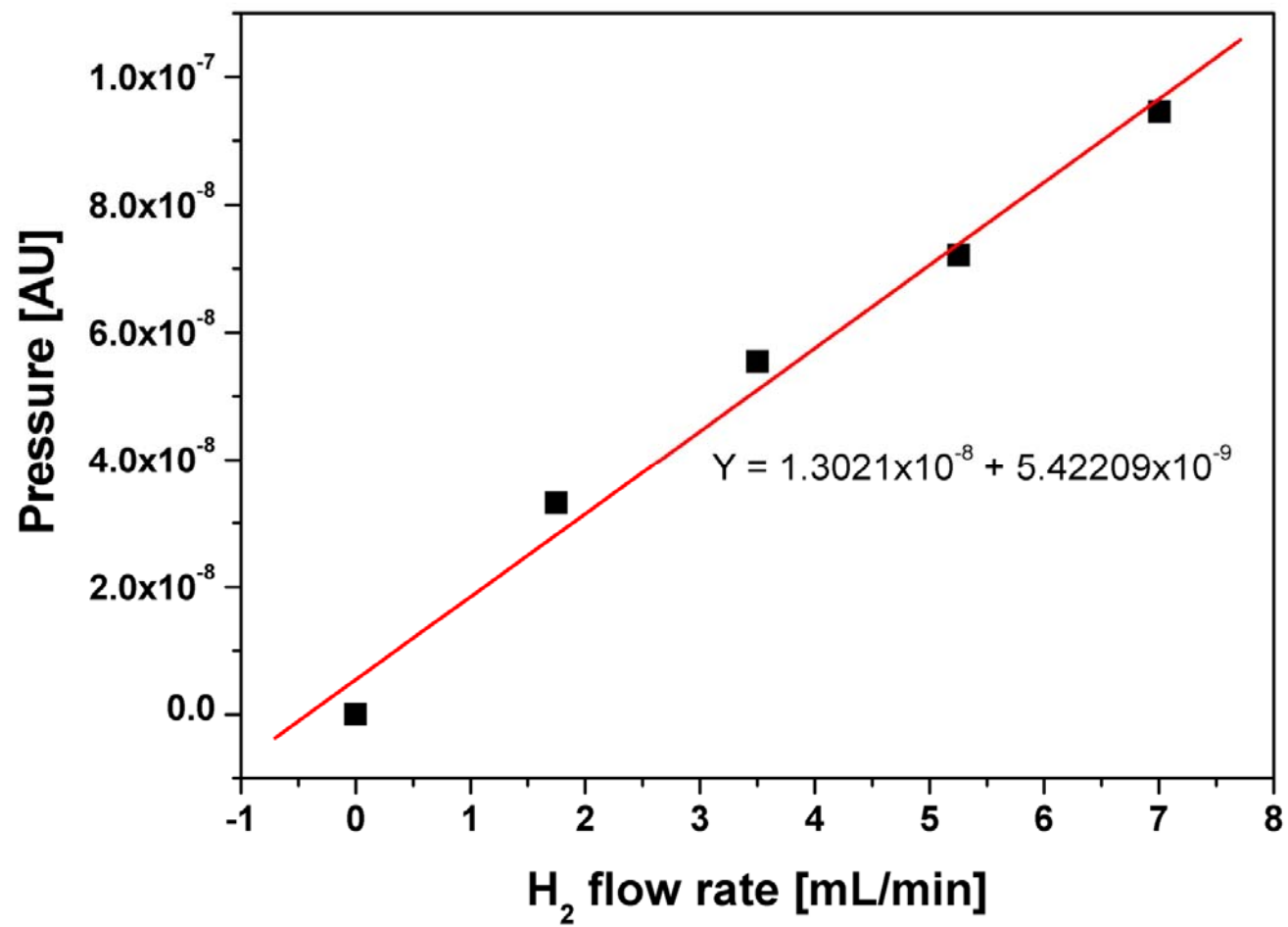


Figure 2.7.3: Calibration curve for mass spectrometer response to various flowrates of H<sub>2</sub>.

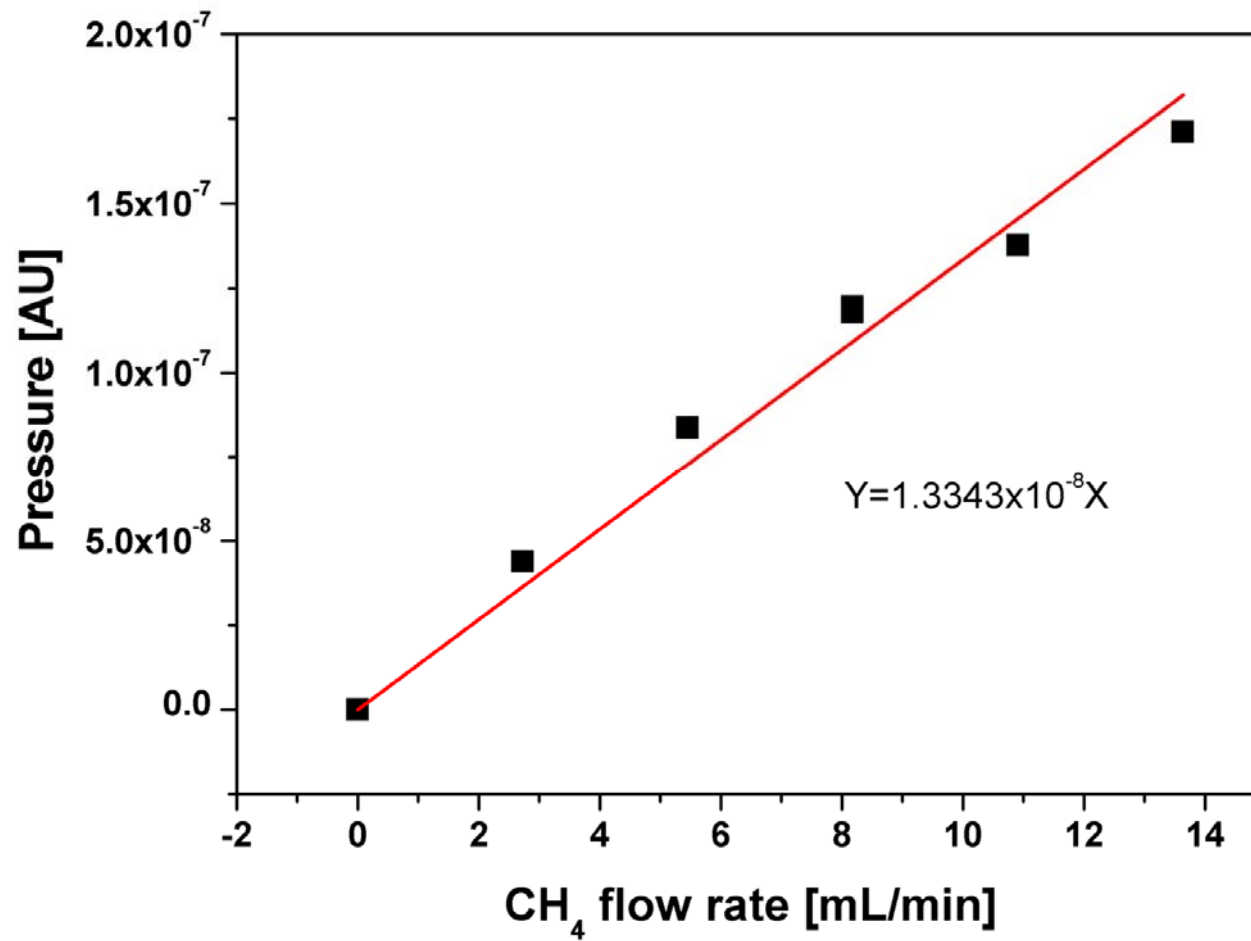


Figure 2.7.4: Calibration curve for mass spectrometer response to various flowrates of CH<sub>4</sub>.

### 2.7.2 Scale-up of microreactor

In order to produce a sufficient quantity of sample for the post-reaction analyses (particularly the INS measurements), the reactions had to be repeated using a much larger reactor. Approximately 30g of  $\text{Fe}_2\text{O}_3$ , sieved to a grain size range of 250-500  $\mu\text{m}$  to minimize plugging of the catalyst bed, was loaded into a  $\frac{3}{4}$ " diameter quartz U-shaped tubular reactor fitted with a ground quartz sinter (shown in Figure 2.7.5), contained within a bucket furnace packed with quartz wool to minimize thermal gradients. The reactor was connected to the large scale gas handling system, previously described in Figure 2.1.3, using Cajon<sup>TM</sup> compression fittings.

Reduction, where performed, was carried out in a flow of  $\text{H}_2$  diluted in He (25%  $\text{H}_2/\text{He}$ , 1L/min) until  $\text{H}_2\text{O}$  evolution, as measured using online quadrupole mass spectrometry, subsided (*ca.* 2 hours). Reactions were carried out using 2:1  $\text{H}_2/\text{CO}$  mixture diluted in helium ( $\text{CO}$ , 75 mL/min;  $\text{H}_2$ , 150 mL/min; He, 775 mL/min; total WHSV =  $0.98 \text{ h}^{-1}$ ) and subjected to a linear heating program of 5 K/min up to the stated reaction temperature. After a period of 6h at the stated reaction temperature the catalyst was allowed to cool to room temperature under a flow of the diluted reactants. The reactor was then purged with flowing helium to remove residual gaseous species before being isolated and transferred to an argon filled glovebox (MBraun custom series). A small quantity of post-reaction catalyst sample was reserved for XRD analysis while the remainder was loaded into aluminium sachets that were then secured in a standard aluminium INS cell [14]. Care was taken to position the sachets inside the cell such that the entire catalyst sample was contained within the boundaries of the neutron beam path (40 x 40 cm) when introduced to the INS spectrometer.

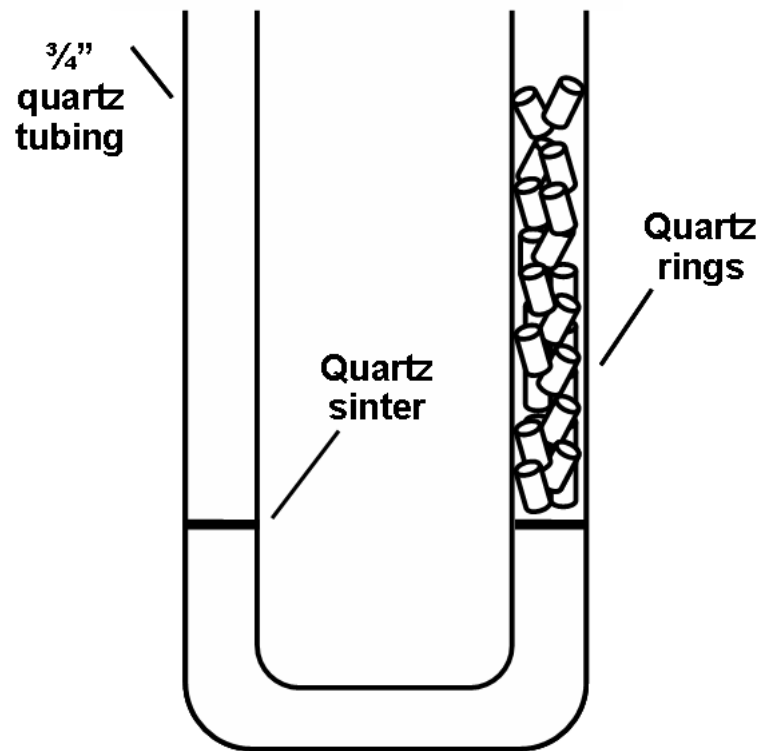


Figure 2.7.5: Schematic diagram describing the quartz reactor used for preparing iron CO hydrogenation catalyst samples for INS measurements.

### **2.7.3 Raman spectroscopy**

The Raman spectrum of a selected sample of iron-based catalysts after exposure to syngas at 723 K for a period of 6 h was acquired in the same manner as the SASOL catalyst fines sample, as described in Section 2.6.1.

### **2.7.4 Infrared spectroscopy**

The infrared spectrum of a selected sample of iron-based catalysts after exposure to syngas at 723 K for a period of 6 h was acquired in the same manner as the SASOL catalyst fines sample, as described in Section 2.6.2.

### **2.7.5 INS spectroscopy**

#### **2.7.5.1 TOSCA**

INS spectra of the  $\text{Fe}_2\text{O}_3$  starting material and a sample of  $\text{Fe}_2\text{O}_3$  after exposure to syngas at 723 K for a period of 6h were acquired using the TOSCA spectrometer. The samples were cooled in liquid nitrogen before being introduced to the spectrometer. The INS spectrum was then acquired at <40 K. After a collection time of *ca.* 16 h the spectrum of the post-reaction catalyst sample still exhibited poor signal-to-noise, indicating the sample to contain a low hydrogen content, and the decision was taken to terminate the experiment.

#### **2.7.5.2 MAPS**

Spectra of the  $\text{Fe}_2\text{O}_3$  starting material and post-reaction samples were recorded using the MAPS spectrometer. The Fermi chopper was phased such that INS spectra were recorded with incident neutron energies of  $4840 \text{ cm}^{-1}$  (600 meV) and  $2017 \text{ cm}^{-1}$  (250 meV). The INS spectra were processed using only data collected from the low angle detector banks (<30°) so that fundamental modes were accentuated and overtone modes minimised.

### **2.7.6 Post-reaction Temperature Programmed Oxidation**

The carbon present in post-reaction catalyst samples was analysed using TPO in the same manner as the SASOL catalyst fines sample, as described in Section 2.5.4.

### **2.7.7 XRD**

Samples (*ca.* 1 g) of the iron-based catalysts after exposure to syngas at various temperatures were ground in a mortar and pestle and then pressed into a silicon sample holder before the XRD patterns were acquired in the same manner as previously described for SASOL catalyst fines samples.

### **2.7.8 TEM**

Samples of iron-based catalysts after exposure to syngas at various temperatures were ground in a mortar and pestle before being dispersed in methanol and analysed by TEM as previously described for the SASOL catalyst fines samples (Section 2.6.5).

# 3

## Chapter 3

### Activation and surface Lewis acidity of transition alumina catalysts

In normal circumstances the term ‘alumina’ plainly refers to the thermodynamically stable corundum phase, otherwise known as  $\alpha\text{-Al}_2\text{O}_3$  [24].  $\alpha\text{-Al}_2\text{O}_3$  is the ultimate product of the thermal treatment of all aluminium oxides and aluminium hydrate systems [34, 35]. However, in terms of heterogeneous catalysis and surface chemistry the term ‘alumina’ also refers to the transition forms of alumina. The structure and chemical properties of these so-called transition aluminas are known to be dependent upon parameters such as the source material, preparative route, purity of the reagents, extent of dehydration, and thermal history [32, 36]. Different transition forms can be expressed, depending on the ore and conditions that are used in the production process [34] as shown in Diagram 3.0.1:

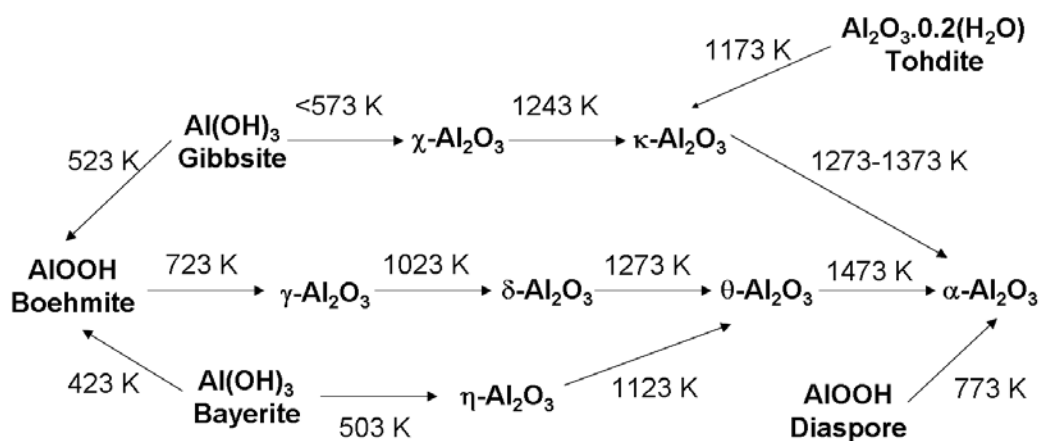


Diagram 3.0.1: Thermal phase diagram for the conversion and interconversion of aluminium oxides and hydroxides (adapted from references [34, 37]).

Transition aluminas, in various forms, are ubiquitous in heterogeneous catalysis and can be generally characterised as metastable phases of low crystallinity with a high surface area and porosity and, partly, for these reasons are the only aluminium oxides of practical interest for catalytic applications [8]. In industrial practice, aluminas are usually employed as support materials to stabilise metal crystallites of small dimensions primarily due to their high mechanical stability and perceived relative inertness towards the reaction medium. In addition, transition alumina supports permit a high degree of metal dispersion in comparison to other metal oxides [38]. Transition aluminas are also prevalent within industry due to their low cost and wide availability. Although transition aluminas are most widely used as catalyst support materials, they also find applications within industry as active catalysts in their own right, albeit to a lower extent, catalysing reactions such as the isomerisation of hydrocarbons [38], and the synthesis of methyl chloride from methanol

[39-42]. However, transition aluminas are more often employed as active catalysts in academic research, where applications such as alkene isomerisation [43-48], alcohol dehydration [49, 50], ortho-para hydrogen conversion [51], and isotopic scrambling [45, 52, 53] processes have been reported. The vast majority of academic research on the catalytic properties of transition aluminas has been carried out on  $\gamma$ -Al<sub>2</sub>O<sub>3</sub> due to its prevalence as a support material in important industrial processes [26]. However, research concerning  $\eta$ -Al<sub>2</sub>O<sub>3</sub> also maintains a significant presence within the literature due to its superior solid acid properties compared to  $\gamma$ -Al<sub>2</sub>O<sub>3</sub> [54]. Transition aluminas possess weak Brønsted acidity due to the presence of hydroxyl groups upon its surface. However, for industrial processes it is the intrinsic Lewis acidity of the transition aluminas, imparted by the presence of coordinatively unsaturated Al<sup>III</sup> centres generated under activation conditions, which is usually emphasized.

### 3.1 Activation of transition aluminas

Normally, for transition aluminas to become catalytically active they must first be subjected to specific activation conditions [26]. Activation of transition alumina catalysts is generally understood to proceed by a dehydroxylation-dehydration mechanism, which leads to the genesis of coordinatively unsaturated oxygen anions and aluminium cations (Al<sup>3+</sup>)[26]. In most instances, coordinatively unsaturated sites are responsible for chemisorption and binding of molecules to a surface. This explains phenomena such as catalyst poisoning, competitive adsorption and the common requirement of heating an oxide to activate it for chemisorption and catalysis. An increase in surface dehydroxylation leads to greater surface unsaturation and has been shown to be directly related to an increase in catalytic activity [51]. This process can be initiated by heating of the material in a vacuum [55] or in a flow of inert gas [38]. The extent of dehydroxylation of metal oxides is known to increase with activation temperature, as has been reported for ZnO [56] and Cr<sub>2</sub>O<sub>3</sub> [54, 57]. A mechanism has been proposed that is common to many metal oxides [54], and is described below:

Metal-oxygen bonds must be broken in the cleavage of a metal oxide crystal. During this process surface anion and cation pairs are created, as described by Lavalley *et al.* [58], which have fewer nearest neighbours than the corresponding ions in the bulk. By definition, such surface ions are coordinatively unsaturated. The coordinatively unsaturated

(cus) metal site,  $M^{n+}$ , behaves as a Lewis acid while the  $O^{2-}$  (cus) ion is more basic than bulk ions. This arrangement is highly strained and results in a chemically active surface. If such a coordinatively unsaturated surface is exposed to water, *i.e.* atmospheric water vapour, then heterolytic dissociative adsorption will occur resulting in the generation of surface hydroxyl groups. Associative adsorption may also take place resulting in the generation of chemisorbed water molecules, which in some metal oxides, *e.g.* titania, can account for up to 50% of the surface layer [8]. An activated oxide surface therefore becomes fully covered with adsorbed water and hydroxyl groups upon exposure to moisture in the atmosphere, *i.e.*:



Conversely, heating of a metal oxide crystal can cause desorption of molecularly adsorbed water molecules and can induce condensation of neighbouring surface hydroxyl groups resulting in further desorption of water and, consequently, the regeneration of coordinatively unsaturated surface ions. Thus, activation of a metal oxide catalyst by heating is required because of the strong, dissociative adsorption of water on exposed metal oxide surfaces.

### 3.2 Acidity of transition aluminas

The dehydration and dehydroxylation of transition aluminas, which results in the genesis of coordinatively unsaturated centres, is a necessary step before the material becomes catalytically active. The coordinatively unsaturated  $Al^{III}$  centres sites are responsible for the Lewis acidity that is necessary for the catalytic function of transition aluminas in several reactions, including: methanol dehydration to form dimethylether [59]; hydrocarbon isomerisation [8]; and the conversion of alkyl ester side products and other high boiling point condensation products in, for example, the oxo process [60]. Literature concerning the Lewis acidity of transition alumina catalysts is well-established and several articles catalogue historical advances in its determination and characterisation has been catalogued [8, 26]. Transition aluminas are also expected to exhibit a small degree of Brønsted acidity, although investigations into this property are poorly represented in the literature [61, 62]. Both types of acid function in transition alumina are discussed in greater detail below:

### 3.2.1 Lewis acidity of transition aluminas

Generation of Lewis acidity in transition aluminas is achieved by the removal of hydroxyl groups and/or water from the surface, thereby revealing coordinatively unsaturated  $\text{Al}^{\text{III}}$  centres. Activation of the surface in this way can be achieved by heating the alumina substrate to elevated temperatures in either a vacuum or a flow of inert gas. Experiments performed by MacIver *et al.* [45] regarding the isomerisation of 1-pentene over  $\eta\text{-Al}_2\text{O}_3$  and  $\gamma\text{-Al}_2\text{O}_3$  catalysts indicate that catalytic activity increases as a function of activation temperature and that a threshold temperature of around 573-673 K must be surpassed in order for the development of catalytic activity. Completely analogous results were described elsewhere by van Cauwelaert and Hall [51]. While the dehydroxylation/dehydration mechanism by which Lewis acid sites are generated in transition aluminas is generally accepted [54, 63], the discrete structure and distribution of Lewis acid sites is more controversial [8, 26, 38, 64]. Pioneering work carried out by Morterra *et al.* [64], which used transmission infrared spectroscopy to observe pyridine adsorbed on  $\eta\text{-Al}_2\text{O}_3$  catalysts activated at various temperatures, reports the presence of four distinct Lewis acid sites as revealed by the  $\nu_{\text{sa}}$  mode of adsorbed pyridine located at 1590, 1598, 1613, and 1623  $\text{cm}^{-1}$ . The precise distribution of these sites was shown to be dependent on the activation conditions that the alumina catalyst had been subjected to. Furthermore, the 1590  $\text{cm}^{-1}$  feature, which is attributed to pyridine adsorbed on the weakest of the Lewis acid sites, was shown to be present only when an over-pressure of pyridine was present. The 1623  $\text{cm}^{-1}$  band was only observed in samples that had previously been activated at temperatures in excess of 373 K. In agreement with Morterra *et al.* [64], a diffuse reflectance infrared (DRIFTS) investigation by Liu and Truitt [65], which investigated pyridine adsorption on thermally activated  $\gamma\text{-Al}_2\text{O}_3$ , also reported pyridine signals located at 1595, 1613, and 1623  $\text{cm}^{-1}$ . The 1590  $\text{cm}^{-1}$  feature was not observed in this investigation, due to the absence of an elevated pyridine pressure.

### 3.2.2 Brønsted acidity of transition aluminas

The surfaces of high purity transition aluminas are widely regarded as being Lewis acidic. The Brønsted acidity of transition alumina catalysts is rarely discussed in the literature, despite the fact that transition aluminas can be catalytically active in processes where Brønsted acidity is required, *e.g.* cracking of cumene and hexane [66]. The Lewis acidity of transition aluminas alone is insufficient to promote the sustained cracking of cumene and hexane [67] and is attributed to Brønsted sites instead [66]. In several cases, transition

aluminas have been demonstrated to be active, albeit poorly, in reactions featuring an intermediary carbenium ion, the presence of which is promoted by Brønsted acidity [68]. This observation suggests that transition aluminas can indeed present significant Brønsted acidity.

Interestingly, however, significant Brønsted acidity is rarely reported for standard high purity transition aluminas and, up until recently, is usually only detectable at an infrared spectroscopic level in cases where particular alumina preparations and/or pre-treatments have been utilised [69]. For example, addition of sulfur [70] or fluorine [71] has been shown to increase the Brønsted acidity of transition aluminas to a spectroscopically detectable level. In these cases, the presence of the additive reduces the O-H bond strength via an inductive mechanism, consequently resulting in an increase in the Brønsted acidity. However, the inability to measure Brønsted acidity at a spectroscopically detectable level in untreated aluminas does not necessarily mean that it is completely absent. For example, Ward and Hansford [72] detected Brønsted acidity in silica-alumina catalysts with an equivalent alumina content as low as 0.25%. They demonstrated a direct correlation between Brønsted acidity and *o*-xylene isomerisation and showed that carbenium ion reactions, which require protonic acidity, were found to be active on the surface of oxides where Brønsted acidity could not be detected by infrared spectroscopic methods [74]. However, Pearson [61] was able to quantify and confirm the presence of Brønsted acid sites on transition alumina by application of wideline NMR, which reported the presence of deuteropyridinium species upon adsorption of deuterated pyridine. The presence of Brønsted acid sites on the surface of alumina was later confirmed by the infrared spectrum of adsorbed 2,6-ditertiarybutyl pyridine, as reported by Dewing, Monks and Youll [73]. Recent work conducted by Shen *et al.* [74, 75] reports the presence of ammonium infrared bands upon adsorption of ammonia on  $\gamma$ -Al<sub>2</sub>O<sub>3</sub>, which is indicative of the presence of Brønsted acid sites.

### 3.3 Vibrational spectroscopy to probe activation mechanism of transition aluminas

The fundamental vibrations of solids are located in the low energy region of the vibrational spectrum, typically at energies below  $1200\text{ cm}^{-1}$ . In cases where alumina samples are presented to an infrared spectrometer in the form of self-supporting pellets or wafers, these fundamental modes are of such high intensity that they become inaccessible and represent an almost complete spectral cut-off for the solid [8] that can obscure diagnostic hydroxyl deformation modes that could be used to study the activation process of metal oxides. The spectral cut-off persists if the spectrum is collected via diffuse reflectance spectroscopy. If, however, the sample is sufficiently diluted in a suitable matrix, *e.g.* KBr for infrared measurements, and presented as an optically thin disk or pellet the low wavenumber region of the spectrum becomes accessible, however under these conditions adsorption and desorption experiments can become unreliable [7, 8].

#### 3.3.1 Infrared spectroscopy

The dehydroxylation and dehydration of various metal oxide systems can be observed spectroscopically by monitoring changes in the regions of the vibrational spectrum that correspond to the stretching modes of surface hydroxyl groups and chemisorbed water. The dehydroxylation of transition aluminas, in particular, has been the subject of many mid- and near-infrared spectroscopic investigations [26, 52, 53, 76]. For example, Liu [77] has shown that thermal dehydration of  $\gamma\text{-Al}_2\text{O}_3$  removes adsorbed water, destroys hydrogen bonding interactions between surface groups, and dehydroxylates the surface. In addition, Liu [77] was able to correlate changes in the  $\nu_{\text{OH}}$  region of the DRIFTS spectra of  $\gamma\text{-Al}_2\text{O}_3$  dehydrated at different temperatures to changes in the population of hydroxyl groups associated with Al centres of specific coordination, based on their discrete wavenumber positions.

As stated previously, observation of the full vibrational spectrum of transition aluminas via infrared spectroscopy is hampered by the presence of high intensity lattice vibrations located at energies below  $\sim 1200\text{ cm}^{-1}$ , which can present an optical cut-off that obfuscates both in-plane ( $\delta$ ) and out-of-plane ( $\gamma$ ) hydroxyl deformation modes that could potentially be diagnostic for the activation mechanism of these industrially relevant substrates. Busca *et al.* [11] have reported infrared spectra of  $\gamma\text{-Al}_2\text{O}_3$  and  $\theta\text{-Al}_2\text{O}_3$  samples in which in-plane

hydroxyl deformation modes, denoted  $\delta_{\text{OH}}$ , are observed, however it must be noted that the samples were not activated (samples had been previously calcined only) and therefore the behaviour of these bands under thermal activation conditions remains unreported.

It is possible to obtain information on the energy position of hydroxyl deformation modes by observation of combination bands in the near-infrared spectra of metal oxides. Kustov *et al.* [78] have determined the position of both  $\delta_{\text{OH}}$  and  $\gamma_{\text{OH}}$  bands present on the surface of a silica substrate from the position of  $\nu_{\text{OH}}+\delta_{\text{OH}}$  and  $\nu_{\text{OH}}+\gamma_{\text{OH}}$  combination bands. Korovchenko *et al.* [79] report hydroxyl combination bands for  $\gamma\text{-Al}_2\text{O}_3$  while Ruan *et al.* [80] observe combination bands for a series of aluminium oxyhydroxides, *e.g.* gibbsite, boehmite, diaspore etc, and clay materials, such as kaolinite. However, investigations of hydroxyl combination bands from transition alumina substrates certainly do not feature strongly in the literature. Infrared combination bands are inherently weak and deconvolution of the band intensity is a non-trivial exercise. Thus, assessing the behaviour of the deformation modes of surface hydroxyl groups on transition aluminas during thermal activation by observation of combination bands is not practical.

In consideration of the factors listed above, application of infrared spectroscopy to directly observe the behaviour of hydroxyl deformation bands during the thermal activation of transition alumina catalysts under reliable and realistic activation conditions therefore appears to be a highly challenging pursuit, which should be supplemented by other spectroscopic techniques that are not impeded by intense lattice vibrations.

### **3.3.2 Raman spectroscopy**

Most catalytic oxides and supports are ionic making them poor Raman scatterers but strong infrared absorbers [81]. It is therefore quite normal to observe only intense background scattering from transition aluminas [54]. This property lends itself to the successful application of laser Raman spectroscopy (LRS) to the study of adsorbed species on the surface of alumina and other metal oxide systems, where Raman signals associated with the support material will be of very low intensity (or non-existent) compared to those of the adsorbate. Conversely, this property also means that the application of Raman spectroscopy to the study of the intrinsic properties of transition alumina systems (and metal oxides in general) is not ideal. Hydroxyl bands are rarely reported in Raman spectra of metal oxides (although very weak hydroxyl signals are sometimes observable for titania

and silica [82, 83]), which is a consequence of the large dipole moment and the relatively low polarizability of the OH bond [56]. In the same manner, unfavourable selection rules prevent the observation of surface bound water molecules. Furthermore, the hydroxyl groups that are present on the surface of some alumina supports can experience electronic excitation during the Raman measurement resulting in very strong background fluorescence [38, 57]. This property hinders the application of Raman spectroscopy to the study of both the intrinsic properties of transition alumina catalysts, and of adsorbed molecules. Thus, Raman spectroscopy is an unsuitable technique to further characterise the processes that occur during thermal activation of transition aluminas.

Nevertheless, Raman spectroscopy can be successfully employed to characterise the surface layers of alumina-supported metal oxide catalysts. For example, Raman spectroscopy provides detailed information on the surface molybdenum structures contained in the outermost layers of a  $\text{MoO}_3/\text{Al}_2\text{O}_3$  catalyst, which is active in metathesis, oxidation and hydrogenation reactions, while the support does not contribute to the spectrum, as reported by Brown [84]. Wachs *et al.* [85] have used Raman spectroscopy to determine the molecular structure of various alumina-supported transition metal oxide catalysts. This study revealed the structure of the catalyst to be highly sensitive to the level of hydration that the catalyst is exposed to.

### 3.3.3 Inelastic neutron scattering (INS) spectroscopy

As stated previously, the Al-O lattice modes, present at energies below  $\sim 1200 \text{ cm}^{-1}$ , can, in some sample preparations, present an effective optical ‘cut-off’ that prohibits observation of both low energy modes of surface hydroxyl and adsorbed probe molecules by infrared spectroscopy. Inelastic neutron scattering (INS) spectroscopy provides an opportunity to access these potentially diagnostic vibrational modes. As INS spectroscopy is particularly sensitive towards vibrational modes involving hydrogen motion, the INS spectrum of alumina is dominated by bands associated with hydroxyl groups. In-plane and out-of-plane hydroxyl deformation modes are observed at  $\sim 890 \text{ cm}^{-1}$  ( $\delta_{\text{OH}}$ ) and  $\sim 200 \text{ cm}^{-1}$  ( $\gamma_{\text{OH}}$ ), respectively, while stretching ( $\nu_{\text{OH}}$ ) bands are located in the energy region  $3800\text{-}3000 \text{ cm}^{-1}$  [86], albeit with an inferior resolution compared with infrared measurements. Depending on the thermal history of the alumina sample, the INS spectrum may also include spectral contributions associated with adsorbed water, located in the energy region  $\sim 3000\text{-}3800 \text{ cm}^{-1}$  ( $\nu_{\text{OH}}$ ),  $\sim 1650 \text{ cm}^{-1}$  ( $\delta_{\text{H}_2\text{O}}$ ), and at *ca.*  $550 \text{ cm}^{-1}$  (*lib.*  $\text{H}_2\text{O}$ ) [14]. The predominance of hydroxyl features over Al-O lattice modes is due to the massively increased neutron

scattering cross section ( $\sigma_{\text{total}}$ ) of hydrogen (82.02 barn) compared with aluminium (1.503 barn) and oxygen (4.232 barn).

Application of INS spectroscopy is also convenient for the observation of spectra of adsorbed species due to the fact that the spectrum of the alumina substrate can be routinely subtracted from that of adsorbed probe molecules to reveal vibrational modes of the adsorbate. In addition, the intensity of an INS signal is directly proportional to the concentration of sample in the neutron beam path, which makes for relatively simple quantification of adsorbed species [14]. The application of INS spectroscopy therefore provides a unique opportunity to access low energy hydroxyl deformation modes, which could potentially help provide spectroscopic evidence for the dehydration/dehydroxylation processes that occur upon thermal activation of transition alumina substrates. In addition, INS can also be used to observe low energy modes of adsorbed pyridine, which could potentially be used to further characterise the Lewis acidity of transition aluminas.

### **3.4 Characterisation of transition alumina surface acidity by vibrational spectroscopy of adsorbed species**

The acidity of polydispersed systems is a very important chemical property for industrial heterogeneous catalysis and its characterisation, which can be time consuming and complex, is of primary technological importance [8]. Transition aluminas, which are among the most complex metal oxide systems, present a number of surfaces with varied acid properties. For this reason, transition aluminas represent some of the most widely studied materials in the field of heterogeneous catalysis. In many of the applications in which transition aluminas are employed as active catalysts, *e.g.* isomerisation of hydrocarbons [48], the ability of the catalyst to behave as a solid acid is imperative. Acidity, if well defined, could be modified selectively to produce catalysts exhibiting improved selectivity for specific reactions [36].

A great multitude of techniques have been used in order to assess and characterise both the Brønsted (protic) and Lewis (aprotic) acidity of these technologically important materials including: standard titration with bases [87]; the use of indicators [88]; and thermal desorption of various probe molecules [47, 64, 89-91]. Unfortunately, the application of many of these techniques has given conflicting and widely differing results from the same

materials [92]. Furthermore, none of these techniques can provide distinction between Brønsted and Lewis acidity. However, the vibrational spectra of adsorbed probe molecules can provide a wealth of information with regard to the local structure and acidity of adsorption sites found on the surface of transition aluminas. To this end, various spectroscopic techniques have been applied, including: Raman scattering [93]; various infrared spectroscopic methods [38, 64, 65, 77, 94]; photoacoustic [95]; and inelastic neutron scattering (INS) [38].

The adsorption of various probe molecules coupled with the application of vibrational spectroscopy to further characterise the surface acidity, both Lewis and Brønsted, of transition aluminas is discussed in detail below:

### **3.4.1 Adsorption of basic probe molecules**

Of the many techniques available for the assessment of surface acidity the adsorption of suitable basic probe molecules, such as pyridine or ammonia, coupled with a quantitative analytical technique, for example: temperature programmed desorption (TPD) [96]; gravimetry [97]; or microcalorimetry [98], can provide detailed information on the surface acidity of heterogeneous catalysts and other solids. However, it has been suggested that whenever the determination of surface acidity is based on the adsorption of probe molecules, these techniques should be supplemented by infrared spectroscopic measurements [8]. Furthermore, it is stated that only the spectroscopic observation of the type and number of species formed and/or of the possible reaction products, may render the analytical determinations completely meaningful [8, 99]. Indeed, the adsorption of suitable probe molecules coupled with the application of vibrational spectroscopy has been widely used in recent times to characterise surface acidity of transition aluminas and has been the subject of several review articles [8, 99]. The infrared technique has been employed extensively and a great variety of probe molecules have been tested:

#### ***Ammonia***

Due to its high basicity and small molecular ‘footprint’, ammonia is regarded as the most sensitive of basic probe molecules and reveals as many acidic sites as possible. Thus, ammonia adsorption can provide an excellent titration of the total number of acid sites present on a given substrate. In addition, due to the characteristic infrared signals associated with the ammonium ion, located at *ca.* 1390, 1450 and 1700  $\text{cm}^{-1}$  [74], which

can arise via abstraction of a proton from a suitably acidic surface hydroxyl group, the infrared spectrum of adsorbed ammonia can clearly differentiate Lewis and Brønsted acidity. In this manner, some authors have recently been able to show that some hydroxyl groups present on the surface of transition aluminas are sufficiently acidic to yield adsorbed ammonium ions when exposed to ammonia [74, 98]. The disadvantages of using ammonia as a probe molecule, however, are numerous. These disadvantages stem from the fact that ammonia can interact with the alumina surface in four different ways and that infrared spectroscopy can rarely differentiate between them. Firstly, ammonia may hydrogen-bond via one of its hydrogens to oxygen atoms in either the surface layer or surface hydroxyl groups, or via the nitrogen lone pair to surface hydroxyls without proton abstraction. Secondly, ammonia may react with a sufficiently Brønsted acidic hydroxyl group, abstracting a proton. Thirdly, it may coordinate to a Lewis acid site, in which case the ammonia infrared bands cannot differentiate between sites of different Lewis acidity. Finally, ammonia may be dissociatively adsorbed on acid-base pair sites, leading to the formation of surface bound  $\text{NH}_2$  species and hydroxyl groups. This process leads to the formation of new species of very high stability of which the concentration is difficult to measure [8]. This combination of outcomes can often lead to broad spectral features that hinder assignments.

### ***2,6-Dimethylpyridine***

2,6-dimethylpyridine, which is also commonly referred to as 2,6-lutidine, in theory, is a particularly good probe for the determination of Brønsted acidity on metal oxides. In comparison to pyridine, 2,6-dimethylpyridine more readily yields protonated species due to its increased basicity, which is a consequence of the electron donating methyl substituents, and its lower affinity for Lewis acid sites due to steric hindrance from the methyl groups. In fact, 2,6-dimethylpyridine interacts first with Brønsted acid sites and subsequently, and only then, with Lewis acid sites [100-102]. The application of 2,6-dimethylpyridine as a probe molecule for the determination of the surface acidity of transition aluminas has been addressed by Oliviero *et al.* [62]. 2,6-dimethylpyridine adsorption leads to coordinated, protonated and hydrogen-bonded species. The infrared spectra of these species permit the differentiation of Lewis acid sites, and both strongly and weakly acidic hydroxyl groups. The position of the  $\nu_{8a}$  mode, which occurs at  $1594\text{ cm}^{-1}$  in liquid phase 2,6-dimethylpyridine [70], is particularly sensitive to each of these adsorption configurations: for protonated species this band is located above  $1625\text{ cm}^{-1}$  and its wavenumber position is sensitive to the strength of the Brønsted acidity, while for

coordinated or hydrogen-bonded species it is located at lower wavenumber positions. In addition, the  $\nu_{\text{NH}}$  band of protonated 2,6-dimethylpyridine (2,6-DMPH<sup>+</sup>) can provide information on the strength of the 2,6-DMPH<sup>+</sup>...O bond and hence the acidity of the substrate hydroxyl group: the lower the wavenumber position of the  $\nu_{\text{NH}}$  band, the stronger the 2,6-DMPH<sup>+</sup>...O bond is and therefore the stronger the Brønsted acidity. Determination of the true wavenumber position of the  $\nu_{\text{NH}}$  signal is, however, complicated by the complex shape of the band [92], which is brought about by a Fermi resonance interaction between the first overtone of the  $\gamma_{\text{NH}}$  and the  $\nu_{\text{NH}}$  signals [62].

### ***Pyridine***

Arguably, the best results for the evaluation of the surface acidity of transition aluminas, and indeed other metal oxide substrate, can be obtained by the adsorption of pyridine [47]. Pyridine is considered to be a relatively ‘hard’ base and can interact with sites of widely different acidity and was first proposed as a probe for the assessment of the surface acidity of transition aluminas and other acidic solids by Parry [92]. Although pyridine may be considered to be a weaker base than ammonia on the basis of liquid phase pKa values, gas phase basicities indicate that pyridine should be the stronger base relative to ammonia [99]. In fact, Parillo *et al.* [103] have shown that that pyridine is more easily protonated than ammonia and that the pyridinium ion is thermally more stable compared with the ammonium ion.

Pyridine does not undergo surface reactions, at least up to quite high temperatures, on systems that are not strongly basic and its adsorption is therefore ideal for the study of transition alumina surfaces. For example, the strongest Lewis acid site on  $\eta\text{-Al}_2\text{O}_3$  can be occupied with pyridine, which will not undergo surface reaction or decomposition at least up to 823 K [91], thus pyridine uptake data yields a better titration of surface acidity than any of the other strong bases, which are comparatively more reactive.

Pyridine can interact with the surface of alumina in three ways: (i) the nitrogen lone pair can hydrogen bond to weakly acidic hydroxyl groups, resulting in a weak perturbation of the adsorbed pyridine; (ii) on sites of sufficiently strong Brønsted acidity, a proton may be abstracted yielding the pyridinium ion, which has a highly characteristic vibrational frequency; and (iii) the nitrogen lone pair can bind via  $\sigma$ -charge donation to coordinatively unsaturated Lewis acidic Al<sup>III</sup> centres, which yields various and specific perturbations of

the adsorbate pyridine depending on the acidity of the Lewis site [8, 47, 99].

The in-plane ring deformation modes  $\nu_{8a}$ ,  $\nu_{8b}$ ,  $\nu_{19a}$  and  $\nu_{19b}$ , according to the notation first introduced by Kline and Turkevich [104], are regarded as the most sensitive vibrations of pyridine with regard to the nature and strength of the adsorptive interaction. This observation was first reported for molecular Lewis acids by Terenin [1, 2], and for both silica and alumina surfaces in early pioneering work conducted by Parry [92]. For this reason, the infrared spectrum of adsorbed pyridine in the energy range 1700-1400  $\text{cm}^{-1}$  is routinely inspected for the assessment of the surface acidity of metal oxides. The  $\nu_{8a}$  mode of adsorbed pyridine, in particular, which is typically located at wavenumber positions in the energy range 1590-1630  $\text{cm}^{-1}$  for metal oxides, has been widely used to obtain information on the surface Lewis acidity of several transition aluminas. On the basis of the observed frequency shift of the  $\nu_{8a}$  mode upon adsorption and of its resistance to thermal desorption, several authors have been able to define the Lewis acid site distribution of several transition aluminas [8, 38, 65]. The surface(s) of activated transition aluminas expose  $\text{Al}^{\text{III}}$  centres in various coordination environments [26, 47] upon which pyridine can coordinate, resulting in a change in the vibrational frequency of some of the vibrational modes of the adsorbed pyridine, as can be demonstrated by infrared spectroscopy [26, 47, 65, 92, 105]. The exhibited energy shift of the  $\nu_{8a}$  mode of chemisorbed pyridine reflects the local bonding geometry of the underlying Lewis acidic centres, for example, the lower degree of coordination achieved by the  $\text{Al}^{\text{IV}}_{\text{cus}}$  cations is responsible for a stronger inductive charge release from the nitrogen lone pair, which results in a greater increase in the vibrational frequency of the  $\nu_{8a}$  mode than the comparatively more saturated  $\text{Al}^{\text{VI}}_{\text{cus}}$  cations. In this manner, the relative distribution of Lewis acid sites present on a surface can be determined from the vibrational spectrum of adsorbed pyridine. For example, Liu and Truitt [65] used a combination of DRIFTS and pyridine adsorption to report/reveal the presence of at least three Lewis acidic sites on the surface of  $\gamma\text{-Al}_2\text{O}_3$ , while Lundie *et al.* [38] recently used a similar approach to describe four distinct Lewis acid sites present on the surface of an activated  $\eta\text{-Al}_2\text{O}_3$  catalyst.

### 3.5 Modification of surface acidity

There are several methods by which the surface acidity of alumina, and indeed other metal oxides, may be chemically modified. The addition of alkali metal modifiers to the alumina is well-established and can lead to an enhancement in both activity and selectivity in catalytic systems [106-112]. Alkali metal modifiers can also be used as dopants for the selective removal of specific active sites. For example, the addition of potassium increases the selectivity of Pt/Al<sub>2</sub>O<sub>3</sub>, Ir/Al<sub>2</sub>O<sub>3</sub>, and Ru/Al<sub>2</sub>O<sub>3</sub> catalysts used in the dehydrogenation processes of saturated hydrocarbons to monoalkenes [113]. This is believed to occur via the selective poisoning of *strong* Lewis acid sites associated with the alumina support, which suppresses secondary pathways towards cracking, isomerisation, and aromatisation products. Dalla Lana *et al.* [107] also report the possibility of elimination of Lewis acid centres on alumina via the addition of alkali metal hydroxides. They proposed that the alkali salt coordinates to Lewis acid sites via the hydroxyl ion and that the poisoning effect on Lewis acid centres increases with increasing ionic radii of the alkali metal ion. It is noted that improvements in catalytic performance can also be caused by an inherent promotional effect produced by the modifier. For example Haneda *et al.* [109] report that the addition of alkali metal promotes the decomposition of NO over alumina-supported cobalt oxide catalysts.

Modification of transition aluminas by addition of silica is also known to effect changes in both Lewis and Brønsted surface acidity. For example, Tanabe [114] reported that mixed alumina-silica materials exhibit a higher degree of Brønsted acidity than can be expected in either of the substituent metal oxides themselves. For samples with a low silica content (<20 wt.%) only coordinatively unsaturated octahedral Al<sup>III</sup> centres are found in the surface layer, whereas as for samples with an intermediate silica loading (20-80 wt.%) a small number of tetrahedral Al<sup>III</sup> centres is detected, as recently reported by Daniell *et al.* [115]. It is proposed that these Lewis acid sites are generated by isomorphous substitution of Si<sup>IV</sup> lattices by Al<sup>III</sup> centres leading to the formation of an aluminosilicate phase. Although the process of silica incorporation into transition aluminas can increase the number of strong Lewis acid sites (*i.e.* tetrahedral Al<sup>III</sup>) exposed at the surface, the total number of exposed Lewis acid sites of the alumina substrate is diminished due to the surface being coated with silica [115].

In addition to the chemical methods described above, the Lewis acid site distribution can be modified by simple physical means. The thermal phase diagram for the transition aluminas, presented in diagram 3.0.1, indicates that heating  $\eta$ -Al<sub>2</sub>O<sub>3</sub> alumina to temperatures in excess of 900 K can lead to a phase transformation towards  $\theta$ -Al<sub>2</sub>O<sub>3</sub> and, eventually,  $\alpha$ -Al<sub>2</sub>O<sub>3</sub>. The reduction of the surface area and the ordering of the tetrahedral Al sublattice that occurs under such thermal treatment causes the defective spinel framework to collapse so that the tetragonal structure of  $\eta$ -Al<sub>2</sub>O<sub>3</sub> settles into monoclinic  $\theta$ -Al<sub>2</sub>O<sub>3</sub> via a *displacive* transformation at intermediate temperatures (1073-1273 K), followed by a *reconstructive* transformation towards hexagonal corundum ( $\alpha$ -Al<sub>2</sub>O<sub>3</sub>) at higher temperatures (>1300 K) [116]. The quoted temperature ranges for stability of the transition aluminas are approximate and depend, amongst other factors, upon the crystallinity and purity of the starting materials and on the thermal treatment conditions [34]. The diffuse nature of the powder diffraction patterns reported for transition aluminas [116] imply a high degree of structural disorder in all of the transition forms. This poor crystallinity makes it impossible to probe the fine and irregular faces of the phases by diffraction based analytical techniques [116].

According to a magic-angle spinning (MAS) NMR investigation conducted by Pecharrómán *et al.* [117]  $\eta$ -Al<sub>2</sub>O<sub>3</sub> is composed of ~72% octahedral Al centres and 28% tetrahedral Al centres. In comparison, the same authors found that  $\theta$ -Al<sub>2</sub>O<sub>3</sub> is composed of approximately equal proportions of octahedral and tetrahedral Al ions, which is in absolute agreement with earlier investigations conducted by Saalfeld [118] and Yamaguchi *et al.* [119]. Thus, thermal pre-treatment of  $\eta$ -Al<sub>2</sub>O<sub>3</sub> at temperatures sufficient to induce a phase transformation from  $\eta$ -Al<sub>2</sub>O<sub>3</sub> to  $\theta$ -Al<sub>2</sub>O<sub>3</sub> will affect the relative population of structural tetrahedral and octahedral Al<sup>III</sup> centres. It then follows that this may then have an effect on the relative population of the Al centres in the surface layer. As coordinatively unsaturated (cus) tetrahedral alumina ions confer stronger Lewis acidity than cus octahedral aluminium ions, this process could therefore affect the populations of the various Lewis acid sites expressed at the surface of the alumina substrate. Thus, careful thermal pre-treatment could, potentially, provide a cost-effective and simple method for modifying the Lewis acidic properties of transition alumina catalysts.

# 4

## **Chapter 4**

### **Activation of transition alumina catalysts**

Alumina is ubiquitous in heterogeneous catalysis, finding uses both as a support material [28] and as an active catalyst in its own right [48]. Alumina catalysts, as received, are catalytically inert and must first be thermally activated in order to expose the coordinatively unsaturated Al<sup>III</sup> centres that are usually responsible for catalytic activity. The following section aims to investigate the physical and chemical changes exerted on an  $\eta$ -Al<sub>2</sub>O<sub>3</sub> catalyst under specified thermal activation conditions.

#### 4.1. Thermogravimetric Analysis (TGA)

Thermogravimetric analysis (TGA) was applied in order to gain a basic understanding of the transformations occurring to the  $\eta$ -Al<sub>2</sub>O<sub>3</sub> catalysts under the activation conditions employed throughout this investigation. Figure 4.1.1 presents thermogravimetric analysis (TGA) profiles for an  $\eta$ -Al<sub>2</sub>O<sub>3</sub> catalyst, where the catalyst was first dehydrated at 373 K for 12 hours followed by activation at 623 K for 150 mins. Throughout this procedure a constant flow of Ar gas was maintained over the sample. Figure 4.1.1(a) presents the dehydration stage of the TGA experiment only, *i.e.* up to 373 K, while Figure 4.1.1(b) shows the TGA experiment during application of the second temperature ramp, *i.e.* 373-623 K. A temperature ramp of 10 K/min was applied to the room temperature sample until a temperature of 373 K was attained, which was maintained for a period of 1 hour. The temperature of the sample was then increased from 373 K to 623 K at a rate of 10 K/min and maintained for a period of 150 mins. From Figure 4.1.1(a) it can be seen that the virgin alumina sample experiences a 3.3% decrease in weight between temperatures of 303-373 K, which is attributed to the desorption of physisorbed water from the alumina surface. After being heated at 373 K for a period of 35 mins there appears to be no further weight loss observed until the second heating ramp (10 K/min from 373 to 623 K), which is applied after a period of 720 mins, where a further 2.9% weight decrease, commencing at a temperature of 393 K, is observed. The temperature was maintained at 623 K for a period of 150 mins, during which a further 0.3% weight loss is observed, *i.e.* after activation the sample is 93.2% of its original weight. The later weight reduction of 2.92% at 393 K is attributed to the thermal desorption of water molecules and/or hydroxyl groups coordinated to weak Lewis acid sites, while the weight reduction of 0.3% at 623 K is assigned to the desorption of hydroxyl groups from relatively stronger Lewis acid sites.

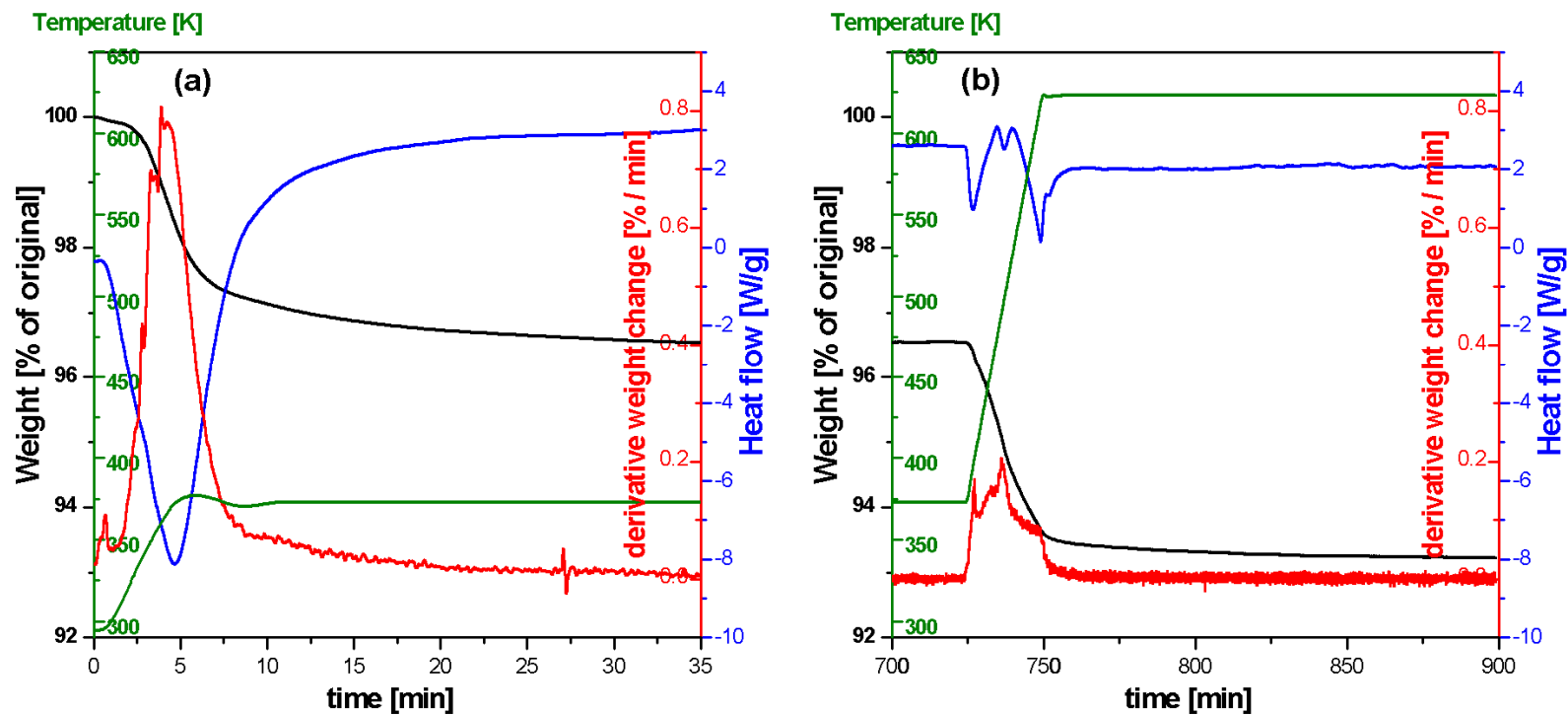


Figure 4.1.1: Thermogravimetric analysis of an  $\eta$ - $\text{Al}_2\text{O}_3$  catalyst. The sample was first heated from room temperature to 373 K at a rate of 10 K/min and held for a period of 1 hour, and then heated from 373 K to 623 K at a rate of 10 K/min and held for a period of 150 mins. The TGA profile during: (a) the first ramp only (*i.e.* room temperature to 373 K); (b) the second ramp only (*i.e.* 373 K to 623 K). The temperature was maintained at 373 K between 60-700 mins, where no changes were observed.

## 4.2 X-ray Diffraction (XRD)

X-ray diffraction (XRD) was applied to determine if any structural transformations occur under the thermal activation conditions employed throughout this investigation. Heating of the  $\eta$ -Al<sub>2</sub>O<sub>3</sub> catalyst could potentially promote a change in particle size, which could negatively impact upon subsequent spectroscopic measurements. This possibility was investigated by *in situ* XRD measurements performed during the thermal activation process. Changes in the particle size of a solid sample are reflected by an associated change in the x-ray scattering domain size, which is manifested by a change in the width of diffraction lines, and can therefore be explored by application of XRD [120].

Figure 4.2.1 presents x-ray diffraction (XRD) patterns for the  $\eta$ -Al<sub>2</sub>O<sub>3</sub> catalyst before and after the activation process. Figure 4.2.1(a) shows the XRD pattern of the catalyst after dehydration at 373 K, while Figure 4.2.1(b) shows the pattern of the catalyst after activation in flowing Ar at 623 K for 150 mins. No significant differences are observed between the two diffractograms as indicated by the difference pattern presented in Figure 4.2.1(c), where the diffractogram of the dehydrated sample has been subtracted from that of the activated sample. Importantly, this observation indicates that no significant structural changes occur within the alumina framework during the thermal activation conditions employed here.

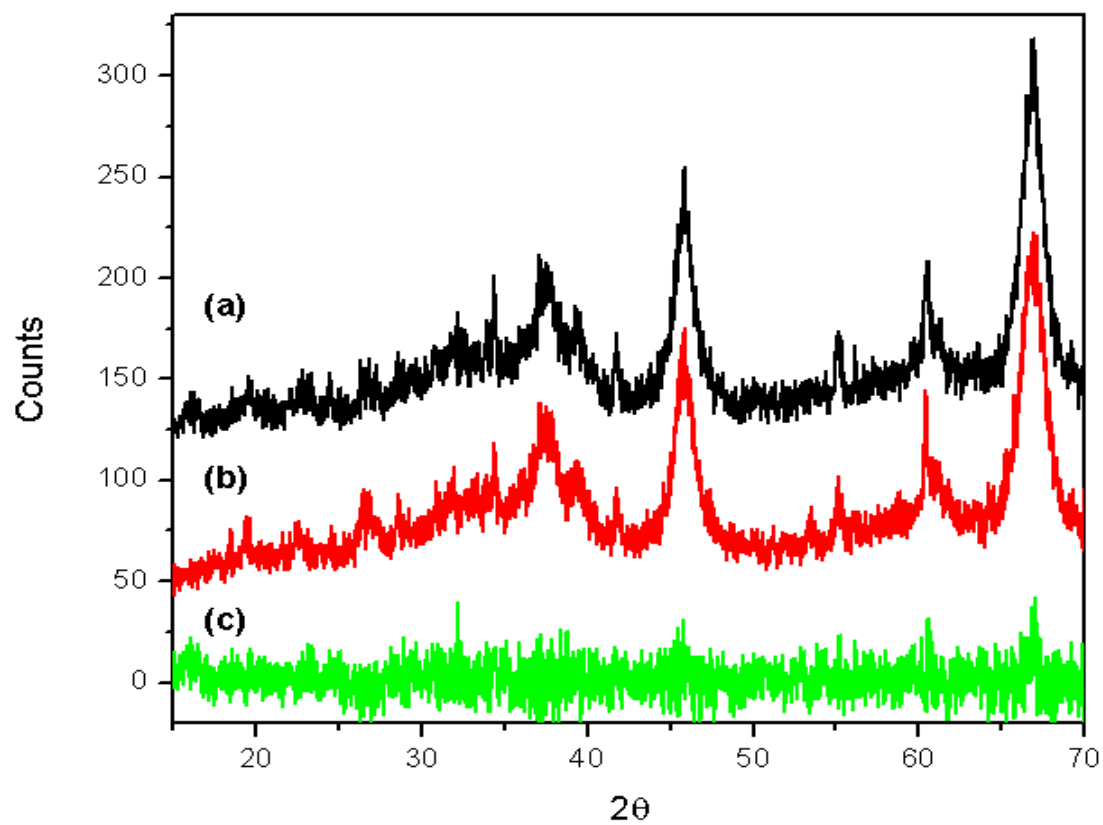


Figure 4.2.1: Recorded diffraction patterns for (a)  $\eta$ -Al<sub>2</sub>O<sub>3</sub> dried at 373 K (black), and (b)  $\eta$ -Al<sub>2</sub>O<sub>3</sub> activated at 623 K. (c) The difference diffractogram where the pattern of the dried catalyst has been removed from the pattern of the activated catalyst, *i.e.* (b)-(a).

### 4.3 Infrared spectroscopy

Identification and speciation of the surface species present on an alumina surface, and confirmation of their desorption upon activation can be attained by application of infrared spectroscopy. The energy position of infrared signals located in the energy range 3800-3000  $\text{cm}^{-1}$  can provide information on the local structure of surface hydroxyl groups [8], while water can be identified by its characteristic deformation mode located at  $\sim 1658 \text{ cm}^{-1}$ . Diffuse reflectance infrared spectroscopy (DRIFTS) was selected for ease of sample preparation and the possibility of conducting adsorption and desorption experiments under realistic conditions.

#### *'Single beam' infrared spectra*

Figures 4.3.1 and 4.3.2 present the infrared spectra of dried, and activated  $\eta\text{-Al}_2\text{O}_3$  catalysts, respectively. In each case the data are presented in the energy ranges of (a) 4000-1000  $\text{cm}^{-1}$ , which shows the spectrum in its entirety, and (b) 4000-2750  $\text{cm}^{-1}$ , which shows only the  $\nu_{\text{OH}}$  region of the spectrum. A previously acquired spectrum of KBr powder, dried *in situ* at 373 K, was removed from each of the single beam spectra of the catalyst according to the transform method described by Kubelka and Munk [12], in order to remove spectroscopic contributions from the environmental chamber of the diffuse reflectance cell. This procedure yielded the difference spectra presented in Figures 4.3.1 and 4.3.2.

The infrared spectrum of the dried  $\eta\text{-Al}_2\text{O}_3$  catalyst (Fig. 4.3.1) is characterised by three distinct features, including: a very broad feature located in the energy range 3800-2500  $\text{cm}^{-1}$ , assigned to  $\nu_{\text{OH}}$  stretching modes of surface hydroxyl groups and molecular water; a small, sharp feature located at 1658  $\text{cm}^{-1}$ , assigned to the deformation mode of surface bound water molecules; and a very intense and broad band commencing at  $\sim 1500 \text{ cm}^{-1}$  that extends beyond  $\sim 1000 \text{ cm}^{-1}$ , which represents highly absorbing Al-O lattice vibrations that are responsible for the 'optical cut-off' presented by alumina. Within the broad  $\nu_{\text{OH}}$  stretching envelope, high energy shoulders are observed at 3730 and 3680  $\text{cm}^{-1}$  that are attributed to isolated hydroxyl groups, which can be accommodated within the surface hydroxyl group model developed by Knözinger [26].

Upon activation of the  $\eta\text{-Al}_2\text{O}_3$  catalyst, two major spectral changes are observed, as seen in Figure 4.3.2. Firstly, the intensity of the band located at 1658  $\text{cm}^{-1}$  is significantly

diminished, which can be simply explained by thermal desorption of water from the catalyst surface (where it no longer contributes to the spectrum). Secondly, the  $\nu_{\text{OH}}$  stretching envelope becomes more structured, which is caused by the desorption of surface hydroxyl groups and adsorbed water molecules, which leads to the breakdown of the extended hydrogen bonding network, thereby allowing previously dampened oscillators to become isolated and free to vibrate at a higher frequency. Four discrete isolated hydroxyl groups can be observed within the spectrum of the activated catalyst, and are located at 3770, 3730, 3680 and 3580  $\text{cm}^{-1}$ . The energy positions of these signals are consistent with those reported in the literature for hydroxyl groups present on dehydrated transition aluminas [8, 26, 65, 77]. According to Lundie *et al.* [38, 121], the signal located at 3770  $\text{cm}^{-1}$  is attributed to hydroxyl groups associated with tetrahedral Al centres, which is referred to as the *medium-strong* Lewis acid site, while the signal located at 3730  $\text{cm}^{-1}$  is assigned to a two-fold bridging hydroxyl group associated with a tetrahedral and an octahedral Al centre, which is referred to as the *medium-weak* Lewis acid site. The band located at 3690  $\text{cm}^{-1}$  is assigned to a three-fold bridging hydroxyl group associated with octahedral Al centres and is referred to as the *weak* Lewis acid site [38, 65, 121]. Finally, the broad signal located at  $\sim 3580 \text{ cm}^{-1}$  is assigned to hydrogen bonded hydroxyl groups, in agreement with the observations of Peri [46] and Knözinger [26], which indicates that some of the surface hydroxyl groups continue to experience hydrogen bonding effects, due to neighbouring hydroxyls, even after exposure of the catalyst sample to the activation conditions stipulated here.

In summary, after dehydration at 373 K, hydroxyl features associated with *medium-weak* and *weak* Lewis acid sites are observed. The sample must be activated at 623 K before hydroxyl features associated with *medium-strong* Lewis acid sites are observed. This might indicate that *weak* and *medium-weak* sites are occupied by molecular water in the passive state, while *medium-strong* sites could potentially be occupied by hydroxyl groups, *i.e.* dissociated water, in the passive state.

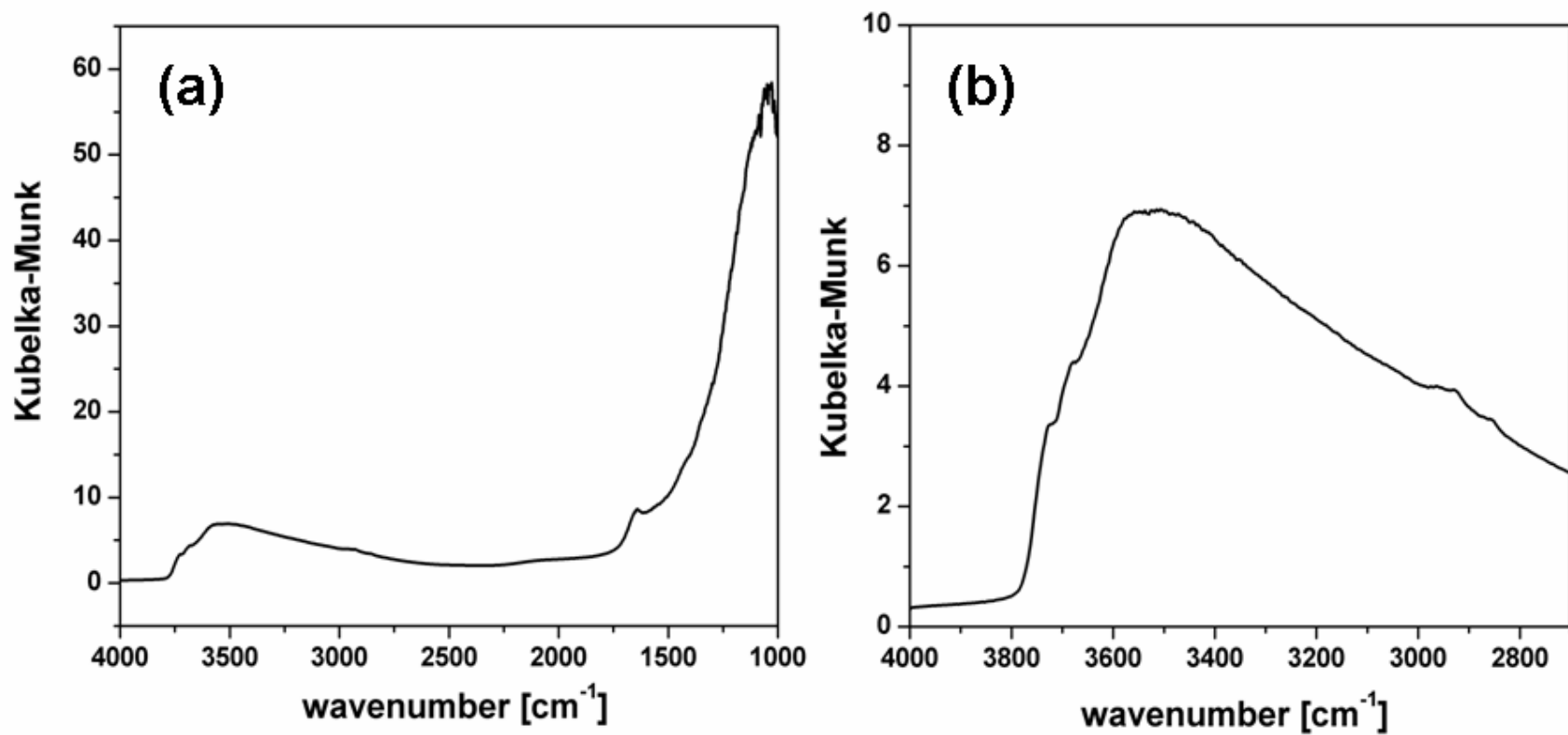


Figure 4.3.1: DRIFTS spectra of a  $\eta$ -Al<sub>2</sub>O<sub>3</sub> catalyst dried at 373 K in flowing helium, recorded in the energy ranges of (a) 4000-1000 cm<sup>-1</sup>, and (b) 4000-2750 cm<sup>-1</sup>.

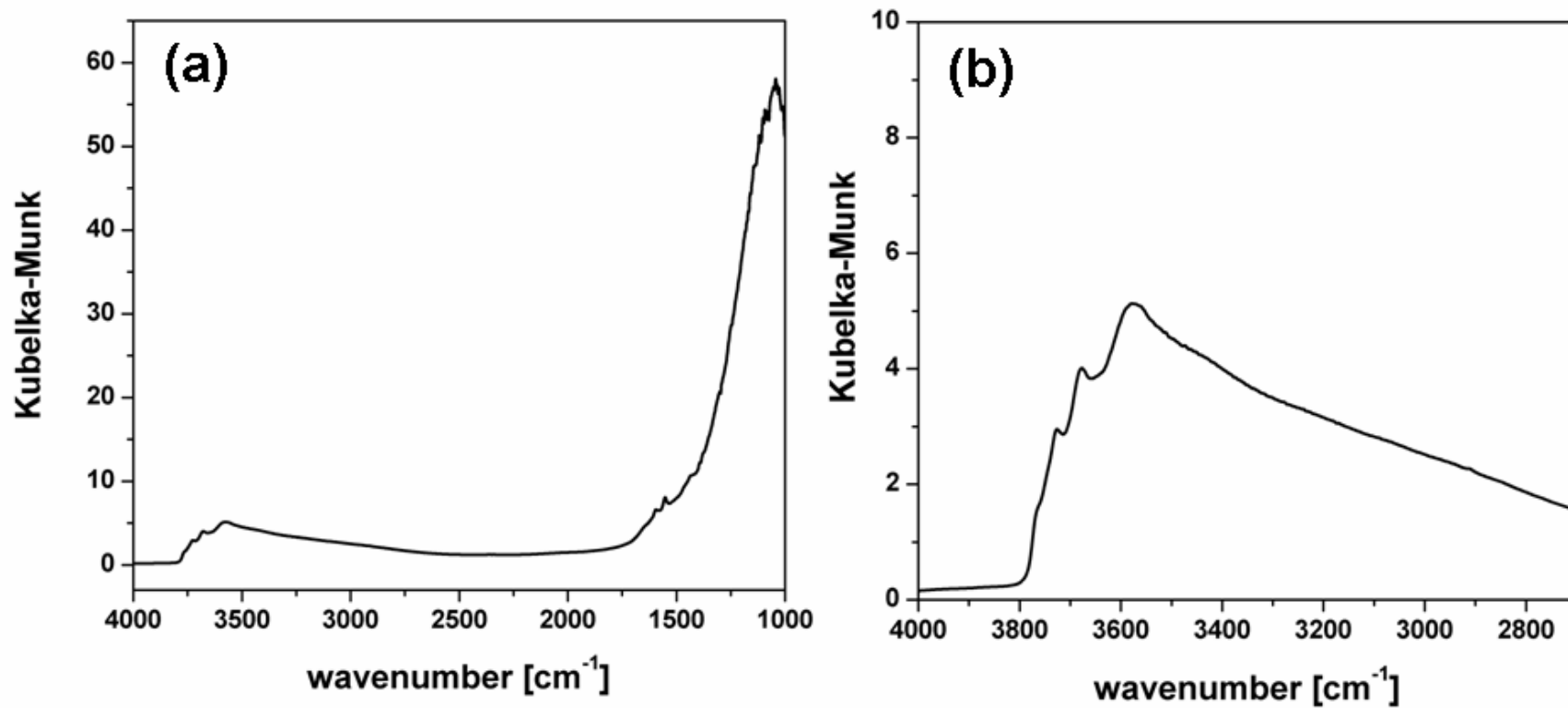


Figure 4.3.2: DRIFTS spectra of a  $\eta$ -Al<sub>2</sub>O<sub>3</sub> catalyst activated at 623 K in flowing helium, recorded in the energy ranges of (a) 4000-1000 cm<sup>-1</sup>, and (b) 4000-2750 cm<sup>-1</sup>.

### *Infrared difference spectra*

Disparities between the spectra of the dried and activated  $\eta$ -Al<sub>2</sub>O<sub>3</sub> catalysts can be more readily observed when the data are presented as a difference spectrum, where a spectrum of the dried catalyst is removed from that of the activated catalyst. In this arrangement, loss of a species is represented by negative intensity, while the generation of new species is indicated by signals of positive intensity [7]. However, the large amount of water that is removed from the  $\eta$ -Al<sub>2</sub>O<sub>3</sub> catalyst upon activation, as evidenced by the 3.2 % weight loss observed in the previous TGA experiment (Fig. 4.1.1), results in a large difference in relative light transmission between the infrared spectra of ‘dried’ and ‘activated’ samples. This situation is not conducive to the generation of reliable difference spectra. Nevertheless, difference spectra, where a spectrum of the dried catalyst functioned as a background spectrum, showing the changes occurring to the  $\eta$ -Al<sub>2</sub>O<sub>3</sub> catalyst during activation are presented in Figure 4.3.3. The data are presented in the energy ranges of (a) 3900-3000 cm<sup>-1</sup>, and (b) 1000-2500 cm<sup>-1</sup>.

The loss of hydrogen-bonded surface-bound water molecules and hydroxyl groups from the system is indicated by the presence of a broad negative feature located at 3600-3000 cm<sup>-1</sup> in Figure 4.3.3(a). The associated increase in the relative population of isolated surface hydroxyl species, brought about by desorption of surface species, results in the appearance of three distinct positive features located at 3770, 3730, and 3670 cm<sup>-1</sup>. The most intense and sharp of these features occurs at 3770 cm<sup>-1</sup> and has previously been assigned to hydroxyl groups adjacent to *medium-strong* Lewis acid sites that are generated upon activation of the alumina sample [8, 38]. This band contains a low-energy shoulder, located at 3730 cm<sup>-1</sup>, which has previously been assigned to hydroxyl groups associated with *medium-weak* Lewis acid sites that exist as bridging units connecting octahedrally coordinated Al centres with tetrahedral coordinatively unsaturated Al<sup>III</sup> centres [38]. A final band is observed at 3670 cm<sup>-1</sup>, which is broadly consistent with previous assignments to hydroxyl groups associated with *weak* Lewis acid sites [38, 77]. It is proposed that this hydroxyl group exists as a bridging unit that connects three octahedral Al centres, one of which is coordinatively unsaturated and therefore represents the *weak* Lewis acid site [38, 91, 121].

The loss of water from the system is evidenced by the reduction in intensity of the water deformation band observed at 1658 cm<sup>-1</sup> in Figure 4.3.3(b). The depopulation of surface hydroxyl groups is expected to yield a similar reduction in intensity within the hydroxyl

deformation region. However, this part of the spectrum is unobservable due to the prohibitively large absorptions presented by bulk Al-O vibrations located at energies below  $\sim 1200 \text{ cm}^{-1}$ .

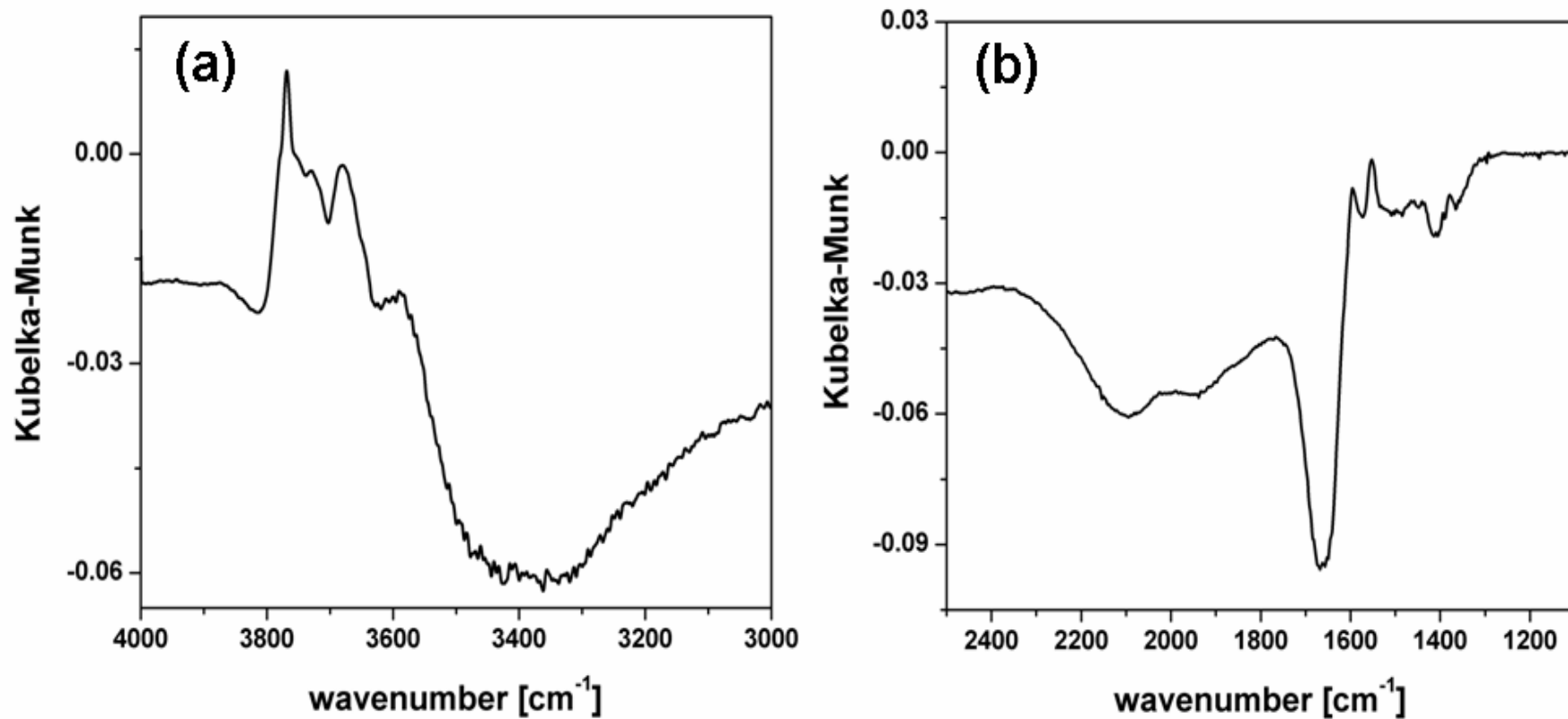


Figure 4.3.3: Difference infrared spectra where the spectrum of the previously dried catalyst has been removed from the spectrum of the activated catalyst in the energy ranges (a) 4000-3000 cm<sup>-1</sup>, and (b) 2500-1100 cm<sup>-1</sup>.

## 4.4 Inelastic neutron Scattering spectroscopy (MAPS)

Inelastic neutron scattering (INS) spectroscopy, using the MARI spectrometer [20] at the ISIS Facility, was applied in order to access the potentially diagnostic, low energy modes located below  $\sim 1200\text{ cm}^{-1}$ , which are obscured by intense lattice absorptions in the infrared measurements (Section 4.3). Large differences in relative light transmission can complicate the generation of reliable difference spectra in optical spectroscopy. Obviously, light transmission levels need not be considered in INS spectroscopic measurements and spectra may be simply subtracted from each other to give reliable difference spectra provided that the spectra are recorded under identical conditions, *i.e.* temperature and sample alignment. When using an indirect geometry chopper-based neutron spectrometer, such as MARI, recording the INS spectra at two different incident neutron energies allows the full vibrational spectrum to be recorded with modest resolution (*ca.*  $50\text{ cm}^{-1}$ ) over the dynamic range of interest, *i.e.*  $0\text{-}4000\text{ cm}^{-1}$ , [14]. INS spectra were therefore recorded at  $5240$  and  $2016\text{ cm}^{-1}$ .

### 4.4.1 Vibrational spectra

Figure 3.4.1 presents the single beam INS spectra that were recorded using an incident neutron energy of  $5240\text{ cm}^{-1}$ , of  $\eta\text{-Al}_2\text{O}_3$  dried at  $323\text{ K}$  (Fig. 4.4.1(a)), and activated at  $623\text{ K}$  (Fig. 4.4.1(b)). Both spectra are dominated by broad features located at  $829\text{ cm}^{-1}$ ,  $1658\text{ cm}^{-1}$  and  $\sim 3720\text{ cm}^{-1}$ , which are assigned to the in-plane deformation of surface hydroxyl groups ( $\delta_{\text{OH}}$ ), deformation modes of chemisorbed water molecules ( $\delta_{\text{H}_2\text{O}}$ ), and to O-H stretching modes ( $\nu_{\text{OH}}$ ) of both surface hydroxyl groups and chemisorbed water molecules, respectively.

The difference spectrum, where the spectrum of the dried catalyst has been simply subtracted from that of the activated catalyst, is presented in Figure 4.4.1(c). In processing vibrational spectra in this manner, new species produced by the activation process are represented by positive intensity spectral features, while species lost during activation are represented by negative features. The difference spectrum is characterised by a series of differential-type bands, which are interpreted as the transformation of hydrogen bonded oscillators into more isolated states. Destruction of the hydrogen bonding network has different effects on different vibrational modes. For example, hydrogen bonding has a damping effect on stretching vibrations, which results in an energy shift to lower

wavenumber position, whereas deformation modes are activated, resulting in an increase in vibrational frequency [122]. In Figure 4.4.1(c) a broad negative band is observed at  $\sim 3450 \text{ cm}^{-1}$  and an associated positive feature at  $\sim 3700 \text{ cm}^{-1}$ . This observation is in agreement with the DRIFTS spectra (Figure 4.3.3) and is consistent with the release of hydroxyl groups from a hydrogen-bonded environment into a comparatively isolated environment. Such a situation arises during activation of metal oxide catalysts where the desorption of surface hydroxyl species and chemisorbed water molecules results in a reduction in the density of neighbouring surface species. In agreement with the DRIFTS spectrum presented in Figure 4.3.3, a negative band is observed at  $\sim 1658 \text{ cm}^{-1}$ , which is consistent with a loss of adsorbed water from the catalyst surface. The absence of an obvious associated positive water signal, which would indicate the presence of isolated coordinated water, suggests that few coordinated water molecules remain on the catalyst surface after activation. In contrast, the single beam infrared spectrum of the activated catalysts, presented in Figure 4.2, exhibits some intensity at  $\sim 1658 \text{ cm}^{-1}$ , which indicates that some water could indeed remain on the surface after exposure to the activation conditions used here. This observation suggests that the concentration of water molecules present on the activated catalyst is below the detection limits of the INS spectrometer.

A small increase in intensity is observed at  $\sim 900 \text{ cm}^{-1}$ , which is assigned to isolated  $\delta_{\text{OH}}$  modes [86], while an associated decrease in intensity is observed at  $1110 \text{ cm}^{-1}$ , which is assigned to H-bonded  $\delta_{\text{OH}}$  modes. This observation is consistent with the transformation of previously hydrogen bonded hydroxyl groups into a more isolated state. The fact that the spectral features associated with  $\delta_{\text{OH}}$  modes seen here are not observed in the DRIFTS spectra due to their obfuscation by the alumina ‘optical cut-off’ highlights one of the advantages of using the INS technique to investigate properties of metal oxide catalysts.

The INS spectra of the ‘dried’ and ‘activated’ catalyst samples, recorded using an incident neutron energy of  $2016 \text{ cm}^{-1}$ , are shown in Figure 4.4.2. Figure 4.4.2(a) presents the INS spectrum of the dried  $\eta\text{-Al}_2\text{O}_3$  while Figure 4.4.2(b) presents that of the activated  $\eta\text{-Al}_2\text{O}_3$  sample. Both spectra are dominated by broad features located at  $201 \text{ cm}^{-1}$  and  $896 \text{ cm}^{-1}$ , which are respectively assigned to out-of-plane ( $\gamma_{\text{OH}}$ ) and in-plane ( $\delta_{\text{OH}}$ ) hydroxyl deformation modes [86]. The  $\gamma_{\text{OH}}$  mode approximates to a torsional motion of the hydroxyl group along the Al-O bond axis [123]. Such modes usually yield intense features in INS spectra [14]. The spectrum of the dried sample (Figure 4.4.2(b)) additionally features broad signals of low intensity located at  $\sim 1680 \text{ cm}^{-1}$ ,  $722 \text{ cm}^{-1}$  and  $540 \text{ cm}^{-1}$ . The band located at

$\sim 1680\text{ cm}^{-1}$  is assigned to the deformation of chemisorbed water molecules, while the  $722\text{ cm}^{-1}$  and  $540\text{ cm}^{-1}$  signals are tentatively assigned to librational modes of chemisorbed water.

This redistribution of INS intensity in the hydroxyl deformation region of the spectrum can be more clearly observed in the difference spectrum presented in Figure 4.4.2(c). In agreement with Figure 4.4.1(c), the loss of chemisorbed water from the system upon activation is clearly indicated by the negative feature located at  $\sim 1658\text{ cm}^{-1}$ . The presence of the positive feature observed at  $\sim 900\text{ cm}^{-1}$  is consistent with an increase in the population of isolated  $\delta_{\text{OH}}$ , which is also in agreement with Figure 4.4.1(c). A decrease in INS intensity is observed at  $766\text{ cm}^{-1}$ , which is broadly attributed to redistribution of various  $\text{H}_2\text{O}$  librational modes upon thermal activation of the sample at  $623\text{ K}$ . Finally, a positive feature is observed at  $\sim 270\text{ cm}^{-1}$ . The location of this feature is consistent with the out-of-plane deformation of isolated hydroxyl groups ( $\gamma_{\text{OH}}$ ) [86]. The apparent enhancement of this feature upon activation is puzzling as dehydroxylation of the surface during thermal activation should produce a negative feature located at this energy. However, it is acknowledged that this feature may also contain a contribution from aluminium phonon modes that occur within this energy range [124, 125]. This hypothesis will be explored in Section 4.4.2 by inspection of the momentum transfer properties of this spectral feature.

Figure 4.4.3 presents the INS spectrum of the activated  $\eta\text{-Al}_2\text{O}_3$  catalyst as recorded using the MERLIN spectrometer, with an incident neutron energy of  $484\text{ cm}^{-1}$ . Here, the enhanced resolving capability of the MERLIN instrument (compared with the older MARI instrument) allows the band located at  $\sim 250\text{ cm}^{-1}$  in Figure 4.4.2 to be resolved into two individual components located at  $185\text{ cm}^{-1}$  and  $265\text{ cm}^{-1}$ . The former is assigned to an alumina phonon mode whilst the latter is assigned to the out-of-plane deformation of surface hydroxyl groups [86]. It is proposed that activation of the catalyst at  $623\text{ K}$  dehydroxylates the surface and leads to a more coherent Al-O phonon mode, which is manifested in Figure 4.4.2 as an increase in intensity at this energy.

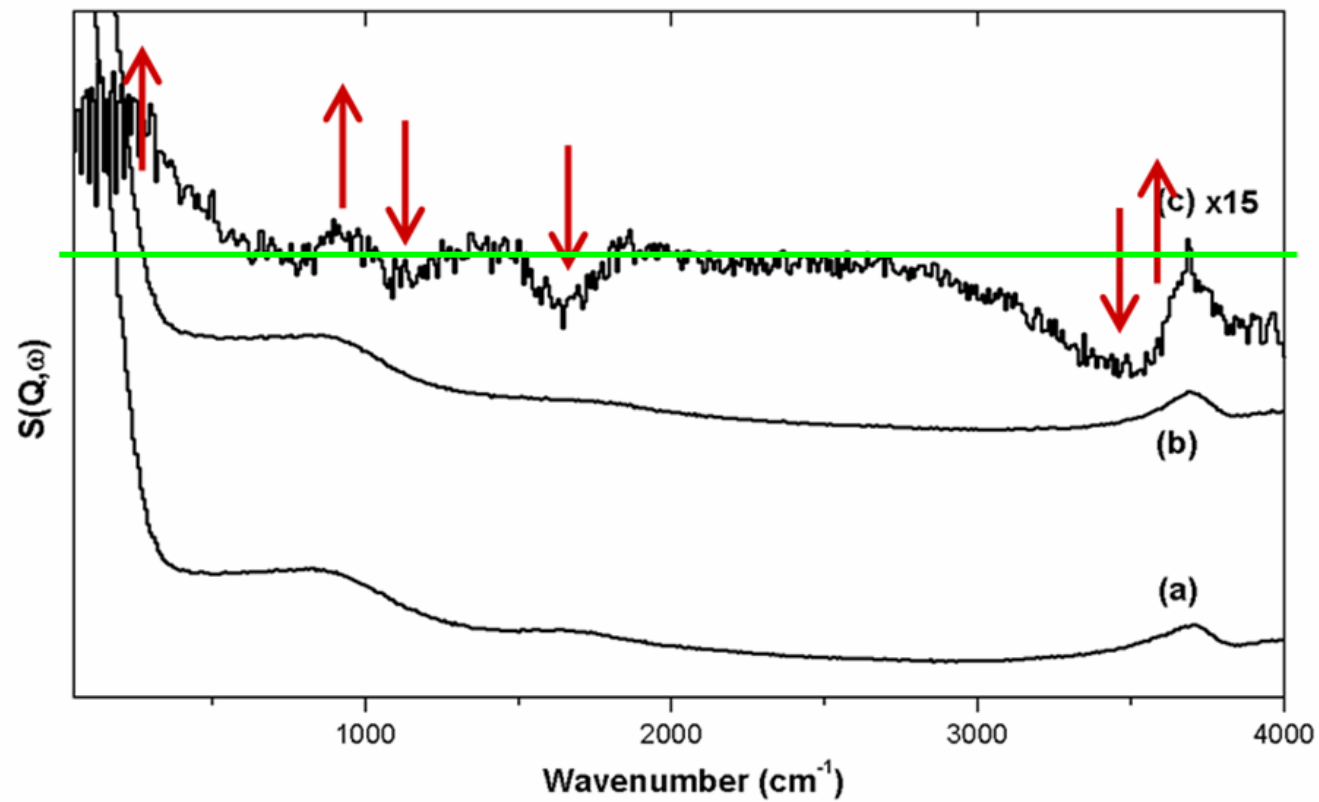


Figure 4.4.1: Inelastic neutron scattering spectra of an  $\eta$ - $\text{Al}_2\text{O}_3$  catalyst heated in flowing helium at (a) 373 K and (b) 623 K. A difference spectrum (623 K – 323 K) is presented in (c). Spectra recorded using the MARI spectrometer with incident neutron energies of 650 meV.

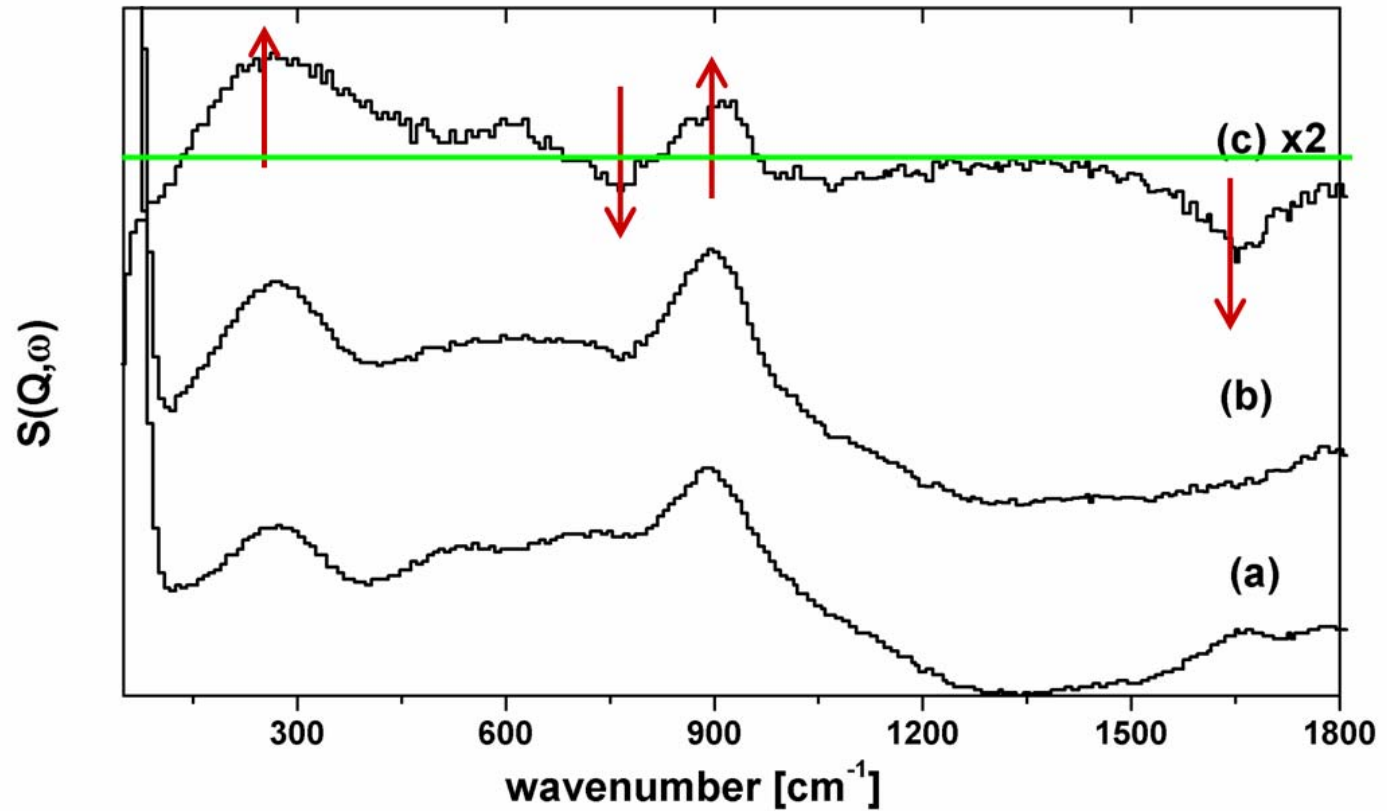


Figure 4.4.2: Inelastic neutron scattering spectra of an  $\eta\text{-Al}_2\text{O}_3$  catalyst heated in flowing helium at (a) 373 K overnight and (b) 623 K for 2.5 h. A difference spectrum (623 K – 323 K) is presented in (c). Spectra recorded using the MARI spectrometer with incident neutron energies of 250 meV.

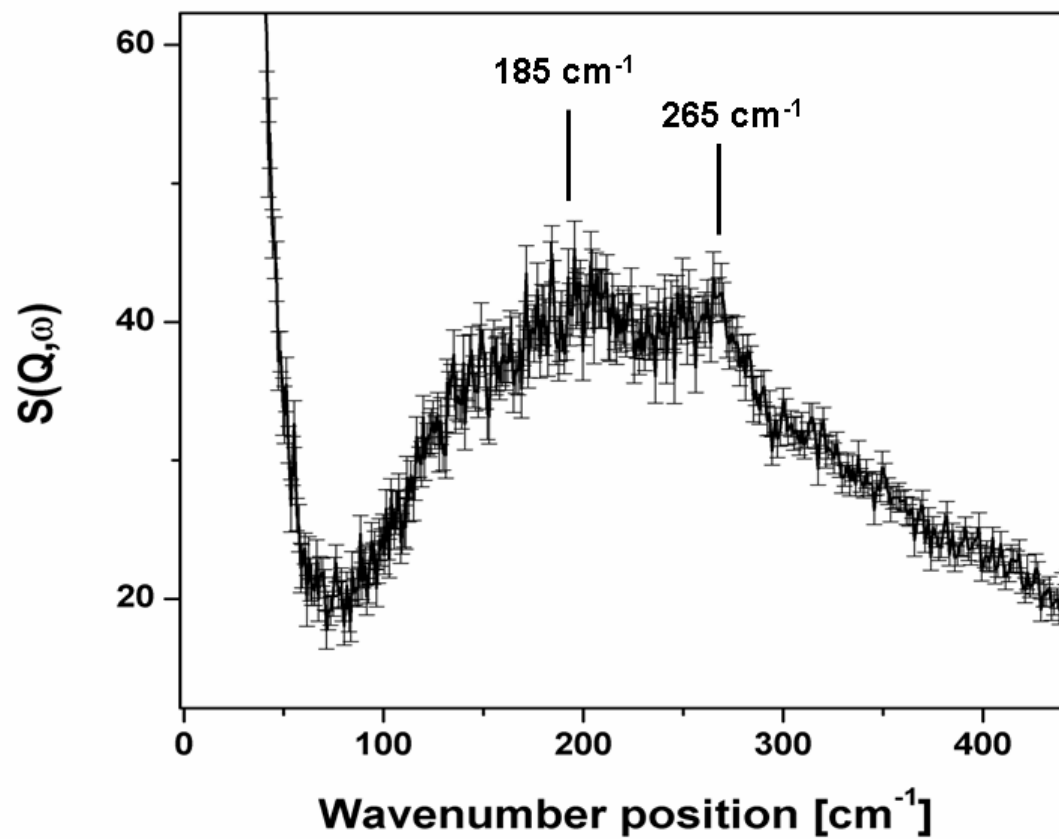


Figure 4.4.3: Inelastic neutron scattering spectrum of an (calcined!)  $\eta$ - $\text{Al}_2\text{O}_3$  catalyst as recorded with an incident neutron energy of  $484 \text{ cm}^{-1}$  using the MERLIN spectrometer (available at ISIS, RAL, UK).

#### 4.4.2 Momentum transfer dependence

The INS spectrum of the activated  $\eta$ -Al<sub>2</sub>O<sub>3</sub> catalyst recorded using the MERLIN spectrometer, presented in Figure 4.4.3, exhibits two features located at 265 cm<sup>-1</sup> and 185 cm<sup>-1</sup>, which are assigned to out-of-plane hydroxyl deformations and Al-O bulk lattice modes, respectively. Inspection of the momentum transfer properties of these features could help to confirm or deny this assertion. Two-dimensional momentum transfer ( $Q$ ) dependence plots are useful in the respect that the momentum transfer dependence of a particular INS signal can indicate if that signal is due to the oscillation of heavy elements, *e.g.* Al-O, or lighter elements, *e.g.* O-H, since an oscillator with a greater reduced mass will absorb more momentum than an oscillator with a comparatively low reduced mass. Therefore, examining the  $Q$  dependence of a given spectral feature can indicate if it can be attributed to vibrations of surface hydroxyl groups, which typically exhibit INS intensity at low values of  $Q$ , or lattice Al-O vibrations, which exhibit intensity at comparatively higher values [14].

As neutron energy,  $E$ , is related to momentum transfer,  $k$ , and neutron mass,  $m_n$ , by the relationship described in Equation 9, (where  $k$  represents momentum transfer,  $Q$ , in real space), the momentum transfer range that can be analysed by a neutron instrument is proportional to the incident energy of the neutrons used [14].

$$E = \frac{\hbar|k|^2}{2m_n} \quad (9)$$

Unfortunately, the two-dimensional momentum transfer plot that corresponds to the INS spectrum (recorded on MERLIN) presented in Figure 4.4.3, which showed energy resolution of the two signals that compose the feature located at ~200 cm<sup>-1</sup> in Figure 4.4.2, does not permit access to a sufficiently wide range of momentum transfer values to allow resolution of these features in terms of  $Q$ . However, using an incident energy of 2016 cm<sup>-1</sup>, as was employed for collection of the INS spectra presented in Figure 4.4.2, allows access to a wider range of momentum transfer values that should allow distinction between lattice modes and surface hydroxyl modes.

Figures 4.4.4 and 4.4.5 show momentum transfer ( $|Q|$ ) versus energy (cm<sup>-1</sup>) plots that describe the  $Q$  dependence of the density of states of ‘dried’ (Fig. 4.4.4) and ‘activated’ (Fig. 4.4.5)  $\eta$ -Al<sub>2</sub>O<sub>3</sub> catalysts recorded using the MARI spectrometer. The INS intensity is represented by the graded colours with blue signifying a low density of states and red

signifying a high density of states. The momentum transfer versus energy plot for the  $\eta$ - $\text{Al}_2\text{O}_3$  catalyst dried at 373 K (Figure 4.4.4) is dominated by the intense band located at  $\sim 250 \text{ cm}^{-1}$ . This band exhibits strong INS intensity over the entire accessible momentum transfer range. This indicates that the band could contain contributions from vibrations of both heavy and light oscillators. It is therefore reasonable to tentatively attribute this band to both Al-O lattice modes, which contribute at high momentum transfer values, and to out-of-plane OH deformations ( $\gamma_{\text{OH}}$ ), which contribute at lower momentum transfer values. In contrast, the band located at  $\sim 900 \text{ cm}^{-1}$  does not exhibit INS intensity at high momentum transfer values and thus it is concluded that this band has evolved solely from the vibrations of light oscillators. This conclusion is consistent with the earlier assignment of this band to in-plane deformations of surface hydroxyl groups ( $\delta_{\text{OH}}$ ).

Similarly, the momentum transfer versus energy plot for the  $\eta$ - $\text{Al}_2\text{O}_3$  catalyst activated at 623 K (Fig. 4.4.5) is also dominated by an intense band located at  $\sim 250 \text{ cm}^{-1}$ . This feature also exhibits INS intensity over the full accessible  $Q$  range. However, in comparison to the momentum transfer versus energy plot of the dried sample (Fig. 4.4.4) the low  $Q$  portion of the band, which has been assigned to out-of-plane hydroxyl deformations, is somewhat diminished. Conversely, the intensity of the high momentum transfer portion of the band, which has been assigned to internal Al-O lattice modes, remains high. Also, the intensity of the band located at  $\sim 900 \text{ cm}^{-1}$  has been significantly diminished upon activation of the  $\eta$ - $\text{Al}_2\text{O}_3$  catalyst. From the momentum transfer versus energy plots presented here, it is indicated that upon activation the catalyst becomes dehydroxylated, as evidenced by the attenuation of both the entire  $\sim 900 \text{ cm}^{-1}$  band and the low momentum transfer component of the  $250 \text{ cm}^{-1}$  band. The Al-O internal lattice modes remain intense after activation.

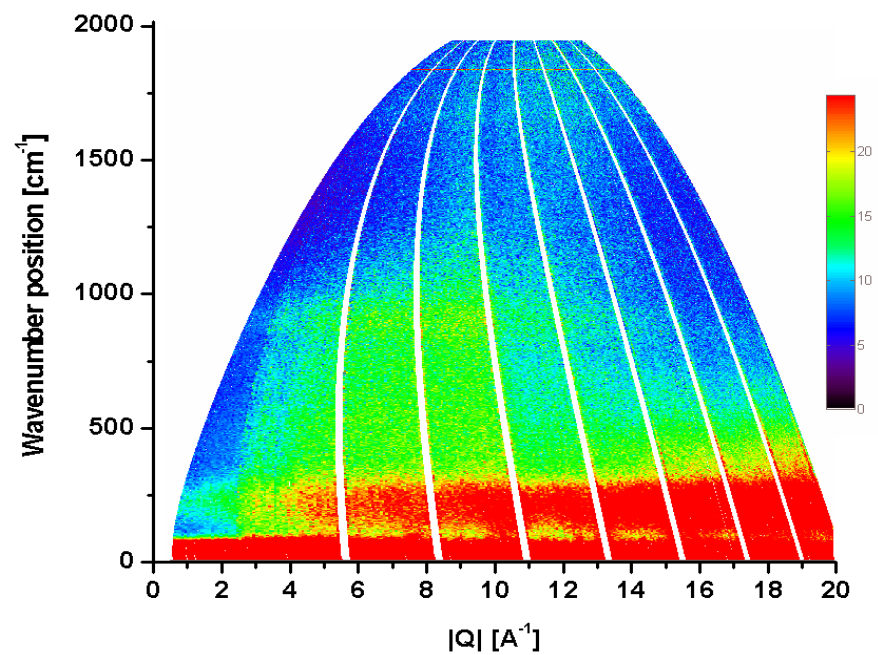


Figure 4.4.4: Two-dimensional INS spectrum of the  $\eta$ - $\text{Al}_2\text{O}_3$  catalyst after being dried at 373 K in flowing helium. Recorded at 10 K using the MARI spectrometer with an incident energy of  $2016 \text{ cm}^{-1}$ , where the neutron scattering intensity is correlated with energy and momentum transfer.

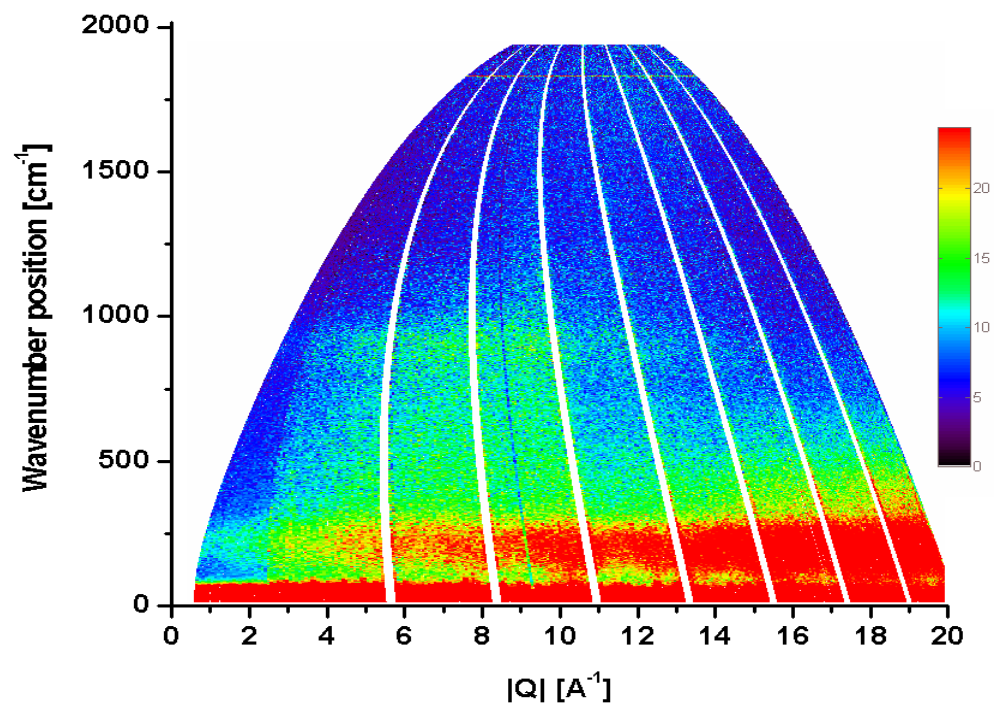


Figure 4.4.5: Two-dimensional INS spectrum of the  $\eta$ - $\text{Al}_2\text{O}_3$  catalyst after being activated at 623 K in flowing helium. Recorded at 10 K using the MARI spectrometer with an incident energy of  $2016 \text{ cm}^{-1}$ , where the neutron scattering intensity is correlated with energy and momentum transfer.

## 4.5 Evidence for the generation of Lewis acidity upon thermal activation

Pyridine adsorption measured by *in situ* infrared spectroscopy, and temperature programmed desorption (TPD) of methanol measured by in-line quadrupole mass spectrometry, experiments were performed in order to assess the Lewis acidity generated after application of the thermal activation conditions employed in this investigation.

### 4.5.1 Pyridine adsorption – infrared spectroscopy

This section describes work examining the chemisorption of pyridine on  $\eta$ -Al<sub>2</sub>O<sub>3</sub> and seeks to replicate the data of McInroy [91] and to confirm the presence of an additional active site recently reported by Lundie *et al.* [38]. This work aims to provide direct spectroscopic evidence for the presence of the so-called medium-strong site [38].

Assignment of the various bands of adsorbed pyridine are usually made according to the convention of Kline and Turkevich [104] who labelled the pyridine modes according to those previously assigned for benzene by Langseth and Lord [126]. The system described by Kline and Turkevich [104] provides excellent correlation for the majority of the vibrational modes, however the assignment of some of the out-of-plane modes are contentious and have more recently been unambiguously assigned by Kearley *et al.* [127] using a combination of inelastic neutron scattering (INS) and density functional theory (DFT) calculations. The pyridine modes of most significance to this investigation are summarised in Table 4.5.1 and a diagrammatic representation of them is given in Figure 4.5.1.

The infrared spectra in the range 1700-1400 cm<sup>-1</sup> after sequential pulse dosing of pyridine over the activated  $\eta$ -Al<sub>2</sub>O<sub>3</sub> catalyst are shown in Figure 4.5.2. The catalyst was maintained at 373 K during the dosing procedure to prevent physisorption of pyridine. The spectra are presented as difference spectra where the spectrum of the activated catalyst has been removed from that of the pyridine-dosed catalyst. Positive features appearing in this energy region are therefore due to modes of chemisorbed pyridine.

Vibrational feature [cm <sup>-1</sup> ]	Assignment
1449	19b mode of pyridine co-ordinately bonded to Lewis acid sites
1492	19a mode of pyridine co-ordinately bonded to Lewis acid sites
1577	8b mode of pyridine coordinatley bonded to Lewis acid sites
1595	8a mode of pyridine coordinatley bonded to <i>weak</i> Lewis acid sites. (Octahedral aluminium acid sites.)
1613	8a mode of pyridine co-ordinately bonded to <i>medium</i> Lewis acid sites. (Tetrahedral aluminium vacancies.)
1623	8a mode of pyridine co-ordinately bonded to <i>strong</i> Lewis acid sites. (Tetrahedral aluminium vacancies.)

Table 4.5.1: Vibrational assignments for pyridine adsorbed on  $\eta$ -Al<sub>2</sub>O<sub>3</sub>.

The signal located at 1577 cm<sup>-1</sup> is assigned to the  $\nu_{8b}$  mode of pyridine co-ordinately bonded to *cus* Al<sup>III</sup> sites and is relatively insensitive to the strength of Lewis acidity. However, the pyridine mode of most significance is the  $\nu_{8a}$  mode, which is deemed to be the most sensitive towards Lewis acidity of a substrate [8, 26, 47, 64, 94, 128], and is located at 1581 cm<sup>-1</sup> in the spectrum of liquid phase pyridine [104]. The observed shift in vibrational energy of this mode upon adsorption reveals the Lewis acid site distribution of the underlying substrate [8]. The spectra presented in Figure 4.5.2 exhibit three distinct  $\nu_{8a}$  derived features located at 1595, 1613 and 1623 cm<sup>-1</sup>, which indicates the presence of at least three types of Lewis acid sites. The band located at 1595 cm<sup>-1</sup> is assigned to pyridine adsorbed on octahedral aluminium sites [8], while the bands located at 1613 and 1623 cm<sup>-1</sup> are assigned to pyridine coordinated to tetrahedral aluminium sites [8]. The higher energy positions observed for the latter bands are due to the adsorbed pyridine experiencing a more polarizing field in the tetrahedral Al<sup>III</sup> centres than in the octahedral Al<sup>III</sup> centres [8]. In agreement with other studies of activated transition aluminas [91], the  $\nu_{19b}$  mode of the pyridinium ion at ~1530 cm<sup>-1</sup> is absent in Figure 4.5.2, which indicates that the  $\eta$ -Al<sub>2</sub>O<sub>3</sub> substrate used here presents no detectable Brønsted acidity.

The intensity profile of the three Lewis acid sites as a function of increased pyridine exposure under a pulse-flow regime is shown in Figure 4.5.3. Population of both the 1613 and 1623 cm<sup>-1</sup> features is observed until the 4th pulse, by which point both of the higher energy features have attained *ca.* 70% of their saturation values. In contrast, progressive

population of the  $1595\text{ cm}^{-1}$  band is observed up to the 6<sup>th</sup> pulse. This behaviour indicates that the Lewis acid sites corresponding to the  $1613$  and  $1623\text{ cm}^{-1}$  features exhibit an enthalpy of adsorption that is substantially greater than that of the Lewis acid sites associated with the infrared signal located at  $1595\text{ cm}^{-1}$ .

The cumulative integrated intensities of all three  $\nu_{8a}$  bands is presented in Figure 4.5.3 (represented by blue triangles) and shows an initially steep rise in the amount of adsorption with increasing pyridine exposure, up to a limiting value. The profile defines a Langmuir (Type 1) adsorption isotherm [129] and is consistent with the formation of a chemisorbed monolayer of pyridine. These results reproduce the trends previously reported by McInroy [91].

The hydroxyl stretching region of the vibrational spectrum of aluminas can provide considerable insight to the surface structure and can therefore provide information on the reaction characteristics of these materials [130-133]. Figure 4.5.4 shows the background-subtracted DRIFTS spectrum in this energy range, as successive aliquots of pyridine are pulsed over the catalyst at  $373\text{ K}$  to form a chemisorbed overlayer. Three bands of negative intensity are observed: a sharp and intense feature at  $3770\text{ cm}^{-1}$ ; a broader feature at  $3730\text{ cm}^{-1}$ ; and a relatively weak and broad feature at *ca.*  $3690\text{ cm}^{-1}$ . The negative form of these bands is due to an interaction between the adsorbed pyridine molecules and isolated, *i.e.* non-hydrogen bonded, hydroxyl groups on the alumina surface, which results in a reduction in the vibrational frequency of the hydroxyl moiety, as described by Liu and Truitt [65]. The intensity of all of the observed features appears to decrease monotonically upon increasing pyridine coverage. The desorption characteristics of this energy region of the spectrum can be used to correlate the hydroxyl bands with pyridine  $\nu_{8a}$  modes and will be described in Section 4.5.2.

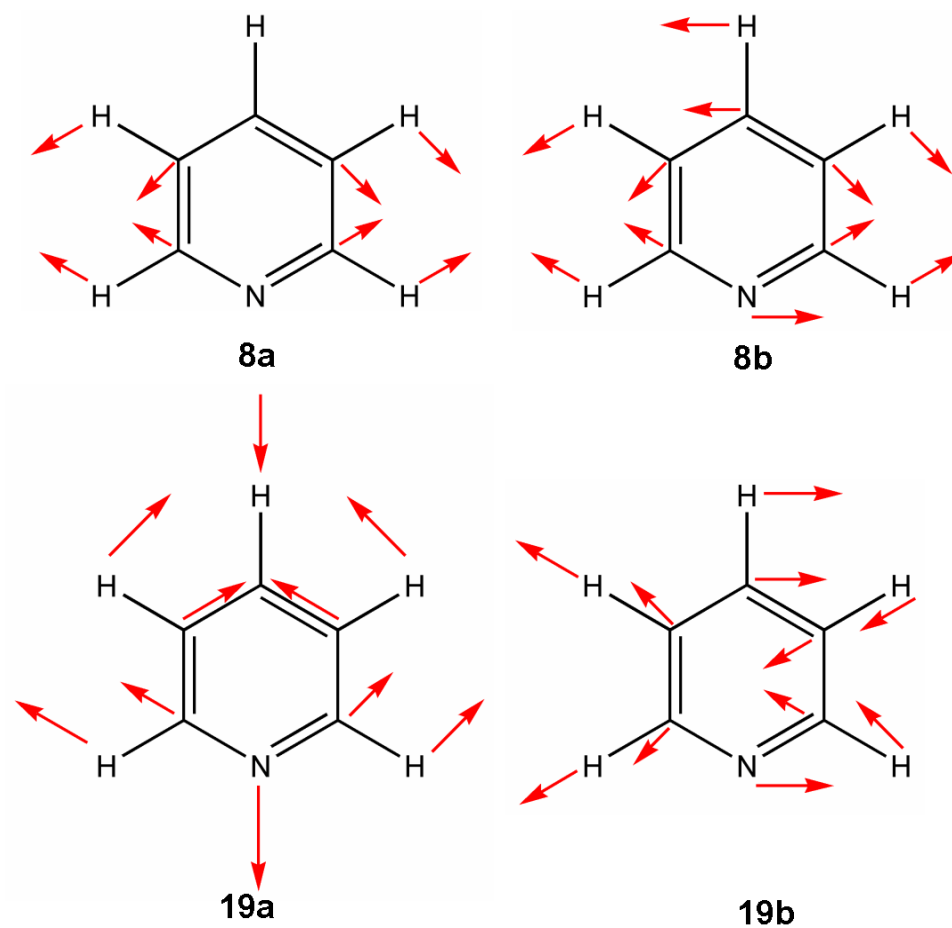


Figure 4.5.1: Schematic representation of pyridine modes found in the energy range  $1700\text{-}1400\text{ cm}^{-1}$ . Reproduced from [104].

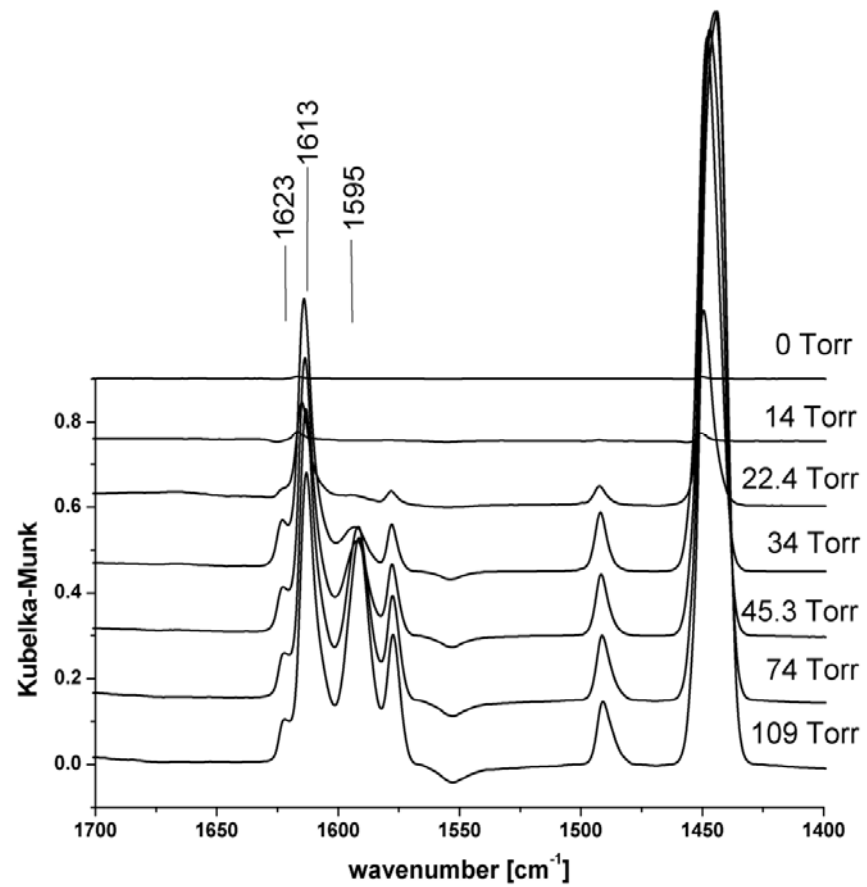


Figure 4.5.2: Infrared difference spectrum for sequential dosing of pyridine on activated  $\eta$ - $\text{Al}_2\text{O}_3$ .

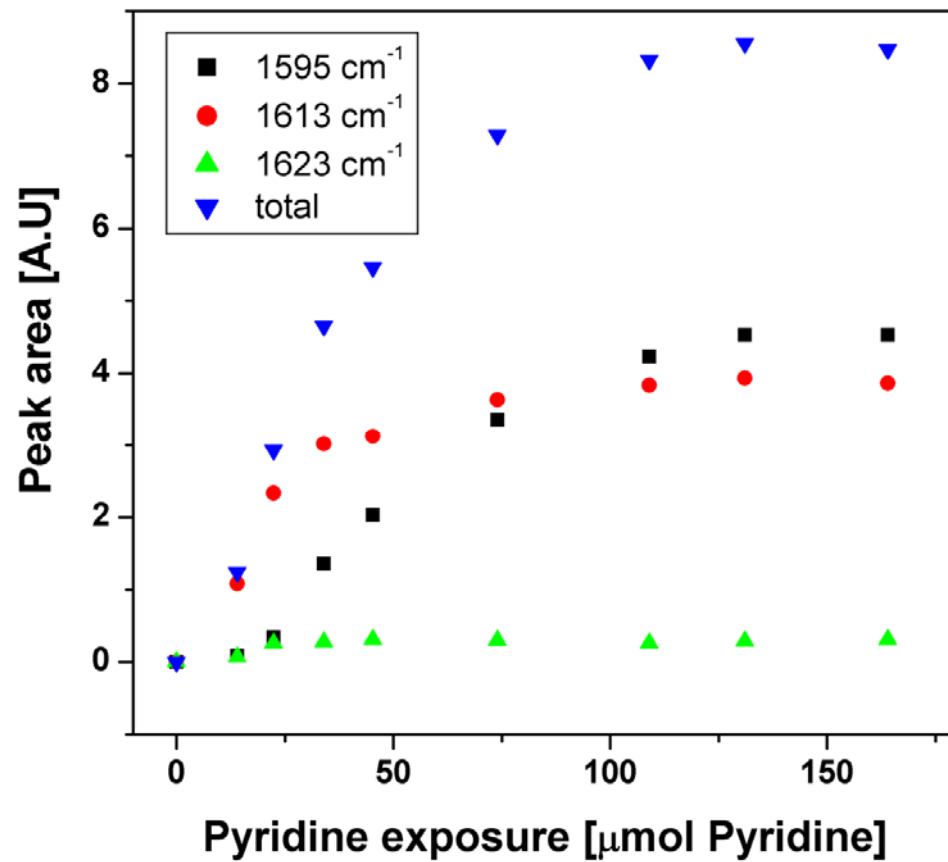


Figure 4.5.3: Integrated intensities of the pyridine  $\nu_{8a}$  modes for a chemisorbed overlayer of pyridine on  $\eta\text{-Al}_2\text{O}_3$ , as a function of pyridine exposure.

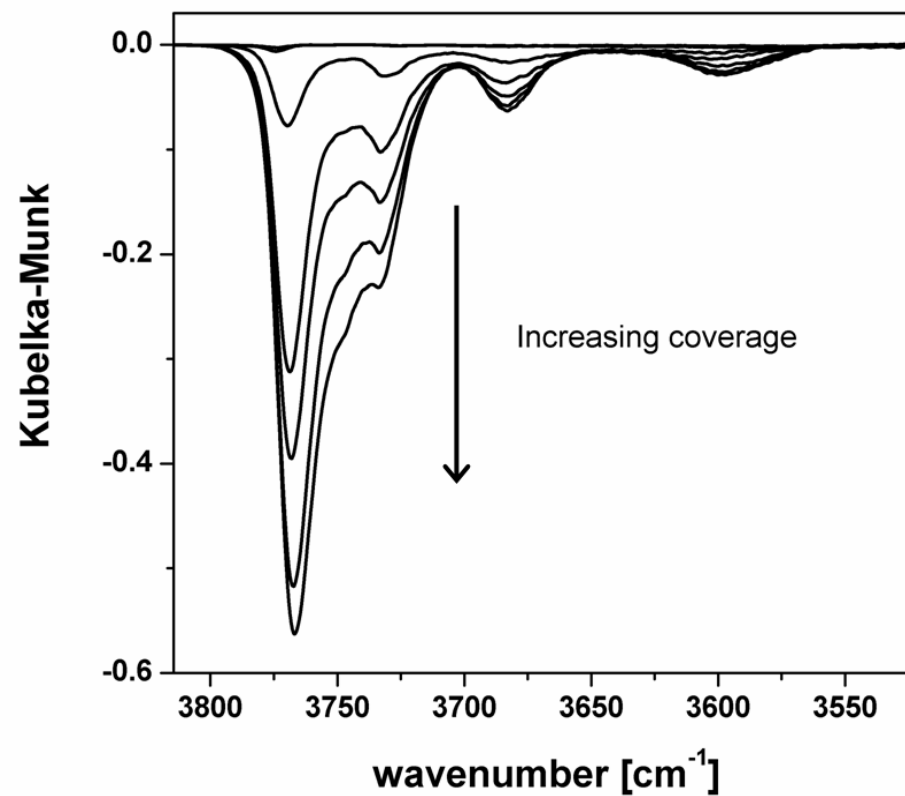


Figure 4.5.4: Background subtracted difference DRIFTS spectra for the hydroxyl stretching region for  $\eta$ -Al<sub>2</sub>O<sub>3</sub> as a function of pyridine exposure.

#### 4.5.2 Temperature programmed desorption infrared spectroscopy

The infrared spectrum of a chemisorbed overlayer of pyridine on the activated  $\eta$ -Al<sub>2</sub>O<sub>3</sub> catalyst as a function of temperature is presented in Figure 4.5.5. Increasing the temperature of the sample leads to progressive pyridine desorption and can provide information on the relative heats of adsorption for each of the Lewis acid sites presented by the  $\eta$ -Al<sub>2</sub>O<sub>3</sub> surface.

The band located at 1595 cm<sup>-1</sup> is removed at low temperatures, thereby indicating a weakly bound species, which is in agreement with the trends observed in Figure 4.5.3. Only minor intensity remains after heating to 423 K and the signal has completely disappeared after heating to 523 K. Additional warming leads to the progressive attenuation of the signal located at 1613 cm<sup>-1</sup> up to 723 K where the band is absent from the spectrum. In contrast, the most strongly perturbed  $\nu_{8a}$  mode, located at 1623 cm<sup>-1</sup>, is relatively insensitive to temperature and appears to maintain the majority of its initial saturation value upon warming to 723 K, indicating a strongly bound species in agreement with Figure 4.5.3.

Collectively, Figures 4.5.2, 4.5.3 and 4.5.5 permit classification of the acid site distribution for the catalyst into *weak*, *medium* and *strong* Lewis acid sites. The signal located at 1595 cm<sup>-1</sup> is assigned to pyridine adsorbed on *weak* Lewis acid sites, exhibiting a pyridine desorption temperature of <523 K. The signal located at 1613 cm<sup>-1</sup> is assigned to pyridine adsorbed to *medium*-strength Lewis acid sites and exhibits a desorption temperature of *ca.* 723 K. In comparison, the signal located at 1623 cm<sup>-1</sup> is relatively unperturbed throughout the applied temperature range and is therefore assigned to pyridine adsorbed on *strong* Lewis acid sites. The trends observed here are consistent with those reported by Liu and Truitt [65], Morterra and Magnacca [8], and Lundie *et al.* [38]. It should be noted that Morterra and Magnacca found that the pyridine assigned to the signal at 1613 cm<sup>-1</sup> to have completely desorbed by 573 K [8]. The lower desorption temperature observed by Morterra and Magnacca is possibly due to differences in the interaction energies in the alumina used by Morterra due to the fact that their sample had been activated at a higher temperature than the sample used in this investigation. In addition, Morterra and Magnacca desorbed the pyridine using a vacuum whereas a flow of helium was used here. However, it is noted that measurements made by McInroy [91] established that similar trends were observed when vacuum assisted TPD experiments were performed, indicating the conducting medium, *i.e.* vacuum or flowing helium, not to be a determining factor affecting the profiles reported here.

The characteristics of the  $\nu_{\text{OH}}$  region of the infrared spectrum upon thermal desorption of pyridine are presented in Figure 4.5.6, which is simply characterised by a progressive decay of all three features upon increasing temperature. The fact that the baseline is almost recovered after heating to 723 K, indicates that the adsorption/desorption process in this region of the spectrum is reversible.

The desorption characteristics of the  $\nu_{\text{OH}}$  region for the alumina surface (Fig. 4.5.6) can be correlated with the band profiles observed for the ring modes of the adsorbed pyridine (Fig. 4.5.5), as reported by Lundie *et al.* [38]. Figure 4.5.6 shows that upon heating to 723 K all of the negative hydroxyl features are essentially absent from the spectra, which is entirely consistent with the work of Lundie *et al.* [38]. Figure 4.5.5 shows that the pyridine  $\nu_{8a}$  feature located at  $1623\text{ cm}^{-1}$ , which is assigned to the *strong* Lewis acid site, remains intact after heating to 723 K, so it therefore appears that there is no observable band in the hydroxyl region associated with *strong* Lewis acid sites. The negative hydroxyl features observed in Figures 4.5.4 and 4.5.6 must therefore be associated with the *weak* and *medium* strength Lewis acid sites. This observation is in contrast to that of Liu and Truitt [65], who attribute their highest energy  $\nu_{\text{OH}}$  band at  $3764\text{ cm}^{-1}$  as arising from hydroxyl groups next to the *strong* Lewis acid site. However, this work suggests that on activated  $\eta\text{-Al}_2\text{O}_3$  the *strong* Lewis acid site associated with the pyridine  $\nu_{8a}$  mode at  $1623\text{ cm}^{-1}$  has no counterpart in the  $\nu_{\text{OH}}$  region of the infrared spectrum. This conclusion supports the assertion of Lundie *et al.* [38] that the *strong* Lewis acid site is a ‘bare’ site, with no neighbouring hydroxyl groups, and so therefore no hydrogen bonding occurs upon adsorption of pyridine.

It is accepted that this observation could be explained by other mechanisms. For example, upon pyridine adsorption on this high-energy site, the electropositive nature of the coordinatively unsaturated  $\text{Al}^{\text{III}}$  centre will concentrate electron density towards the Al. The consequential reduction in electron density at the nitrogen atom could then weaken hydrogen bonding interactions to neighbouring hydroxyl groups so that no perturbation of neighbouring hydroxyl groups is observed at this site. This would be expected to produce shifts in the  $\nu_{\text{OH}}$  stretching frequency as a function of pyridine coverage, which is not observed in Figure 4.5.4 and for this reason, the latter hypothesis is rejected.

The trends independently observed here for the both the  $\nu_{\text{OH}}$  and pyridine  $\nu_{8a}$  modes are in excellent agreement with those reported by Lundie *et al.* [38]. The desorption behaviour of the hydroxyl feature located at  $3690\text{ cm}^{-1}$  correlates well with the pyridine  $\nu_{8a}$  mode located at  $1595\text{ cm}^{-1}$  associated with *weak* Lewis acid sites, whilst the  $\nu_{\text{OH}}$  modes located at  $3730$  and  $3770\text{ cm}^{-1}$  correlate well with the pyridine  $\nu_{8a}$  mode located at  $1613\text{ cm}^{-1}$ . Lundie *et al.* [38] were able to show by a combination of the methodology employed above (*i.e.* infrared spectroscopy of chemisorbed pyridine) and pyridine temperature programmed desorption (TPD) that the *medium* strength Lewis acid site could be subdivided into *medium-weak* and *medium-strong* components. Furthermore, based on the temperature dependence of the  $\nu_{\text{OH}}$  modes, the features located at  $3730$  and  $3770\text{ cm}^{-1}$  were assigned to hydroxyl groups adjacent to *medium-weak* and *medium-strong* Lewis acid sites, respectively. Interestingly, the  $\nu_{\text{OH}}$  region appears to allow distinction between the *medium-strong* and *medium-weak* Lewis acid sites; a distinction that could not be made using the pyridine acid site diagnostic region of the spectrum. The assignments of the bands observed in the spectra presented here are summarised in Table 4.5.2.

Lewis acid site	Pyridine 8a mode [ $\text{cm}^{-1}$ ]	alumina $\nu_{\text{OH}}$ [ $\text{cm}^{-1}$ ]
<i>Weak</i>	1595	3690
<i>Medium-weak</i>	1613	3730
<i>Medium-strong</i>	1613	3770
<i>Strong</i>	1623	-

Table 4.5.2: Correspondence between the Lewis acid site, adsorbed pyridine  $\nu_{8a}$  mode, and  $\nu_{\text{OH}}$  stretch of activated  $\eta\text{-Al}_2\text{O}_3$  (reproduced from [38]).

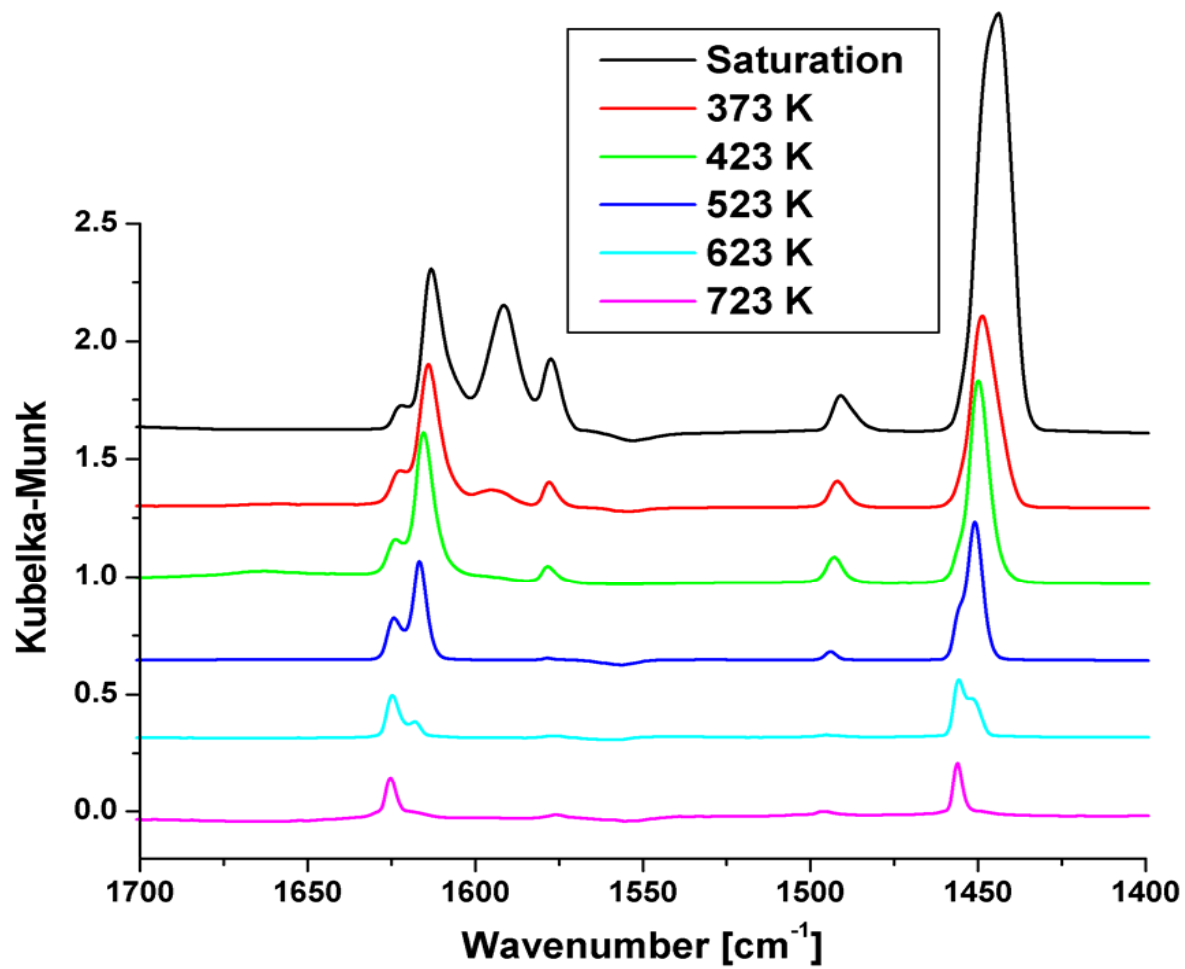


Figure 4.5.5: Infrared spectrum of a saturated overlayer of pyridine on activated  $\eta$ - $\text{Al}_2\text{O}_3$  as a function of temperature.

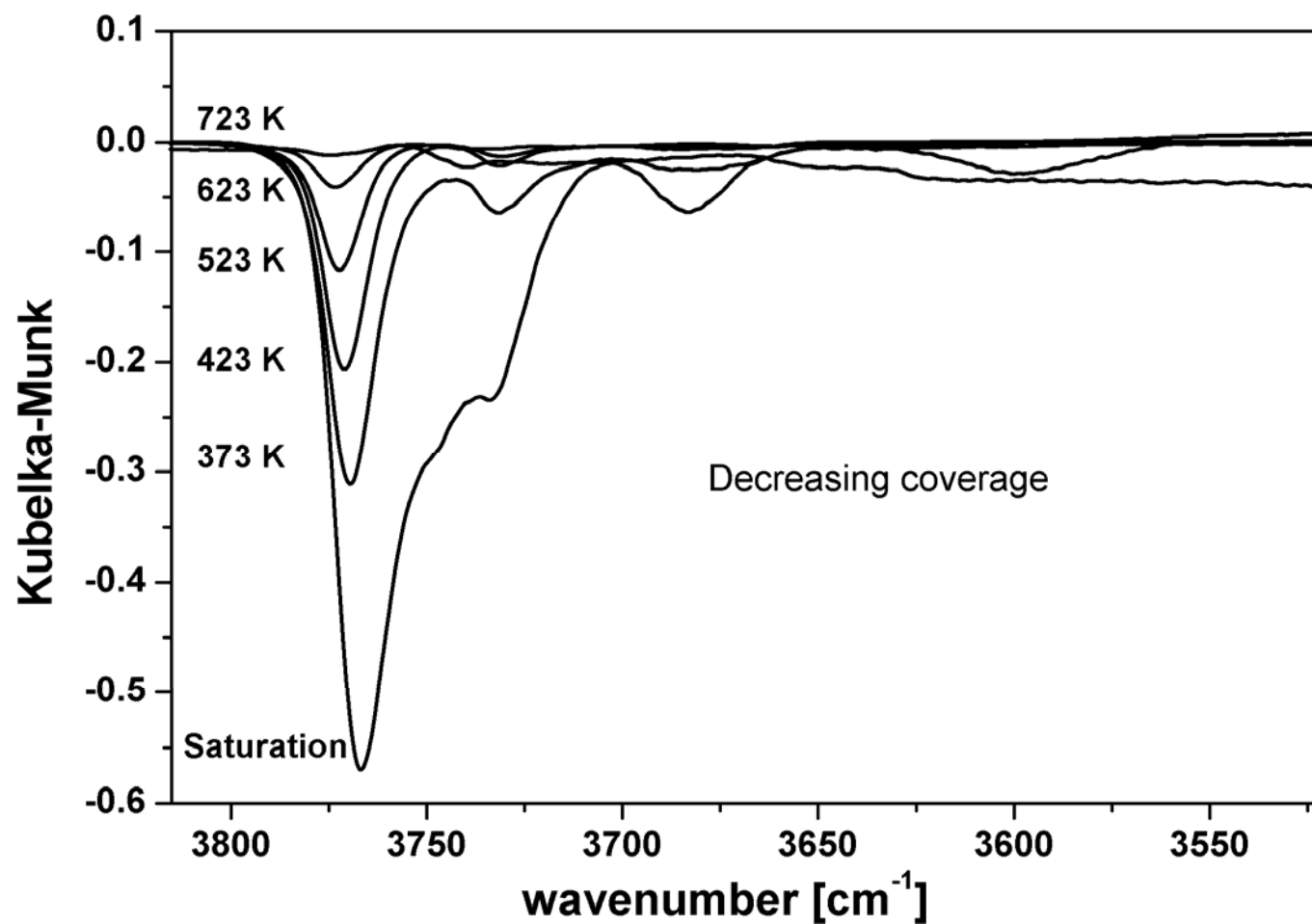


Figure 4.5.6: Background subtracted difference DRIFTS spectra for the hydroxyl stretching region of  $\eta$ -Al<sub>2</sub>O<sub>3</sub> as a chemisorbed saturation overlayer is sequentially heated to increasing temperatures.

### 4.5.3 Mass selective temperature programmed desorption of methanol

The dehydration of alcohols over alumina catalysts to form olefinic and ether products has been known for over 200 years [134-136], however the exact mechanism for the formation of the ether remains unresolved [137]. The reaction of methanol over solid acid heterogeneous catalysts can lead to the formation of dimethyl ether (DME), hydrocarbons (including olefins), and water.

DME formation is associated with Equation 10:



Strong acid sites are required to produce hydrocarbons from methanol, whereas sites of comparatively moderate acidity are sufficient to catalyse DME formation [59, 138]. For this reason, the dehydration of methanol over a catalyst surface may be used as a test of surface acidity. The condensation of methanol to give DME can proceed by either Brønsted or Lewis acid mechanisms [50, 137], however in cases where the catalyst presents no measurable Brønsted acidity, the Lewis acid-mediated mechanism will dominate.

Mechanistically, the formation of DME from methanol over an activated alumina catalyst has been proposed to proceed via the condensation of two adsorbed methoxy species [59, 138]. It has been reported that methanol adsorbs only associatively at weaker Lewis acid sites, while dissociative adsorption can occur on comparatively more acidic Lewis sites [38, 91].

The temperature programmed desorption (TPD) profile, as measured by on-line quadrupole mass spectrometry, for a saturated overlayer of methanol on  $\eta\text{-Al}_2\text{O}_3$  is presented in Figure 4.5.7. The TPD experiment was performed after an overnight purge in flowing helium to ensure that physisorbed methanol could play no part in the resulting TPD profile. Figure 4.5.7 is consistent with that previously obtained by Lundie [121] and McNroy [91, 138] and is characterised by two distinct features: a  $m/z = 31$  peak centred at 390 K, which is assigned to methanol; and a  $m/z = 45$  peak at 460 K, which is attributed to DME formation. A minimum temperature of 400 K is required for dimethyl ether production. The profile is also consistent with that previously reported by DeVore *et al.* [139] for methanol adsorbed on poorly crystalline  $\gamma\text{-Al}_2\text{O}_3$ . Both methanol and DME signals tail to high temperatures, reaching approximate baseline levels at *ca.* 700 K.

Importantly, the methanol TPD presented in Figure 4.5.7 also confirms that the activation procedure adopted throughout this investigation produces a catalyst that is sufficiently acidic to promote the formation of DME from methanol, which is consistent with the observations of Tleimatmanzalji *et al.* [140].

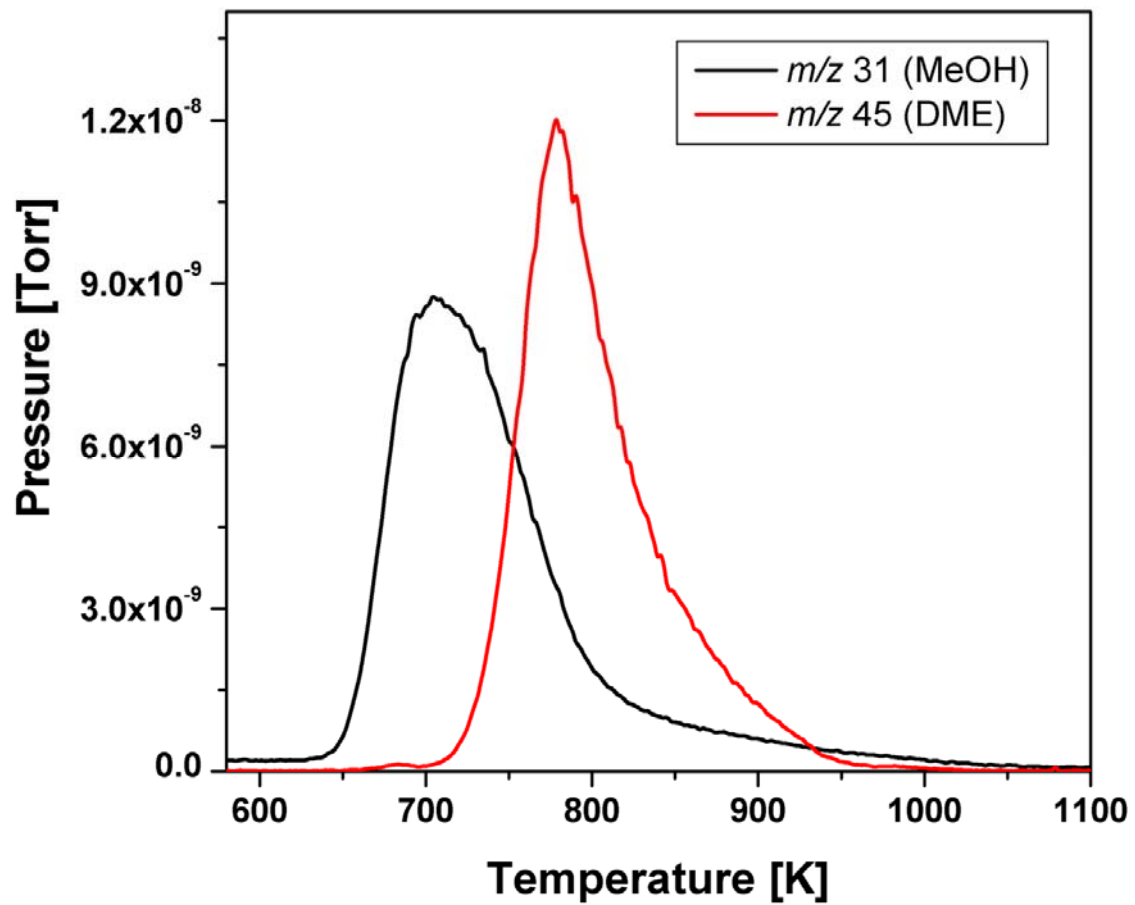


Figure 4.5.7: Temperature programmed desorption spectrum for a saturation chemisorption dose of methanol on activated  $\eta$ - $\text{Al}_2\text{O}_3$ .

## 4.6 Conclusions

Inelastic neutron scattering was used to characterise, on a molecular level, the thermal activation of an  $\eta$ -Al<sub>2</sub>O<sub>3</sub> catalyst. As a spectroscopic characterisation technique, INS is uniquely diagnostic in the respect that it allows observation of both out-of-plane and in-plane hydroxyl deformation modes under realistic sample handling and preparation conditions. INS provided spectroscopic evidence for the desorption of both chemisorbed water and surface hydroxyl species upon thermal activation, which is in agreement with the generally accepted activation mechanism for metal oxides described by Kung [54]. The spectra show that after activation some hydroxyl groups remain on the surface and that some hydrogen bonding persists. The activation process is diagrammatically represented in Figure 4.6.1. The surface Lewis acidity generated upon exposure of the  $\eta$ -Al<sub>2</sub>O<sub>3</sub> catalyst to the activation conditions described here is sufficient to catalyse the dehydration of methanol to yield dimethyl ether. The surface acidity of the activated catalyst was further characterised by observation of the infrared spectra of chemisorbed pyridine and was found to conform to the surface model proposed by Lundie *et al.* [38].



# 5

## Chapter 5

### **Modification of surface Lewis acidity of transition alumina catalysts**

The Lewis acidity of activated transition alumina catalysts is complex and varied [8, 26, 47]. When chosen as a *bona fide* active catalyst the coordinatively unsaturated Lewis acid sites that are generated upon thermal activation can be usefully employed in many acid mediated chemical reactions. However, in some circumstances, the most acidic sites can promote undesirable side reactions. For example, one may consider the dehydration of methanol where very strong acidity can lead to the formation of unwanted hydrocarbon side-products, while comparatively less acidic Lewis sites yield the desired dimethyl ether (DME) product [91, 121, 138]. Selective attenuation of only the strongest Lewis acid sites represents a highly desirable prospect in cases such as this [36].

A combination of x-ray diffraction (XRD), nitrogen adsorption isotherms and infrared spectroscopic measurements was employed in order to investigate the physical changes occurring within the structure of an  $\eta$ -Al<sub>2</sub>O<sub>3</sub> catalyst under thermal pre-treatment conditions and to assess the effect this has on the Lewis acidity expressed at the catalyst surface.

The possibility that physical treatments, *i.e.* thermal conditioning, could be used to control acid site distributions is an enticing prospect, offering a simpler method than chemical modification techniques outlined elsewhere [42].

## 5.1 Thermal effects on alumina structure

The thermal dependence of the expressed transition alumina phase is summarised by the thermal phase diagram of alumina, as published by Wefers and Misra [34], which is reproduced in Diagram 3.0.1. The thermal phase diagram indicates that heat treatment of  $\eta$ -Al<sub>2</sub>O<sub>3</sub> at temperatures in excess of 900 K can promote a phase transformation towards  $\theta$ -Al<sub>2</sub>O<sub>3</sub>.

According to <sup>27</sup>Al NMR spectrometry,  $\theta$ -Al<sub>2</sub>O<sub>3</sub> is structurally different to  $\eta$ -Al<sub>2</sub>O<sub>3</sub> in that the  $\eta$ -Al<sub>2</sub>O<sub>3</sub> is formally a tetragonal phase while  $\theta$ -Al<sub>2</sub>O<sub>3</sub> is a more ordered monoclinic phase [116]. More specifically,  $\eta$ -Al<sub>2</sub>O<sub>3</sub> contains approximately 35% tetrahedral Al<sup>III</sup> centres in its structure whereas  $\theta$ -Al<sub>2</sub>O<sub>3</sub> is composed of around ~50% tetrahedral Al<sup>III</sup> centres [117]. In both phases octahedral Al<sup>III</sup> centres make up the balance [116, 117, 141]. Exposed coordinatively unsaturated (cus) Al<sup>III</sup> centres are responsible for the Lewis acidity observed for thermally activated transition alumina catalysts: exposed tetrahedral Al<sup>III</sup> centres confer strong Lewis acidity, while exposed octahedral Al<sup>III</sup> sites provide weaker acidity. It is therefore possible that heating an  $\eta$ -Al<sub>2</sub>O<sub>3</sub> catalyst to temperatures that promote a phase transformation towards  $\theta$ -Al<sub>2</sub>O<sub>3</sub> could increase the proportion of tetrahedral Al<sup>III</sup> centres in the bulk structure. This process could alter the relative proportion of cus tetrahedral and octahedral Al<sup>III</sup> centres exposed at the surface of the activated catalyst. Thus, careful thermal pre-treatment could potentially provide a simple and cost-effective method to perturb the surface acidity of transition alumina catalysts. In order to explore this possibility a series of transition alumina catalysts were prepared by calcining  $\eta$ -Al<sub>2</sub>O<sub>3</sub> at various different temperatures. The thermal history of each of these samples is given in Table 5.1.1.

<i>Thermal history of <math>\eta</math>-Al<sub>2</sub>O<sub>3</sub> catalyst</i>
1. Calcined at 773 K, 1 hour.
2. Calcined at 923 K, 1 hour.
3. Calcined at 1073 K, 1 hour.
4. Calcined at 1173 K, 1 hour.

Table 5.1.1: Series of catalysts prepared to investigate thermal pre-treatment on alumina structure and acidity.

## 5.2 X-ray diffraction (XRD) analysis

Initial characterisation of the differentially calcined  $\text{Al}_2\text{O}_3$  catalysts was obtained by powder X-ray diffraction (XRD). The XRD patterns measured for samples calcined at 773, 923, 1073, and 1173 K are presented in Figures 5.2.1-5.2.4 and can be used to identify the phase composition of each sample. A stacked plot of the XRD profiles is presented in Figure 5.2.5. The diffractograms presented here are entirely consistent with those reported by Snyder *et al.* [116] and Pecharroman [117], and indicates a progressive phase transformation from  $\eta\text{-Al}_2\text{O}_3$  to  $\theta\text{-Al}_2\text{O}_3$  to have occurred on increasing calcination temperature. The alumina suppliers, Ineos [142, 143], report 773 K to be the lowest temperature at which they can reliably prepare  $\eta\text{-Al}_2\text{O}_3$  [142]. The  $\eta\text{-Al}_2\text{O}_3$  catalyst used here has not previously been calcined above 773 K.

The diffuse nature of the reflections contained within the powder patterns indicates a high degree of structural disorder in all of the samples considered here [116, 120]. However, the similarities in the patterns indicate that certain structural motifs pervade all of the samples, as has previously been reported for several transition aluminas [116]. The powder x-ray diffraction patterns for samples heated to 773 K and 923 K, respectively presented in Figures 5.2.1 and 5.2.2, are almost identical and show these particular samples to be composed of poorly crystalline  $\eta\text{-Al}_2\text{O}_3$ . Figure 5.2.3 shows that on increasing the calcination temperature to 1073 K, a similar powder diffraction pattern is yielded but that an additional small proportion of  $\theta\text{-Al}_2\text{O}_3$  is also present, as indicated by the presence of additional diffraction lines located at  $30.7^\circ$ ,  $32.6^\circ$ ,  $50.0^\circ$ , and  $61.7^\circ$ , which are assigned to the (401), (-202), (331) and (113) reflections of  $\theta\text{-Al}_2\text{O}_3$ , respectively [116]. In addition, on increasing calcination temperature, asymmetry is progressively developed in the signal located at  $45.4^\circ$  in the sample calcined at 773 K. Finally, the XRD pattern of  $\eta\text{-Al}_2\text{O}_3$  calcined at 1173 K (Figure 5.2.4) reveals this sample to contain a substantial proportion of  $\theta\text{-Al}_2\text{O}_3$ , however, the presence of some  $\eta\text{-Al}_2\text{O}_3$  in this sample cannot be completely ruled out due to the presence of overlapping diffraction lines native to both of the pure  $\eta\text{-Al}_2\text{O}_3$  and  $\theta\text{-Al}_2\text{O}_3$  transition forms [116].

Lippens and DeBoer [35] originally proposed that  $\eta\text{-Al}_2\text{O}_3$  transforms into  $\theta\text{-Al}_2\text{O}_3$  in a *reconstructive* process but the very similar ABC stacking pattern of both transition forms indicates that this need not necessarily be the case. A distinct phase *transition* is not observed from this investigation, instead a gradual splitting and sharpening of diffraction

lines is observed, which is consistent with transformation of  $\eta\text{-Al}_2\text{O}_3$  to  $\theta\text{-Al}_2\text{O}_3$  occurring via a *displacive* process [116]. These results confirm that a continuous and progressive phase *transformation* from  $\eta\text{-Al}_2\text{O}_3$  to  $\theta\text{-Al}_2\text{O}_3$  is induced upon heating the samples to temperatures of *ca.* 1073 K and above. This is in agreement with the literature where calcination temperatures of at least 1273 K are reported to be necessary for the complete transformation of  $\eta\text{-Al}_2\text{O}_3$  to  $\theta\text{-Al}_2\text{O}_3$  [34, 116]. It must be noted, however, that the phase transformation temperatures indicated in the literature for transition aluminas are approximate and depend on, amongst other external factors, purity of starting material.

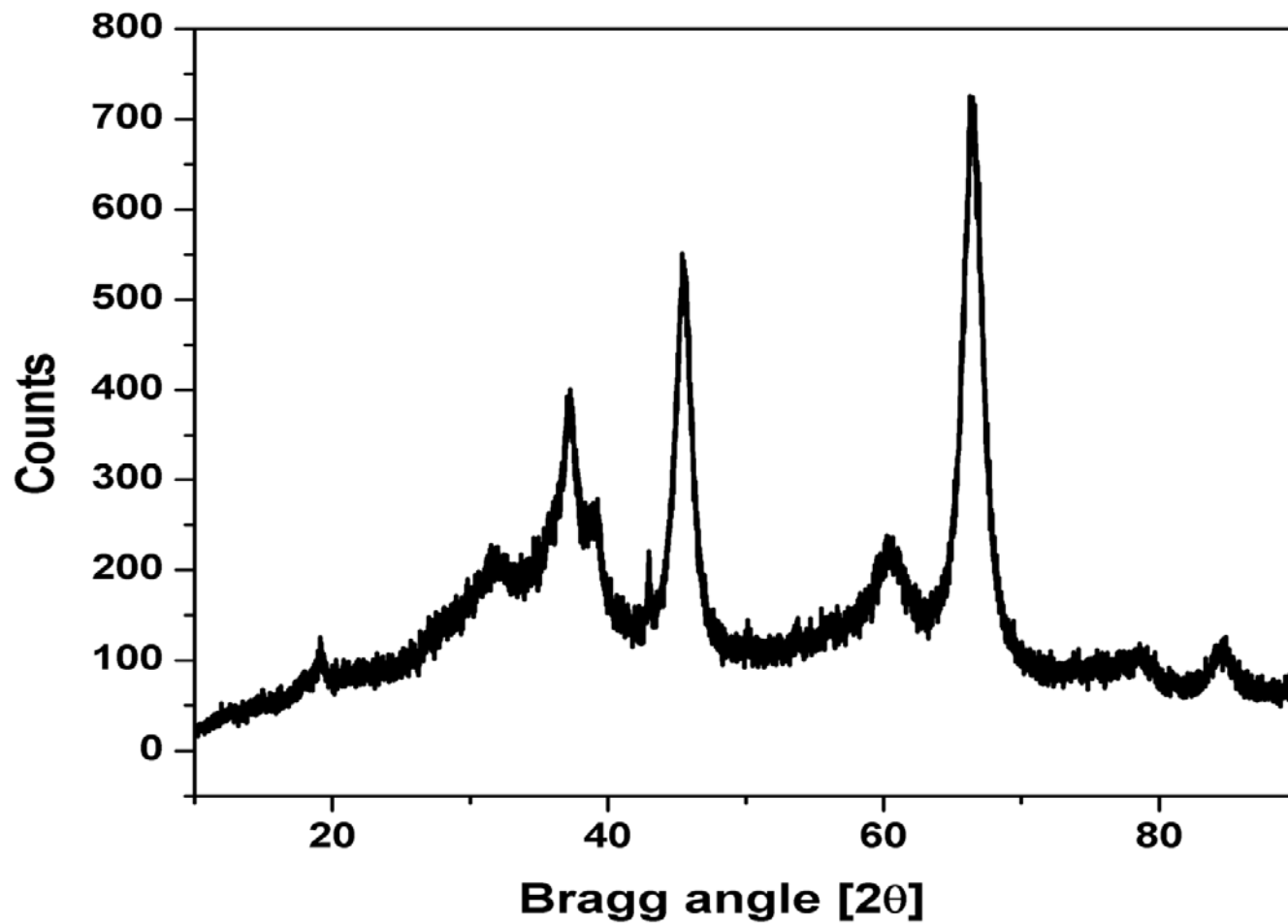


Figure 5.2.1: Powder x-ray diffractogram for an  $\eta$ - $\text{Al}_2\text{O}_3$  sample calcined at 773 K.

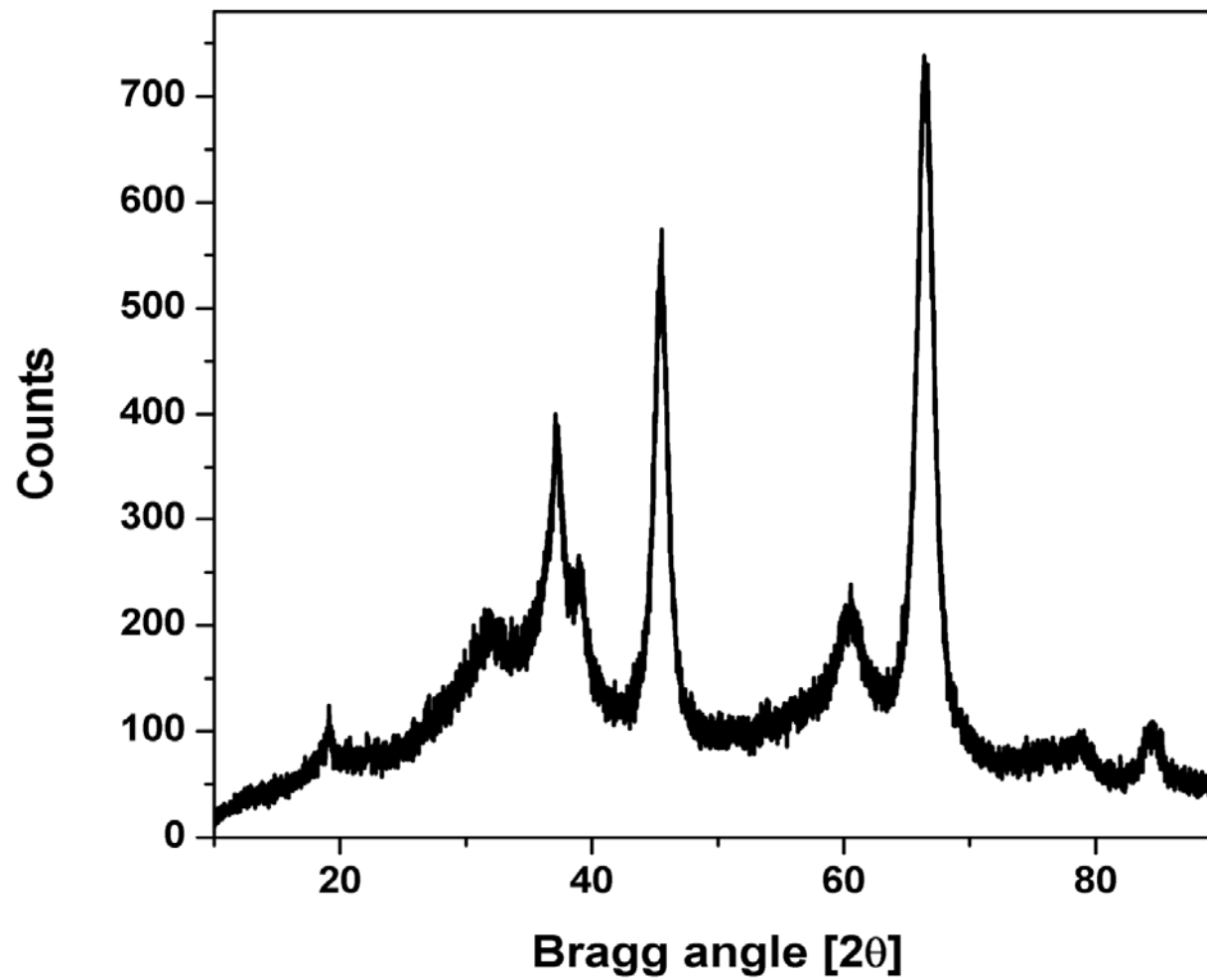


Figure 5.2.2: Powder x-ray diffractogram for an  $\eta$ - $\text{Al}_2\text{O}_3$  sample calcined at 923 K.

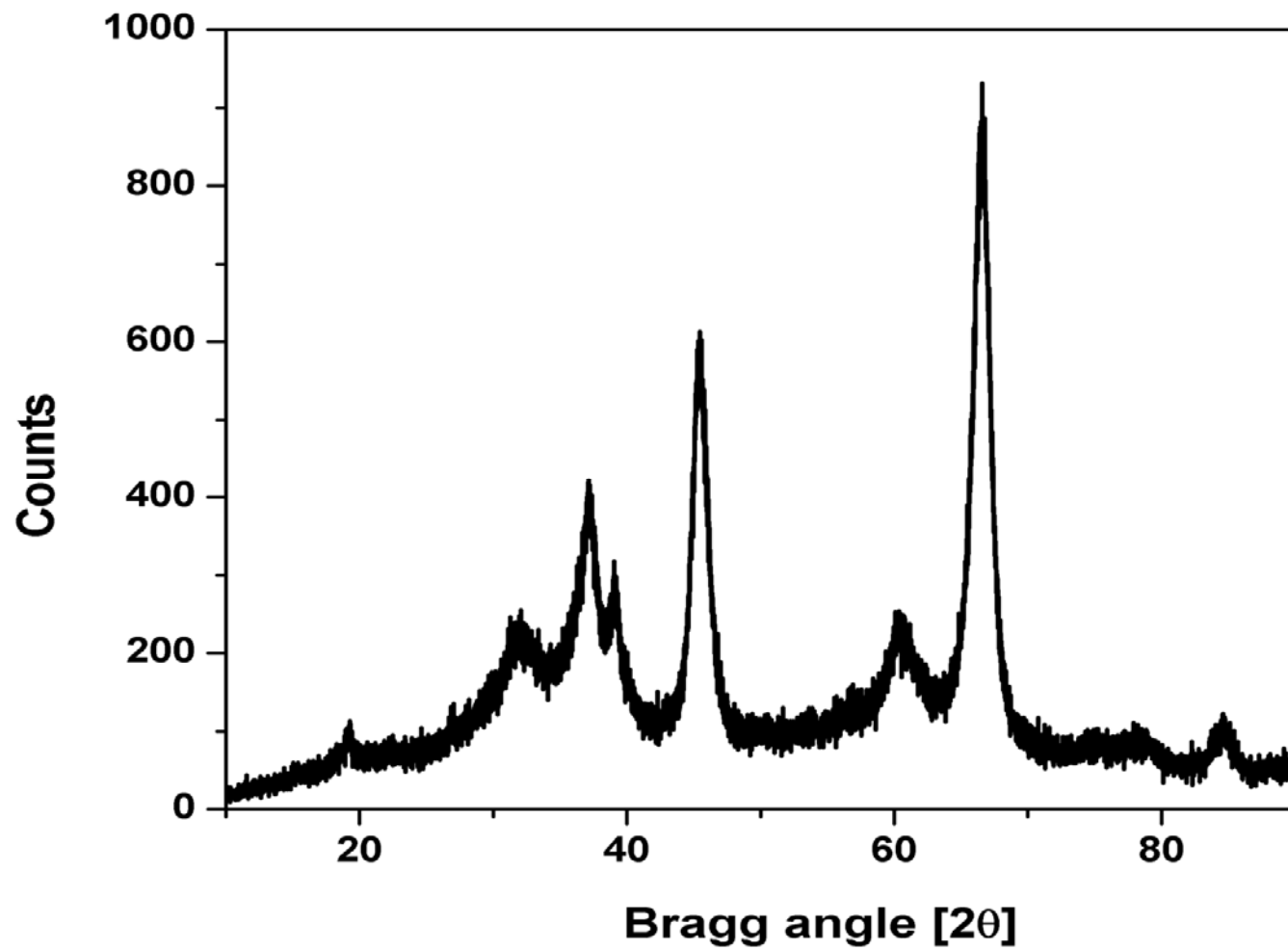


Figure 5.2.3: Powder x-ray diffractogram for an  $\eta$ - $\text{Al}_2\text{O}_3$  sample calcined at 1073 K.

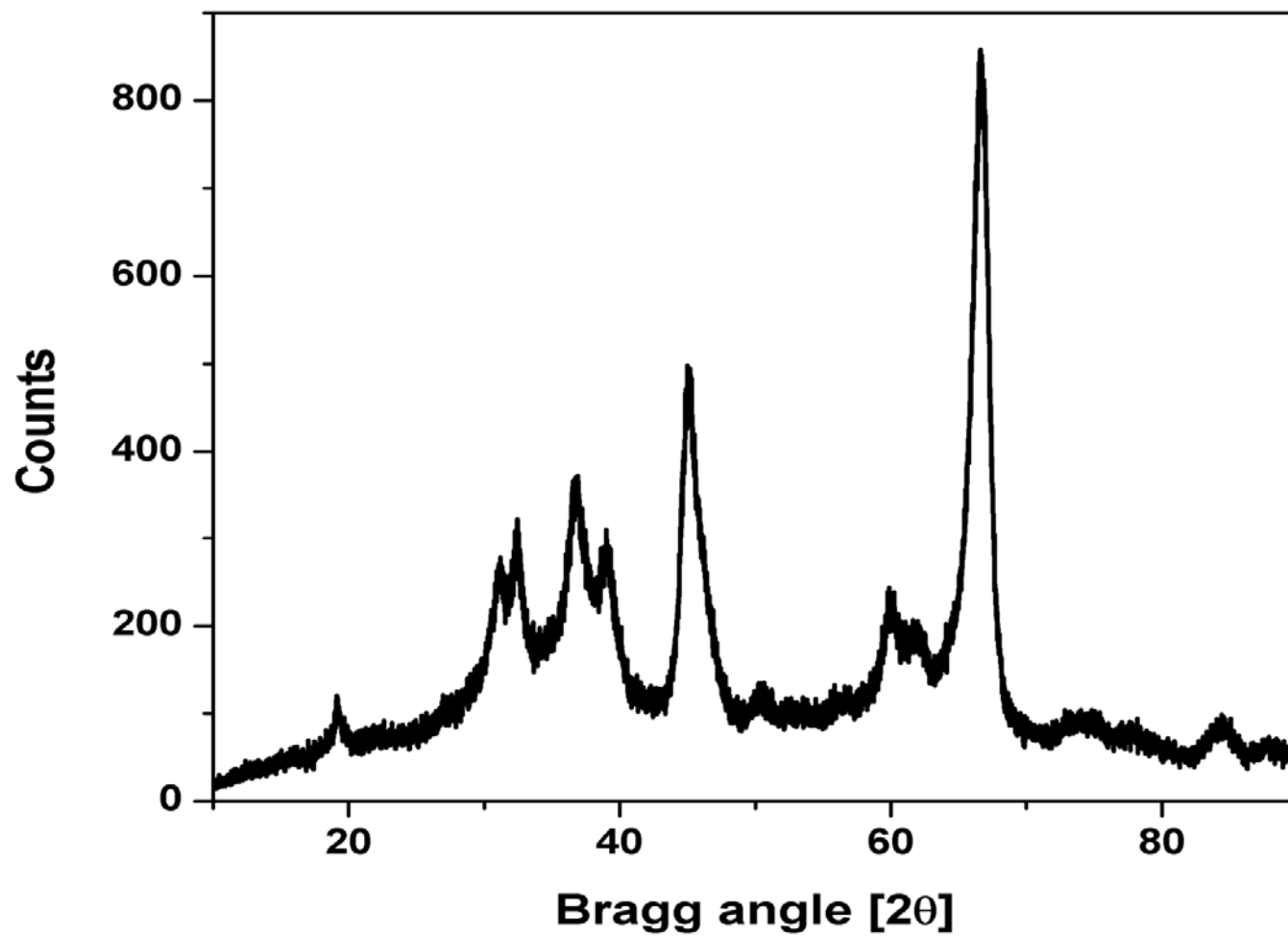


Figure 5.2.4: Powder x-ray diffractogram for an  $\eta$ - $\text{Al}_2\text{O}_3$  sample calcined at 1173 K.

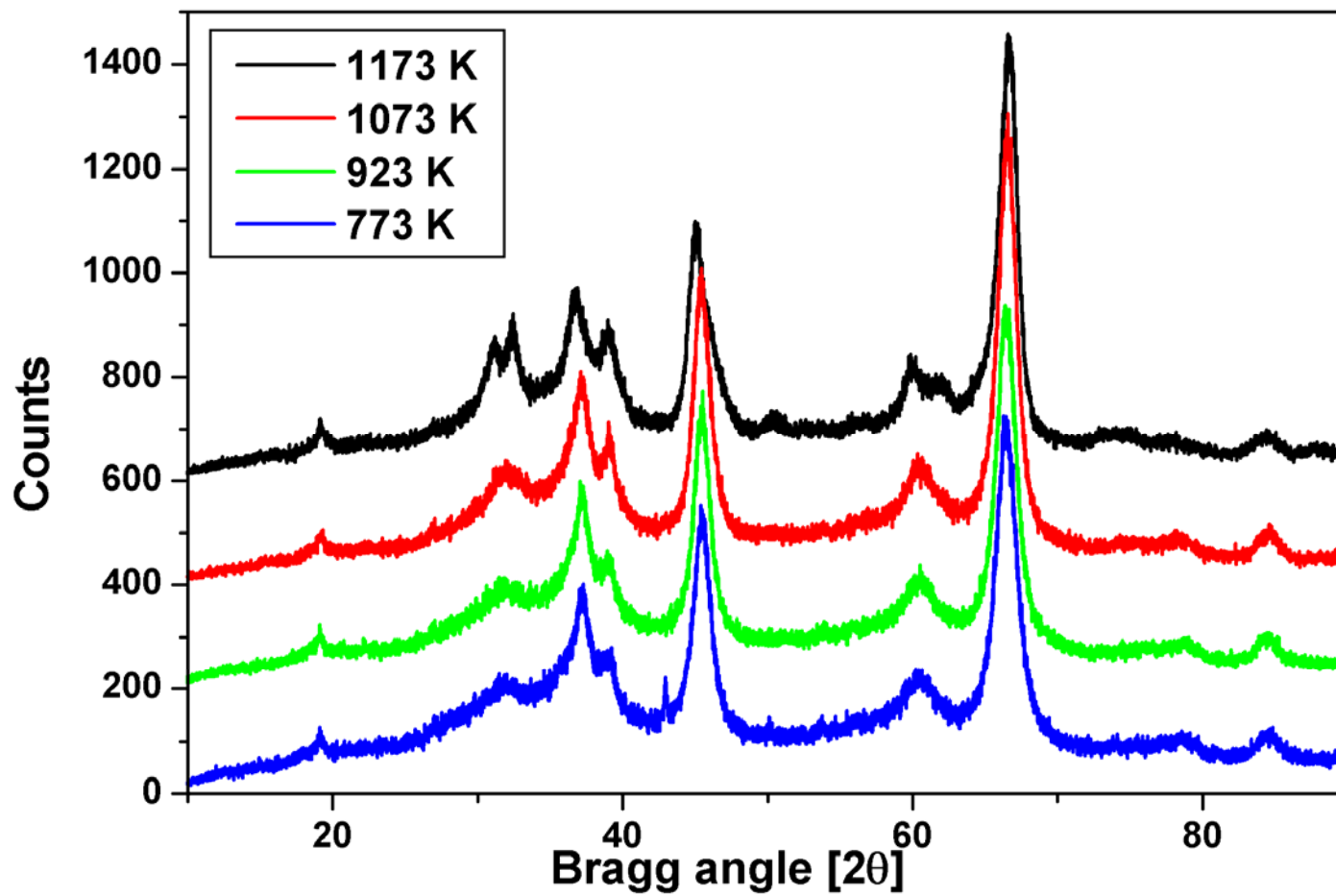


Figure 5.2.5: Stacked plot showing XRD profiles for  $\eta$ - $\text{Al}_2\text{O}_3$  catalyst calcined at various temperatures.

### 5.3 Surface area analysis

The phase transformation from  $\eta$ -Al<sub>2</sub>O<sub>3</sub> to  $\theta$ -Al<sub>2</sub>O<sub>3</sub>, implicated by the XRD patterns presented in Figures 5.2.1-5.2.5, is reported to progress via a displacive process where the order of the structure is increased. The increased order of  $\theta$ -Al<sub>2</sub>O<sub>3</sub> compared to  $\eta$ -Al<sub>2</sub>O<sub>3</sub> suggests that increasing the calcination temperature will result in a reduced surface area.

Figure 5.3.1 shows the variation in recorded surface area and average pore size for the range of catalysts calcined at increasing temperatures, as calculated using the BET (Brunauer, Emmett and Teller) method [30]. These show a significant and approximately linear decrease in surface area as the calcination temperature is increased. This decrease is consistent with the formation of a more ordered alumina phase on increasing the calcination temperature [116, 144]. Conversely, the average pore size is observed to increase as a function of calcination temperature. There are two possible mechanisms by which this increase in average pore size can proceed: small diameter pores may be filled or destroyed with no change in the number or volume of larger diameter pores; or, small pores can coalesce and/or combine with larger diameter pores resulting in an increase in the diameter and volume of larger pores.

Figure 5.3.2 presents a plot of pore volume versus BJH (Barret, Joyner, and Halenda) pore diameter as a function calcination temperature. The pore size distribution, calculated using the BJH method [31] is observed to increase upon increasing calcination temperature. This indicates that, in this case, the increase in average pore size observed upon increasing calcination temperature (Figure 5.3.1) is due to the genesis of larger pores and not solely to the destruction of small pores. This is consistent with the alumina crystal structure increasing its order at higher calcination temperatures by aligning and merging the lamellae that define the  $\eta$ -Al<sub>2</sub>O<sub>3</sub> mesostructure [35, 116].

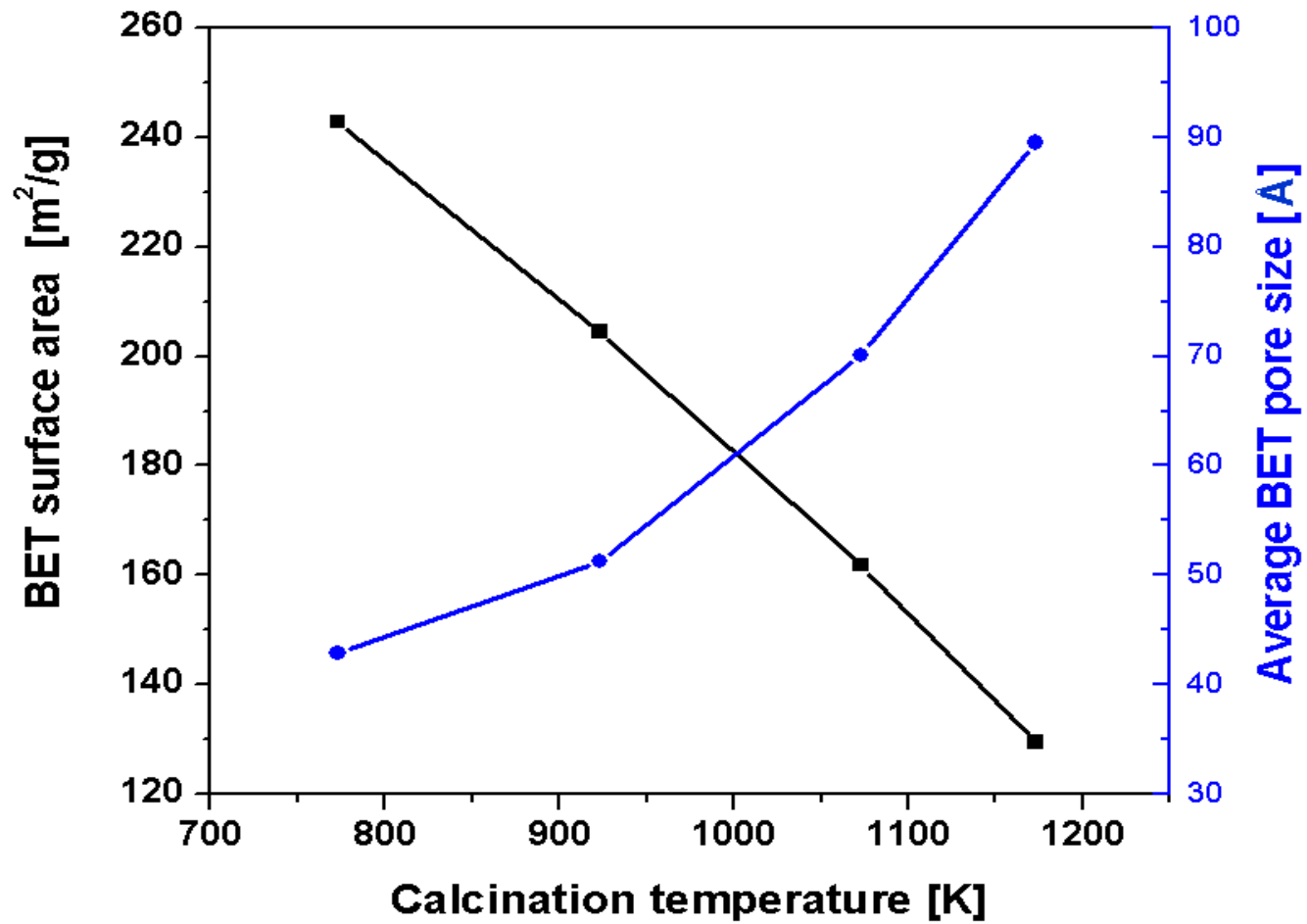


Figure 5.3.1: Variation in BET surface area and average BET pore size as a function of calcination temperature.

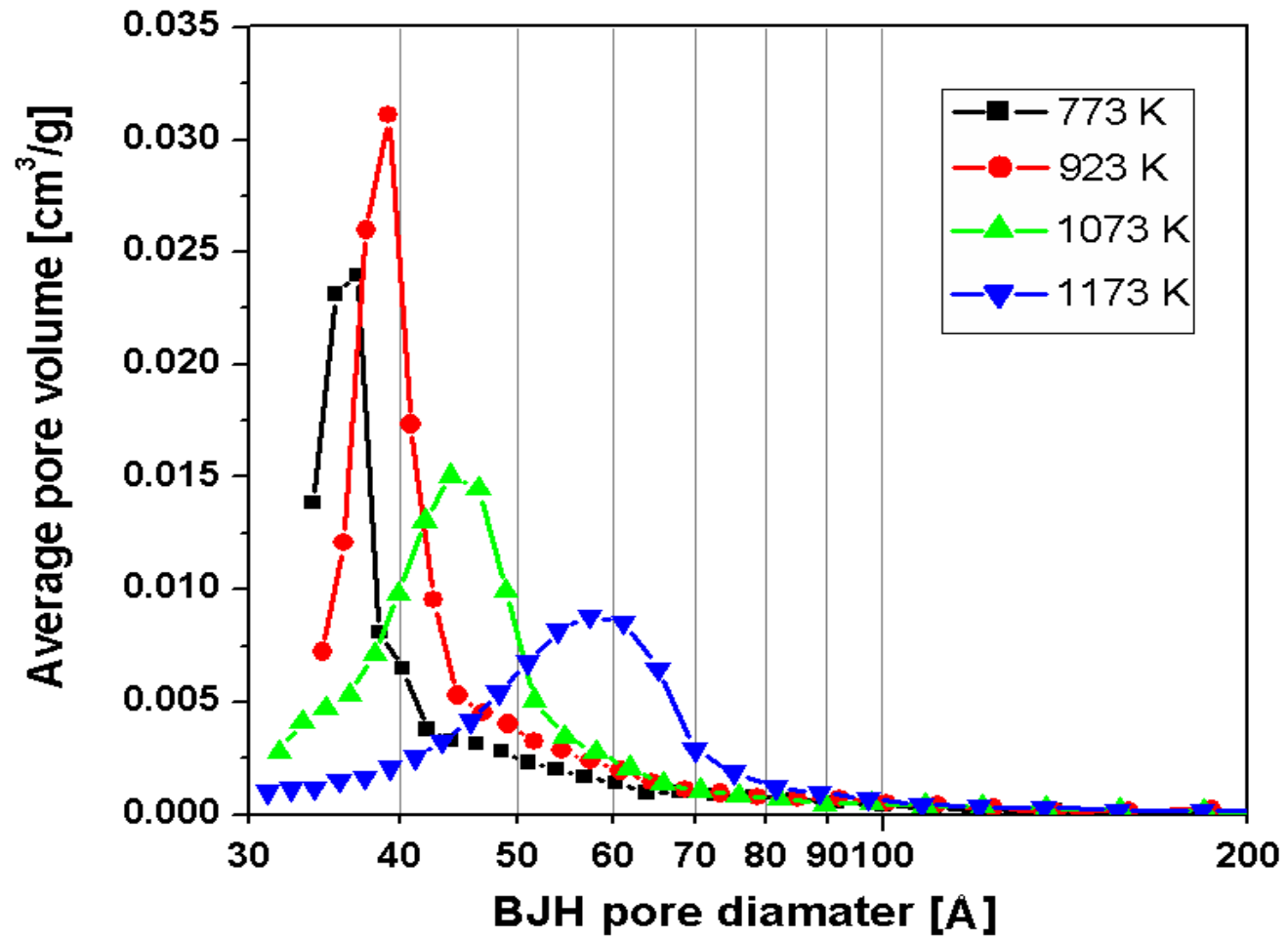


Figure 5.3.2: Variation in BJK pore size distribution as a function of calcination temperature.

## 5.4 Diffuse Reflectance Infrared Spectroscopy (DRIFTS)

As a consequence of the reduction in surface area, the absolute population of surface hydroxyl groups and coordinated water is expected to be significantly lower for  $\eta$ -Al<sub>2</sub>O<sub>3</sub> samples calcined at higher temperatures. For this reason, the samples calcined at higher temperatures are expected to be less absorbent in the infrared region compared to the sample calcined at lower temperatures.

### 5.4.1 Infrared spectra of the calcined alumina catalysts

Here, we examine  $\eta$ -Al<sub>2</sub>O<sub>3</sub> catalysts that have previously been calcined at various temperatures, after activation at 623 K in flowing helium, by analysis of single beam spectra. These measurements allow identification of changes in the relative hydroxyl group population during the calcination process.

The single-beam spectra of the series of calcined and activated alumina catalyst samples are presented in Figure 5.4.1. In all cases the energy spectrum is similar, however increased light transmission levels over the entire dynamic range are observed for samples heated to higher temperatures, as evidenced by increased spectral throughput. Thus, comparisons of the relative populations of adsorbed probe molecules between differently pre-treated catalysts could be misleading due to the higher light transmission levels observed for catalysts calcined at high temperatures. Pyridine studies described in the following section are therefore used only to obtain relative intensities within each spectrum. Comparisons of pyridine band intensities between infrared measurements of differently calcined catalysts are likely to be invalid and would require careful normalisation to account for the different optical transmission levels observed at each frequency for each of the samples.

As established above, it is not relevant to make comparisons between spectra of differently pre-treated samples; however it is possible to make a qualitative comparison between features contained within each single spectrum. It is known that samples calcined at higher temperatures will have a lower overall hydroxyl population but, as far as the author is aware, the *relative* distribution of different hydroxyl groups has not yet been discussed in the literature.

Figure 5.4.2 presents the difference infrared spectra for the series of calcined and activated

$\eta$ -Al<sub>2</sub>O<sub>3</sub> catalysts, where a spectrum of dried KBr has been subtracted from the presented spectra in order to remove spectral contributions associated with the environmental cell. The spectrum of the sample calcined at 773 K is characterised by two relatively sharp absorption features located at 3770 and 3730 cm<sup>-1</sup>, and a broader absorption feature located at 3680 cm<sup>-1</sup>, which are respectively assigned to hydroxyl groups adjacent to *medium-strong*, *medium-weak* and *weak* Lewis acid sites, based on the nomenclature adopted by Lundie *et al.* [38]. A fourth, broad and intense band is observed at *ca.* 3580 cm<sup>-1</sup>, which is assigned to hydrogen-bonded hydroxyl groups.

Upon increasing calcination temperature, the relative contribution of the absorption feature located at 3770 cm<sup>-1</sup> (*medium-strong* Lewis acid site) to the infrared spectrum becomes progressively diminished. In the infrared spectra of the samples calcined at 1073 and 1173 K, this absorption appears to be absent. In contrast, however, the absorption located at 3730 cm<sup>-1</sup>, which is associated with hydroxyl groups adjacent to *medium-weak* Lewis acid sites, constitutes a progressively greater contribution to the spectrum upon increasing calcination temperature.

Interestingly, in the infrared spectrum of the sample calcined at 773 K the band located at *ca.* 3580 cm<sup>-1</sup> is observed to split upon increasing calcination temperature. Upon increasing the calcination temperature to 923 K the 3580 cm<sup>-1</sup> band begins to exhibit asymmetry. The asymmetry is further developed in the spectrum of the sample calcined at 1073 K and for the sample calcined at 1173 K two distinct peaks, located at 3510 and 3570 cm<sup>-1</sup> become discernible. A further analysis of this site specific phenomenon is required but was deemed to be beyond the scope of the current workplan.

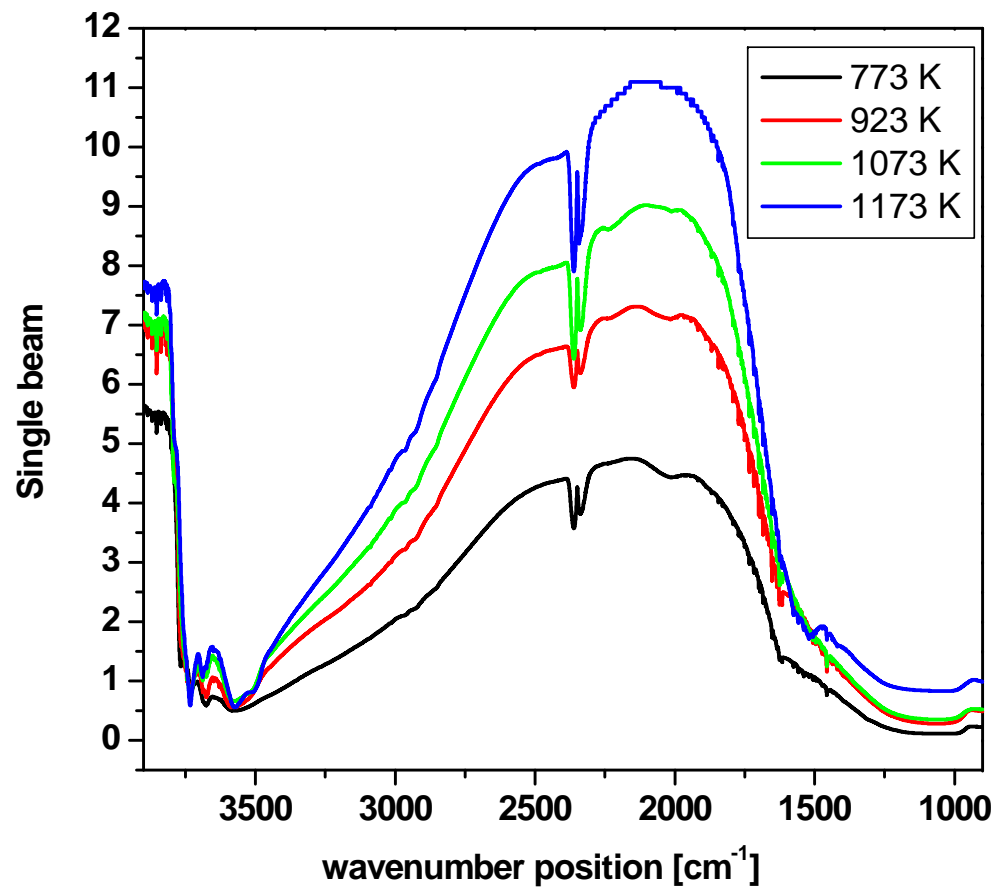


Figure 5.4.1: Single beam infrared spectra obtained for alumina samples calcined at various temperatures.

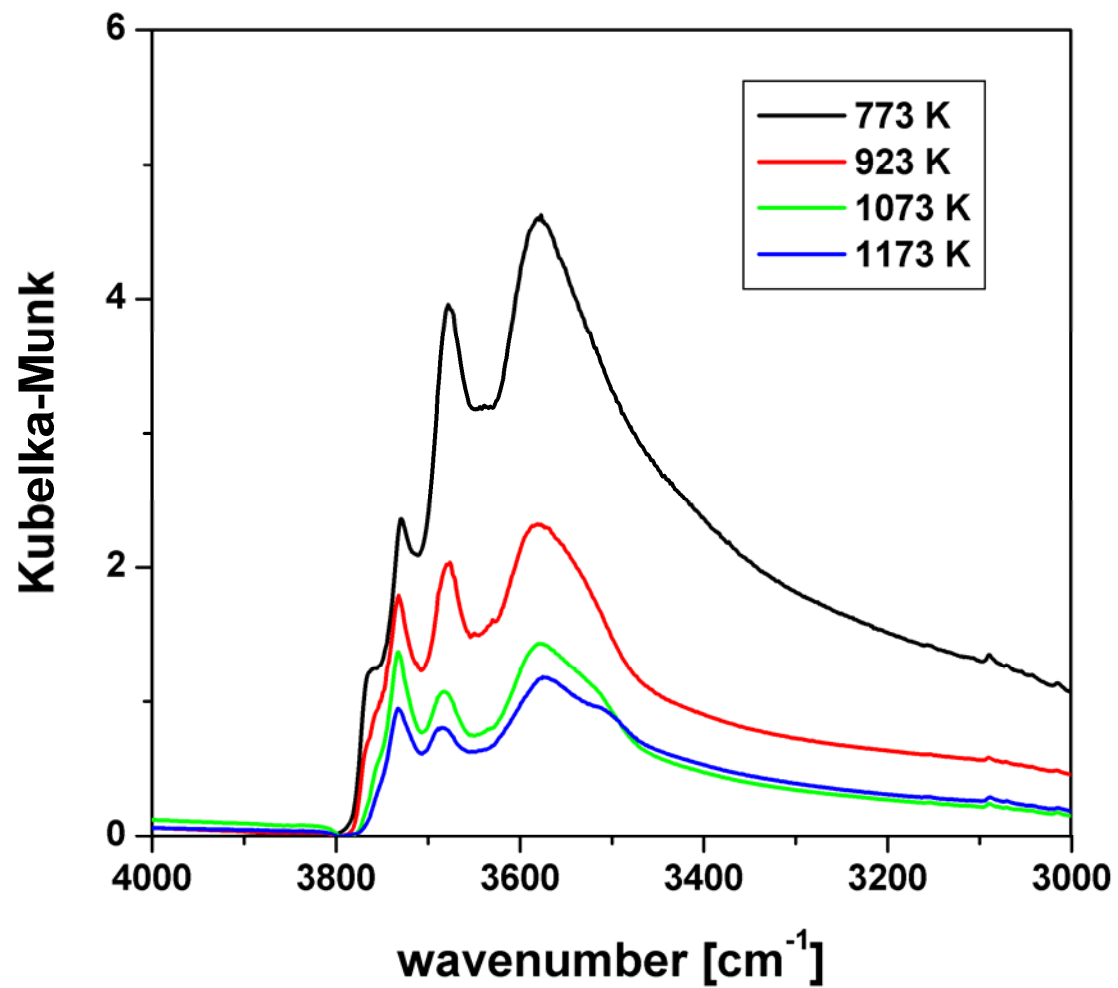


Figure 5.4.2: DRIFTS spectra of differently calcined  $\eta$ - $\text{Al}_2\text{O}_3$  catalysts activated at 623 K in flowing helium, recorded in the energy range 4000-3000  $\text{cm}^{-1}$ .

#### 5.4.2 Infrared difference spectra of adsorbed pyridine

Pyridine was employed as a probe molecule to evaluate the effect of increasing calcination temperature on the Lewis acid site distribution of the  $\eta$ -Al<sub>2</sub>O<sub>3</sub> catalyst. Figure 5.4.3 presents infrared spectra of a saturated overlayer of pyridine on each of the calcined alumina samples. Similar spectra are obtained for the samples calcined at 773 K and 923 K, both of which are consistent with other transition alumina catalysts reported in the literature in the respect that signals associated with *strong*, *medium* and *weak* Lewis acid sites can be clearly observed at 1623, 1613, and 1595 cm<sup>-1</sup>, respectively [8, 38]. This observation is consistent with the similar thermal pre-treatment of the catalysts studied here and  $\eta$ -Al<sub>2</sub>O<sub>3</sub> catalysts reported elsewhere [38, 91, 121]. Interestingly, the sample calcined at 923 K begins to display asymmetry in the  $\nu_{8a}$  pyridine band associated with *medium* Lewis acid sites, located at 1613 cm<sup>-1</sup>. This observation becomes more apparent for the samples calcined at 1073 and 1173 K, where two distinct peaks are observed at 1606 cm<sup>-1</sup> and 1613 cm<sup>-1</sup>. The signal located at 1606 cm<sup>-1</sup> is assigned to the  $\nu_{8a}$  mode of pyridine associated with the *medium-weak* Lewis acid sites implicated in the 4-site model proposed by Lundie *et al.* [38], while the feature observed at 1613 cm<sup>-1</sup> is associated with the *medium-strong* Lewis site. Therefore, increasing the temperature at which an  $\eta$ -Al<sub>2</sub>O<sub>3</sub> catalyst is pre-treated allows the *medium-weak* and *medium-strong* Lewis acid sites to be resolved, based on the energy shift of the  $\nu_{8a}$  mode of adsorbed pyridine. It is believed that this is the first time that this has been observed spectroscopically during pyridine adsorption studies on alumina. This distinction is made possible due to the change in relative intensities of the bands associated with the two medium strength Lewis acid sites. It is proposed that, previously, the dominant signal associated with *medium-strong* Lewis acid sites has effectively obscured that associated with *medium-weak* Lewis acid sites. However, as the relative populations of the Lewis acid sites change upon increasing calcination temperature, the low energy shoulder of the 1613 cm<sup>-1</sup> band becomes more pronounced. There are two mechanisms by which the ratio of *medium-weak* to *medium-strong* sites can increase, as observed here. It is conceivable that the population of the *medium-weak* sites increases with increasing calcination temperature. However, the more likely explanation is that the population of *medium-strong* sites is preferentially attenuated during calcination at the higher temperatures resulting in a greater relative proportion of the surface sites being of *medium-weak* Lewis acidity.

It is noted that this series of infrared spectra demonstrates the effectiveness of the apparatus described in Section 2.1.1. This is a non-trivial matter as control of the sample environment is essential in being able to reproduce these spectra and to provide this new

insight as to the surface properties of this technologically important material.

The observed infrared intensity of pyridine  $\nu_{8a}$  modes associated with *strong* Lewis acid sites may be misleading as a result of the greater light transmission observed for samples calcined at higher temperatures (Figs. 5.4.1 and 5.4.2). However, the sample calcined at 1173 K does indeed appear to show a decrease in the intensity of the  $\nu_{8a}$  mode of pyridine coordinated to *strong* Lewis acid sites relative to the other pyridine modes. This observation suggests that increasing the temperature at which  $\eta$ -Al<sub>2</sub>O<sub>3</sub> is calcined can effect a selective decrease in the population of *strong* and *medium-strong* Lewis acid sites. This process constitutes an overall decrease in surface Lewis acid strength during the transition from  $\eta$ -Al<sub>2</sub>O<sub>3</sub> to  $\theta$ -Al<sub>2</sub>O<sub>3</sub>.

Resolution of the *medium-weak* and *medium-strong* Lewis acid sites can also be attained by examination of the free hydroxyl region of the infrared spectrum upon adsorption of pyridine, based on the characteristic energy position of the hydroxyl groups that are associated with each of these sites, as described in Section 4.5. Figure 5.4.4 shows a stacked plot of the infrared difference spectra, presented in the free hydroxyl region (4000-3500 cm<sup>-1</sup>), for pyridine adsorbed on the range of calcined and activated catalysts. The spectra obtained for catalyst samples calcined at 773 K and 923 K show three negative bands located at 3770, 3730, and 3680 cm<sup>-1</sup>, associated with *medium-strong*, *medium-weak* and *weak* Lewis acid sites, respectively, as previously reported [38]. A decrease in the relative intensity of the band located at 3770 cm<sup>-1</sup>, previously assigned to *medium-strong* Lewis acid sites [38], is observed upon increasing the calcination temperature to 1073 K and 1173 K. The band located at 3730 cm<sup>-1</sup>, which is associated with *medium-weak* sites [38], appears to be attenuated to a lesser extent. These observations are consistent with the trends observed for the  $\nu_{8a}$  mode of adsorbed pyridine and reinforce the supposition that resolution of the two medium-strength Lewis acid sites is due to a decrease in the relative population of *medium-strong* sites. In addition, new hydroxyl features are observed at 3790 and 3760 cm<sup>-1</sup> in the spectra of samples calcined at temperatures of 1073 K and 1173 K. The energy position of the 3760 cm<sup>-1</sup> signal indicates that it is associated with isolated coordinatively unsaturated octahedral Al<sup>III</sup> centres as observed for activated  $\gamma$ -Al<sub>2</sub>O<sub>3</sub> [65, 77]. It is possible that the 3760 cm<sup>-1</sup> feature may also be present in the samples calcined at lower temperature, where it could potentially be obscured by the intense signal located at 3770 cm<sup>-1</sup> that is associated with hydroxyl groups adjacent to *medium-strong* Lewis acid sites. Depletion of the *medium-strong* Lewis acid sites, which, according to temperature

programmed desorption measurements [91], occurs during calcination at temperatures of 1073 K and above, could therefore allow observation of this previously obscured feature. As the  $3790\text{ cm}^{-1}$  feature is observed only in the samples calcined at 1073 K and above, which contain a substantial quantity/proportion of  $\theta\text{-Al}_2\text{O}_3$ , it is assigned to hydroxyl groups native to the new  $\theta\text{-Al}_2\text{O}_3$  phase. The energy position of the  $3790\text{ cm}^{-1}$  signal indicates it to be a non-bridging hydroxyl group associated with tetrahedral Al centres [94] and its negative form upon pyridine adsorption indicates that it is adjacent to a coordinatively unsaturated  $\text{Al}^{\text{III}}$  site. The presence of this signal in samples calcined at higher temperatures is consistent with the proportional increase in the population of tetrahedral Al centres that occurs upon the formation of  $\theta\text{-Al}_2\text{O}_3$  from thermal pre-treatment of  $\eta\text{-Al}_2\text{O}_3$  [117].

McInroy [91] has shown via both methanol and pyridine TPD measurements that increasing the temperature at which an  $\eta\text{-Al}_2\text{O}_3$  catalyst is calcined does indeed result in a reduction in the relative population of *medium-strong* Lewis acid sites and that the observed reduction in Lewis acidity is not solely due to the observed reduction in surface area between  $\eta\text{-Al}_2\text{O}_3$  and  $\theta\text{-Al}_2\text{O}_3$ . From a structural perspective, the proportion of tetrahedral Al centres increases with calcination temperature yet the spectroscopic measurements described above indicate that *strong* and *medium-strong* Lewis acidity, which is conferred by tetrahedral  $\text{Al}^{\text{III}}$  centres [8, 26, 38, 65], is in decline. A possible explanation is that although the bulk  $\theta\text{-Al}_2\text{O}_3$  contains proportionally more tetrahedral  $\text{Al}^{\text{III}}$  centres compared with  $\eta\text{-Al}_2\text{O}_3$ , octahedral  $\text{Al}^{\text{III}}$  may be preferentially segregated to the surface. This hypothesis could be explored further by application of x-ray photoelectron spectroscopy (XPS), which can identify the coordination geometry of metal centres in the surface layers of a solid material. The fact that alumina can behave as a semi-conductor could lead to charging of the sample, thereby complicating the analysis [81], although it might be possible to alleviate this difficulty using an electron flood gun. Another possibility is that the new tetrahedral  $\text{Al}^{\text{III}}$  centres generated by the phase transformation towards  $\theta\text{-Al}_2\text{O}_3$  are of such high acidity that the activation conditions employed here are insufficient to remove hydroxyl groups coordinated to them.

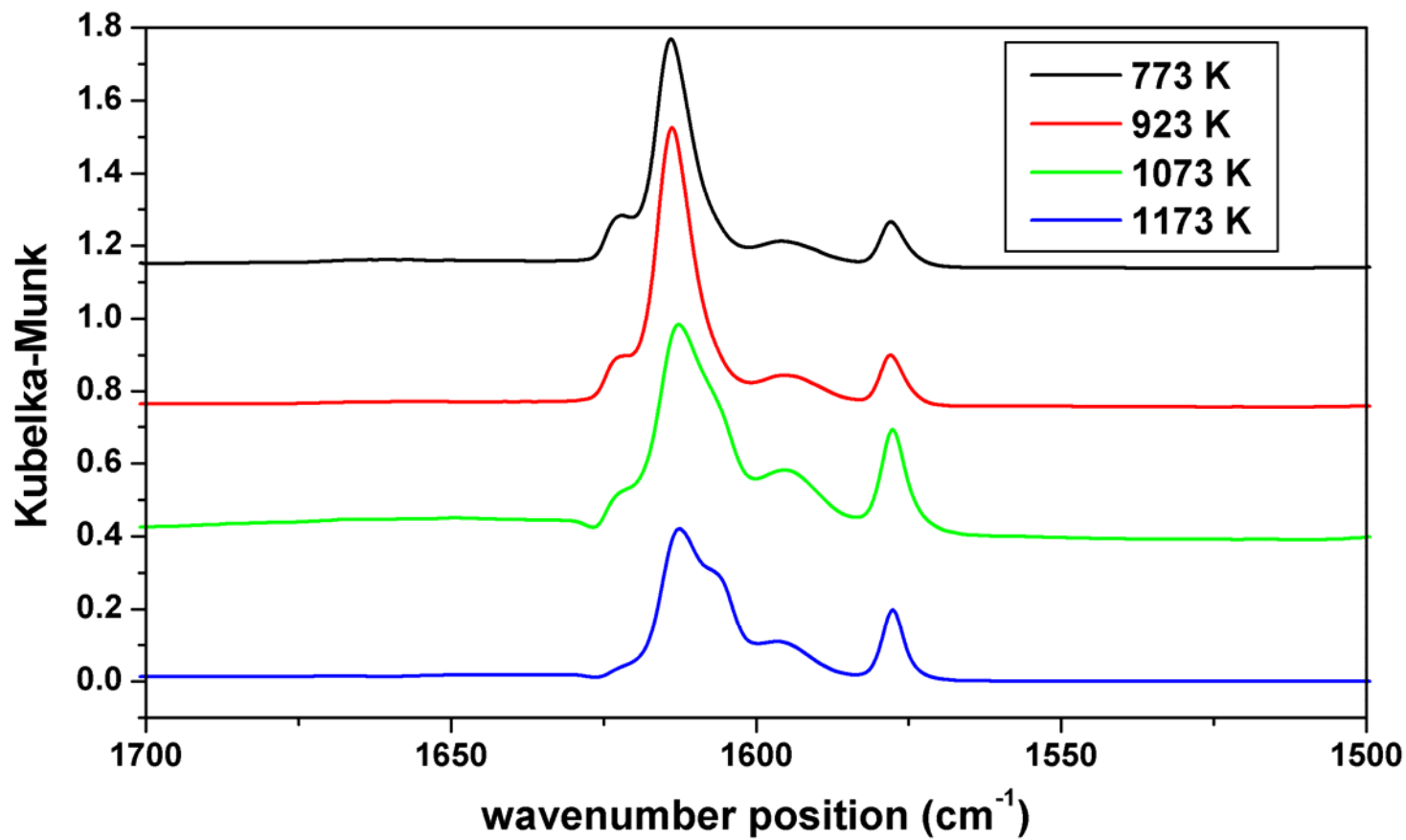


Figure 5.4.3: Stacked plot of infrared difference spectra, recorded in the energy range 1700-1500 cm<sup>-1</sup>, for pyridine adsorbed on alumina catalysts calcined at various temperatures.

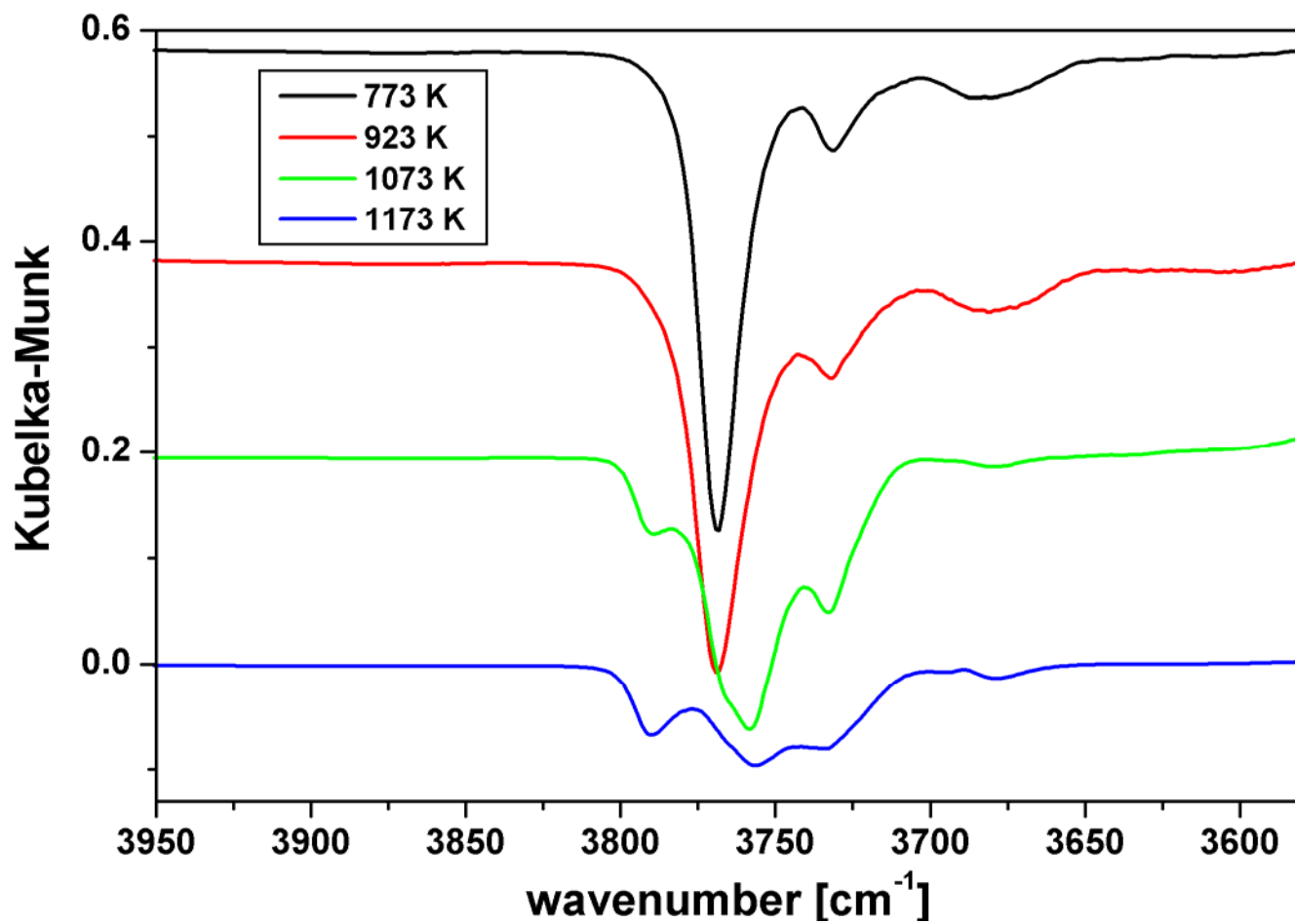


Figure 5.4.4:

Stacked plot of infrared difference spectra, recorded in the free hydroxyl region, for pyridine adsorbed on alumina catalysts calcined at various temperatures.

## 5.5 Conclusions

X-ray diffraction (XRD) measurements have revealed that calcination of an  $\eta$ - $\text{Al}_2\text{O}_3$  catalyst at temperatures  $\geq 1073$  K can promote a progressive phase transformation towards  $\theta$ - $\text{Al}_2\text{O}_3$ . Nitrogen adsorption measurements showed that a reduction in surface area was associated with the phase transformation that could be attributed to a displacive merging of the lamellar structure, as indicated by the pore size distribution profiles of catalyst calcined at various temperatures. Infrared spectroscopic measurements of adsorbed pyridine showed that the surface Lewis acidity of a  $\eta$ - $\text{Al}_2\text{O}_3$  could be modified by calcination of the catalyst at different temperatures. The total population of Lewis acid sites was observed to decline on increasing calcination temperature, as would be expected given the observed reduction in surface area. However, so-called *medium-strong* Lewis acid sites were observed to be preferentially attenuated in favour of *medium-weak* Lewis sites; an observation that is consistent with results from temperature programmed measurements observed in the literature [91, 121].

# 6

## Chapter 6

### A new vibrational probe for Lewis acidity

In this section, the results of studies of the activated  $\eta\text{-Al}_2\text{O}_3$ /pyridine adsorption system using both FT-IR and INS spectroscopic techniques are reported. The findings presented here build on the current understanding of the Lewis acid site distribution of  $\eta\text{-Al}_2\text{O}_3$ . Inelastic neutron scattering (INS) measurements have revealed a low energy vibrational mode that appears to be highly sensitive to Lewis acidity, which exhibits an apparent frequency shift of unprecedented magnitude upon chemisorption to the alumina surface. In order to assign this highly sensitive vibrational mode, and to substantiate the observed energy shift upon adsorption, periodic DFT calculations of a pyridine molecule adsorbed on the surface of  $\alpha\text{-Al}_2\text{O}_3$  have been carried out in collaboration with colleagues at the Cardiff University. In order to link the experimental and theoretical aspects of this workplan, the computer simulation results are presented here as well.

## 6.1 Infrared spectroscopy – pyridine adsorption

Figure 6.1.1 presents infrared spectra of liquid pyridine and pyridine overlayers adsorbed on the surface of an activated  $\eta\text{-Al}_2\text{O}_3$  catalyst in the energy range  $1700\text{-}1400\text{ cm}^{-1}$ . The bands observed in this energy range are due to  $\nu_{\text{C-C}}$  ring modes of pyridine and are assigned in Table 4.5.1 (Section 4.5), following the convention of Kline and Turkevich [104].

The infrared spectrum of a liquid sample of pyridine in the energy range of  $1700\text{-}1400\text{ cm}^{-1}$  is presented in Figure 6.1.1(a). Four intense bands associated with pyridine ring deformations are observed within this energy range. The most intense of these occurs at  $1437\text{ cm}^{-1}$  and is assigned to the  $\nu_{19b}$  mode in agreement with the literature [104, 127]. The less intense signal located at  $1482\text{ cm}^{-1}$  is assigned to the  $\nu_{19a}$  mode [104, 127]. The signal currently of most interest with regard to assessment of Lewis acidity is located at  $1580\text{ cm}^{-1}$  and is assigned to the  $\nu_{8a}$  mode. This feature has a shoulder to lower wavenumber located at approximately  $1573\text{ cm}^{-1}$  that is assigned to the  $\nu_{8b}$  mode. Finally, the band located at  $1597\text{ cm}^{-1}$  is assigned to a combination of the  $\nu_1$  and  $\nu_{6a}$  signals [104, 127], which are respectively located at  $994$  and  $603\text{ cm}^{-1}$  in the INS spectrum of solid pyridine [127].

Figure 6.1.1(b) presents the infrared spectra of a saturated overlayer of pyridine on the surface of the activated  $\eta\text{-Al}_2\text{O}_3$  catalyst after sequential pulse dosing of pyridine vapour at  $373\text{ K}$ . Two distinct  $\nu_{8a}$ -derived features are observed at  $1595$  and  $1613\text{ cm}^{-1}$ , while a third feature located at  $1623\text{ cm}^{-1}$ , is present as a high energy shoulder on the  $1613\text{ cm}^{-1}$  band.

As with the spectra presented in Section 4.5, the  $1595\text{ cm}^{-1}$  band is assigned to the  $\nu_{8a}$  mode of pyridine chemisorbed on *weak* Lewis acid sites, while the bands located at  $1613$  and  $1623\text{ cm}^{-1}$  are assigned to pyridine coordinated to *medium* and *strong* Lewis acid sites, respectively. The band at  $1613\text{ cm}^{-1}$  exhibits a degree of asymmetry, which has already been established to be due to the fact that the *medium* Lewis acid site can be subdivided into two different Lewis acid sites, namely *medium-weak* and *medium-strong* Lewis sites, as defined by their respective local coordination geometries [38, 91].

The temperature of the cell was then raised to  $473\text{ K}$  and maintained for  $30$  mins. The resulting spectrum is presented in Figure 6.1.1(c). Lundie *et al.* [38] have shown that warming the sample to  $473\text{ K}$  leads to total desorption of pyridine from the *weak* Lewis acid site and a loss of  $35\%$  of pyridine coordinated to the *medium-strength* sites. Indeed, inspection of Figure 6.1.1(c) reveals that this process results in total elimination of the  $1595\text{ cm}^{-1}$  band while the  $1613\text{ cm}^{-1}$  band undergoes a significant reduction in intensity compared to the spectrum of the overlayer before heating (Figure 6.1.1(b)). Figure 6.1.1(c) therefore represents the infrared spectrum of chemisorbed pyridine coordinated to *medium* and *strong* Lewis acid sites.

In addition to the  $\nu_{8a}$ -derived bands other vibrational features are observed in Figure 6.1.1, signals observed at  $1449$ ,  $1492$  and  $1577\text{ cm}^{-1}$  are assigned to the  $\nu_{19b}$ ,  $\nu_{19a}$  and  $\nu_{8b}$  modes of adsorbed pyridine, respectively. While the  $\nu_{8b}$  and  $\nu_{19a}$  mode show limited sensitivity to the Lewis acidity of the underlying substrate the  $\nu_{19b}$  mode exhibits a negative energy shift of  $11\text{ cm}^{-1}$  upon adsorption relative to its position in the spectrum of liquid pyridine (Fig. 6.1.1(a)), albeit modest in comparison to the  $\nu_{8a}$  mode. In the saturation spectrum (Fig. 6.1.1(b)) the  $\nu_{19b}$  mode has a bandhead located at  $1447\text{ cm}^{-1}$ . The intensity of this feature is attenuated upon heating to  $473\text{ K}$  leaving an intense feature located at  $1451\text{ cm}^{-1}$ . Thus, the weak Lewis acid site presents a  $\nu_{19b}$ -derived feature at  $1447\text{ cm}^{-1}$ . The remaining intensity of the  $\nu_{19b}$  feature after heating to  $473\text{ K}$  arises from pyridine located on medium and strong sites as indicated by the distribution of the  $\nu_{8a}$  mode within this spectrum.

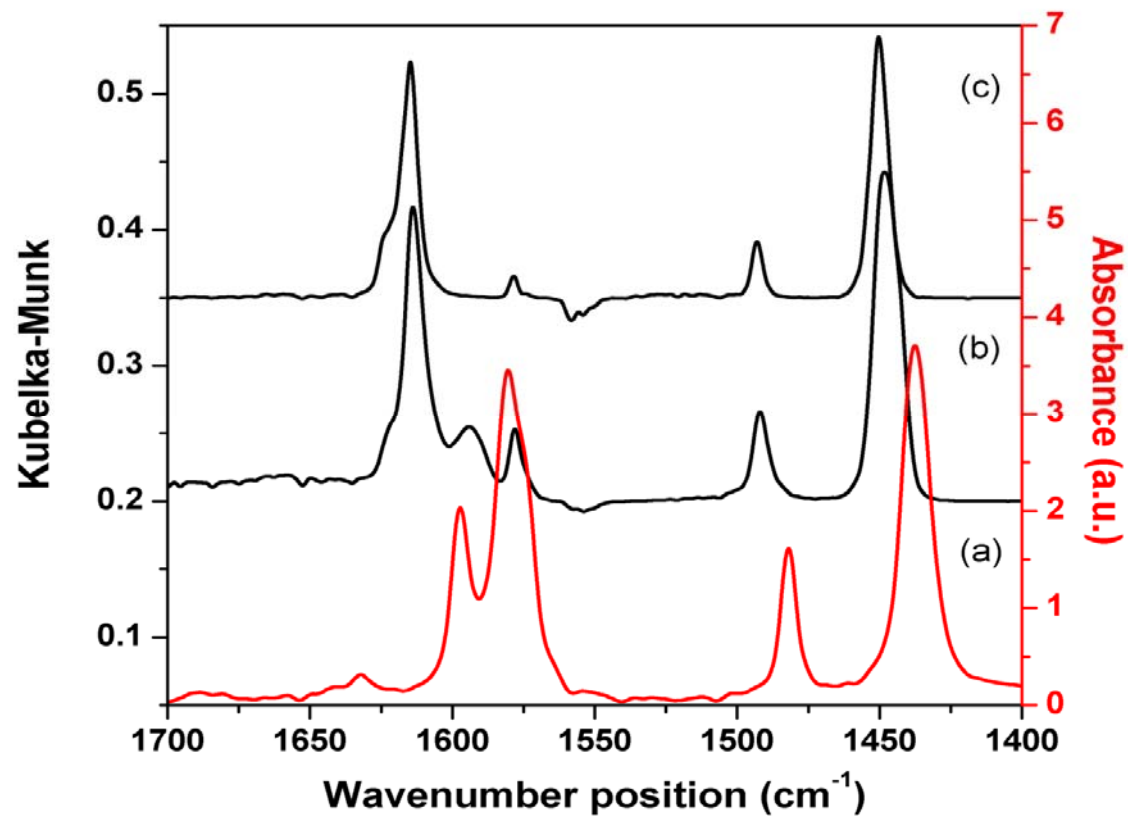


Figure 6.1.1: (a) Infrared reference spectrum of liquid pyridine recorded at 298 K. (b) Infrared difference spectrum of a saturated chemisorbed overlayer of pyridine on activated  $\eta$ -Al<sub>2</sub>O<sub>3</sub> recorded at 298 K. (c) Infrared spectrum of a saturated overlayer of pyridine on activated  $\eta$ -Al<sub>2</sub>O<sub>3</sub> subsequently purged in flowing helium at 473 K.

## 6.2 Inelastic neutron scattering – pyridine adsorption

Inelastic neutron scattering (INS) experiments were performed to assess the potential application of low energy pyridine modes, inaccessible by infrared spectroscopy, to further characterise the local Lewis acidity functions of activated  $\eta$ -Al<sub>2</sub>O<sub>3</sub>. Lundie *et al.* [38] have reported the spectrum of pyridine adsorbed on activated  $\eta$ -Al<sub>2</sub>O<sub>3</sub>. However, that work revealed some anomalies, which are examined here.

The INS spectrum of pyridine is presented in Figure 6.2.1(a) and exhibits a multitude of distinct features below 1400 cm<sup>-1</sup>. The spectrum is in excellent agreement with recent studies reported in the literature [127]. Figure 6.2.1(b) presents the INS spectrum of a saturated pyridine overlayer on activated  $\eta$ -alumina. Gravimetric analysis reveals the pyridine loading to be 621  $\mu\text{mol g}_{\text{cat}}^{-1}$ . With reference to ancillary volumetric isotherms performed on this system [91], this amount of pyridine retention by the activated alumina suggests a significant physisorbed component. It is therefore unsurprising that the spectrum of the saturated overlayer is similar to that of the solid pyridine reference spectrum, with the exception of broadening of spectral features, which reflects the range of local environments presented by the activated  $\eta$ -Al<sub>2</sub>O<sub>3</sub> surface in which the adsorbed pyridine molecules occupy. There are, however, some notable differences between the spectra presented in Figure 6.2.1(a) and Figure 6.2.1(b). Firstly, the  $\nu_{6a}$  mode, located at 600 cm<sup>-1</sup> in the reference spectrum, is attenuated and appears to have shifted to the slightly higher energy of 611 cm<sup>-1</sup> upon adsorption to the activated  $\eta$ -Al<sub>2</sub>O<sub>3</sub> substrate, however the poor signal:noise prevents unequivocal assignment of this band. Secondly, upon adsorption, a new low intensity feature is observed at 436 cm<sup>-1</sup> that is absent from the solid pyridine reference spectrum. Finally, the pyridine  $\nu_{16b}$  mode, located at 406 cm<sup>-1</sup> in the reference spectrum, appears to be attenuated to a greater extent than the  $\nu_{16a}$  mode located at 380 cm<sup>-1</sup> upon adsorption to the alumina surface. The reason why the  $\nu_{6a}$  and  $\nu_{16b}$  modes should be selectively attenuated upon adsorption is unclear at this point. A speculative explanation for the appearance of the as yet unidentified signal located at 436 cm<sup>-1</sup> is that the  $\nu_{16b}$  mode is sensitive to Lewis acidity: exposure of this mode to strong Lewis acidity (such as that presented by the so-called *strong* Lewis site present on the activated  $\eta$ -Al<sub>2</sub>O<sub>3</sub> substrate) could result in this mode shifting to higher energy, whilst exposure to weaker Lewis acid sites would result in no change in energy. This process would result in a redistribution of INS intensity thus giving rise to the appearance of a second  $\nu_{16b}$  feature at 436 cm<sup>-1</sup> with an associated attenuation of the original  $\nu_{16b}$  feature at 404 cm<sup>-1</sup>. The 436 cm<sup>-1</sup> band is broad

and could conceivably incorporate signals associated with sites of varying Lewis acidity.

These observations were investigated further by warming the overlayer in flowing helium at 473 K. The TPD-FTIR measurements presented in Figure 4.5.5 indicate that this treatment is sufficient to remove physisorbed and weakly bound pyridine from the alumina surface. The sample was then cooled to <40 K before recording the INS spectrum, which is presented in Figure 6.2.1(c). The INS spectrum presented in Figure 6.2.1(c) therefore corresponds to pyridine adsorbed on *strong* and *medium*-strength Lewis acid sites. As expected, the spectrum exhibits an overall reduction in INS intensity compared with Figure 6.2.1(b), with some modes attenuated to a greater extent than others. Complete attenuation of the  $\nu_{16b}$  mode at  $408\text{ cm}^{-1}$  is observed while the  $\nu_{16a}$  signal located at  $382\text{ cm}^{-1}$  remains intact. With reference to the INS spectrum of solid pyridine (Figure 6.2.1(a)) the  $\nu_{16b}$  mode is inherently weaker than the  $\nu_{16a}$  mode. However, it is unlikely that the absence of the  $\nu_{16b}$  mode from Figure 6.2.1(c) is due its attenuation beyond the detection limits of the spectrometer, given the high intensity of the  $\nu_{16a}$  mode within the same spectrum. The relatively weak signal located at  $436\text{ cm}^{-1}$  remains intact after the heating process and its relative intensity compared to the  $\nu_{16b}$  signal remains unchanged. The feature located at  $436\text{ cm}^{-1}$  remains unassigned, however its presence could be caused by a shift in the energy position of either the  $\nu_{16a}$  or  $\nu_{16b}$  signals. A relatively large shift to higher energy of  $57\text{ cm}^{-1}$  is required of the  $\nu_{16a}$  mode, whereas a more modest shift of  $31\text{ cm}^{-1}$  would be required for the  $\nu_{16b}$  mode. Furthermore, an energy shift associated with the  $\nu_{16b}$  mode would explain, at least in part, the reduction in intensity of the spectrum at  $382\text{ cm}^{-1}$ . Equally, the feature located at  $436\text{ cm}^{-1}$  could result from a shift of the  $\nu_{6a}$  mode, which is located at  $605\text{ cm}^{-1}$  in the solid pyridine reference spectrum (Figure 6.2.1(a)), to lower energy. This would require an energy shift in excess of  $150\text{ cm}^{-1}$ , which seems unlikely given that a dynamic energy shift range of  $\sim 30\text{ cm}^{-1}$ , associated with the  $\nu_{8a}$  mode, is currently used when infrared spectroscopy is applied.

It is thus tentatively proposed that the pyridine  $\nu_{16b}$  mode splits upon adsorption to the activated alumina surface: pyridine molecules coordinated to *medium* and *strong* Lewis acid sites experience a shift of the  $\nu_{16b}$  mode from  $404\text{ cm}^{-1}$  to  $440\text{ cm}^{-1}$ , while for pyridine coordinated to *weak* Lewis acid sites the mode remains unperturbed. In addition, compared to the solid pyridine reference spectrum (Figure 6.2.1(a)), relative shifts of -10, -15 and +9  $\text{cm}^{-1}$  are respectively observed for the  $\nu_{11}$ ,  $\nu_{10a}$  and  $\nu_{18a}$  pyridine modes upon adsorption to the activated alumina catalyst. The  $\nu_{6a}$  mode, which is proposed to shift to the higher

energy of  $611\text{ cm}^{-1}$  upon adsorption to the alumina surface (Fig. 6.2.1(b)), is completely absent from the spectrum upon heating the sample to 473 K (Fig. 6.2.1(c)). This observation suggests that this feature is attributed to pyridine coordinated to *weak* Lewis acid sites. Finally, the absence of any obvious intensity enhancement of the  $\nu_{18a}$  in-plane C-H deformation located at *ca.*  $1060\text{ cm}^{-1}$ , which dominates the INS spectrum of the pyridinium ion [145], indicates an absence of substantial Brønsted acidity for this catalyst, which is consistent with the infrared measurements presented in Section 4. These results indicate that the INS spectrum of adsorbed pyridine, employed as a probe molecule, can potentially be used to evaluate the surface Lewis acidity of an industrially viable technical catalyst. The application of INS to extend the accessible dynamic range, as demonstrated in this investigation, provides additional boundary conditions against which theoretical efforts to further define the alumina/pyridine interaction can be evaluated and refined. DFT calculations will be used in the following section to further explore the adsorptive interaction of pyridine on an alumina surface.

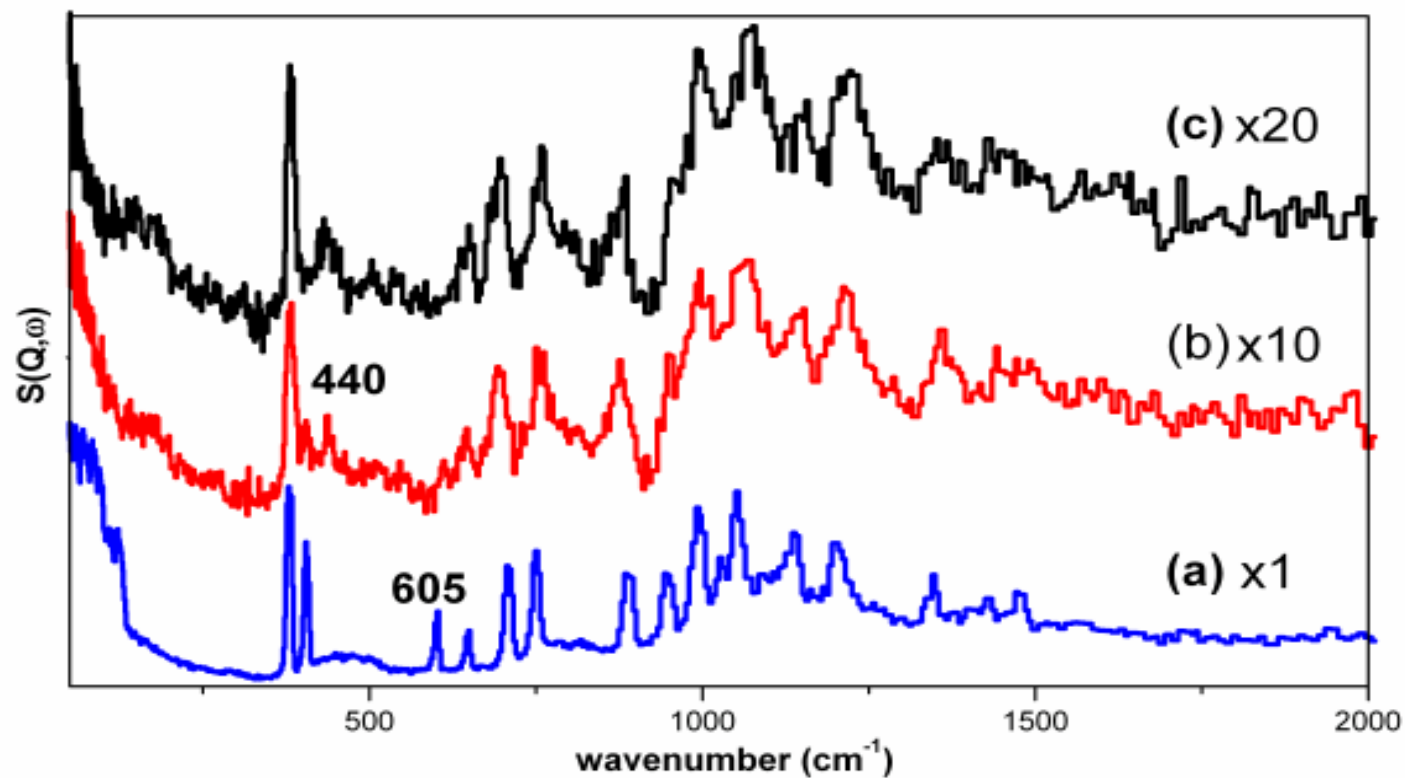


Figure 6.2.1: (a) INS spectrum of solid pyridine. (b) Background subtracted INS spectrum of a saturated overlayer of pyridine on activated  $\eta$ - $\text{Al}_2\text{O}_3$  ( $621 \mu\text{mol}$  of pyridine  $\text{g}_{\text{cat}}^{-1}$ ). (c) Background subtracted INS spectrum of the saturated overlayer after thermal desorption in flowing helium at  $473 \text{ K}$  for 30 mins.

### 6.3 *Ab initio* methods to investigate pyridine adsorption

*Ab initio* methods have been increasingly applied to the calculation of molecular structures and dynamics over the past twenty years. The application of *ab initio* methods to the interpretation of INS spectra is particularly relevant due to the fact that INS signals are not subject to the photon selection rules that complicate the calculation of infrared and Raman spectral intensities [14]. Simulated infrared and Raman intensities are calculated by determining the response of the electron cloud upon nuclear displacement during each normal mode of vibration [14, 17, 18]. Inconsistencies in the calculation of electron density can therefore result in inaccurate intensities of simulated infrared and Raman spectra. INS spectroscopy measures nuclear displacement *directly* and due to the fact that INS intensity is directly proportional to nuclear displacement the calculation of INS intensity of each normal mode of vibration is therefore comparatively simple. This property of INS spectroscopy improves the certainty of spectral assignments made with the assistance of theoretical calculations and provides a rigorous test of the veracity of the theoretical model.

Periodic DFT calculations were performed at Cardiff University in order to aid the assignment of various bands contained in the INS spectra of pyridine chemisorbed on activated  $\eta$ -Al<sub>2</sub>O<sub>3</sub> presented in Figure 6.2.1. The signal located at 440 cm<sup>-1</sup> in Figure 6.2.1(c) is of particular interest as it appears to be sensitive to Lewis acidity and its accurate assignment is therefore important.

$\alpha$ -Al<sub>2</sub>O<sub>3</sub>, which is exclusively composed of octahedral Al centres, was selected as the substrate as it is, from a computational perspective, significantly less demanding than the comparatively more complex  $\eta$ -Al<sub>2</sub>O<sub>3</sub> transition phase, which is composed from both tetrahedral and octahedral aluminium centres. From both a theoretical [37, 146, 147] and experimental [148] point of view,  $\alpha$ -Al<sub>2</sub>O<sub>3</sub> is reasonably well characterised. The fact that the cleaved surface of  $\alpha$ -Al<sub>2</sub>O<sub>3</sub> exclusively presents coordinatively unsaturated octahedral Al<sup>III</sup> centres means that its exposed Al ions are analogous to the *weak* Lewis acid sites [8, 38, 65] present on the surface of activated  $\eta$ -Al<sub>2</sub>O<sub>3</sub>. The *ab initio* calculations presented here, performed in collaboration with Dr. David Willock at Cardiff University, were carried out using the SIESTA program [149], which was used to generate an optimised  $\alpha$ -Al<sub>2</sub>O<sub>3</sub> surface with exposed coordinatively unsaturated Al centres onto which a molecule of pyridine was tethered. The computed eigenvalues were used to determine the vibrational frequencies of the normal modes of vibration of the adsorbed pyridine molecule within the

harmonic oscillator approximation, which were then compared against those of ‘free’ pyridine. Key results from this investigation are presented below.

### 6.3.1 Optimisation of the $\alpha$ -Al<sub>2</sub>O<sub>3</sub> bulk and (0001) surface

The optimised unit cell, containing 12 aluminium atoms and 18 oxygen atoms, has the lattice parameters listed in Table 6.3.1. The difference between the calculated and experimental lattice parameters is 0.88% for the **a** and **b** vectors, and 0.67% for the **c** vector. The surface was formed by cleaving the optimised crystal along the (0001) plane. This cleavage plane was favoured as it is the only non-dipolar cut possible. A slab model containing four layers of oxygen atoms was used in all calculations as the surface energy was found to converge at this point as shown in Figure 6.3.1. A slab thickness of four oxygen layers was therefore selected for all subsequent calculations. A vacuum gap of 10 Å between each slab was used throughout.

<b>a</b> / Å	<b>b</b> / Å	<b>c</b> / Å	<b>α</b> / °	<b>β</b> / °	<b>γ</b> / °
4.8009	4.8009	13.0777	90.0	90.0	120.0

Table 6.3.1 Lattice parameters for the optimised  $\alpha$ -Al<sub>2</sub>O<sub>3</sub> unit cell.

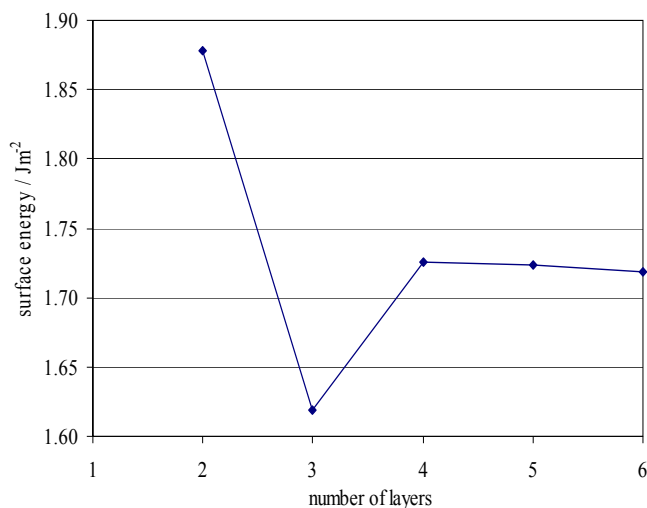


Figure 6.3.1: Convergence of surface energy with number of oxygen layers in  $\alpha$ -Al<sub>2</sub>O<sub>3</sub> slab.

The initial input and final relaxed geometries for the four-layer slab model are presented in Figure 6.3.2. The surface aluminium atoms retract towards the bulk upon relaxation of the surface resulting in a reduction in the spacing between the surface Al and O layers of 92%, from 0.836 Å to 0.063 Å. This type of surface relaxation has been observed elsewhere [150] and is a result of the low coordination number of the surface aluminium ion.

### 6.3.2 Pyridine on $\alpha$ -Al<sub>2</sub>O<sub>3</sub> (0001) surface

A molecule of pyridine was first optimized within a 15 Å periodic box and subsequently adsorbed onto a coordinatively unsaturated aluminium atom on a 2x2 supercell of the  $\alpha$ -Al<sub>2</sub>O<sub>3</sub> surface. The optimised structure is given in Figure 6.3.3. Upon adsorption of pyridine the coordinative aluminium atom moves towards the nitrogen of the pyridine ring by 0.417 Å.

The vibrational frequencies of the individual normal modes of vibration for both ‘free’ pyridine and pyridine adsorbed on the  $\alpha$ -Al<sub>2</sub>O<sub>3</sub> surface were calculated using the VIBRA code contained within the SIESTA program. VIBRA was modified to calculate the force constants for a subset of the atoms, *e.g.* only the pyridine molecule at the Al atom it is adsorbed upon, ignoring the rest of the alumina slab. This procedure is relevant as the experimental INS spectrum, which the calculated spectrum will ultimately be compared against, presents minimal contributions from the alumina substrate due to the low incoherent neutron scattering cross section of aluminium and oxygen atoms.

Assignment of the individual vibrational modes was achieved by observation of each of the associated animations with reference to previous studies [104, 127, 151]. A table of assignments for each normal mode and the associated change in wavenumber position upon adsorption to the alumina surface is presented in Table 6.3.2. According to the calculations presented here, every normal mode of vibration of pyridine is perturbed in some way, with varying magnitudes and direction, upon adsorption to the alumina surface. The trends of the  $\nu_{8a}$  mode are of interest and, in comparison to the infrared spectrum of pyridine adsorbed on activated transition alumina catalysts [38], have been reproduced. In this theoretical investigation, the energy position of the  $\nu_{8a}$  mode of ‘free’ pyridine is calculated as 1605 cm<sup>-1</sup>, which shifts to 1644 cm<sup>-1</sup> upon coordination to the model  $\alpha$ -Al<sub>2</sub>O<sub>3</sub> surface. This equates to an energy shift of 39 cm<sup>-1</sup> to higher wavenumber upon adsorption, which compares favourably with the experimentally observed energy shift of +43 cm<sup>-1</sup> to higher wavenumber that occurs when pyridine is chemisorbed on the *strong* Lewis acid site

present on the surface of activated  $\eta$ -Al<sub>2</sub>O<sub>3</sub>, relative to its location in the liquid pyridine reference spectrum (Fig. 6.2.1). The  $\nu_{8a}$  mode occurs at 1580 cm<sup>-1</sup> for liquid pyridine, as measured by infrared spectroscopy (Fig. 6.2.1(a)), and is observed at 1623 cm<sup>-1</sup> when chemisorbed on the *strong* Lewis acid site on  $\eta$ -Al<sub>2</sub>O<sub>3</sub>, as measured by DRIFTS (Fig. 6.1.1(b)).

The  $\nu_{6a}$  mode, which has a calculated wavenumber position of 573 cm<sup>-1</sup> for free pyridine, splits into two discrete vibrational states upon adsorption to the model alumina surface. The modes have calculated energies of 645 and 426 cm<sup>-1</sup> and are illustrated in Figure 6.3.4. According to the animation, the splitting of the  $\nu_{6a}$  mode upon coordination to the model alumina surface is due to the fact that the aluminium ion to which the pyridine is bound can either move in phase with the nitrogen of the pyridine, yielding the vibrational state at 426 cm<sup>-1</sup>, or contrary to it, yielding the vibrational state at 645 cm<sup>-1</sup>. This *ab initio* investigation therefore suggests that the  $\nu_{6a}$  mode is subject to an unprecedented negative energy shift of -147 cm<sup>-1</sup> when pyridine is introduced to the surface of a model activated alumina surface. A less dramatic calculated positive energy shift of +72 cm<sup>-1</sup> is also observed. This could account for the attenuation of the pyridine  $\nu_{6a}$  mode at 605 cm<sup>-1</sup> in the INS spectra (Figure 6.2.1) upon adsorption to the activated  $\eta$ -Al<sub>2</sub>O<sub>3</sub> surface and the appearance of the feature located at 436 cm<sup>-1</sup> in the INS spectra of pyridine adsorbed on  $\eta$ -Al<sub>2</sub>O<sub>3</sub>.

Further *ab initio* investigations incorporating more complex transition alumina phases that present a variety Lewis acidic environments as the active substrate, would aid the assessment of whether or not the frequency shift observed for the pyridine  $\nu_{6a}$  mode is exclusive to exposure of pyridine to strong Lewis acidity and, although not reported here, have been initiated. It is certainly possible that this might be the case given that there is only one feature in the region of 436 cm<sup>-1</sup> in the INS spectrum, though it must be acknowledged that the 436 cm<sup>-1</sup> is broad and could potentially incorporate signals associated with several classes of Lewis acid site. A number of discrete features associated with sites of different Lewis acidity, similar to that observed for the splitting of the  $\nu_{8a}$  mode upon adsorption to an activated  $\eta$ -Al<sub>2</sub>O<sub>3</sub> surface observed in the infrared spectra presented in Figure 6.1.1, might be expected. The population of *strong* Lewis acid sites present on the surface of activated  $\eta$ -Al<sub>2</sub>O<sub>3</sub> is known to be small relative to the population of weaker Lewis acid sites [38, 91]. In consideration of this one would expect the  $\nu_{6a}$  mode of pyridine bound to the weaker sites, presumably occurring in the energy range of 436-

605  $\text{cm}^{-1}$ , to exhibit greater INS intensity than that associated with the *strong* Lewis acid site.

It may also be the case that although the  $\nu_{6a}$  mode undergoes a large shift upon exposure to a Lewis acidic substrate, as shown by this *ab initio* investigation, it may not be particularly sensitive to the strength of the Lewis acid site. Thus, it is conceivable that the band observed at  $\sim 436 \text{ cm}^{-1}$  in the INS spectra of adsorbed pyridine, presented in Figures 6.2.1(b) and 6.2.1(c), incorporates the  $\nu_{6a}$  mode of pyridine molecules located in all of the Lewis acid sites presented by the surface of the activated  $\eta\text{-Al}_2\text{O}_3$  substrate. Figure 6.2.1(b) includes contributions from pyridine bound to *weak* Lewis acid sites whereas Figure 6.2.1(c) does not, yet there appears to be no selective loss of INS intensity in any of the features between the two spectra, *i.e.* all features appear to be attenuated to a similar extent, including the band located at  $436 \text{ cm}^{-1}$ . This suggests that the band located at  $436 \text{ cm}^{-1}$  does indeed include the  $\nu_{6a}$  mode of pyridine molecules bound to all Lewis acid sites. If the  $436 \text{ cm}^{-1}$  band selectively represents pyridine bound to *strong* Lewis acid sites then one would anticipate an increase in intensity of this band relative to the other features in the spectrum upon desorption of weakly bound pyridine, however, with reference to Figures 6.2.1(b) and 6.2.1(c) this is not the case.

Having now established that the  $\nu_{6a}$  mode splits into two discrete vibrational states upon adsorption, it then follows that the  $\nu_1+\nu_{6a}$  combination band, located at  $1597 \text{ cm}^{-1}$  in the infrared spectrum of liquid pyridine (Fig. 6.1.1(a)), should also be perturbed upon adsorption to the alumina surface. Calculations show the  $\nu_1$  mode to increase in energy upon adsorption while the  $\nu_{6a}$  splits into low energy and high energy features. The final position of the  $\nu_1+\nu_{6a}$  combination band is unknown but it is reasonable that it could become obscured by other features and is certainly not an obvious feature in the DRIFTS spectra of adsorbed pyridine, which is most likely due to the inherent weakness of combination bands in infrared spectroscopy [7]. The  $\nu_1+\nu_{6a}$  combination band of adsorbed pyridine may be more accessible by application by Raman spectroscopy as this feature is known to be in resonance with the  $\nu_8$  mode [104].

### 6.3.3 Simulation of the INS spectrum of pyridine on $\alpha$ -Al<sub>2</sub>O<sub>3</sub> (0001)

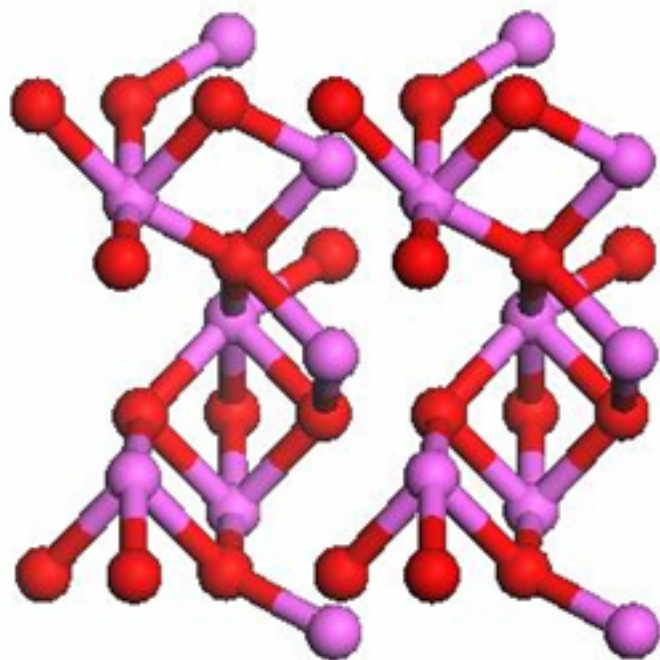
The eigenvalues and eigenvectors for each normal mode, calculated by SIESTA [149], were imported into the aCLIMAX 4.0.1 program [18], which was used to generate the simulated INS spectrum. The calculated INS spectrum is compared with the experimental INS spectrum of a partially desorbed overlayer of pyridine on activated  $\eta$ -Al<sub>2</sub>O<sub>3</sub> (previously presented in Figure 5.2.1(c)) in Figure 6.3.5. In terms of energy position, the simulated spectrum presents an excellent fit to the experimental data with a typical energy difference of  $\sim 3.5\%$  between associated spectral features. Generally, the intensity of calculated spectral features compares well to the experimental data, with one exception: the  $\nu_5$  mode of adsorbed pyridine, located at  $962\text{ cm}^{-1}$  in the simulated spectrum, has significantly less intensity than is observed in the experimental INS spectrum. The origins of this anomaly are unknown at present.

Analysis of the aCLIMAX output indicates that the broad, low intensity features located in the energy range  $410\text{-}540\text{ cm}^{-1}$  of both the theoretical and experimental INS spectra, arise from a first order phonon wing associated with the adsorbed pyridine molecules, which indicates some ordering of active sites [14].

mode	symmetry	frequency / cm <sup>-1</sup>		
		free pyridine	pyridine on Al <sub>2</sub> O <sub>3</sub>	change on adsorption
2	A <sub>1</sub>	3139	3162	23
20a	A <sub>1</sub>	3118	3133	15
8a	A <sub>1</sub>	1605	1644	39
19a	A <sub>1</sub>	1441	1459	18
9a	A <sub>1</sub>	1176	1183	7
18a	A <sub>1</sub>	1042	1062	20
12	A <sub>1</sub>	1018	1002	-16
1	A <sub>1</sub>	961	1032	71
6a	A <sub>1</sub>	573	645	72
			426	-147
17a	A <sub>2</sub>	936	945	9
10a	A <sub>2</sub>	845	847	2
16a	A <sub>2</sub>	336	365	29
20b	B <sub>1</sub>	3134	3156	22
8b	B <sub>1</sub>	1600	1595	-5
19b	B <sub>1</sub>	1421	1449	28
14	B <sub>1</sub>	1330	1348	18
3	B <sub>1</sub>	1291	1301	10
15	B <sub>1</sub>	1101	1115	14
18b	B <sub>1</sub>	1037	1058	21
6b	B <sub>1</sub>	631	627	-4
5	B <sub>2</sub>	948	962	14
10b	B <sub>2</sub>	896	917	21
4	B <sub>2</sub>	714	733	19
11	B <sub>2</sub>	675	668	-7
16b	B <sub>2</sub>	383	409	26
13 / 7b		3091	3126	35
		3090	3107	17

Table 6.3.2: Vibrational modes for free pyridine and pyridine adsorbed on the Al<sub>2</sub>O<sub>3</sub> (0001) surface.

Input



Optimised

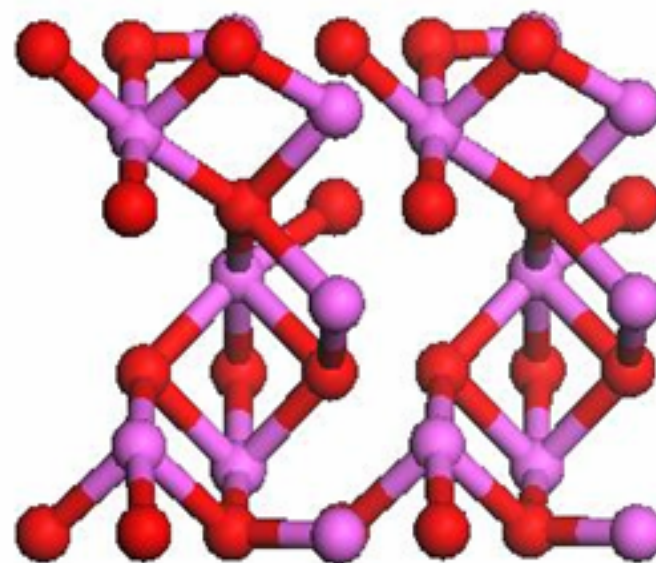


Figure 6.3.2: Geometry for the 4-layer  $\alpha$ - $\text{Al}_2\text{O}_3$  slab cleaved along the (0001) plane, before and after optimisation at the GGA-PBA-DZP level.

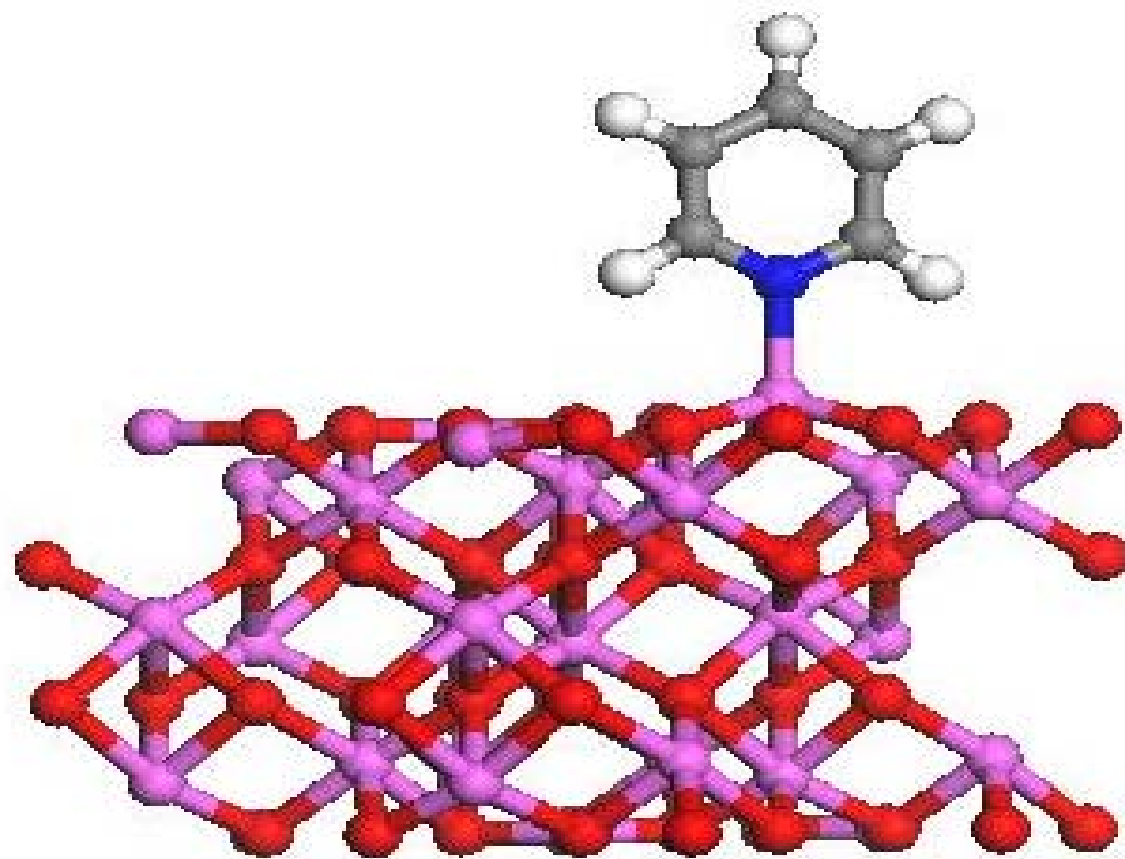


Figure 6.3.3: A molecule of pyridine coordinated to the relaxed  $\alpha\text{-Al}_2\text{O}_3$  (0001) surface.

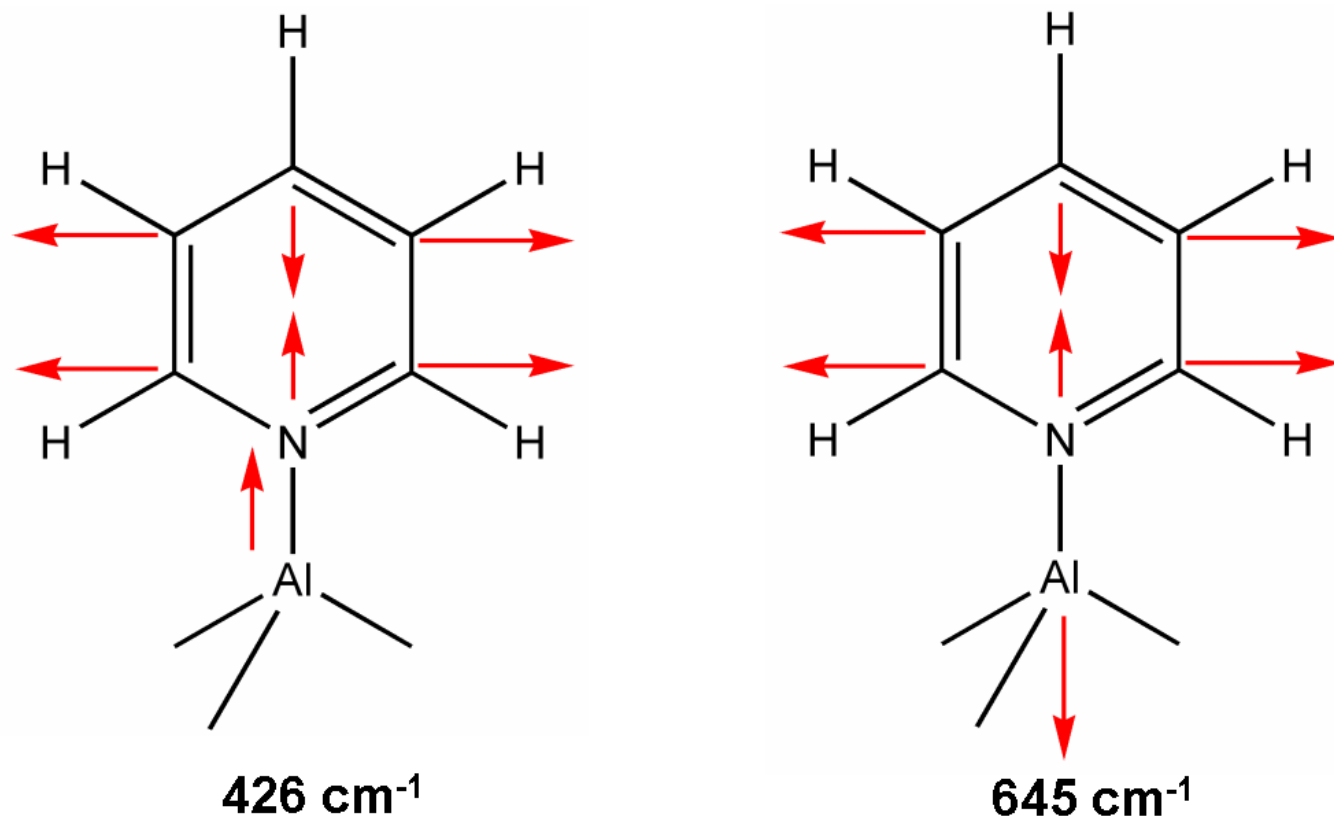


Figure 6.3.4: Graphical representation of the splitting of the  $\nu_{6a}$  mode observed when pyridine is adsorbed on a  $\alpha\text{-Al}_2\text{O}_3$  (0001) surface.

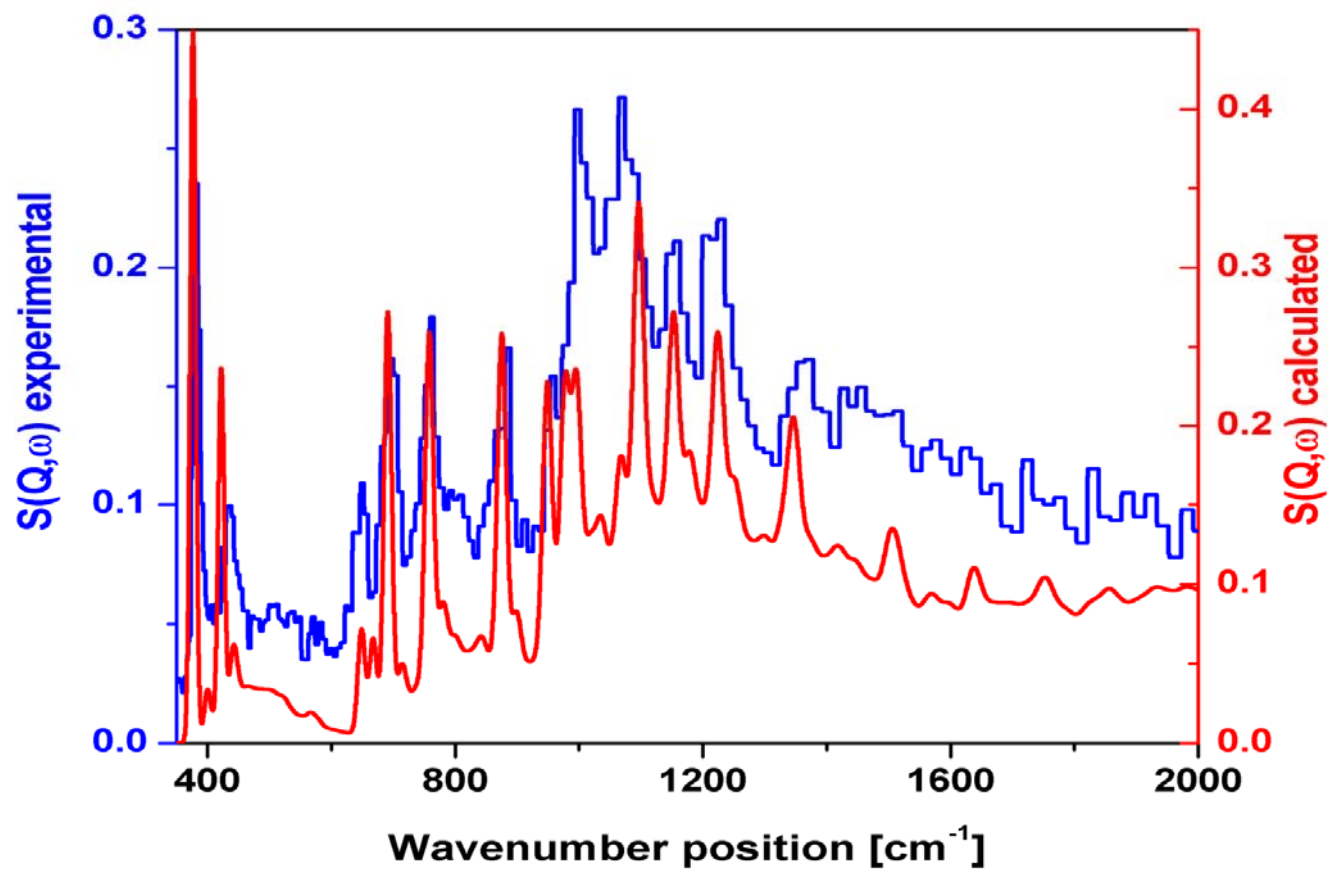


Figure 6.3.5: Comparison of simulated INS spectrum pyridine on  $\alpha$ -Al<sub>2</sub>O<sub>3</sub> and experimental INS spectrum of a saturated overlayer of pyridine on  $\eta$ -Al<sub>2</sub>O<sub>3</sub> desorbed at 463 K.

Interestingly, the vibrations with energies of 3090 and 3091  $\text{cm}^{-1}$  could not be assigned to the  $\nu_{13}$  or  $\nu_{7b}$  modes, following the commonly adopted convention of Kline and Turkevich [104]. Instead, two localised modes are observed in the animation. Interestingly, only a single proton in each of the modes exhibits significant displacement in each case. A similar effect has been observed for simulations of the vibrational modes of a series of benzyl-substituted aniline compounds, as reported elsewhere [152]. An illustrative description of these modes is presented in Figure 6.3.6. The frequency of each of the two modes indicates that they are essentially energetically degenerate, which can lead to mixing, thus giving ‘ $A_1 + B_1$ ’ and ‘ $A_1 - B_1$ ’ modes.

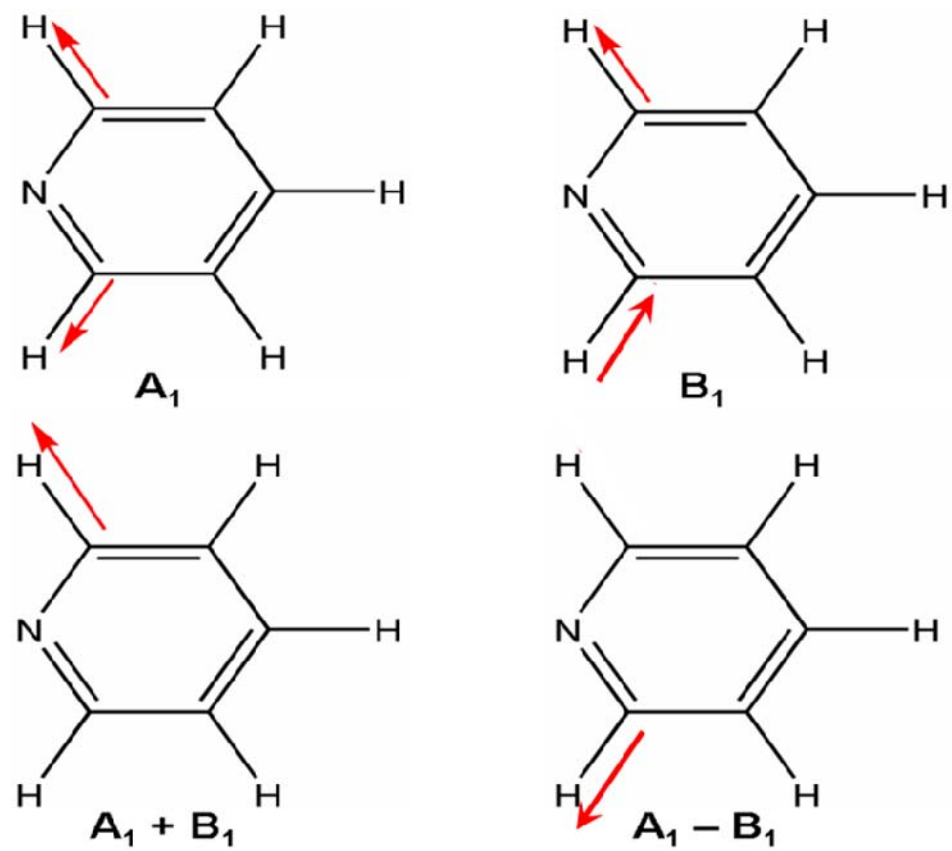


Figure 6.3.6: Description of vibrational modes observed at 3090 and 3091 cm<sup>-1</sup>.

## 6.4 Conclusions

INS spectroscopy was employed to investigate the adsorption of pyridine on an industrial grade  $\eta$ - $\text{Al}_2\text{O}_3$  catalyst and revealed a number of low energy modes of adsorbed pyridine that are inaccessible via conventional optical spectroscopic techniques, *e.g.* infrared and Raman. Some of these modes were observed to be sensitive to Lewis acidity. In particular, the  $\nu_{6a}$  mode, which is located at  $440\text{ cm}^{-1}$  in the spectrum of solid pyridine, was observed to be highly sensitive to Lewis acidity, exhibiting an unprecedented energy shift of  $-165\text{ cm}^{-1}$  upon adsorption to the Lewis acidic  $\eta$ - $\text{Al}_2\text{O}_3$  substrate. A periodic DFT investigation supported the vibrational assignment of adsorbed pyridine modes and revealed the  $\nu_{6a}$  mode to split into two discrete vibrational states upon adsorption. Output from the DFT calculations was used to simulate the INS spectrum of pyridine adsorbed on an  $\alpha$ - $\text{Al}_2\text{O}_3$  (0001) surface, which gave a satisfactory correlation with an experimentally acquired spectrum of pyridine adsorbed on  $\eta$ - $\text{Al}_2\text{O}_3$ , thereby ratifying the validity of the DFT model.

# 7

## Chapter 7

### **Fischer-Tropsch Synthesis and CO hydrogenation over Fe-based catalysts**

The Fischer-Tropsch synthesis (FTS) process describes a series of heterogeneously catalysed chemical reactions of carbon monoxide (CO) and hydrogen (H<sub>2</sub>) gases, which can be derived from coal [153], natural gas [154] or biomass [155], to produce liquid hydrocarbons of various forms [156, 157]. CO and H<sub>2</sub> combine in a polymerization reaction to produce predominantly straight chain alkanes (Equation 11), while competing reactions result in the formation of other hydrocarbon species, including alkenes and alcohols [156].



The FTS process provides a method to produce various hydrocarbon products, including high purity fuels and feedstocks for the production of fine chemicals, which utilizes starting materials that can be acquired from a number of renewable sources. The main obstacle preventing wider implementation of FTS is its poor financial competitiveness against the production of similar liquid hydrocarbon feedstocks derived from traditional crude oil [158]. However, as oil reserves become increasingly more difficult to access, from both a technological and political perspective, the price of conventional crude oil is expected to increase, thus driving interest in alternative energy sources, *e.g.* FTS derived oil. Within the current climate of unstable oil prices, and other political factors affecting the accessibility of crude oil reserves, FTS is receiving renewed interest in both academic and industrial circles [158]. A 2007 report described the FTS process as being economically viable only when global oil prices rise above \$55 per barrel [157]. One of the conclusions drawn from a 1974 study on the economy of the FTS process was that to improve the economical viability of the process an improvement in the selectivity towards more valuable products, such as light olefins, had to be realized [159]. It is reported that iron-based catalysts are the most selective towards high value low mass olefins when compared with Co-, Ni- and Ru-based analogues [160]. In this respect, iron catalysts are used extensively for the FTS process and are the catalyst of choice for use in the Synthol™ reactors in the commercial operations of Sasol (1982) [153].

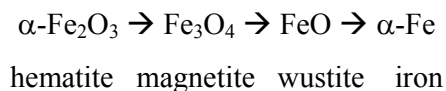
The oxides of groups 8, 9, and 10 metals (Co, Ni, Ru, and Fe) are the typical catalyst precursors used in FTS [158]. As the oxide form is inactive for the reaction, the samples must be subjected to an activation treatment to obtain the active Fischer–Tropsch catalyst. Cobalt-, nickel-, and ruthenium based samples require an H<sub>2</sub> treatment in the temperature range of 473-723 K in order to become active, and remain in their metallic state during FTS [161]. However, the activation process is not so simple for the iron-based catalysts,

which can be activated under carbon monoxide [23, 162], hydrogen [156], or synthesis gas [163, 164] treatments.

Cobalt based catalysts are currently the most widely used in industrial FTS plants due to their high selectivity towards paraffins that can be used for fuels [156]. The use of iron based catalysts, however, is very attractive due their low cost, high activity and their potential as reverse water-gas shift (Equation 12) catalysts at high temperatures [156, 165, 166]. The presence of CO<sub>2</sub> in the syngas feedstream is a serious financial drawback for the overall process, typically costing around \$5/MT of CO<sub>2</sub> produced [167]. In principal iron based samples would therefore represent ideal candidates as catalysts in the FTS from CO-lean, or CO<sub>2</sub>-rich, syngas feedstreams as the reverse WGS reaction can be used to boost the CO content of the system, depending on the conditions employed. Iron can be active in both forward and reverse WGS depending on the conditions used.



Nickel, ruthenium, and cobalt catalysts typically have an initially high activity in FTS and although carbides of these metals exist [167-169], no bulk carbides are formed during FTS conditions [170]. In contrast, the FTS activity of iron catalysts is initially low and slowly increases to a maximum over time, while simultaneously bulk iron carbide species are formed [170-174]. Much of the early research into FTS employed fused or sintered iron catalysts, which could only be made active by reducing the material to metallic iron in a hydrogen atmosphere [175]. Subsequent exposure to syngas converted the iron, at least in part, to iron carbide species. However, unsupported bulk iron oxides and various supported and/or promoted iron catalysts can be activated in a quite different manner and undergo several phase transformations during activation and also under FTS conditions [25]. The reduction of iron oxide proceeds in a stepwise manner as described by Kock *et al.* [176]:



The phases produced during the pre-treatment step that are most stable under reaction conditions will ultimately determine the catalytic performance. It is widely accepted that hematite is initially converted to magnetite regardless of the reducing atmosphere [186]. From this point on the identity of the final iron phase is dependent upon the composition of the reducing atmosphere employed. Some controversy remains in the literature regarding the transformations occurring to the iron catalyst during reduction of the magnetite phase. Fierro *et al.* [158] state that reduction of magnetite in a syngas atmosphere leads to formation of iron carbide species but make no mention of a metallic Fe<sup>0</sup> intermediate. This is in contrast to observation of several other authors [170, 177-181], who are in agreement that activation in syngas or carbon monoxide results in the step-wise reduction to the metallic state, where the solvation of surface carbon (generated by the dissociative adsorption of carbon monoxide) into the underlying metallic iron crystallites is thermodynamically favoured, which then yields iron carbide species. If hydrogen is employed as the reducing atmosphere then the reduction process is terminated at metallic iron. The catalyst may then undergo further transformation under FTS reaction conditions yielding bulk iron carbide species [158, 171, 182]. Indeed, iron carbides residing in both trigonal prismatic interstices ( $\chi$ -Fe<sub>2.5</sub>C (Hägg carbide) and  $\theta$ -Fe<sub>3</sub>C (cementite)) and octahedral interstices ( $\varepsilon$ -Fe<sub>2</sub>C,  $\varepsilon'$ -Fe<sub>2.2</sub>C) have been identified [183]. Additionally, it is reported that the actual nature of the iron phase(s) formed during the pretreatment period depends not only on the composition of the reducing atmosphere but also on the duration of exposure to the reactant feed, reactor design, temperature and pressure employed [172].

Iron-based FTS catalysts are usually employed unsupported [156]. One of the major inconveniences in using such unsupported catalysts is their physical degradation, producing catalyst fines. These fine particles present several problems: (i) they will plug fixed-bed reactors, generating a large pressure drop [156]; (ii) they retard catalyst separation in slurry reactors [23, 184, 185]; and (iii) they can result in a loss of bed fluidity in a fluidized bed reactor [186]. The use of supported iron catalysts presents several advantages, such as improved catalytic stability and a lower rate of deactivation [187, 188]. Silica (SiO<sub>2</sub>), alumina (Al<sub>2</sub>O<sub>3</sub>), titania (TiO<sub>2</sub>), magnesia (MgO), manganese oxide (MnO) and zirconia (ZrO<sub>2</sub>) are among the most frequently used supports. However, catalysts containing a binding material or support usually display a lower activity than the unsupported analogues [188]. The lower activity of the supported iron catalysts can be attributed to the development of metal-support interactions that negatively affect the reducibility of the iron phases [189].

Severe coking is a major problem affecting the hydrogenation of CO by transition metal catalysts, which occurs under normal operating conditions and increases with reaction time [190]. In this situation coking is understood as being the deposition of various carbon species with or without a hydrogenated component [191]. Carbon deposition from syngas mixtures over transition metal catalysts is facilitated by the facile disproportionation of CO on the metal surface [178-181, 192-195]. Iron catalysts are particularly active for CO disproportionation [178, 180, 181, 196, 197] and hence exhibit a high rate of carbon deposition under both Fischer-Tropsch and carbon monoxide hydrogenation conditions [185, 198-200]. Significant carbon deposition is universally observed in Fischer-Tropsch synthesis operating at elevated pressures [171, 172, 174] and is also observed, to a lesser degree, during the activation of precipitated iron Fischer-Tropsch catalysts [158, 172]. While deposition of certain types of carbon can be detrimental to catalytic activity, *e.g.* graphite [201, 202], other types of carbon are necessary for the reaction to proceed [191, 200, 203]. Indeed, a correlation between catalytic activity towards CO hydrogenation and carbon deposition on clean iron surfaces has been clearly demonstrated [204, 205]. Characterization of the carbonaceous species present on iron-based catalysts is therefore of fundamental importance to the progression of the understanding of iron-mediated Fischer-Tropsch catalysis.

Vibrational spectroscopy has been used for the characterisation of hydrocarbonaceous surface species on metal single crystal surfaces [206] and supported metal catalysts [207]. However, finely divided metal particles of catalysts absorb electromagnetic radiation from the infrared through the visible region of the electromagnetic spectrum. As a result, Raman spectroscopy, using either visible or near-infrared excitation, and infrared spectroscopy can be highly challenging [208].

A study by Bonzel and Krebs [191] on the chemical nature of carbonaceous species deposited on a Fe (110) surface during CO hydrogenation employed Auger electron spectroscopy (AES) and x-ray photoelectron spectroscopy (XPS) to provide evidence of graphitic carbon, carbidic carbon, and a heavily hydrogenated  $\text{CH}_x$  carbon species. Similarly, Erley *et al.* [209] observed a  $\text{CH}_x$  carbon species using electron energy loss spectroscopy (EELS). An infrared investigation by Galuszka *et al.* [210] revealed the presence of at least five different types of carbonaceous materials, including aliphatic, aromatic, oxygenated, carbidic, and amorphous species on the surface of various oxide supported iron catalysts after Fischer-Tropsch synthesis under ‘semi-industrial’ conditions, *i.e.* 573 K, 15.15 bar,  $\text{H}_2/\text{CO} = 1$ . Loaiza-Gil *et al.* [211] presented a transmission FT-IR

spectrum of an unsupported natural iron catalyst that had undergone extensive Fischer-Tropsch synthesis at 3.5 bar, the assignment of which was in close agreement with the observations of Galuszka *et al.* [210].

Raman scattering spectroscopy has been used to demonstrate the presence of a carbonaceous overlayer formed on iron Fischer-Tropsch catalysts in both post-activation [158] and post-reaction iron-based catalyst samples [174, 212, 213]. The observation of bands located at  $\sim 1300\text{ cm}^{-1}$  and  $1600\text{ cm}^{-1}$ , which are characteristic of polyaromatic carbonaceous species [214], is common to all of the Raman investigations listed here. Ding *et al.* [213] assign these bands to an amorphous carbonaceous species. Fierro *et al.* [158] suggest that several carbon phases, including graphite, are present in syngas activated iron catalysts but that only the graphitic phase is observable by Raman spectroscopy. The results of these studies indicate that, although it can provide valuable insight, Raman spectroscopy alone cannot provide a complete description of the nature of the carbonaceous deposits present on iron-based FTS catalysts.

Inelastic neutron scattering (INS) spectroscopy presents an alternative to conventional laboratory-based optical spectroscopic techniques for the study of heavily coked heterogeneous catalysts [14]. By virtue of the large incoherent scattering cross section for hydrogen and its low mass, INS spectra are dominated by vibrational modes involving hydrogen motion. In contrast, metal and oxygen atoms have a very low incoherent scattering cross section and their vibrational modes usually contribute little, if at all, to INS spectra [14]. In this manner, INS is ideally suited for the study of carbonaceous overlayers containing a hydrogenated component present on the surface of metal catalysts. INS spectroscopy has previously been successfully employed to observe methyl groups that poison the surface of palladium-based hydrogenation catalysts [208]. This raises the possibility of employing INS spectroscopy to observe hydrogenated carbonaceous deposits on iron-based Fischer-Tropsch catalysts. Historically, progress in the understanding of Fischer-Tropsch catalysis has followed the availability and adoption of new research tools and methods [215]. Interrogation of the carbonaceous species deposited on iron catalysts during activation in syngas (or Fischer-Tropsch synthesis) by INS spectroscopy represents an unexplored avenue that has, thus far, not been reported in the literature.

In the present investigation a combination of techniques, including INS spectroscopy, Raman spectroscopy, temperature programmed oxidation (TPO), x-ray diffraction (XRD), and transmission electron microscopy (TEM) is applied to investigate the effect of several

activation procedures on the final phase of prototype precipitated iron Fischer-Tropsch catalysts and to the characterization of the carbonaceous deposits formed on the surface of activated and post-reaction catalysts. The catalyst under investigation was selected in consultation with SASOL Technology Ltd., a major organization in the world-wide delivery of Fischer-Tropsch technology.

# 8

## Chapter 8

### **Analysis of a post-reaction fused iron Fischer-Tropsch catalyst**

SASOL have operated high temperature fluidised bed Fischer-Tropsch synthesis reactors at their plant located in Secunda, South Africa, since *ca.* 1950 [156]. The catalyst used in these reactors is formed from an unsupported fused iron oxide precursor [156]. After a period of *ca.* 1 year online the catalyst begins to degrade due to an unacceptable level of catalyst attrition, which leads to the formation of catalyst fines. These fines still possess intrinsic activity in catalysing the FTS process; however an inability to maintain their fluidity within the bed results in a decrease in the observed FTS activity. The fines are periodically replaced with fresh catalyst and FTS activity is then re-established. SASOL Technology UK provided two samples of these fines: one sample had undergone standard toluene Soxhlet extraction; and the other had undergone additional Soxhlet extraction in dichloromethane. These extraction processes are commonplace and are employed in order to remove heavy wax residues from the surface and pores of the catalyst [22, 23]. The material remaining on the catalyst surface is strongly bound. In some cases strongly bound hydrocarbonaceous overlayers have been shown to constitute at least a component of the active site of heterogeneously catalyzed process [216, 217], whereas in other processes strongly bound material can represent a poisonous surface species, *e.g.* in Ni-catalysed methane reforming [202]. It is possible that the strongly bound residue remaining on the surface of the catalyst fines could potentially represent an important component of the active site of Fe-based catalysts employed in FTS. Characterisation of this species is therefore important for improving the current understanding of the behaviour of iron based catalysts under FTS conditions. It has recently been shown that Soxhlet extraction can negatively affect the composition of the catalyst by encouraging the formation of Hägg carbide ( $\chi$ -Fe<sub>5</sub>C<sub>2</sub>) and Fe<sub>3</sub>O<sub>4</sub> phases [24]. Nevertheless, this extraction procedure is deemed necessary for this investigation as the high molecular weight wax residues that would otherwise occupy the surface and pores of the catalyst would dominate subsequent INS measurements and other analyses, whereas it is the properties of the underlying catalyst and strongly bound hydrocarbonaceous residue that are of primary interest to this investigation.

## 8.1 Infrared spectroscopy

Initial characterisation of the catalyst fines was attempted by infrared spectroscopy. The DRIFTS spectrum for the toluene extracted sample is presented in Figure 8.1.1, while that of the sample that had undergone additional extraction in dichloromethane is presented in Figure 8.1.2. The spectra are virtually identical to each other. It is noted that the dark colouration (black) and high opacity of these samples makes acquisition of these spectra rather challenging. Features located at 2846, 2869, 2927, and 2953  $\text{cm}^{-1}$  are assigned to C-H stretching modes of various aliphatic hydrocarbonaceous components and indicate the presence of a hydrocarbonaceous overlayer. The broad feature located at 3047  $\text{cm}^{-1}$  is assigned to an olefinic hydrocarbonaceous component. The large broad feature located in the energy range 3100-3300  $\text{cm}^{-1}$  is assigned to hydroxyl groups associated with  $\text{Fe}_3\text{O}_4$ . Oxidation of iron catalysts is known to occur upon exposure to FTS reaction conditions [22, 218] and post-reaction samples are often reported to contain a significant proportion of  $\text{Fe}_3\text{O}_4$  [24, 171, 172, 219, 220].

Figure 8.1.3 presents the infrared spectrum recorded for a sample of magnetite (1:5 dilution in KBr) and, surprisingly, shows a similar vibrational spectrum to the catalyst fines sample in the energy range 3600-2500  $\text{cm}^{-1}$ . This suggests that the features observed at 2846, 2869, 2927, and 2953  $\text{cm}^{-1}$  may not necessarily be associated with an overlayer present on the catalyst surface. Instead, it is proposed that these bands are due to the presence of oil that has contaminated the infrared environmental cell. It was anticipated that recording the spectra as difference spectra by removing a spectrum of dried KBr from the sample spectra, as was performed for all the spectra presented here, would remove contributions associated with the environmental cell and trace contaminants. However, it appears that the presence of an optically opaque sample within the cell has increased the relative spectral contribution of contaminants that exist somewhere in the optical path of the infrared beam. Interestingly, Galuszka *et al.* [210] report the presence of infrared bands located at similar energies (2970  $\text{cm}^{-1}$ , 2926  $\text{cm}^{-1}$ , and 2853  $\text{cm}^{-1}$ ) for a series of post-reaction supported iron catalysts after exposure to FTS conditions to those reported here for magnetite. The fact that very similar infrared spectra are observed for the catalyst fines samples and the high purity magnetite sample is unexpected and indicates serious difficulties in the application of infrared spectroscopy to characterise hydrocarbonaceous deposits present on highly opaque samples.

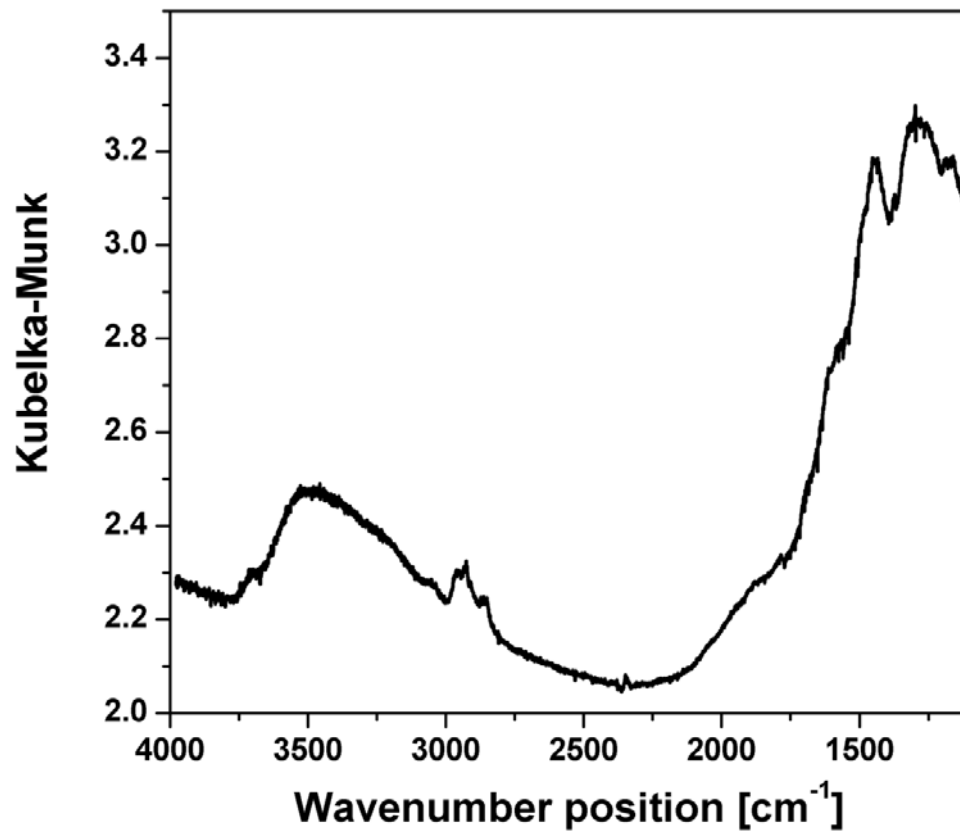


Figure 8.1.1: Diffuse reflectance infrared spectrum of a sample of catalyst fines removed from SASOL Secunda plant after Soxhlet extraction in toluene, presented in the energy range 4000-1400  $\text{cm}^{-1}$ .

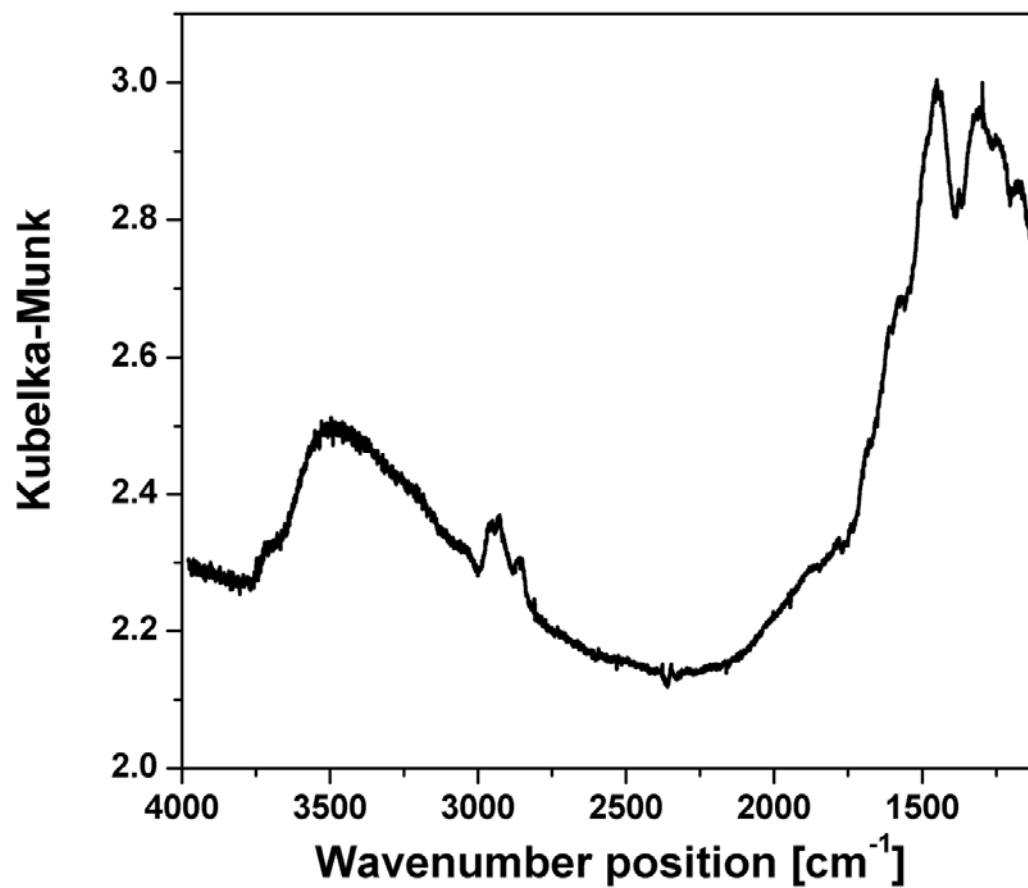


Figure 8.1.2: Diffuse reflectance infrared spectrum of a sample of catalyst fines removed from SASOL Secunda plant after Soxhlet extractions in toluene and dichloromethane, presented in the energy range 4000-1400  $\text{cm}^{-1}$ .

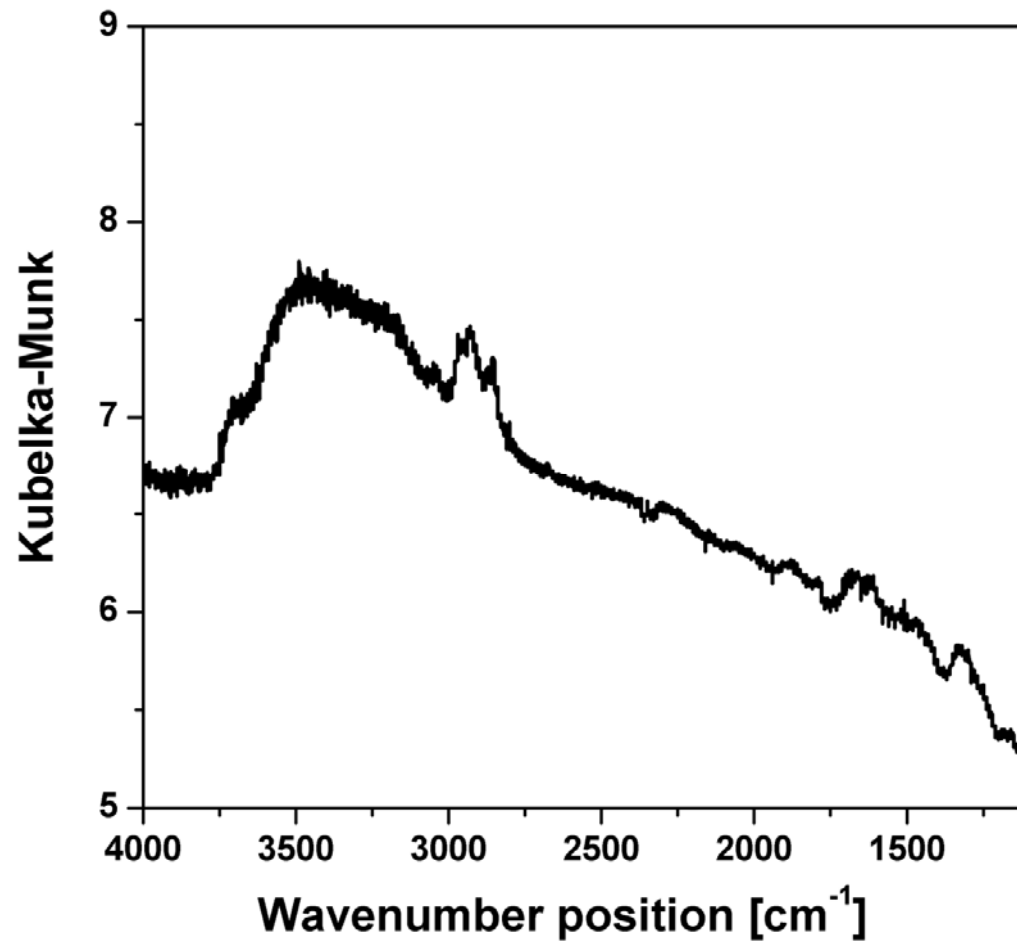


Figure 8.1.3: Diffuse reflectance infrared spectrum of a sample of high purity Fe<sub>3</sub>O<sub>4</sub>, presented in the energy range 4000-1400 cm<sup>-1</sup>.

## 8.2 Raman scattering spectroscopy

Raman scattering spectroscopy is a spectroscopic technique that provides information complementary to that attainable by infrared spectroscopy [16], and is ideal for the observation of carbon-carbon bonds within hydrocarbonaceous overlayers present on the surfaces of heterogeneous catalysts [214, 221, 222].

Both samples of catalyst fines yield similar Raman spectra, which are characterised by a broad and intense envelope (due to fluorescence, possibly caused by the KBr matrix in which the samples were dispersed not being perfectly clean) with superimposed sharp and intense signals associated with carbon species. The Raman spectra of both the toluene extracted (8.2.1(a)) and additionally dichloromethane extracted (8.2.1(b)) are identical with respect to the shape and energy position of the bands associated with carbon, located at  $1604\text{ cm}^{-1}$ ,  $1334\text{ cm}^{-1}$  and *ca.*  $1255\text{ cm}^{-1}$ .

The signal located at  $1604\text{ cm}^{-1}$ , which is often referred to as the ‘G’ band as it dominates the Raman spectrum of pure and highly ordered graphite [223, 224], is attributed to C=C stretching modes of  $sp^2$  hybridised carbon atoms. The signal occurring at  $1334\text{ cm}^{-1}$ , which is referred to as the ‘D’ band as it represents disorder in graphite systems [224], is attributed to the stretching modes of  $sp^3$  and/or  $sp$  hybridised carbon atoms. Both spectra are comparable to polycyclic aromatic carbonaceous compounds reported elsewhere in the literature [214]. The absence of a significantly intense signal located at *ca.*  $1500\text{ cm}^{-1}$  indicates the presence of a relatively hydrogen deficient polyaromatic ‘coke’ species, such as naphthalene or anthracene [214]. Finally the shoulder located at *ca.*  $1255\text{ cm}^{-1}$  is assigned to in-plane olefinic CH rocking deformations [225], which are likely to be isolated to the outer boundary of the hydrocarbonaceous residue. Such rocking deformation modes usually yield relatively intense Raman signals [225].

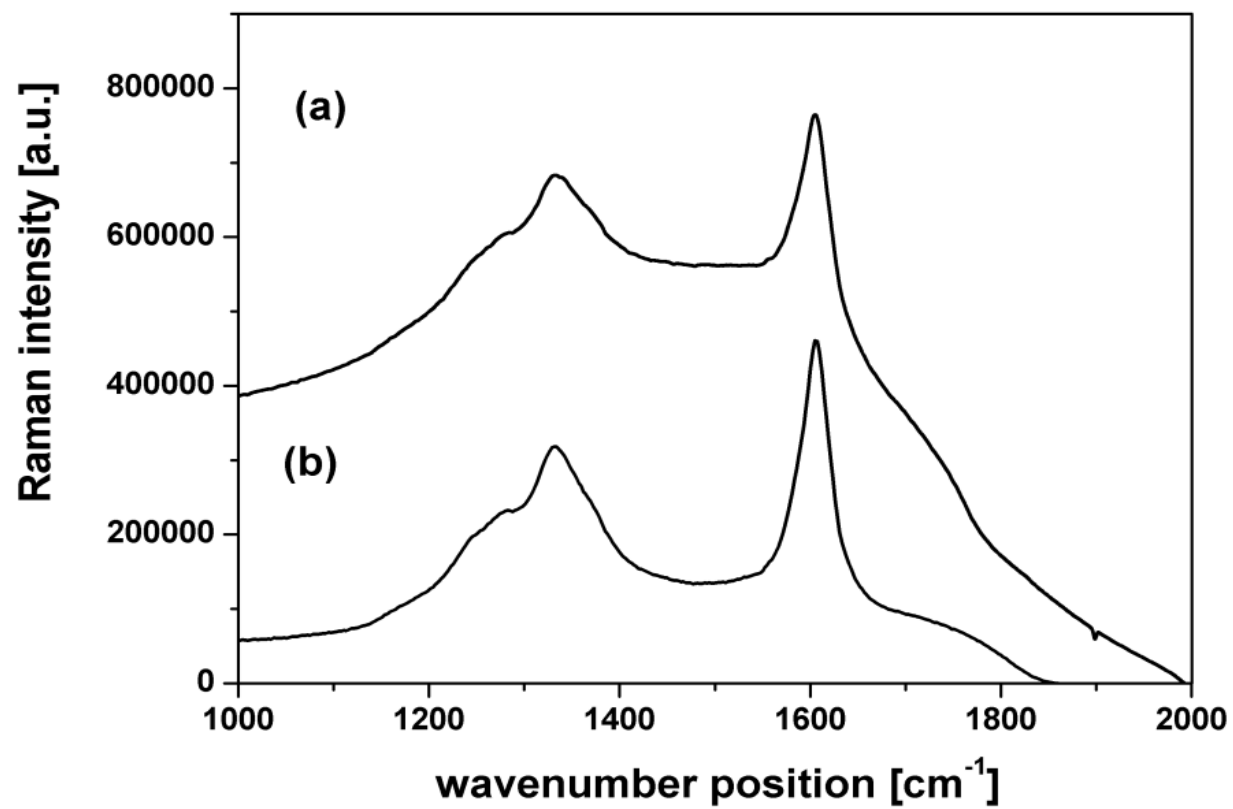


Figure 8.2.1: Raman scattering spectrum of catalyst fines that have undergone Soxhlet extraction in (a) toluene, and (b) toluene followed by dichloromethane. Presented in the energy range 1000-2000  $\text{cm}^{-1}$ .

### 8.3 Inelastic Neutron Scattering (INS) spectroscopy

Samples of each of the catalyst fines were cooled to <40 K before INS spectra were recorded using the TOSCA spectrometer at the ISIS Facility (Rutherford Appleton Laboratory, Chilton, UK). The spectra, which, in accordance with the infrared and Raman spectra, are almost identical to each other, are presented in Figures 8.3.1-8.3.2. The collective similarity of the INS, Raman and infrared spectra indicates that the additional dichloromethane extraction procedure has had no measurable effect on the nature of the hydrocarbonaceous overlayer present of the post-reaction catalyst fines samples. As a consequence, the interpretation of each spectrum is the same and is summarised in Table 8.3:

Wavenumber (cm <sup>-1</sup> )	Shape/Intensity	Assignment
85	Sharp, intense	Bulk Fe or Fe-O phonon
238	Sharp, medium	CH <sub>3</sub> torsion / Fe-O phonon
440	Broad, weak	C-C skeletal deformation
574	Broad, weak	Fe-O phonon
737	Sharp, weak	5-6 ring deformation
792	Sharp, weak	Substituted 6-member ring breathing
867	Sharp, intense	C-C stretch/6 ring breathing/CH <sub>2</sub> wag
940	Sharp, intense	In-plane OH deformation
1029	Sharp, medium	=CH <sub>2</sub> rock
1162	Sharp, medium	CH bend
1215-1295	Broad, medium	=CH rock
1369	Medium, medium	CH <sub>2</sub> wag and/or CH <sub>3</sub> umbrella
1451	Medium, medium	CH <sub>2</sub> scissors (1470 cm <sup>-1</sup> ) and/or CH <sub>3</sub> bend
3021	Intense, broad	Aliphatic/olefinic C-H stretch
3216	Intense, broad	Olefinic C-H stretch

Table 8.3: Tabulated assignments for INS spectra of Soxhlet extracted catalyst fines.

Qualitatively, the INS spectra compare favourably to those previously observed for hydrogenated amorphous carbon [14, 226]. The presence of methyl groups in hydrocarbonaceous species can be shown via diagnostic bands corresponding to methyl torsions, which are usually located at *ca.* 250 ±10 cm<sup>-1</sup> in hydrocarbons [14] (or at *ca.* 300 cm<sup>-1</sup> when adsorbed on metals such as Pd [208]), and umbrella deformation modes typically located at 1395–1365 cm<sup>-1</sup> [225]. In this case, bands are observed at 238 cm<sup>-1</sup> and 1369 cm<sup>-1</sup>, which might be assigned to methyl torsion and methyl umbrella modes, respectively. However, the methyl torsion mode typically exhibits a more intense and sharp band in INS spectra than is observed here. This may be due to a relatively low methyl

concentration compared with CH<sub>2</sub> groups, which could arise from a surface species dominated by cyclical alkenes. This argument is supported by the associated Raman spectra presented in Figure 8.2.1. The presence of long chain alkyl groups is discounted due to the absence of a very intense signal located at *ca.* 1300 cm<sup>-1</sup> that typically dominates the INS spectra of molecules containing alkyl chains greater than 4 carbon atoms [14, 227]. It is also possible that the band located at *ca.* 238 cm<sup>-1</sup> could arise from, or at least contain a component associated with, phonon modes associated with the underlying substrate. This possibility could be explored further using an indirect geometry instrument, such as MARI or MAPS, which allows access to the momentum transfer properties of a vibrational feature, as described earlier in Section 1.2.2.3. The broadness and energy position of the signal located at 3021 cm<sup>-1</sup> in the C-H stretching region indicates that the hydrocarbonaceous overlayer is composed primarily of olefinic material but may also contain a minor contribution from aliphatic material. Iron based Fischer-Tropsch catalysts produce a range of products including both olefins and aliphatic hydrocarbons [156]. It would therefore be unsurprising if the hydrocarbonaceous overlayer produced by this process consisted of more than one component. The dichloromethane Soxhlet extraction does not appear to significantly alter this distribution as can be seen from close inspection of the  $\nu_{\text{CH}}$  stretching regions of both spectra, presented in the insets in Figure 8.3.1 and 8.3.2. Importantly, the relative intensity of the various methylene features (rocking and bending modes located at *ca.* 1029 and 1250 cm<sup>-1</sup>, and 1162 cm<sup>-1</sup>, respectively) indicate the absence of extensive alkyl chains, which supports the assignment of the spectrum to that of a polycyclic structure rather than extended linear chains.

While the INS spectra presented here contain many overlapping and broad features that prevent an unequivocal assignment to be made, it allows observation of several potentially diagnostic bands that are not accessible by infrared spectroscopy, and others that cannot be observed by Raman due to unfavourable selection rules. The INS intensity observed for these catalyst samples compared to molecular samples [14, 227] indicates the hydrocarbonaceous overlayer to contain a relatively low hydrogen concentration, which is in agreement with the Raman spectra presented previously in Section 8.2. In qualitative terms, the INS spectrum indicates an unsaturated polycyclic ring compound that may contain a small proportion of aliphatic carbon present as methyl group decorations.

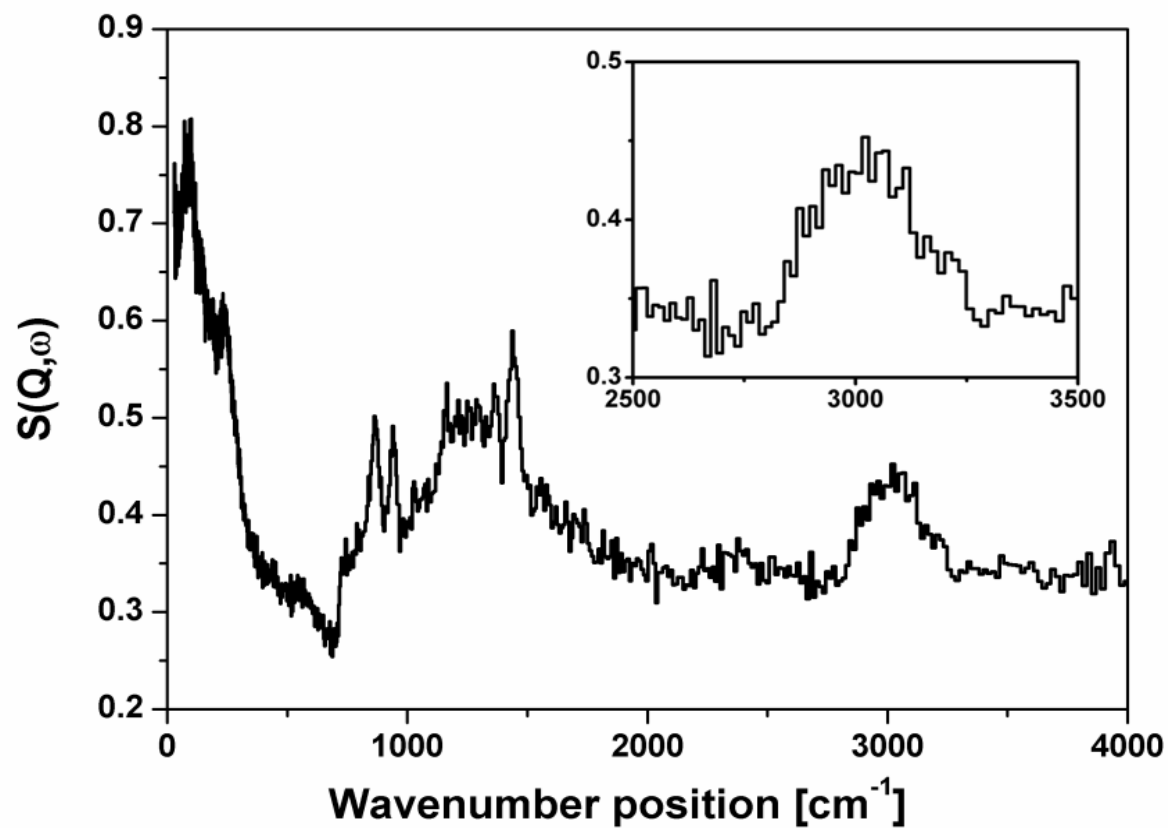


Figure 8.3.1: INS spectrum of catalyst fines removed from SASOL Secunda plant after Soxhlet extraction in toluene, presented in the energy range 0-4000  $\text{cm}^{-1}$ . Inset: spectrum shown in the energy range 2500-3500  $\text{cm}^{-1}$  only.

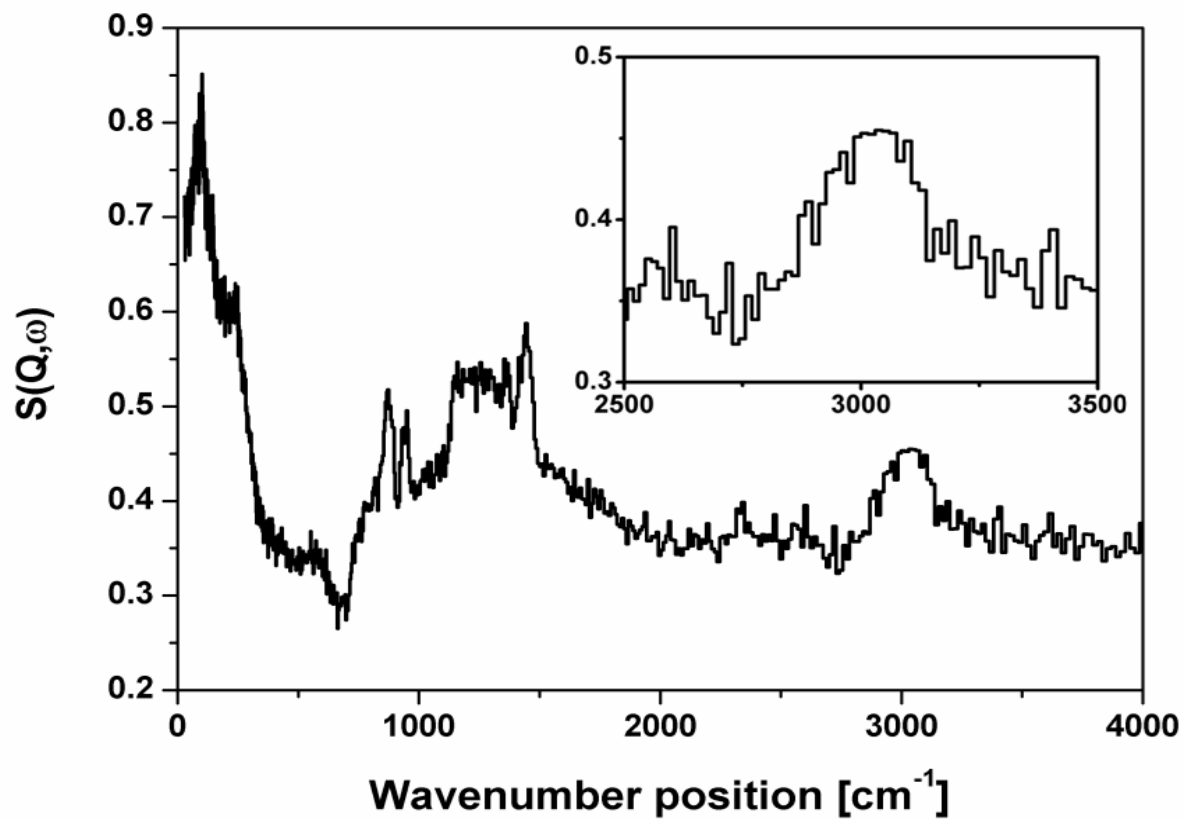


Figure 8.3.2: INS spectrum of catalyst fines removed from SASOL Secunda plant after Soxhlet extractions in toluene and dichloromethane, presented in the energy range 0-4000  $\text{cm}^{-1}$ . Inset: spectrum shown in the energy range 2500-3500  $\text{cm}^{-1}$  only.

## 8.4 Density Functional Theory calculations

The hydrocarbonaceous overlayer present in the extracted catalysts fines exhibits INS bands that can be correlated with both olefinic and aliphatic species. Density functional theory (DFT) calculations have been applied in order to assist the identification of this hydrocarbonaceous overlayer. The Gaussian04 program [228] was used to calculate, firstly the lowest energy conformation, followed by the vibrational frequencies of a series of candidate molecules at the B3LYP/6-31G level. The eigenvalues and eigenvectors calculated using Gaussian04 [228] were then used to predict the theoretical inelastic neutron scattering (INS) spectrum using the aCLIMAX program [18]. The major deficiency in using this method to calculate the vibrational spectra of isolated model compounds and to compare them against a hydrocarbonaceous overlayer is the fact that the effects of the underlying substrate are not considered in the simulation. This is partly mitigated against by the fact that the components of the catalyst substrate, Fe and O in this case, present very low inelastic neutron scattering cross-sections and will therefore not feature prominently, if at all, in the experimental INS spectra. In any case, the DFT calculations presented here are used only to reinforce assignments made for the INS spectra presented previously.

Figure 8.4.1 presents the simulated INS spectrum of a partially hydrogenated anthracene molecule, where one of the outer rings was fully saturated (see inset), compared against the INS spectrum of the sample catalyst fine that had undergone toluene extraction only. The catalyst fines sample that had undergone additional dichloromethane extraction will not be compared as its INS spectrum is almost identical to that of the toluene only extracted sample. Figure 8.4.2 presents a comparison of the simulated INS spectrum of partially hydrogenated naphthalene against the experimentally acquired INS spectrum of the catalyst fines. For each of the simulated INS spectra, a uniform scaling factor of 0.95 has been applied to the vibrational energies in order to account for the harmonic approximation used in the DFT calculations [229]. As observed in Figures 8.4.1 and 8.4.2 both candidate molecules yield similar simulated INS spectra, each presenting a reasonable fit to the experimentally acquired INS spectrum of the extracted catalyst fines. This supports the earlier assignment of the INS (Figs. 8.4.1 and 8.4.2) and Raman (Fig. 8.3.1) spectra to a polycyclic aromatic hydrocarbon species containing a proportion of aliphatic material. A more detailed DFT survey considering a wider variety of candidate molecules, using periodic DFT methods where the catalyst surface could be factored into the calculation,

might allow the INS spectra to be more accurately modelled. However, the controversy that exists within the literature as to the identity of the underlying phase of an iron-based FTS catalyst [158, 170, 200, 205, 220, 230], which would also be likely to support the hydrocarbonaceous overlayer, would impede an investigation of this nature.

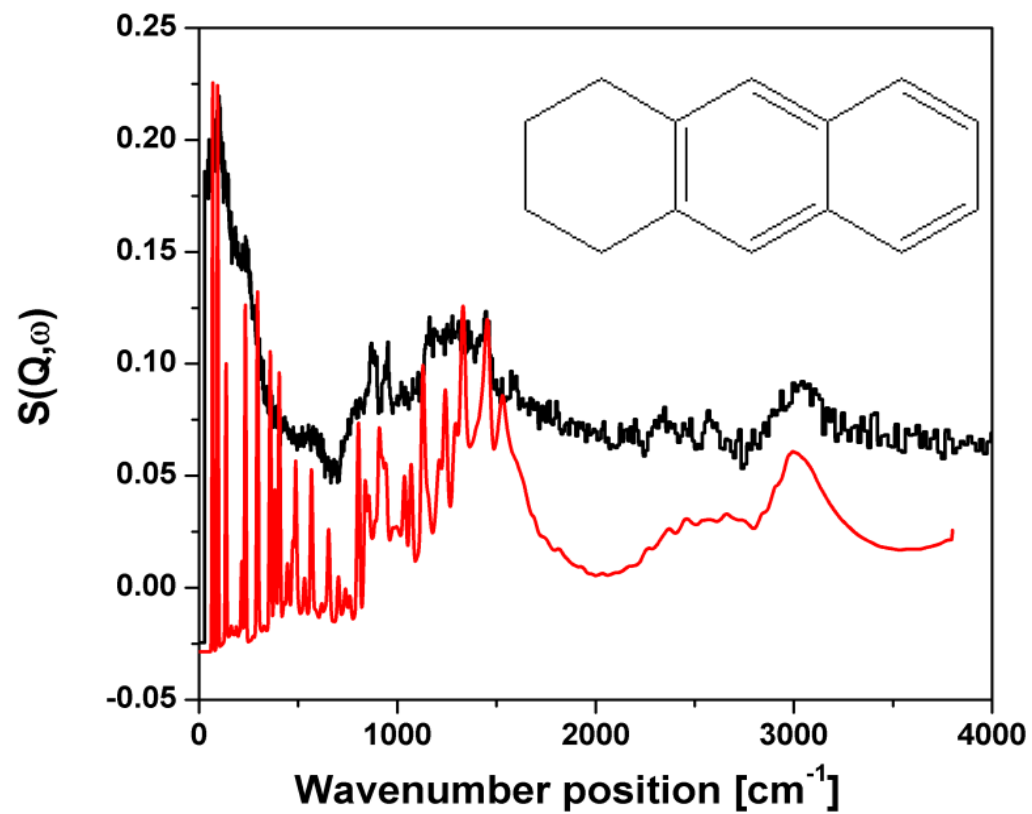


Figure 8.4.1: Comparison of the simulated INS spectrum of a partially hydrogenated anthracene molecule (red trace, see inset) against the experimentally acquired INS spectrum of a sample of extracted Fe-based FTS catalyst fines (black trace).

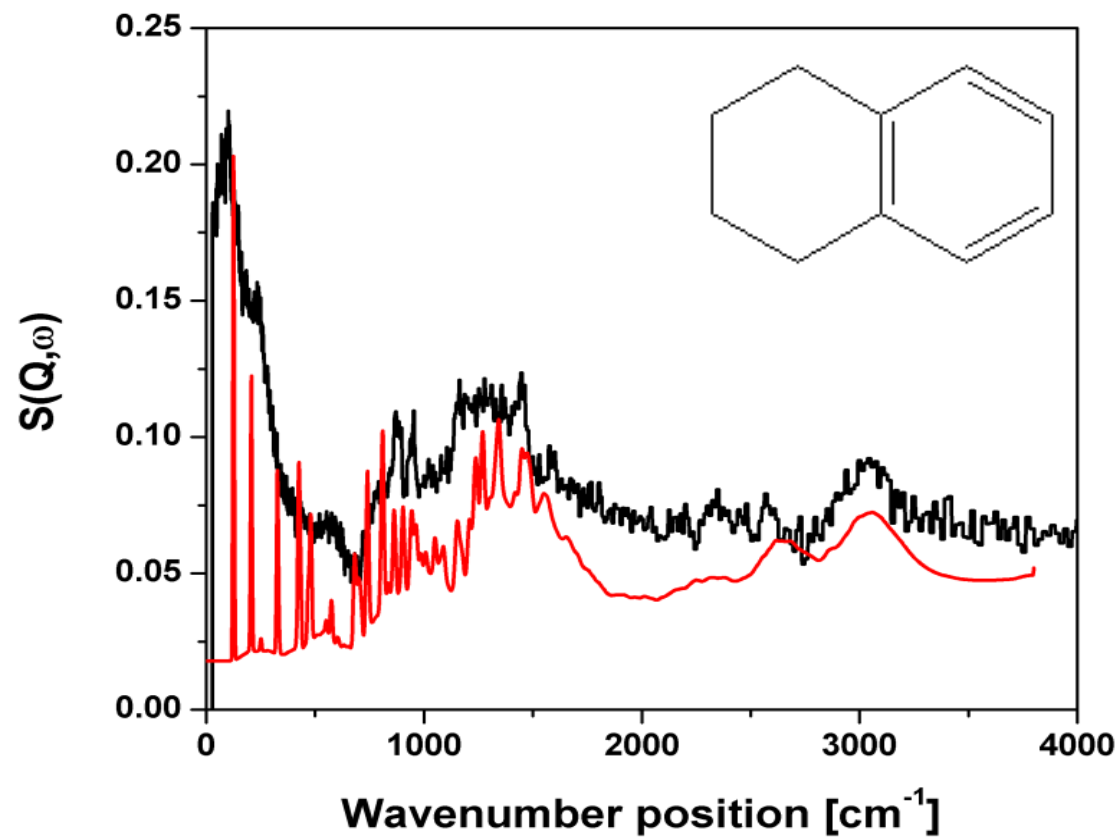


Figure 8.4.2: Comparison of the simulated INS spectrum of a partially hydrogenated naphthalene molecule (red trace, see inset) against the experimentally acquired INS spectrum of a sample of extracted Fe-based FTS catalyst fines (black trace).

## 8.5 X-ray diffraction of post-reaction catalyst fines

X-ray powder diffraction patterns were acquired for each of the samples of extracted catalyst fines samples in order to determine the bulk composition of each sample.

The diffraction pattern for the toluene only and toluene followed by dichloromethane extracted samples are almost identical and are presented in Figures 8.5.1 and 8.5.2 respectively. Both patterns are dominated by reflections associated with magnetite ( $\text{Fe}_3\text{O}_4$ ), with the most intense of those located at  $2\theta$  values of  $17^\circ$ ,  $29^\circ$ ,  $35^\circ$ ,  $42^\circ$ ,  $56^\circ$ , and  $62^\circ$ . Magnetite is known to be a major component of post-reaction iron catalysts due to the effect of oxidation of metallic iron and iron carbide species by water [156, 166], which is the major product obtained in FTS [156, 231]. In addition to magnetite reflections, there is a manifold of signals located in the  $2\theta$  range of  $42\text{--}45^\circ$ , which is characteristic of iron carbide species [24, 158, 198]. Hägg carbide,  $\chi\text{-Fe}_5\text{C}_2$ , has been shown to be abundantly present in iron-based FTS in post-reaction samples and also in catalysts that have been activated in syngas at atmospheric pressure [158] and its presence has been correlated with subsequent FTS activity [158, 171, 182]. Samples treated in pure syngas have been reported to yield cementite,  $\theta\text{-Fe}_3\text{C}$  [158, 172]. Assignment of the carbide phase as either  $\chi\text{-Fe}_5\text{C}_2$  and  $\theta\text{-Fe}_3\text{C}$  should be done very carefully as pure  $\chi\text{-Fe}_5\text{C}_2$  and  $\theta\text{-Fe}_3\text{C}$  have very similar diffraction patterns, based upon reference database diffractograms of each carbide phase ( $\chi\text{-Fe}_5\text{C}_2$  reference: ICSD-89328,  $\theta\text{-Fe}_3\text{C}$  reference: JCPDS-76-1877). Fierro *et al.* [158] claim to be able to differentiate between each of these carbide phases that are contained in iron based FTS catalysts based on reflections associated with  $\theta\text{-Fe}_3\text{C}$  located at  $2\theta$  values of  $70.1^\circ$  and  $78.0^\circ$  that are absent from the diffractogram of  $\chi\text{-Fe}_5\text{C}_2$ . However, in the case of the patterns presented in Figures 8.5.1 and 8.5.2 the lack of sufficient resolution and signal-to-noise ratio does not allow this distinction to be made with absolute certainty.

The dominance of magnetite and  $\chi\text{-Fe}_5\text{C}_2$  reflections contained within the diffraction patterns of these samples may also be partially due to the Soxhlet extraction procedure that they have been subjected to. Datye *et al.* [24] have recently shown that Soxhlet extraction of iron-based FTS catalysts can encourage the production of significant quantities of magnetite and  $\chi\text{-Fe}_5\text{C}_2$  in iron FTS catalysts. A small quantity of iron may also be present in the sample. The most intense reflection of metallic iron occurs at a Bragg angle of  $44.4^\circ$ ; the next most intense reflection occurs at  $82^\circ$ . In the diffractograms of the catalyst fines

samples (Figs. 8.5.1 and 8.5.2) a signal occurs at *ca.*  $44.4^\circ$  that overlaps with the manifold of features associated with iron carbides. A very weak signal can be observed at a Bragg angle  $82^\circ$ , which could be assigned to metallic iron. Thus, the diffractograms of the catalyst fines samples indicate that the samples are predominantly composed of magnetite with a significant quantity of iron carbides present, while the presence of a very small quantity of metallic iron cannot be discounted.

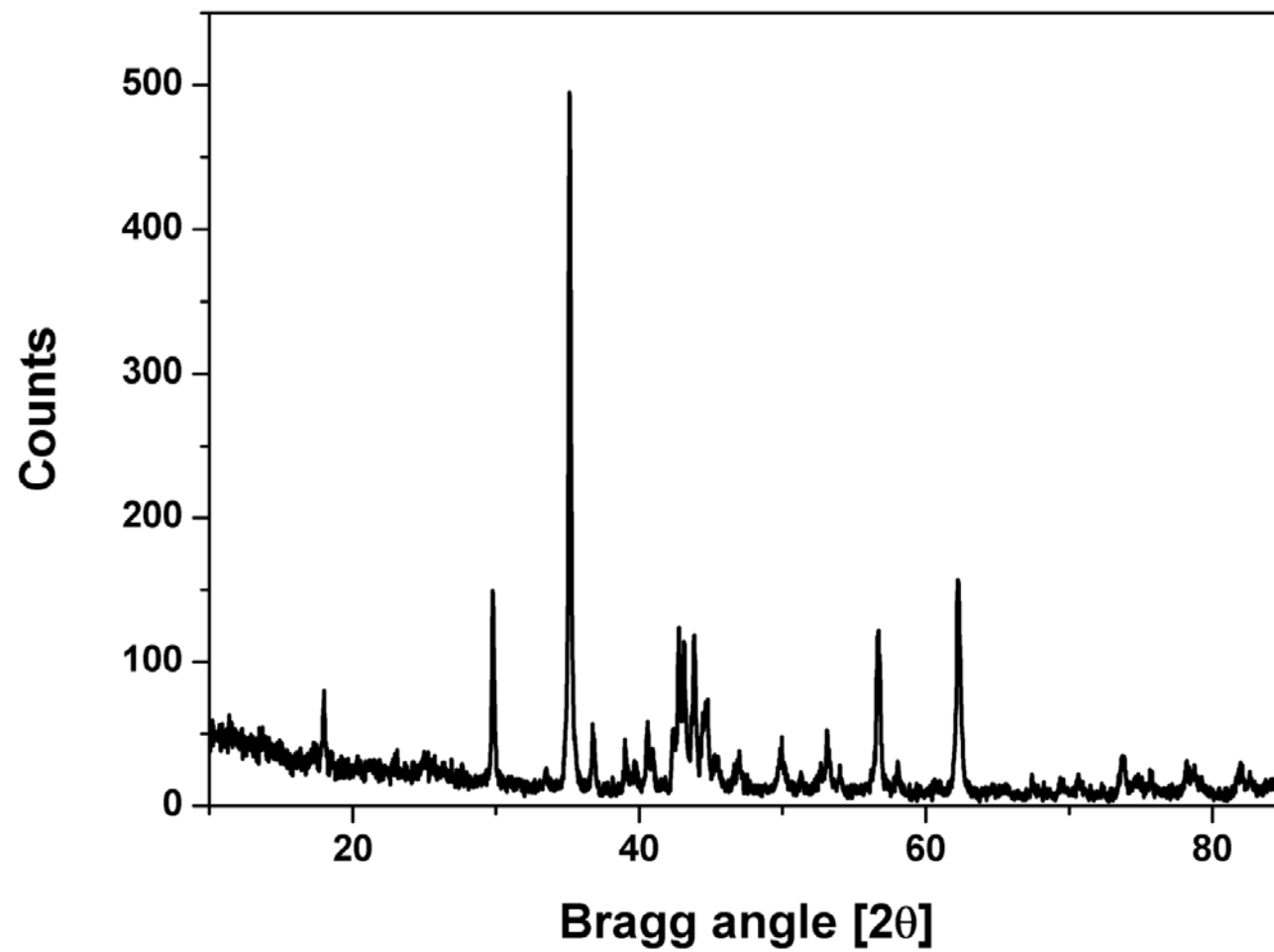


Figure 8.5.1: Powder x-ray diffraction pattern of a sample of post-reaction catalyst fines after Soxhlet extraction in toluene.

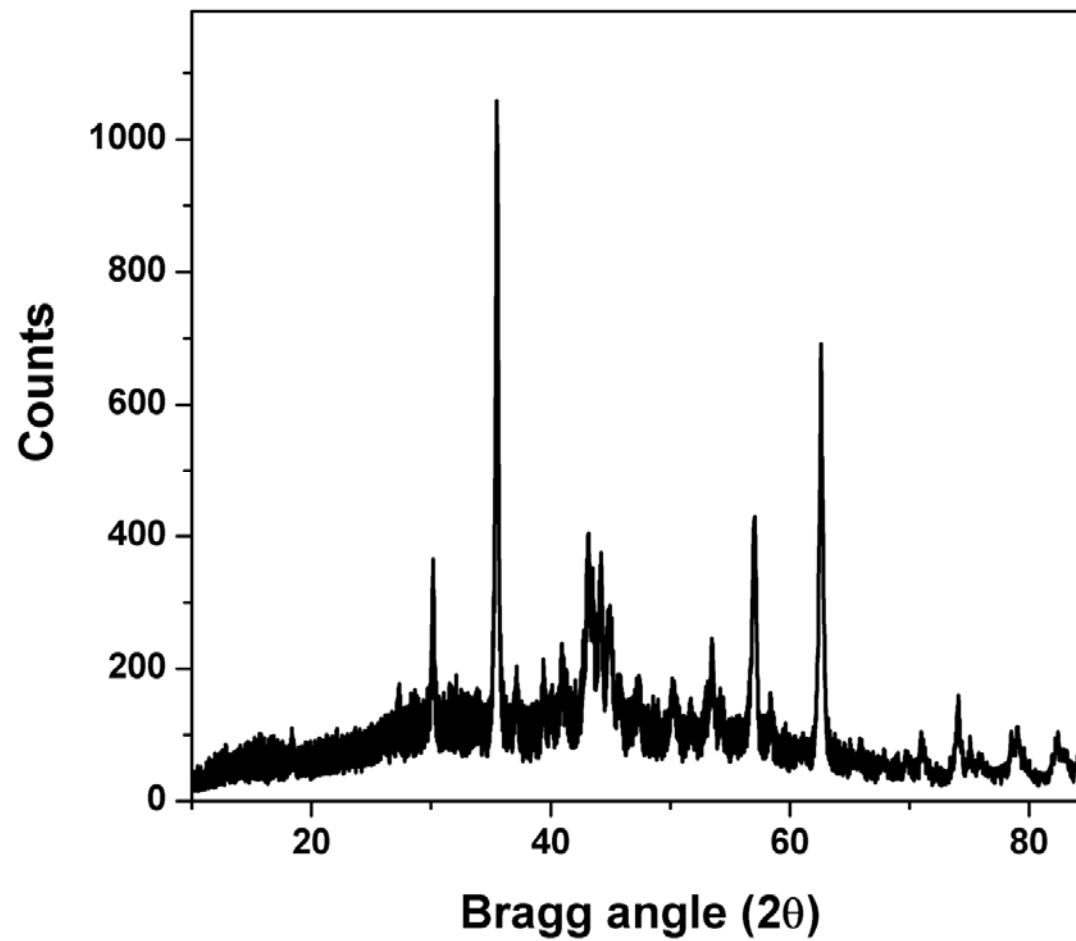


Figure 8.5.2: Powder x-ray diffraction pattern of a sample of post-reaction catalyst fines after Soxhlet extraction in toluene followed by dichloromethane.

## 8.6 Transmission Electron Microscopy

TEM analysis was performed on the extracted catalyst fines in order to observe their microstructure.

The TEM image of the sample after toluene Soxhlet extraction is presented in Figure 8.6.1. The micrograph is poorly defined and is characterised by a collection of relatively low density material. A number of small high density ‘spots’ with an average diameter of <5nm are superimposed upon the low density material, which is assigned as magnetite ( $\text{Fe}_3\text{O}_4$ ) based on its prominence in the associated XRD pattern of this sample (Fig. 8.5.1). Despite the low quality, the micrograph compares well to those reported elsewhere for industrial grade post reaction iron FTS catalysts [232]. Thus, Figure 8.6.1 is interpreted as representing a magnetite substrate upon which iron carbide and/or metallic iron crystallites are supported.

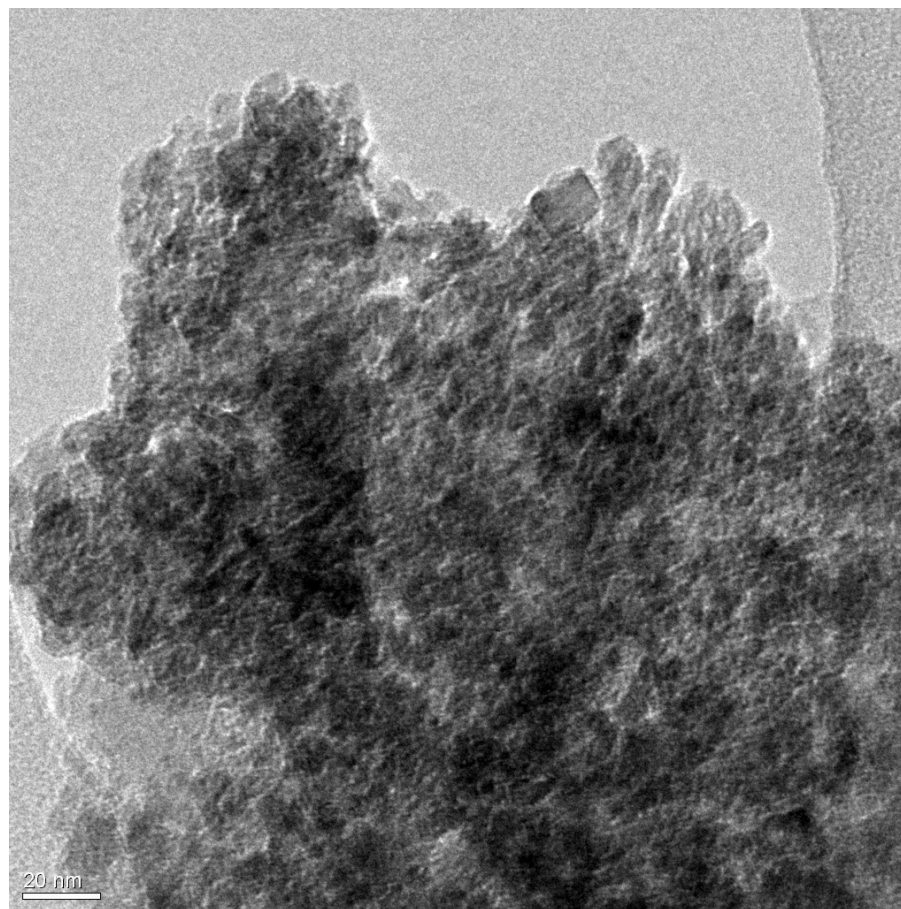


Figure 8.6.1: Transmission electron micrograph of a sample of catalyst fines previously subjected to Soxhlet extraction in toluene.

## 8.7 Quantification of hydrocarbonaceous deposits by temperature programmed oxidation (TPO)

Temperature programmed oxidation (TPO) analysis was performed in order to characterise and quantify the carbon contained in the catalyst fines samples. The amount of carbon oxidised was determined by quantification of the CO<sub>2</sub> produced as described in Section 2.6.4.

### Quantification of carbon content of post-reaction catalyst fines samples

The TPO profile for a sample of post-reaction catalyst fines Soxhlet extracted with toluene is presented in Figure 8.6.4. The integrated area of the  $m/z$  44 feature is  $3.9008 \times 10^{-6}$  a.u., which corresponds to  $1.553 \times 10^{-3}$  moles of evolved CO<sub>2</sub>. Assuming complete oxidation of all the carbon containing species in the sample, this indicates a carbon loading of 19.6 %  $w/w$ , which compares reasonably well with ancillary CHN microanalysis measurements of the sample that indicated a carbon loading of 17.5%. The TPO profile for a sample of the post-reaction catalyst fines that had been Soxhlet extracted in both toluene and dichloromethane is presented in Figure 8.6.5. The integrated area of the  $m/z$  44 feature in this case was equal to  $2.45802 \times 10^{-6}$  a.u., which equates to  $0.978 \times 10^{-3}$  moles of evolved CO<sub>2</sub>. Assuming complete oxidation of the carbonaceous species contained in the sample, this equates to a carbon loading of 14.2%  $w/w$ , which also compares favourably with CHN microanalysis of the sample that indicated a carbon loading of 15.8%. Both samples appear to contain carbonaceous deposits of identical character, as indicated by the fact both profiles are of identical shape, with maxima located at 760 K and 815 K, which indicates the majority of the carbon oxidised to be of a non-graphitic nature. An  $m/z$  44 feature of much lower intensity is also observed at *ca.* 1030 K, which, in contrast, could be of a graphitic nature [233].

The TPO measurements presented here indicate both the toluene extracted sample and the sample that had undergone additional dichloromethane extraction to contain carbonaceous deposits of identical character. The additional dichloromethane extraction process appears to have removed a small proportion of carbonaceous deposits that were not be removed by toluene extraction as indicated by the lower carbon loading of the sample, measured by both TPO and CHN microanalysis. This might also account for the lower Raman intensity observed for the dichloromethane extracted sample.

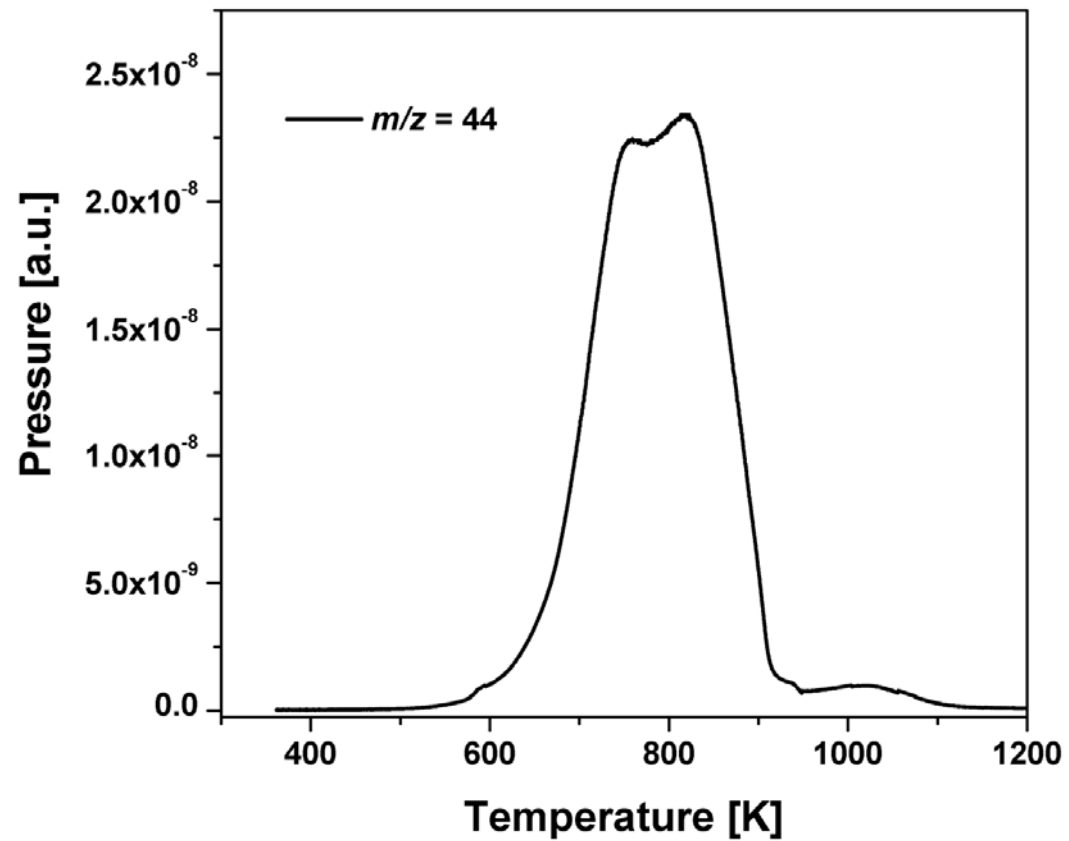


Figure 8.6.4: Temperature programmed oxidation profile for a 95 mg sample of post-reaction catalyst fines previously subjected to Soxhlet extraction in toluene.

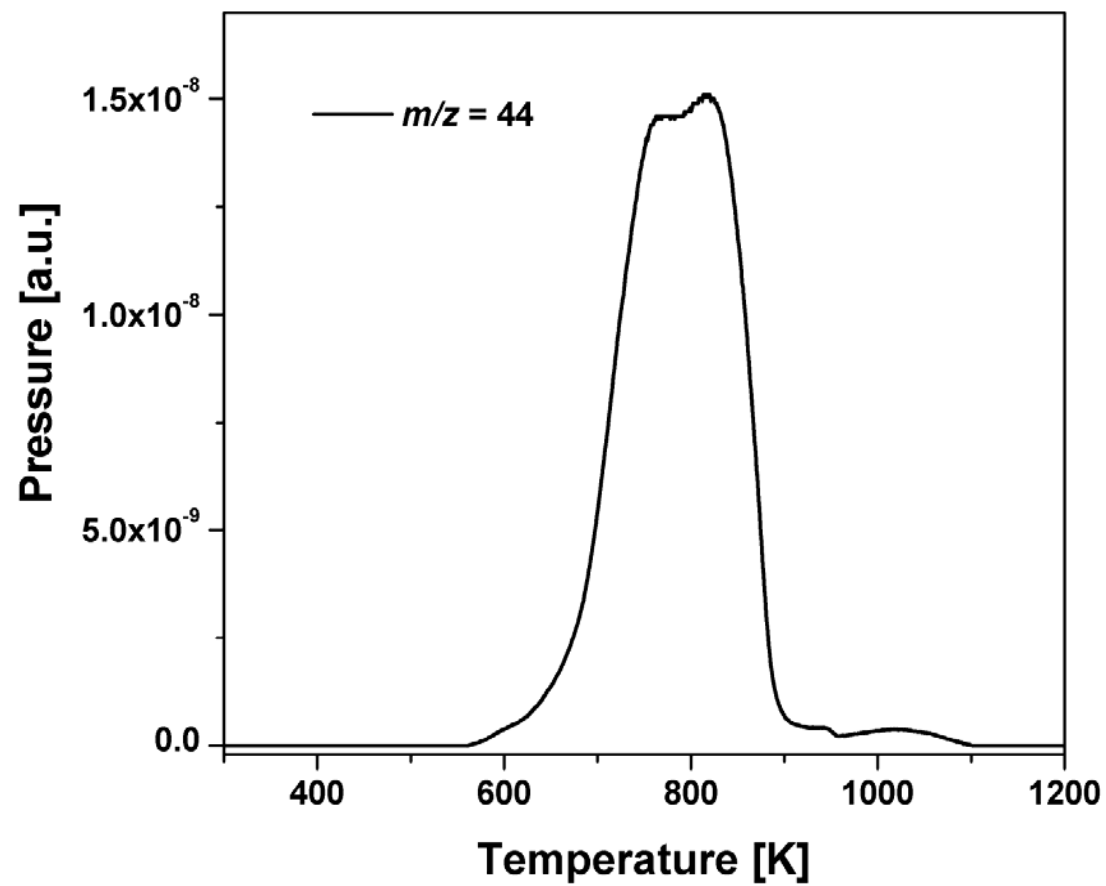


Figure 8.6.5: Temperature programmed oxidation profile for an 83 mg sample of post-reaction catalyst fines previously subjected to Soxhlet extraction in toluene followed by dichloromethane.

## 8.8 Conclusions

Infrared measurements were hampered by the high opacity of the sample but allowed observation of  $\nu_{\text{CH}}$  bands that indicated the presence of a hydrocarbonaceous overlayer containing both olefinic and aliphatic moieties. However, the fact that the spectra of the catalyst fines samples were similar to that of fresh  $\text{Fe}_3\text{O}_4$  indicates that infrared spectra of highly opaque catalyst samples should be interpreted with great care. Complementary Raman scattering spectroscopic measurements indicate the catalyst fines samples to contain a carbon-rich polyaromatic ring compound containing  $sp^2$  carbon atoms. The presence of either  $sp^3$  or  $sp$  carbon atoms is implied by the presence of the intense band located at *ca.*  $1300\text{ cm}^{-1}$ . From a spectroscopic perspective, additional dichloromethane Soxhlet extraction appears to have no effect on the nature of the carbonaceous overlayer present on the catalyst fines samples. INS measurements were compliant with deductions made from Raman measurements and indicated the carbonaceous overlayer to be composed of a carbonaceous polycyclic aromatic compound that possibly contained a small proportion of aliphatic moieties. The INS spectra of the catalyst fines compared favourably against simulated INS spectra of candidate partially hydrogenated polyaromatic ring compounds, which supported the supposition that the overlayer contained aliphatic and olefinic cyclic hydrocarbon moieties as deduced from the spectroscopic measurements. Powder x-ray diffraction (XRD) measurements revealed both catalyst fines samples to be largely composed of magnetite with contributions from iron carbide species. The presence of a very small proportion of metallic iron was also indicated. Temperature programmed oxidation (TPO) measurements revealed the catalyst fines to present a number of largely non-graphitic carbon environments. The presence of a small population of graphitic carbon was also implied. The TPO system was calibrated to allow quantification of carbon, which revealed the catalyst fines samples to have carbon loading of *ca.* 15% w/w, which compared favourably with parallel CHN microanalysis. The sample that had been subjected to additional dichloromethane extraction exhibited a slightly lower carbon content compared with the sample that had been extracted in toluene. This indicates that additional dichloromethane extraction was able to remove some additional carbon. However, the fact that the vibrational spectra and TPO profile of both samples were essentially identical indicated that the additional extraction procedure was not selectively removing a particular carbonaceous species.

Collectively, the analyses reported here indicate post-reaction catalyst samples active in the high-temperature FTS process to contain a significant quantity of carbon, which is partitioned within the catalyst in several environments, including iron carbides and polycyclic aromatic hydrocarbon species.

# 9

## **Chapter 9**

### **Carbon monoxide hydrogenation over an iron oxide precursor**

As was shown in the previous chapter, the INS spectra of post-reaction industrial grade Fischer-Tropsch synthesis (FTS) catalysts are complex and difficult to fully assign. Simplification of the FTS process is therefore desired in order to understand the surface species formed on the catalyst during the preliminary activation process that leads to Fe-based catalysts that are immediately active in FTS. Fierro *et al.* [158] have shown that treatment of  $\text{Fe}_2\text{O}_3$  in syngas at elevated temperatures leads to a catalyst that is highly active under real FTS conditions.

Wentreck *et al.* [234] and Araki and Poncic [235] have shown that the surface carbon formed from the dissociative adsorption of CO is the initial intermediate in the formation of methane. The  $\text{CH}_x$  species formed by the successive hydrogenation of this deposited carbon are assumed to be further intermediates in the production of methane [236-238]. A popular FTS mechanism reviewed by Biloen and Sachtler [238] proposes that the polymerisation of  $\text{CH}_2$  units leads to the formation of higher hydrocarbons while the hydrogenation of this species produces methane. Indeed there is experimental evidence that the chain growth of higher hydrocarbons during FTS is propagated by insertion of methylene units [236, 239, 240]. Erley *et al.* [209] have shown that  $\text{CH}_2$ , produced from atmospheric pressure reaction of CO and  $\text{H}_2$ , is stable on the surface of an Fe (110) surface as measured by electron energy loss spectroscopy (EELS).

The ambient pressure hydrogenation of CO to  $\text{CH}_4$  is not formally regarded as Fischer-Tropsch chemistry as no polymerisation reaction takes place, however it can be representative of FTS chemistry. The main benefit of employing CO hydrogenation in this investigation is that the small product range is anticipated to yield simplified INS spectra, which can help to form a knowledge base that can later be applied to more complex Fischer-Tropsch catalysts may be developed.

## 9.1 Temperature programmed reaction testing

The hydrogenation of carbon monoxide was performed over an iron oxide precursor at atmospheric pressure at two different temperatures. The reaction was carried out in a quartz microreactor and was continuously monitored by in-line quadrupole mass spectrometry as described in Section 2.6.1

### 9.1.1 Temperature programmed reduction

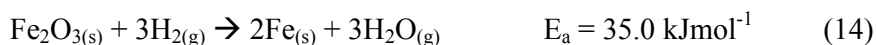
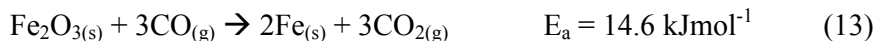
Where stated, some of the reactions were carried out over a sample of  $\text{Fe}_2\text{O}_3$  that was previously reduced in diluted  $\text{H}_2$ . The temperature programmed reduction (TPR) profile for the  $\text{Fe}_2\text{O}_3$  starting material is presented in Figure 9.1.1. Based on the work of Kadkhodayan and Brenner [241], the  $\text{H}_2\text{O}$  evolution features located at *ca.* 650 K, 900 K and 990 K are attributed to the sequential reduction of  $\text{Fe}_2\text{O}_3$  to  $\text{Fe}_3\text{O}_4$ ,  $\text{FeO}$  and  $\text{Fe}^0$ , respectively. The TPR profile therefore indicates that the reduction conditions employed for the reactions described here, *i.e.* reduction in  $\text{H}_2$  at 773K, should produce  $\text{FeO}$ . However,  $\text{FeO}$  is a metastable phase and rapidly disproportionates at temperatures below 833 K to yield  $\text{Fe}_3\text{O}_4$  and  $\text{Fe}^0$  [242]. Thus, the reduction conditions employed in these studies will produce a mixture of  $\text{Fe}_3\text{O}_4$  and  $\text{Fe}^0$ . An XRD pattern for a sample of  $\text{Fe}_2\text{O}_3$  after reduction in diluted  $\text{H}_2$  is presented in Figure 9.1.2 and shows the sample to be composed primarily of  $\text{Fe}_3\text{O}_4$ . The presence of a small proportion of  $\text{Fe}^0$  is indicated by the diffraction lines located at  $44.4^\circ$  and  $82.2^\circ$ . The sample was unavoidably exposed to air during the transfer from the microreactor to the diffractometer and oxidation of small  $\text{Fe}^0$  crystallites is likely. The catalyst is therefore likely to contain a greater proportion of  $\text{Fe}^0$  under reaction conditions than is indicated by the XRD pattern presented in Figure 9.1.2.

### 9.1.2 CO hydrogenation over iron samples at 623 K

#### *Fe<sub>2</sub>O<sub>3</sub> starting material*

The reaction profile for CO hydrogenation over  $\text{Fe}_2\text{O}_3$  at 623 K is presented in Figure 9.1.3 while the associated conversion and selectivity profile is presented in Figure 9.1.4. During application of the linear temperature ramp the profile is characterized by two  $m/z$  44 (420 K and 605 K) and two  $m/z$  18 (465 K and 620 K) features, attributed to the evolution of  $\text{CO}_2$  and  $\text{H}_2\text{O}$ , respectively. Simultaneously,  $\text{CO}$  ( $m/z$  28) and  $\text{H}_2$  ( $m/z$  2) are observed to be consumed. These events are interpreted as the sequential reduction of the  $\text{Fe}_2\text{O}_3$  starting material towards  $\text{Fe}_3\text{O}_4$  and  $\text{Fe}^0$  by  $\text{CO}$  and  $\text{H}_2$ , resulting in the evolution of  $\text{CO}_2$  and  $\text{H}_2\text{O}$ , respectively. The conversion profile for the reaction, presented in Figure 9.1.4, indicates

that in the early stages of reaction (T=440 K) H<sub>2</sub> and CO are consumed in approximately equal measure, however in the later stages of reaction (T=600 K) CO is preferentially consumed. Combined with the fact that CO consumption precedes H<sub>2</sub> consumption, these observations indicate CO to be the more effective reducing agent, which is consistent with the activation energies quoted for the reduction of Fe<sub>2</sub>O<sub>3</sub> with CO and H<sub>2</sub> as reported by Moon and Rhee [243], indicated in Equations 13 and 14, respectively. When the reaction temperature reaches 623 K no further consumption of CO or H<sub>2</sub> is observed.



### ***Fe<sub>2</sub>O<sub>3</sub> reduced at 773 K***

The reaction was repeated using a sample of Fe<sub>2</sub>O<sub>3</sub> that had previously been reduced *in situ* with diluted hydrogen at 773 K for 60 mins. Reduction of the catalyst in this manner converts the Fe<sub>2</sub>O<sub>3</sub> starting material into a mixture of magnetite (Fe<sub>3</sub>O<sub>4</sub>) and metallic iron ( $\alpha\text{-Fe}^0$ ), as confirmed by the XRD pattern of the reduced sample presented in Figure 9.1.2. The reaction profile for the pre-reduced Fe<sub>2</sub>O<sub>3</sub> sample subjected to the syngas mixture at 623 K is presented in Figure 9.1.5 and is essentially featureless. No consumption of either CO or H<sub>2</sub> is observed. This indicates that the consumption of H<sub>2</sub> and CO observed in the reaction profile of the Fe<sub>2</sub>O<sub>3</sub> starting material subjected to syngas at 623 K is due to reduction of the starting material at least to Fe<sub>3</sub>O<sub>4</sub>.

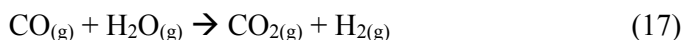
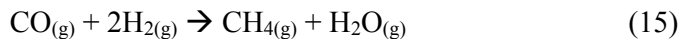
Collectively, these experiments indicate that a temperature of 623 K is insufficient to promote the hydrogenation of CO to CH<sub>4</sub> over Fe<sub>2</sub>O<sub>3</sub>, Fe<sub>3</sub>O<sub>4</sub> or Fe<sup>0</sup> species.

### **9.1.3 CO hydrogenation over iron samples at 723 K**

#### ***Fe<sub>2</sub>O<sub>3</sub> starting material***

The reaction profile for the hydrogenation of carbon monoxide at 723 K is presented in Figure 9.1.6. Within the first 100 min on stream, *i.e.* up to 623 K, the features of the reaction profile are, of course, identical to those observed in Figure 9.1.3. After 110 min on stream, where T=723 K, an increase in the *m/z* 15 signal, which corresponds to a major cracking component of CH<sub>4</sub>, is observed. The more intense *m/z* 16 signal cannot be used because it also represents a major cracking component of CO. The rate of CH<sub>4</sub> production continues to increase for the first *ca.* 220 min on stream before reaching steady state. CH<sub>4</sub>

production is accompanied by the production of water, which is indicated by the  $m/z$  18 trace. The water production profile is the same shape as the  $\text{CH}_4$  production profile, indicating that the two processes are linked, which would be expected given the stoichiometry of the carbon monoxide hydrogenation reaction (Equation 15).



After 100 mins on stream significant production of  $\text{CO}_2$ , indicated by the  $m/z$  44 signal, is observed. The  $\text{CO}_2$  evolution profile differs from that of  $\text{CH}_4$  and  $\text{H}_2\text{O}$  in the respect that it reaches steady state production almost immediately, which indicates that it may not be intimately related to the carbon monoxide hydrogenation process. The production of  $\text{CO}_2$  is attributed to a number of possible processes: the disproportionation of CO (Equation 16), also known as the Boudouard reaction, towards  $\text{CO}_2$  and surface carbon, which is known to proceed rapidly over metallic iron [244, 245]; the water gas shift reaction (Equation 17), where CO is oxidized by  $\text{H}_2\text{O}$  to produce  $\text{CO}_2$  and  $\text{H}_2$ , which can also be active over iron catalysts [156]; and the reduction of iron oxide by CO [243]. The former process is expected to produce some carbon deposition on the catalyst surface. Carbon dissolves rapidly into metallic iron and so the carbon produced in the Boudouard reaction constitutes a source of carbon from which iron carbide species may be produced. The CO and  $\text{H}_2$  conversion profiles and their relative associated selectivities towards  $\text{CH}_4$  are presented in Figure 9.1.7. The CO conversion is observed to be almost double that of  $\text{H}_2$ , which represents a substantial deviation from the stoichiometry of the carbon monoxide hydrogenation reaction (Equation 13) (where  $\text{H}_2$  conversion should be twice that of CO), indicating that a large proportion of the converted CO is being consumed by a competing reaction, *i.e.* Boudouard reaction (Equation 16) or water gas shift (Equation 17). This hypothesis is supported by the fact that the selectivity to methane in CO is significantly lower than that in  $\text{H}_2$ , which indicates that the vast majority of hydrogen is converted into the methane product. In fact the methane selectivity in  $\text{H}_2$  at reaction temperature, *i.e.* 723 K, is never less than 75 %, which is higher than the stoichiometric value of 66% that would be expected if the  $\text{H}_2$  were consumed in a complete carbon monoxide hydrogenation reaction. This disparity could arise from the production of extra  $\text{H}_2$  in the system formed via the water-gas shift reaction, which also produces  $\text{CO}_2$ . Methane yield, defined as the product of  $\text{H}_2$  conversion and  $\text{CH}_4$  selectivity, is observed to increase from baseline levels at *ca.* 100 mins (600 K) on stream up to a maximum of 12.5% after 200 mins on stream

(723 K) followed by modest deactivation to 12%, as observed in the CH<sub>4</sub> yield profile presented in Figure 9.1.8. The catalyst was then passivated using a standard procedure where the concentration of oxygen that the sample is exposed to is gradually increased up to atmospheric levels [167], and the XRD pattern collected, which is presented in Figure 9.1.12. The XRD pattern is characterized firstly by the presence of a broad feature located at a Bragg angle,  $2\theta$ , of *ca.* 25°, which has previously been assigned to an amorphous carbon reflection [158]. A broad manifold of features located in the Bragg angle range 40–50° indicates the presence of iron carbide species and metallic iron. A peak located at 82°  $2\theta$  indicates the presence of metallic iron. The fact that iron carbide species are present in the post reaction sample indicates the Boudouard reaction to be active since the solvation of surface carbon, which is produced in the Boudouard reaction, readily proceeds in metallic iron to yield iron carbides [170, 245]. Thus, the observed evolution of CO<sub>2</sub> is attributed to the Boudouard reaction, the forward water-gas shift reaction, and possibly the reduction of iron oxide towards Fe<sup>0</sup> by CO.

#### ***Fe<sub>2</sub>O<sub>3</sub> reduced at 773 K***

The profile for the CO hydrogenation reaction at 723 K over a sample of Fe<sub>2</sub>O<sub>3</sub> previously reduced in H<sub>2</sub> at 773 K is presented in Figure 9.1.13. Evolution of CH<sub>4</sub> is observed from *ca.* 125 mins, where the temperature reaches 723 K. Methane evolution is accompanied by production of CO<sub>2</sub> and H<sub>2</sub>O. These products approach steady state formation within the 6h time period. Interestingly, the CO, CH<sub>4</sub> and H<sub>2</sub>O traces all appear to exhibit the same evolution behaviour, unlike in the case of the Figure 9.1.9 where CO<sub>2</sub> evolution appeared to reach steady-state almost immediately when the temperature reached 723 K. This observation indicates that initial increase in CO<sub>2</sub> when the reaction temperature reached 723 K in Figure 9.1.9 is due to further reduction of iron oxide species towards Fe<sup>0</sup>.

The associated conversion and selectivity profiles for the experiment are presented in Figure 9.1.14. The CO conversion is much greater than the observed H<sub>2</sub> conversion, which indicates that, in accordance with the conversion and selectivity profiles observed when the catalyst is not reduced prior to exposure to syngas (Figure 9.1.10), some CO is consumed in a competing reaction. The presence of iron carbide species in the XRD pattern for the post-reaction sample would indicate the Boudouard reaction to be active under the conditions employed here. However, unfortunately, it was not possible to acquire an XRD pattern for this sample due to the fact it was of such low volume and was also texturally very hard. Grinding the sample in a ball mill left insufficient recoverable material with which to prepare a sample for XRD analysis.

The CH<sub>4</sub> yield as a function of time on stream is presented in Figure 9.1.15. The rate of increase in the CH<sub>4</sub> yield decreases over time and approximates to steady state operation towards the end of the 6h time period and, at an apparent maximum of 1.2%, is considerably lower compared with the non pre-reduced analogue. This could potentially be due to the lower surface area observed for post-reaction samples of catalyst that had been reduced prior to syngas exposure (13.3 m<sup>2</sup>/g) compared to those that had not been (22.8 m<sup>2</sup>/g). Of course, the BET measurement used to determine surface area also includes a contribution from carbonaceous deposits and so the intrinsic surface area of the actual catalyst would be difficult to accurately determine.

Collectively, these results suggest that a temperature greater than 623 K is required to induce the hydrogenation of CO over Fe<sub>2</sub>O<sub>3</sub>, or Fe<sub>2</sub>O<sub>3</sub> previously reduced to a mixture of Fe<sub>3</sub>O<sub>4</sub> and Fe<sup>0</sup>. Reduction of a precipitated Fe<sub>2</sub>O<sub>3</sub> catalyst prior to syngas exposure produces a catalyst that is apparently less active in CO hydrogenation at atmospheric pressure compared to a Fe<sub>2</sub>O<sub>3</sub> catalyst without prior reduction. The same behavior is also observed under true FTS conditions, where catalysts pretreated in syngas are reportedly more active than catalysts that have been pretreated in hydrogen only [158].

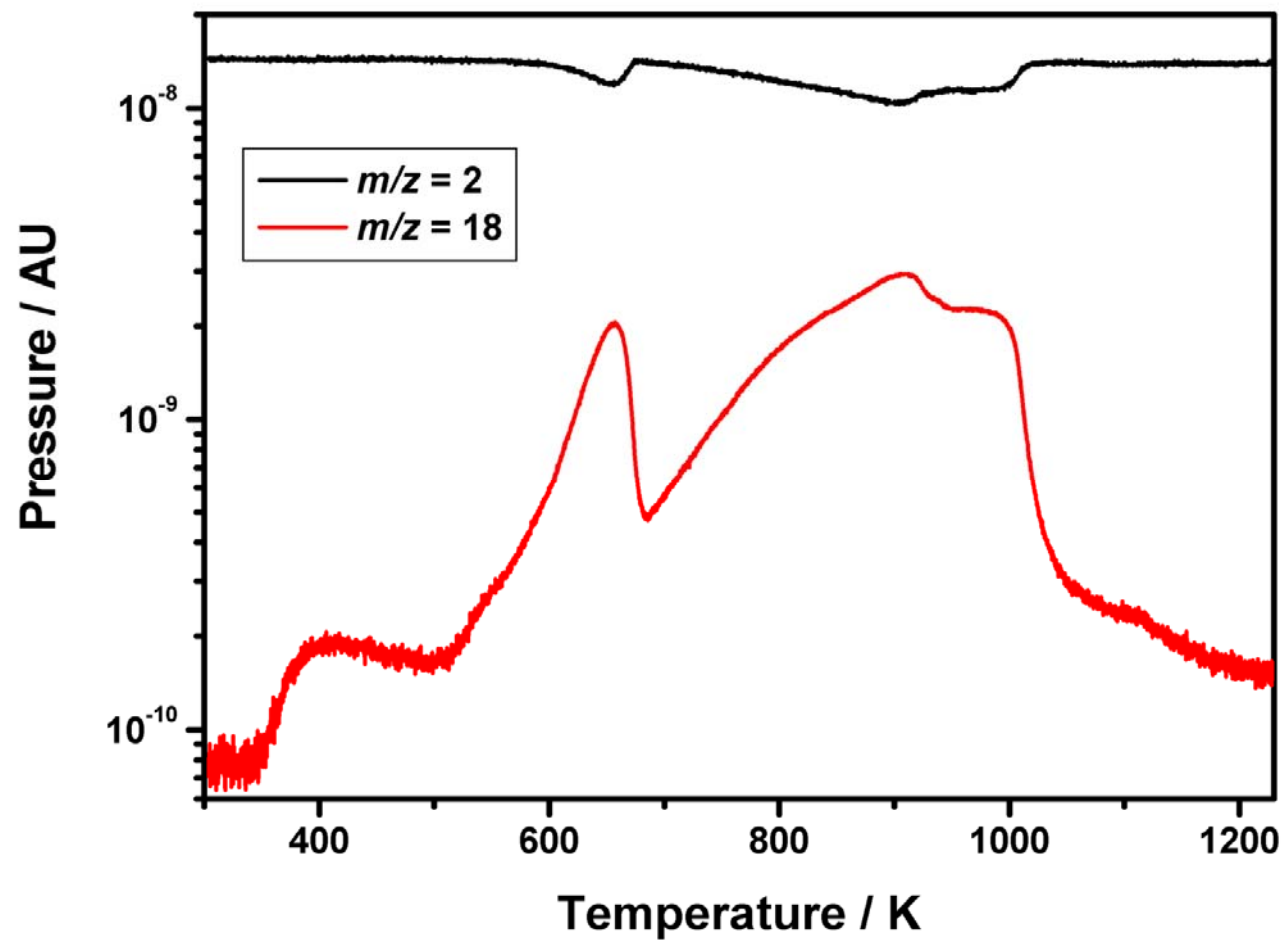


Figure 9.1.1: Temperature programmed reduction profile for the  $\text{Fe}_2\text{O}_3$  starting material.

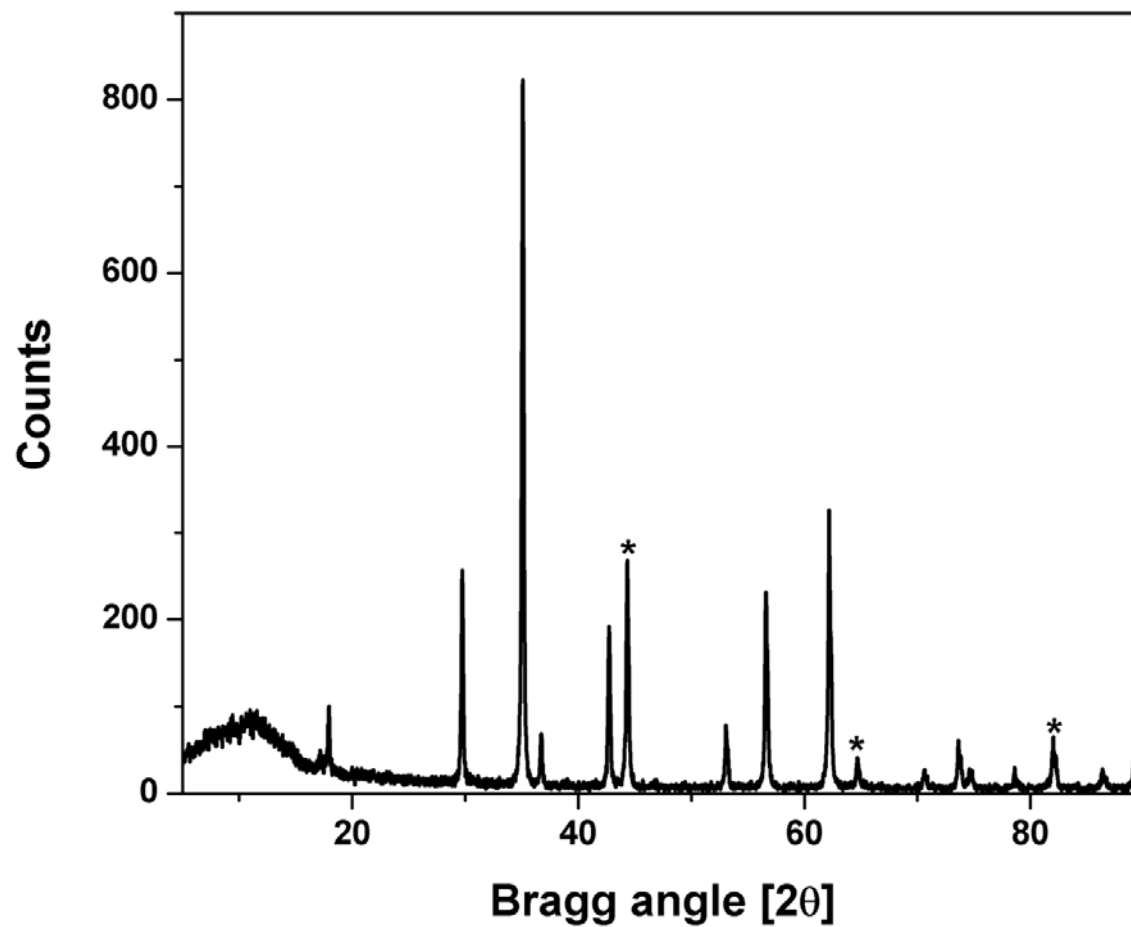


Figure 9.1.2: X-ray diffractogram of  $\text{Fe}_2\text{O}_3$  starting material after reduction in  $\text{H}_2$  diluted in He (30%  $\text{H}_2/\text{He}$ ) at 773 K for 60 mins. Reflections associated with  $\text{Fe}^0$  are indicated by asterisks.

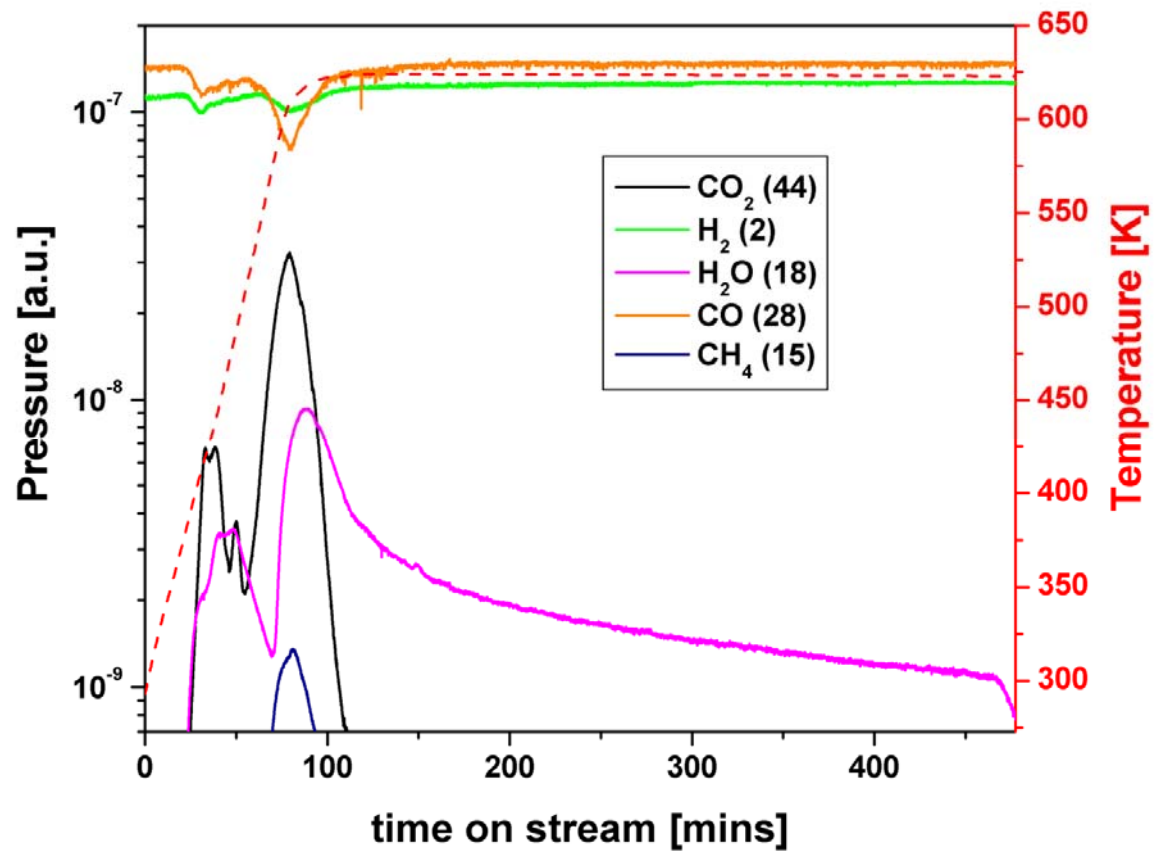


Figure 9.1.3: Reaction profile for a sample of  $\text{Fe}_2\text{O}_3$  reacted in a  $\text{CO}/\text{H}_2$  mixture (2:1) at 623 K for 6 h.

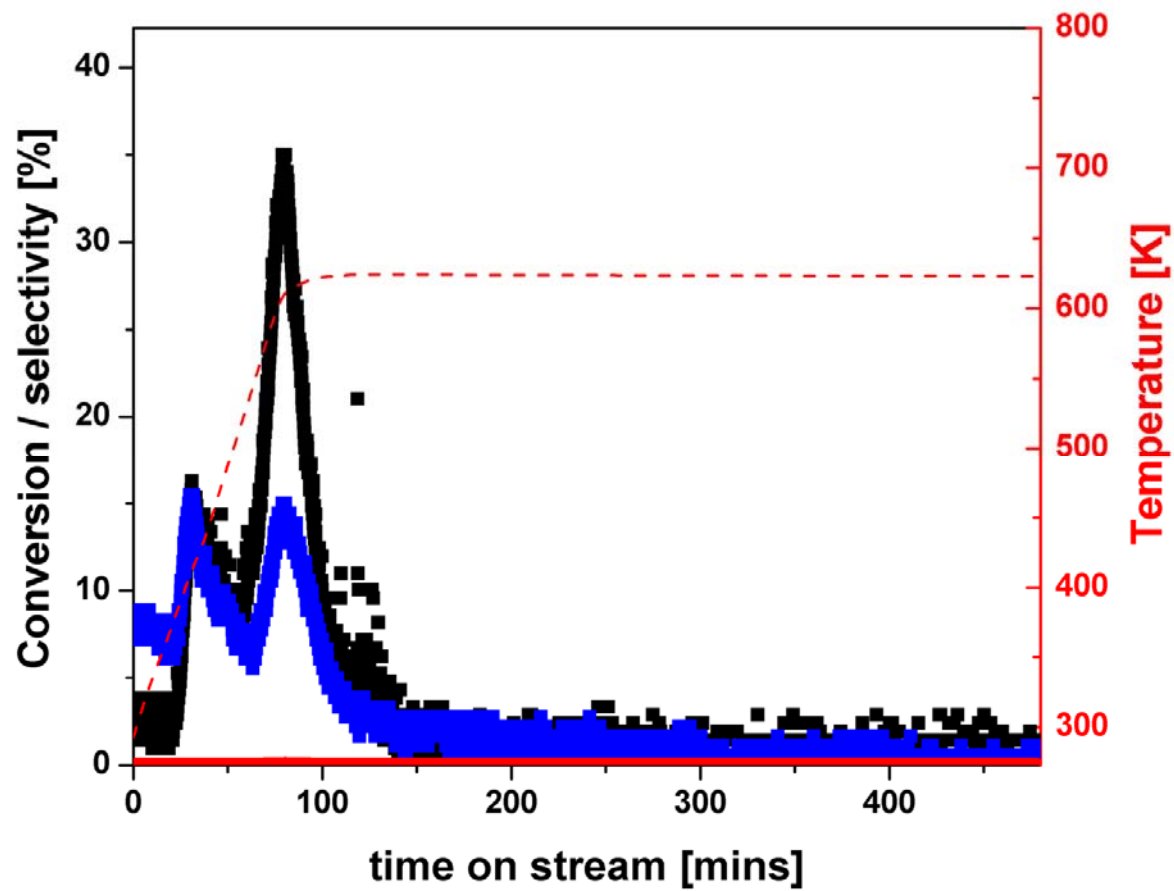


Figure 9.1.4: Conversion and selectivity profile for a CO hydrogenation over Fe<sub>2</sub>O<sub>3</sub> at 623 K for 6 h (●=CO conversion, ●=H<sub>2</sub> conversion, and ●=CH<sub>4</sub> selectivity).

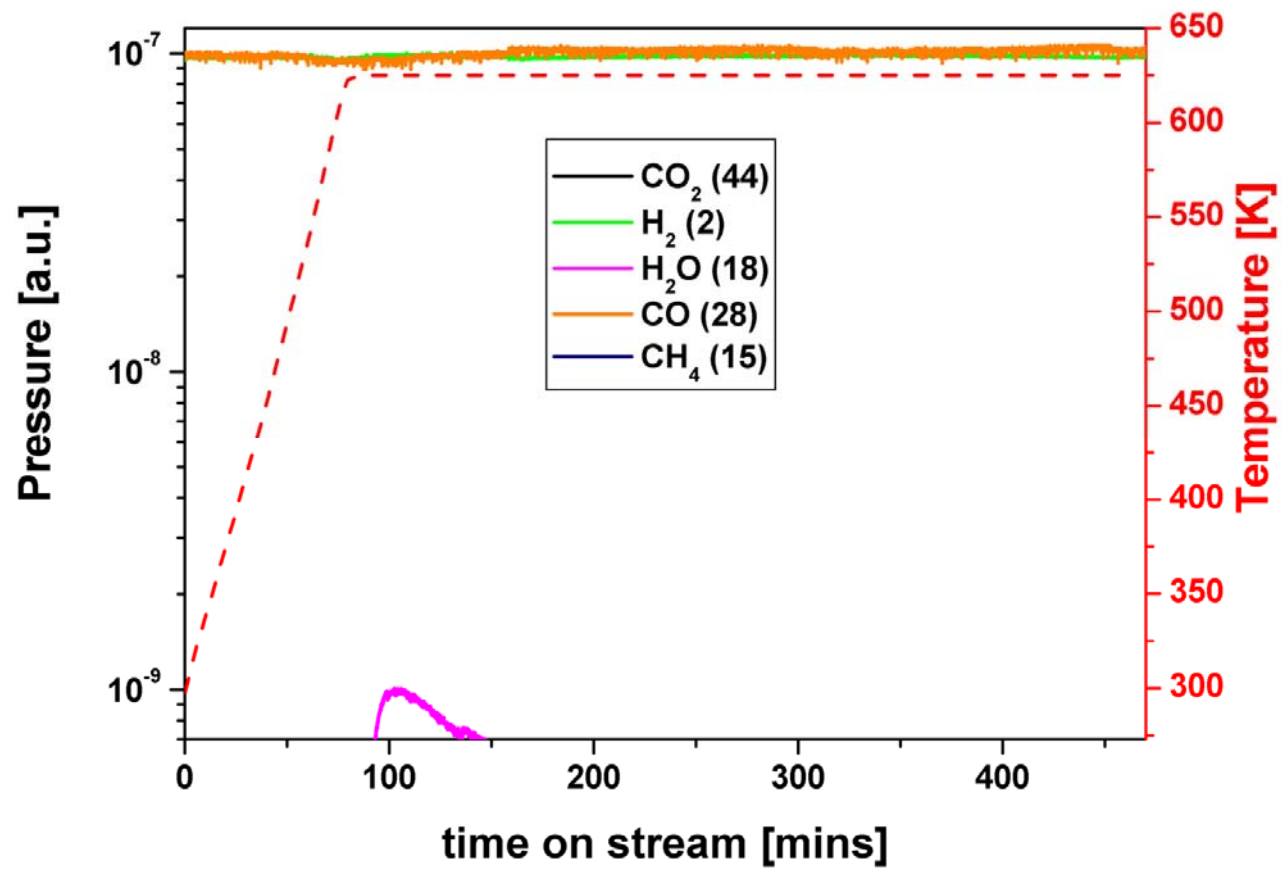


Figure 9.1.5: Reaction profile for a sample of Fe<sub>2</sub>O<sub>3</sub> reduced in H<sub>2</sub> at 773 K for 60 mins followed by reaction in a CO/H<sub>2</sub> mixture (2:1) at 623 K for 6 h.

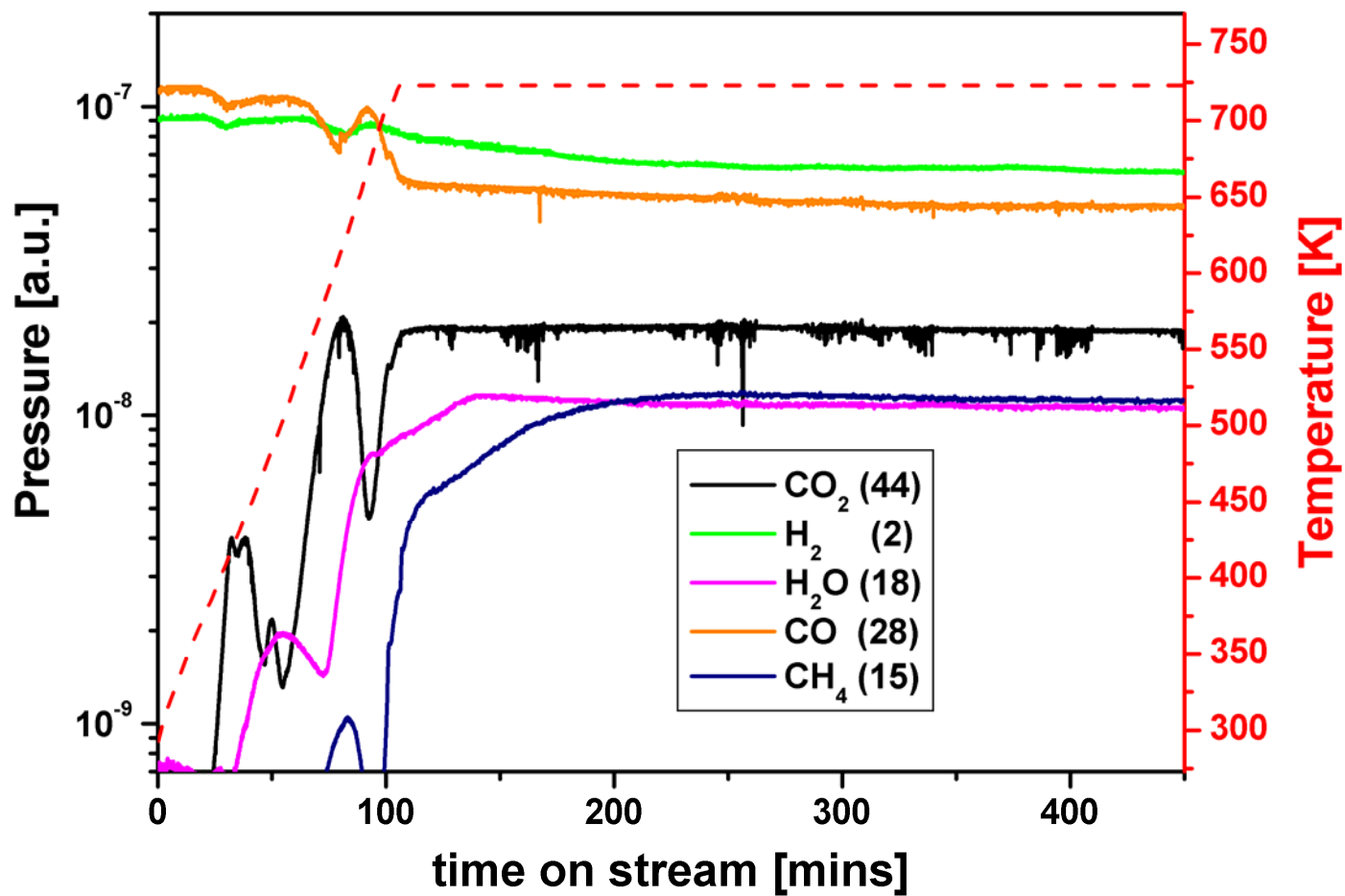


Figure 9.1.6: Reaction profile for a sample of Fe<sub>2</sub>O<sub>3</sub> reacted in a CO/H<sub>2</sub> mixture (2:1) at 723 K for 6 h (360 mins).

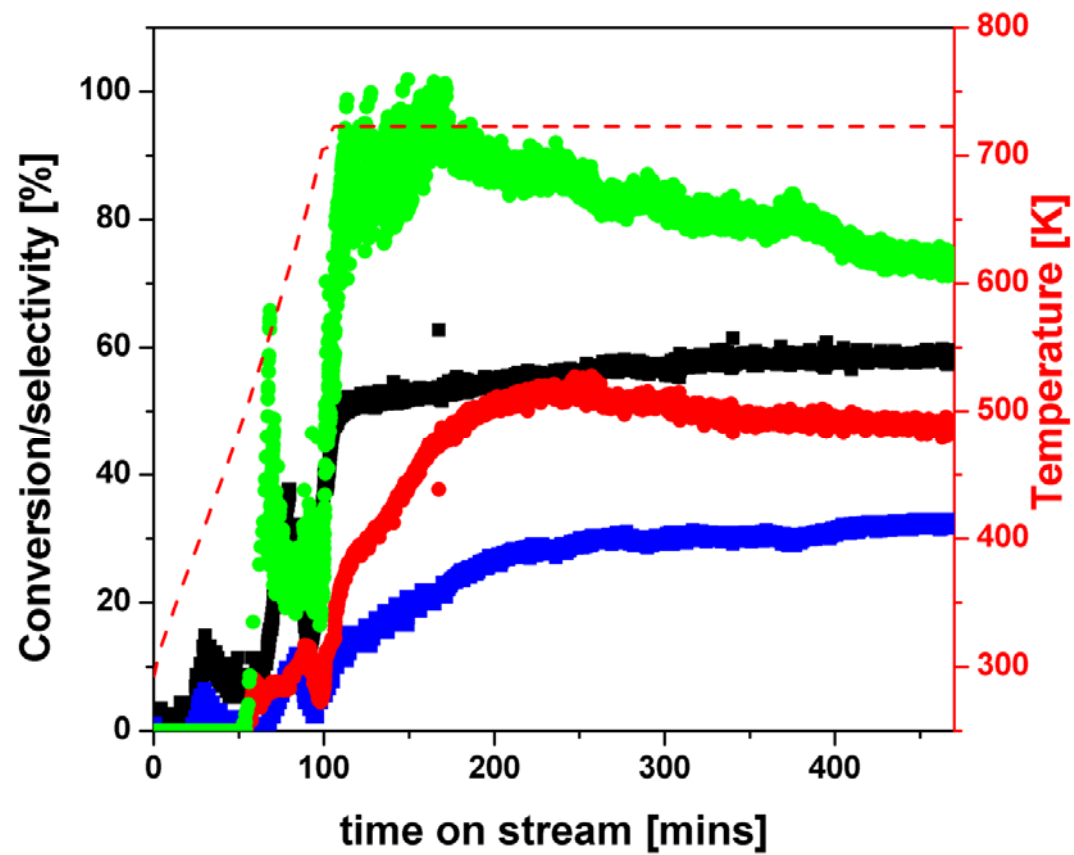


Figure 9.1.7: Conversion and selectivity profile for a CO hydrogenation over  $\text{Fe}_2\text{O}_3$  at 723 K for 6 h. (●=CO conversion, ●=H<sub>2</sub> conversion, and ● =CH<sub>4</sub> selectivity in CO, and ●=CH<sub>4</sub> selectivity in H<sub>2</sub>).

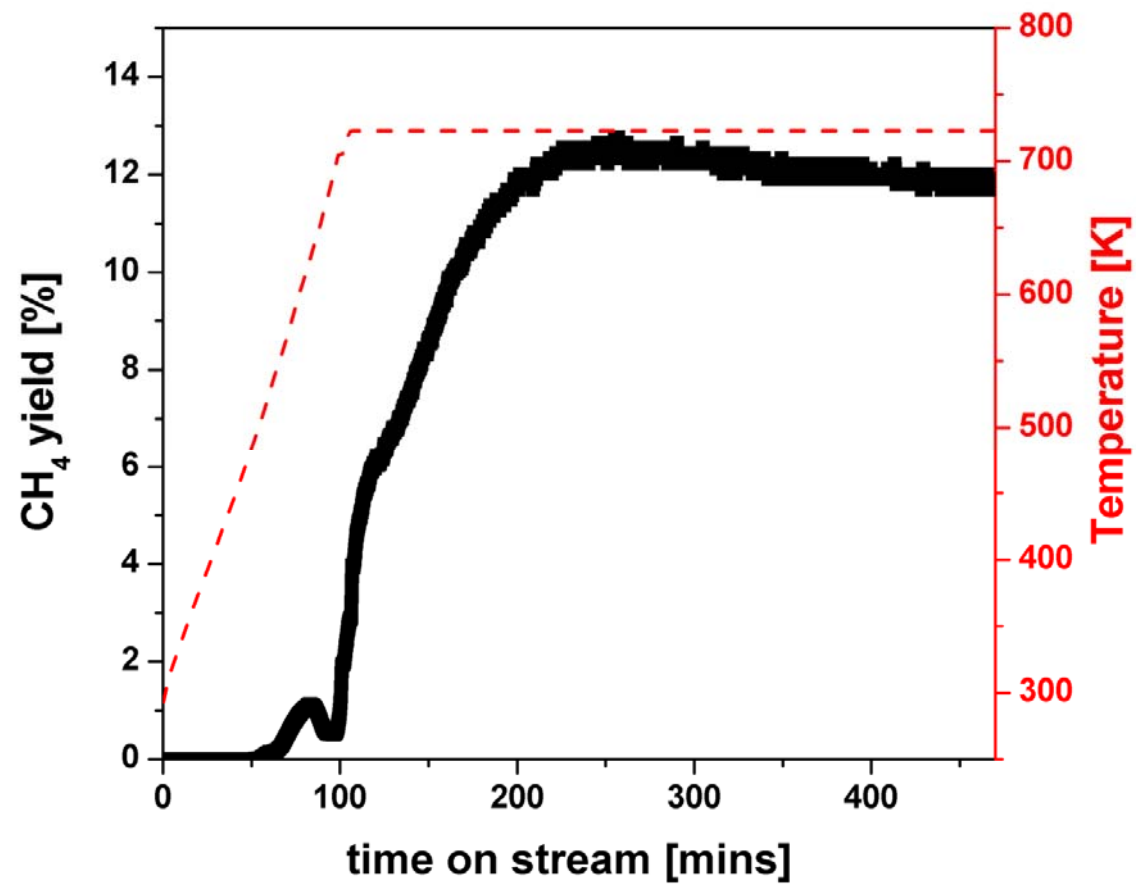


Figure 9.1.8: CH<sub>4</sub> yield as a function of H<sub>2</sub> conversion for CO hydrogenation over Fe<sub>2</sub>O<sub>3</sub> at 723 K.

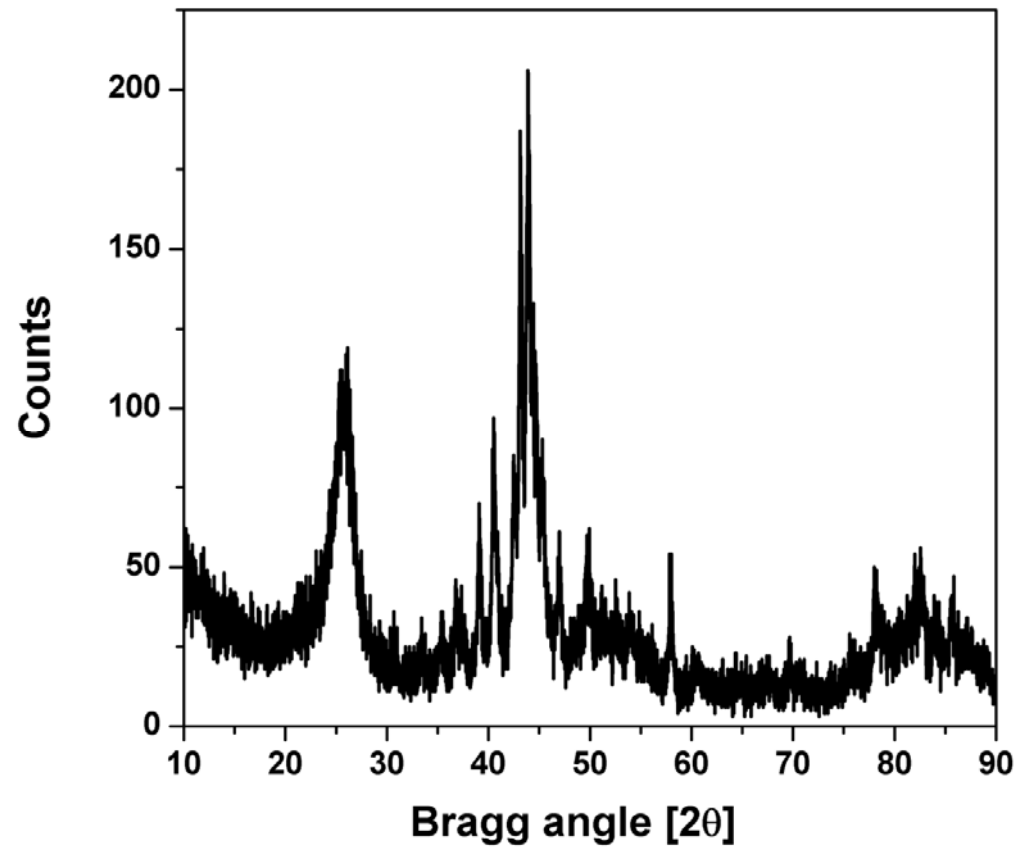


Figure 9.1.9: X-ray diffractogram of  $\text{Fe}_2\text{O}_3$  starting material after reaction in syngas at 723 K for 6 h.

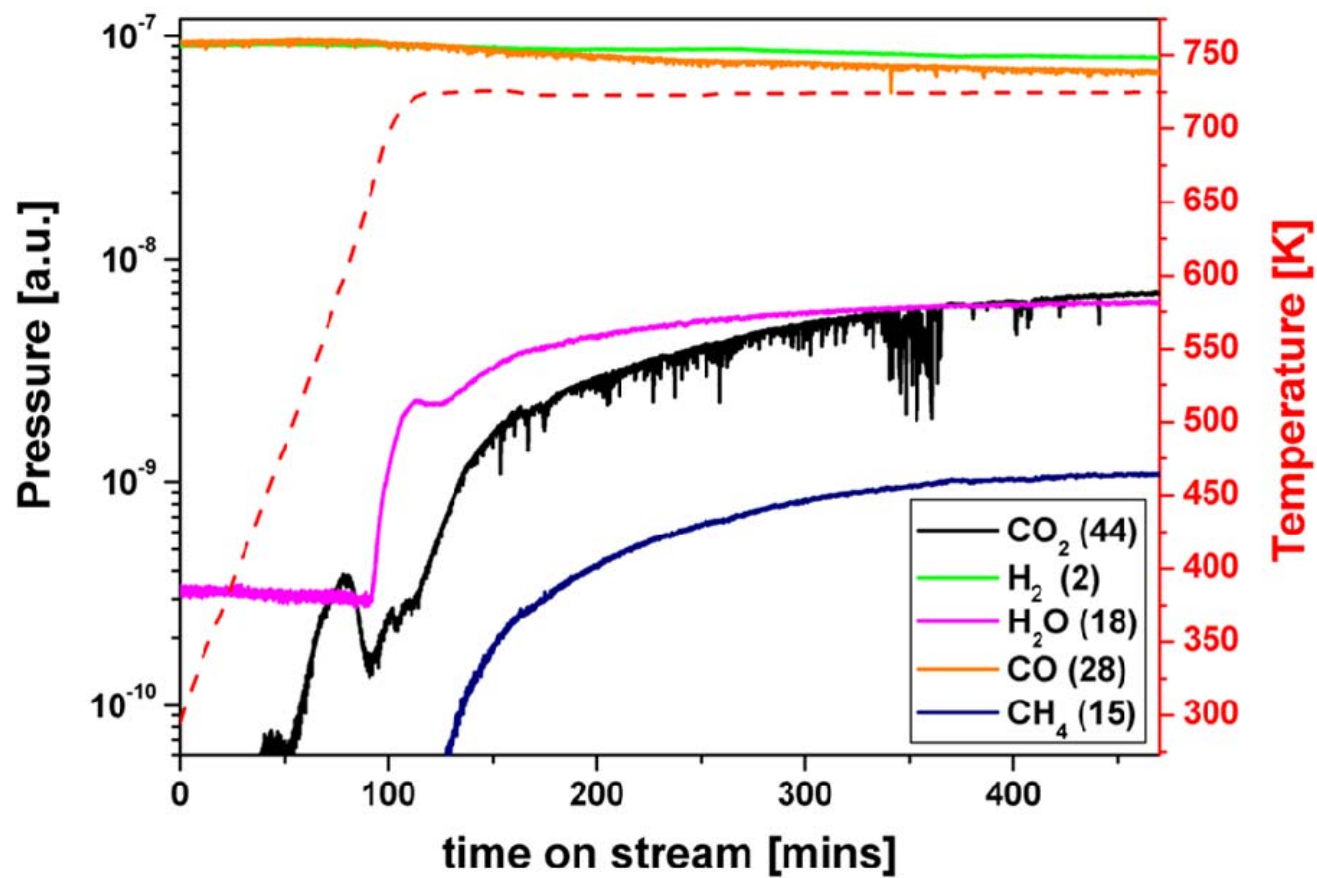


Figure 9.1.10: Reaction profile for a sample of Fe<sub>2</sub>O<sub>3</sub>, previously reduced in hydrogen at 773 K for 60 mins, exposed to a CO/H<sub>2</sub> mixture (2:1) at 723 K for 6 h.

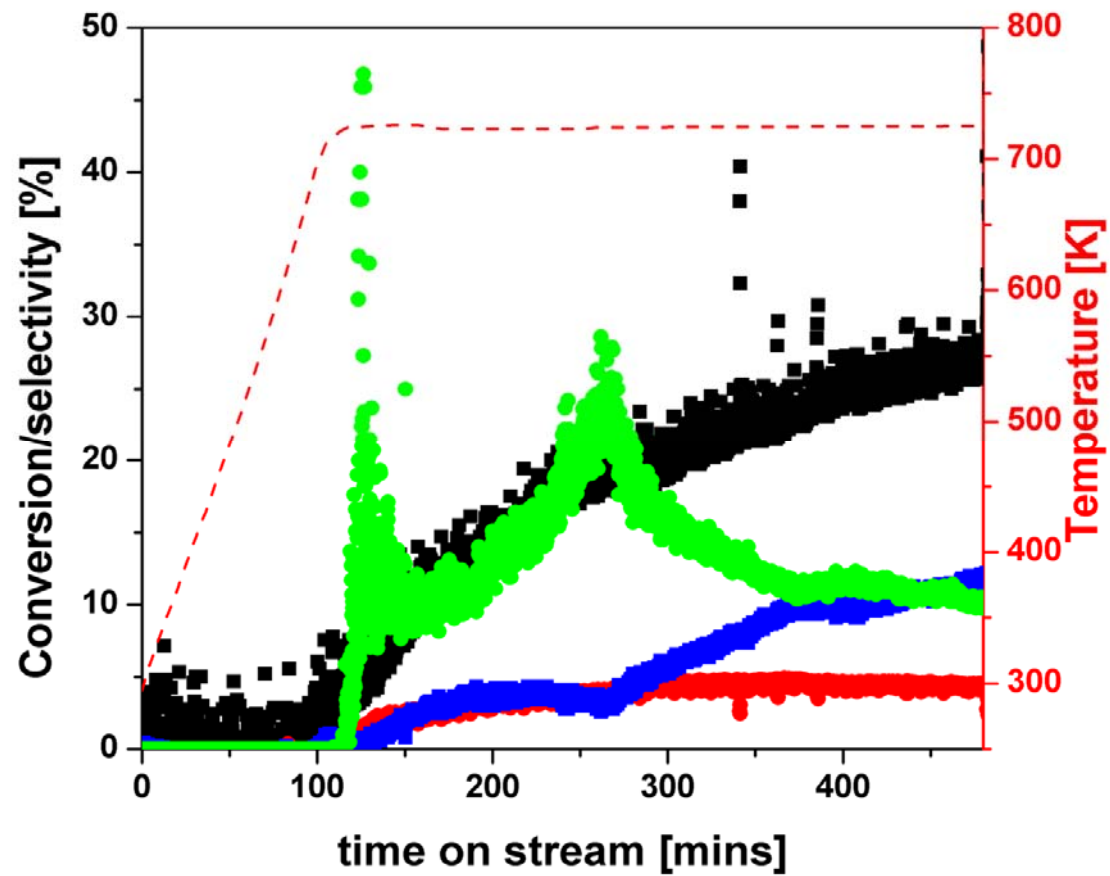


Figure 9.1.11: Conversion and selectivity profile for a sample of  $\text{Fe}_2\text{O}_3$ , previously reduced in hydrogen at 773 K for 60 mins, exposed to a  $\text{CO}/\text{H}_2$  mixture (2:1) at 723 K for 6 h (•=CO conversion, •= $\text{H}_2$  conversion, and •= $\text{CH}_4$  selectivity in CO, and •= $\text{CH}_4$  selectivity in  $\text{H}_2$ ).

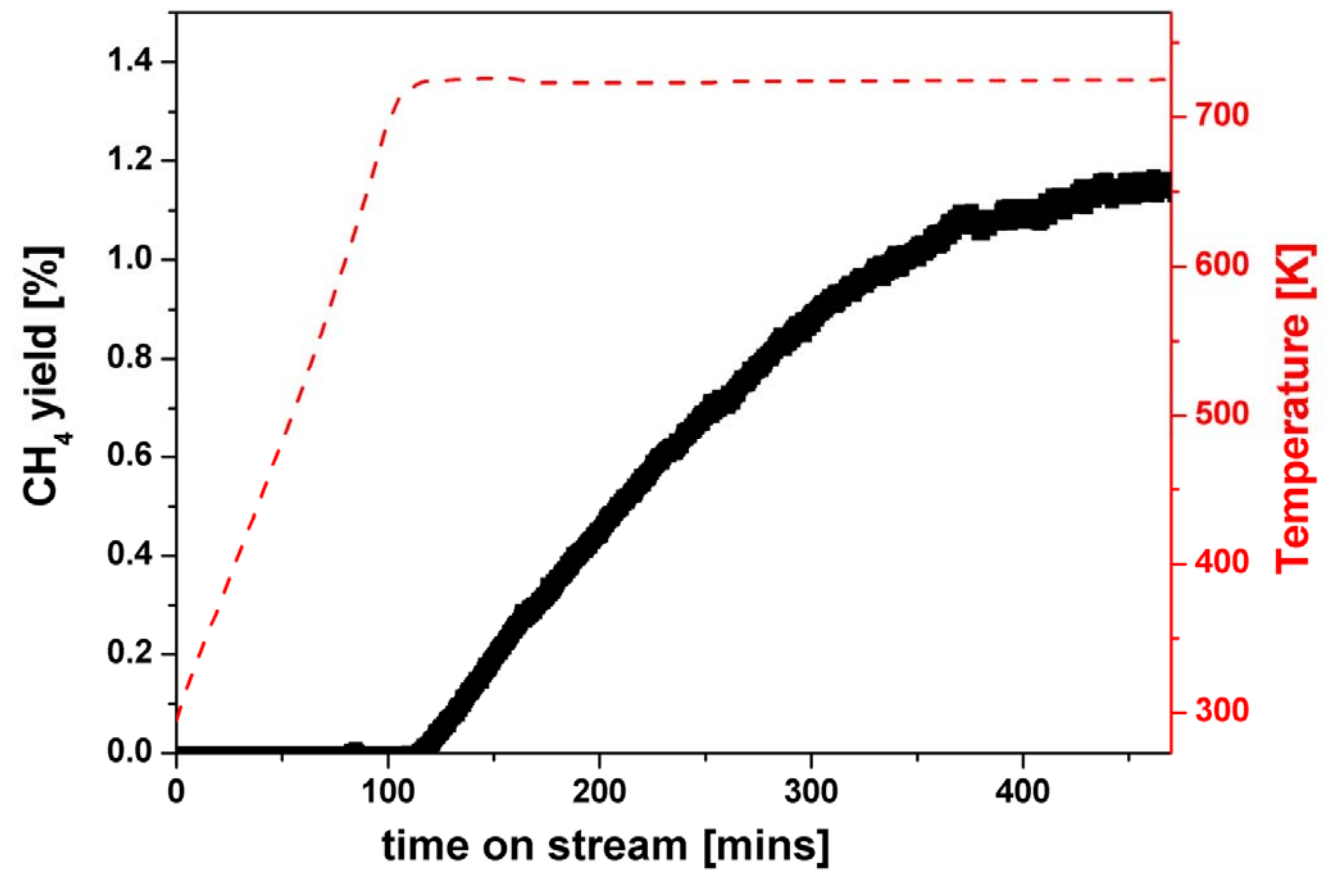


Figure 9.1.12: CH<sub>4</sub> yield as a function of H<sub>2</sub> conversion for a sample of Fe<sub>2</sub>O<sub>3</sub>, previously reduced in hydrogen at 773 K for 60 mins, exposed to a CO/H<sub>2</sub> mixture (2:1) at 723 K for 6 h.

## 9.2 Scale-up of microreactor studies

In order to produce a sufficient quantity of sample for the post-reaction analyses (particularly the INS measurements), the reactions had to be repeated using a much larger reactor as described in Section 2.7.2. The following sections described post-reaction analysis of samples prepared in the large-scale reactor.

## 9.3 X-ray diffraction (XRD)

X-ray diffraction was employed in order to determine the bulk composition of each of the post-reaction catalyst samples. The XRD patterns for the series of post-reaction catalysts are presented in Figures 9.3.1-9.3.4.

The pattern for the  $\text{Fe}_2\text{O}_3$  sample after exposure to syngas at 623 K is presented in Figure 9.3.1 and reveals the sample to be composed primarily of magnetite. The presence of a small quantity of metallic iron ( $\text{Fe}^0$ ) is indicated by the low intensity reflections located at Bragg angles of  $44.4^\circ$  and  $82.2^\circ$  (red asterisks). The sample was unavoidably exposed to air during the transfer from the glovebox to the diffractometer and some oxidation of the sample is presumed to occur. The proportion of metallic iron in the sample under reaction conditions is therefore likely to be higher than indicated in the post-reaction XRD pattern. Reduction of the catalyst in  $\text{H}_2$  at 773 K prior to syngas exposure also produced a catalyst composed predominantly by  $\text{Fe}_3\text{O}_4$  but with a greater relative proportion of metallic iron, as indicated by the XRD pattern for this sample, which is presented in Figure 9.3.2.

Increasing the reaction temperature to 723 K has a significant effect on the XRD pattern for the post-reaction samples. The XRD pattern for the  $\text{Fe}_2\text{O}_3$  sample after exposure to syngas at 723 K is presented in Figure 9.3.3 and shows this sample to contain a significant proportion of iron carbides as inferred by the manifold of reflections located in the Bragg angle range of  $42\text{-}45^\circ$ . Fierro *et al.* [158] reported a similar pattern to that observed here and assigned it to the presence of Hägg carbide ( $\chi\text{-Fe}_5\text{C}_2$ ). However, the diffraction patterns here are of insufficient resolution and signal:noise in order to make this assignment with absolute certainty. In common with the samples treated in syngas at 623 K a large proportion of magnetite is observed. The presence of a small proportion of metallic iron cannot be ruled out due to the presence of diffraction lines at  $44.4^\circ$  and  $82.2^\circ$ , however the fact that the  $44.4^\circ$  signal overlaps with the carbide manifold and the  $82.2^\circ$  feature is broad and of low signal:noise prevents this assertion to be made with absolute confidence.

In comparison to the XRD pattern of the sample after exposure to syngas at 723 K in the microreactor, this sample contains a much greater proportion of  $\text{Fe}_3\text{O}_4$ . This is possibly due to the much lower WHSV (weight hourly space velocity) employed here, which would lead to a greater partial pressure of water in the system that would promote oxidation of the catalyst. The microreactor sample also contained a broad reflection located at *ca.*  $22^\circ$  that was assigned to the presence of amorphous carbon, which is not observed in this post-reaction XRD pattern. The higher partial pressure of water assumed for this reactor configuration due to the lower WHSV employed could facilitate oxidation of deposited carbon, thereby removing it from the system.

The XRD pattern for the sample reduced in  $\text{H}_2$  at 773 K prior to syngas exposure at 723 K is presented in Figure 9.3.4 and contains approximately equal contributions from  $\text{Fe}_3\text{O}_4$  and iron carbide. Similar to the other post-reaction samples, the presence of metallic iron is inferred by the presence of diffraction lines located at  $44.4^\circ$  and  $82.2^\circ$ . The  $44.4^\circ$  signal overlaps with the carbide manifold but in this case the  $82.2^\circ$  signal is more apparent compared with previously presented samples. As mentioned in Section 8.5, assignment of iron carbides should be performed with care as  $\theta\text{-Fe}_3\text{C}$  and  $\chi\text{-Fe}_5\text{C}_2$  have very similar diffraction patterns. Nevertheless, the XRD pattern for the sample reduced in  $\text{H}_2$  prior to exposure to syngas, which contains the greatest proportion of carbide of all the samples, does represent an excellent fit to  $\chi\text{-Fe}_5\text{C}_2$ , as shown in the inset figure (Figure 9.3.4). Fierro *et al.* [158] suggest that  $\theta\text{-Fe}_3\text{C}$  supports so-called  $\text{C}_\alpha$  species, which lead to  $\text{CH}_4$  production, while  $\chi\text{-Fe}_5\text{C}_2$  supports so-called  $\text{C}_\beta$  species, which promote the formation of longer chain hydrocarbons. In this study, only methane was produced and the presence of  $\chi\text{-Fe}_5\text{C}_2$  was supported by post-reaction XRD analysis. This suggests that the  $\chi\text{-Fe}_5\text{C}_2$  can also stabilise  $\text{C}_\alpha$  species at atmospheric pressures. Schulz *et al.* [246] endorse the  $\chi\text{-Fe}_5\text{C}_2$  phase as being crucial to FTS activity. While the role of carbide species is still not completely understood density functional theory (DFT) calculations support the supposition that iron carbide species are more active in CO hydrogenation than metallic iron [247].

Collectively, the XRD patterns presented here indicate that iron carbide species are present in post-reaction samples previously treated in syngas at 723 K at atmospheric pressure. Reaction at this temperature produced significant quantities of methane as indicated by the microreactor reaction testing (Section 8.2). Little, if any, iron carbide species were observed for samples treated in syngas at 623 K. This observation is in agreement with

Shroff *et al.* [172] who could only observe carbide phases after an  $\text{Fe}_2\text{O}_3$  catalyst was exposed to syngas at 543 K for 2 h using *in situ* TEM and electron diffraction measurements. In contrast, powder XRD measurements showed no carbide phases, as is the case here. Interestingly, no detectable methane was produced under these reaction conditions, which indicates that the production of methane is accompanied by the development of iron carbide species. This behavior is also observed in studies performed at elevated pressures where the production of heavier hydrocarbons can be correlated with the generation of iron carbide species [170-174]. The catalyst that was previously reduced in  $\text{H}_2$  before exposure to syngas yielded the greatest relative proportion of iron carbide species. This observation is unsurprising as metallic iron is produced under both the reduction and reaction conditions that this particular sample was subjected to, and carbon is known to dissolve rapidly into metallic iron to yield carbide species [170, 171, 248].

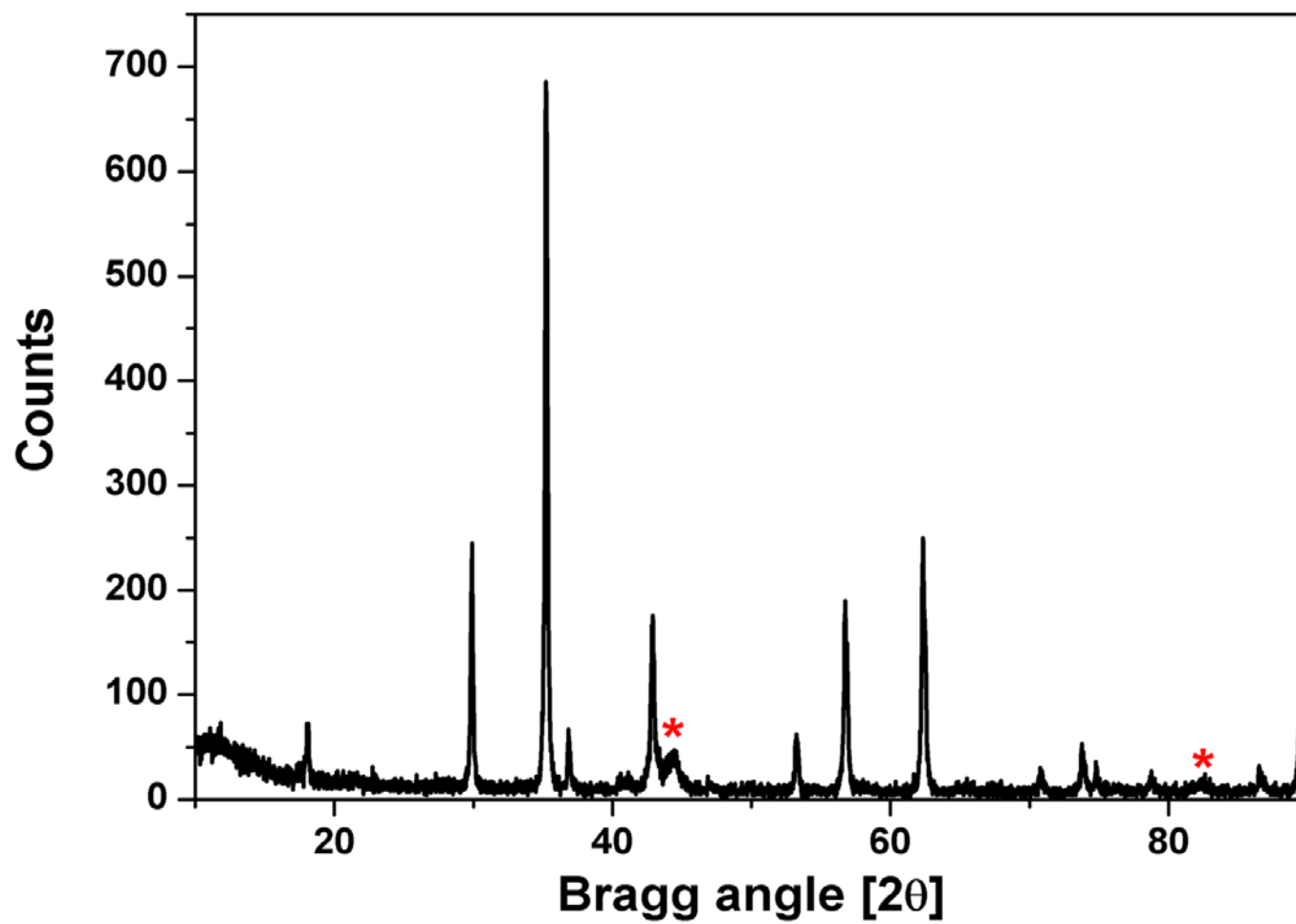


Figure 9.3.1: XRD pattern for post-reaction sample of  $\text{Fe}_2\text{O}_3$  exposed to syngas at 623 K for 6 h.

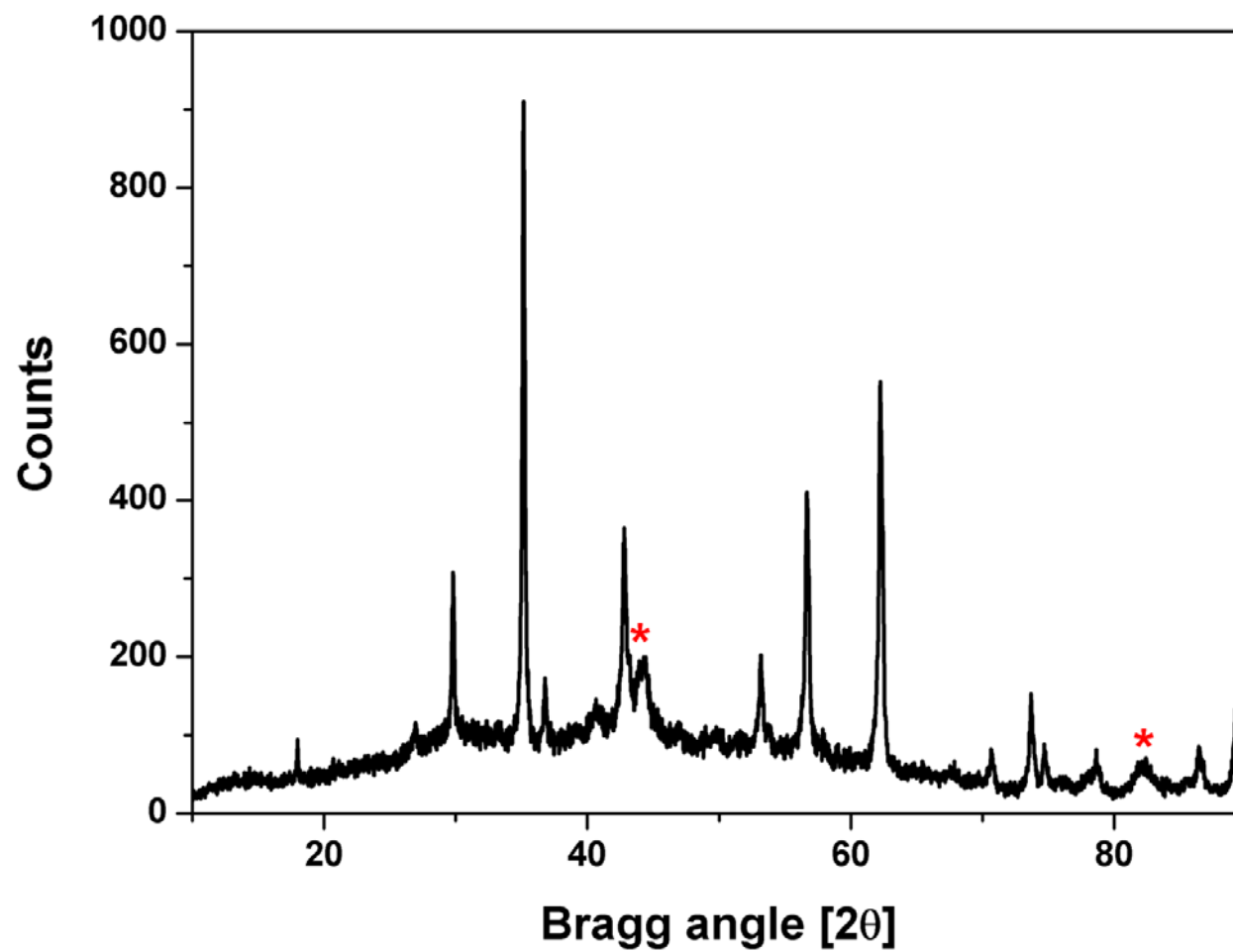


Figure 9.3.2: XRD pattern for post-reaction sample of  $\text{Fe}_2\text{O}_3$ , previously reduced in  $\text{H}_2$  at 773 K, exposed to syngas at 623 K for 6 h.

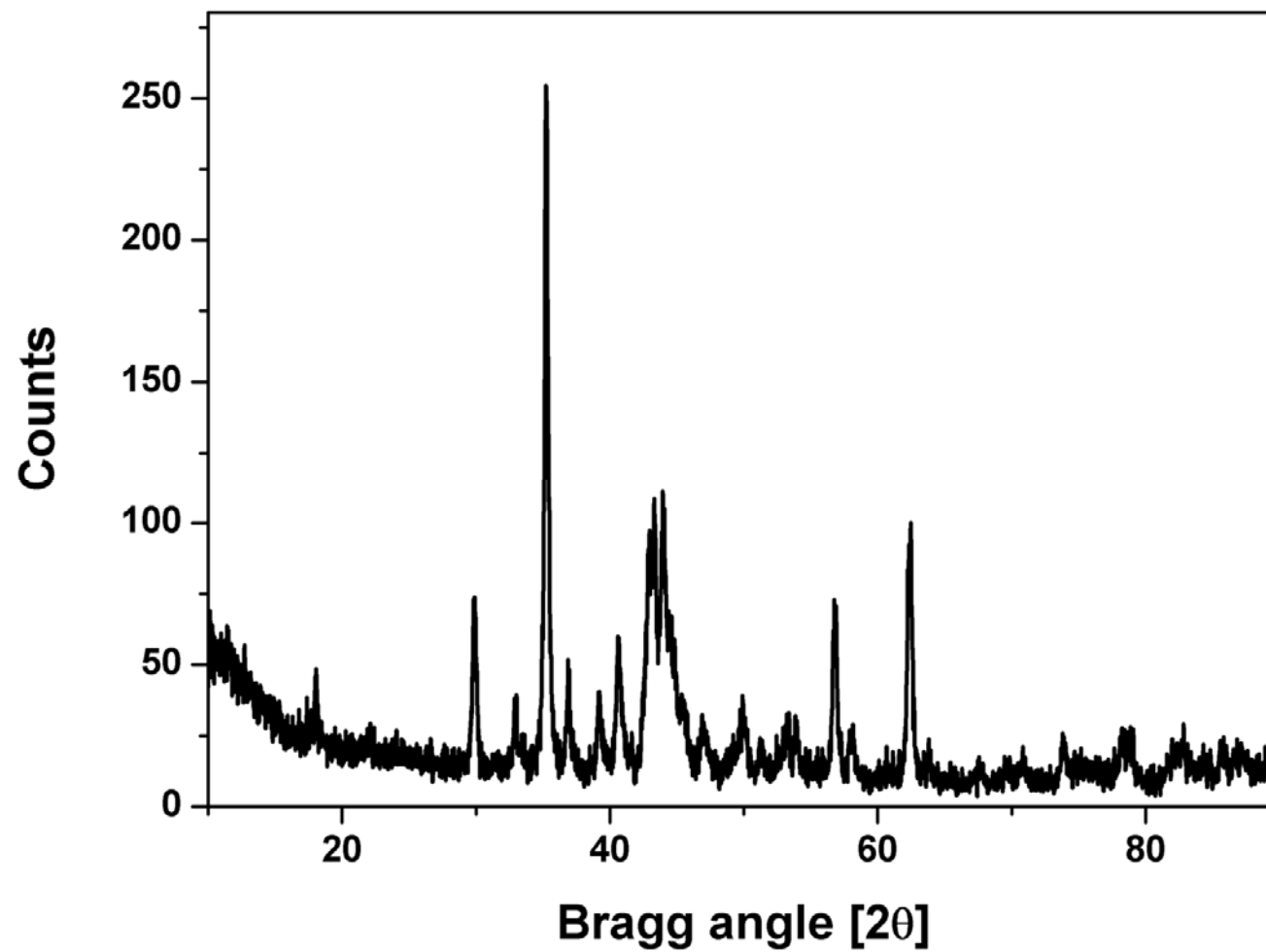


Figure 9.3.3: XRD pattern for post-reaction sample of  $\text{Fe}_2\text{O}_3$  exposed to syngas at 723 K for 6h.

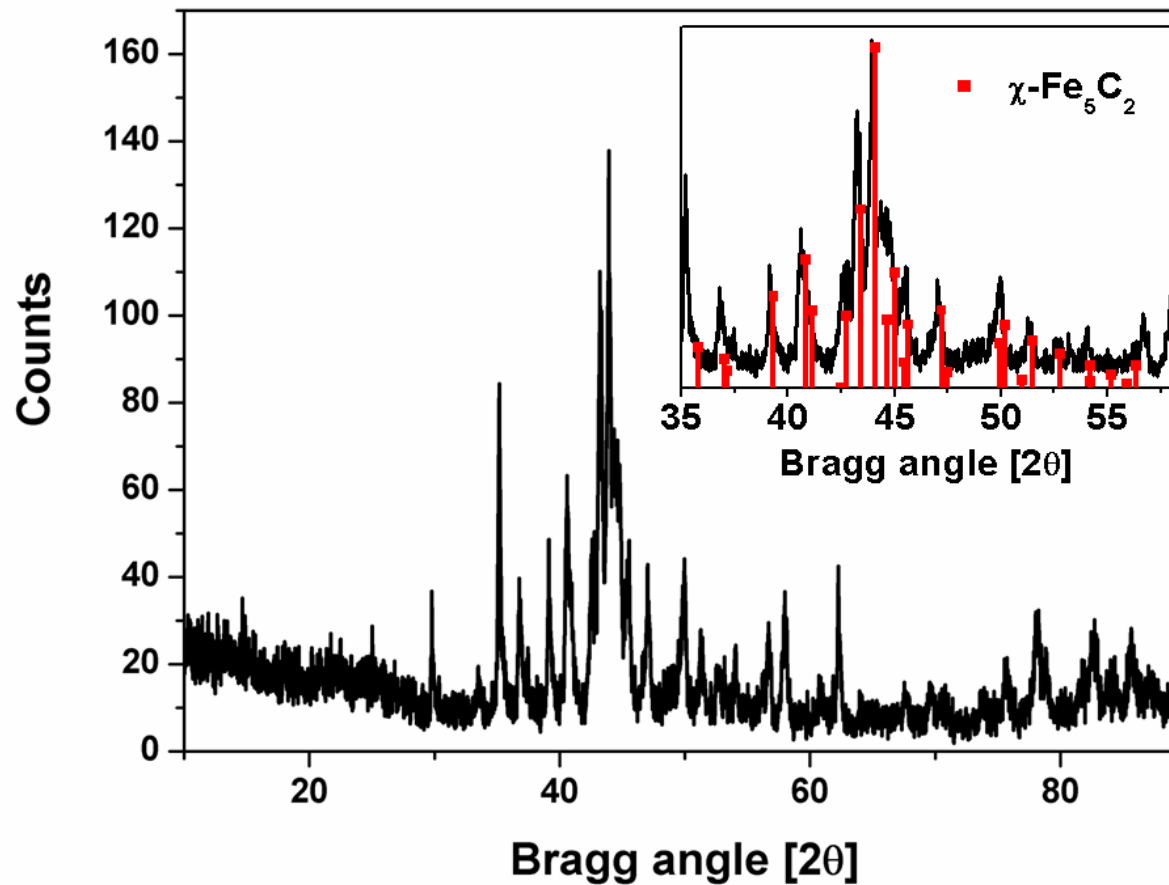


Figure 9.3.4: XRD pattern for post-reaction sample of Fe<sub>2</sub>O<sub>3</sub>, previously reduced in H<sub>2</sub> at 773 K, exposed to syngas at 723 K for 6h. The inset figure shows the favourable fit of the sample to the database pattern for Hägg carbide ( $\chi$ -Fe<sub>5</sub>C<sub>2</sub>, ICSD-89328).

## 9.4 Infrared and Raman vibrational spectroscopy

Infrared and Raman spectra were recorded for the catalyst samples that had been treated in syngas at 723 K, which, according to the microreactor studies presented in Section 9.1, produced the greatest methane yield.

The infrared spectrum of the post-reaction catalyst is presented in Figure 9.4.1 and, like the infrared spectra of the industrial catalyst fines presented in Section 8.1, is characterized by a sloping background with several superimposed vibrational bands. A broad  $\nu_{\text{OH}}$  feature is seen at *ca.*  $3600\text{ cm}^{-1}$ , whilst  $\nu_{\text{CH}}$  bands are observed at 2855, 2930, and  $2958\text{ cm}^{-1}$ . These energies indicate the presence of aliphatic moieties, which is in agreement with the infrared studies of the SASOL catalyst fines samples (Fig. 8.1.1), but in contrast to the INS spectrum of that material (Fig. 8.3.1). A weak feature is observed at *ca.*  $1660\text{ cm}^{-1}$  that can be attributed to the in-plane deformation of water ( $\delta_{\text{OH}}$ ). Collectively, Figure 9.4.1 indicates the surface to be composed of an aliphatic hydrocarbonaceous overlayer and hydroxyl groups. The small  $\delta_{\text{OH}}$  feature indicates an additional presence of a small quantity of water. Further analysis of this spectrum is hindered by the very strong absorption of infrared radiation by the sample.

The Raman scattering spectrum of the sample is presented in Figure 9.4.2 and, in similarity to the industrial catalyst fines samples, is dominated by the so called D and G bands located at  $1340\text{ cm}^{-1}$  and  $1603\text{ cm}^{-1}$ , respectively. This observation suggests that a common polycyclic aromatic hydrocarbon species with a relatively low hydrogen content could be present on both the industrial catalyst fines samples, which have been exposed to real Fischer-Tropsch synthesis conditions over an extended period of time, and on the samples considered here, which had merely been exposed to syngas at 723 K at atmospheric pressure for a comparatively short period of time. The band located at  $664\text{ cm}^{-1}$  is assigned to an  $E_{\text{u}}$  mode associated with the magnetite component of the sample. The sharp spike located at  $1553\text{ cm}^{-1}$  is attributed to the  $\nu_{\text{O}=\text{O}}$  stretching mode of atmospheric oxygen [249].

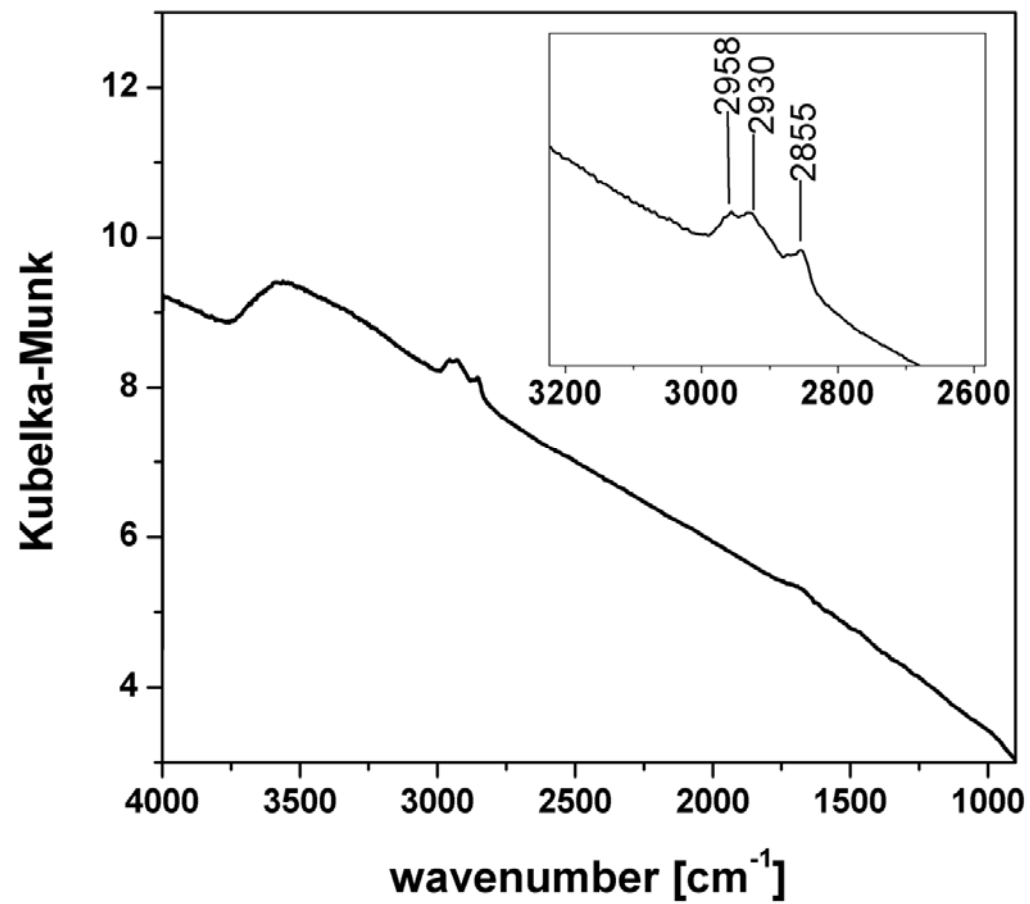


Figure 9.4.1: Diffuse reflectance infrared spectrum of post-reaction catalyst after reaction in syngas at 723 K for 6 h. The C-H stretching region is expanded in the inset figure.

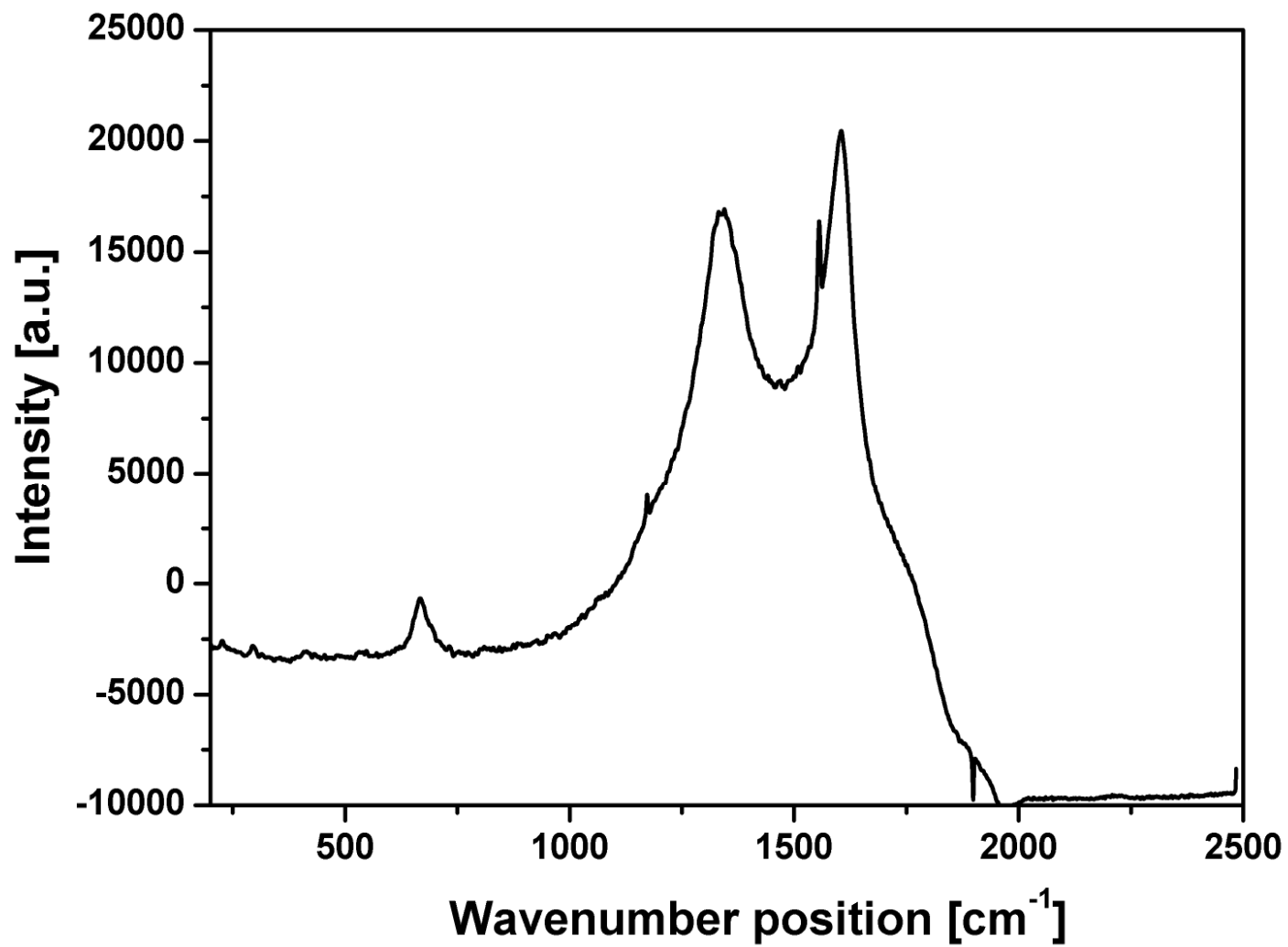


Figure 9.4.2: Raman spectrum of post-reaction catalyst after reaction in syngas at 723 K for 6 h.

## 9.5 Inelastic neutron scattering (INS) spectroscopy

Infrared spectroscopic analysis of a post-reaction sample of the catalyst has been shown to be of limited worth due to the prohibitively large absorption presented by the high opacity of the post-reaction catalyst samples. In order to address this issue, INS spectroscopy, which is not hindered by highly absorbing samples, was applied in order to acquire the vibrational spectrum of the post reaction catalyst samples. This pursuit was initially hindered due to the requirement of large quantities of sample needed to successfully collect INS spectra of overlayers present on heterogeneous catalysts [14]. This requirement is especially pertinent for materials that contain a low proportion of hydrogen, which Raman spectroscopic measurements have shown to be the case for the post-reaction catalyst samples considered here.

The TOSCA INS spectrometer was initially selected as the instrument of choice for acquisition of the vibrational spectra of the post-reaction catalyst samples due to its ability to access a wide dynamic range ( $5\text{-}4000\text{ cm}^{-1}$ ) with relatively high resolution (*ca.*  $20\text{ cm}^{-1}$ ) in the energy range  $0\text{-}2000\text{ cm}^{-1}$ . The INS spectrum of the  $\text{Fe}_2\text{O}_3$  starting material, as recorded using TOSCA, is presented in Figure 9.5.1, and exhibits several sharp and intense signals located at energies below *ca.*  $900\text{ cm}^{-1}$ , which are attributed to various Fe-O phonon modes [250]. A band located at *ca.*  $3500\text{ cm}^{-1}$  is assigned to the  $\nu_{\text{OH}}$  of hydroxyl groups on the surface of the  $\text{Fe}_2\text{O}_3$ . The INS spectrum for the material after exposure to syngas at 723 K for a period of 6h is presented in Figure 9.5.2, and in comparison to the spectrum of the  $\text{Fe}_2\text{O}_3$  before exposure to syngas is relatively featureless and noisy, which suggests that the hydrogen content is insufficient for the acquisition of a usable INS spectrum. Though very noisy, there appears to be a weak signal located at *ca.*  $3000\text{ cm}^{-1}$ , which indicates that a small proportion of hydrocarbonaceous material may be present on the post-reaction catalyst sample. In contrast, the INS spectra of the post-reaction industrial catalyst fines samples (Figures 8.3.1 and 8.3.2) are very well defined with obvious contributions from polyaromatic hydrocarbonaceous species dominating the spectra. This indicates that the catalysts exposed to real Fischer-Tropsch conditions, *i.e.* the SASOL catalyst fines, contain a comparatively greater content of hydrogenous species than the samples investigated here, which were exposed to syngas at atmospheric pressure.

Clearly, the hydrogen content of the overlayer present on the catalysts after reaction in syngas at atmospheric pressure is insufficient to acquire a useful spectrum from the TOSCA spectrometer. In order to surmount this issue, the MAPS spectrometer, which

offers vastly superior sensitivity (at the expense of resolution and ease of use), was employed to acquire the INS spectra of the entire suite of post-reaction catalyst samples. MAPS, a direct geometry chopper instrument, has a resolution of approximately 1-2% of the incident neutron energy employed. So, in order to sample the entire dynamic range of interest, *i.e.* 0-4000  $\text{cm}^{-1}$ , spectra were acquired using two different incident energies: 4840  $\text{cm}^{-1}$  (600 meV) in order to observe  $\nu_{\text{CH}}$  modes; and 2017  $\text{cm}^{-1}$  (250 meV) in order to observe lower energy deformational modes with improved resolution.

The INS spectra of the  $\text{Fe}_2\text{O}_3$  starting material, as recorded using the MAPS spectrometer with incident neutron energies of 4840  $\text{cm}^{-1}$  and 2017  $\text{cm}^{-1}$  are presented in Figures 9.5.3 and 9.5.4, respectively. In both figures the spectrum of  $\text{Fe}_2\text{O}_3$  as recorded using the TOSCA instrument has been overlaid and demonstrates good correlation in the energy position of the vibrational features of each spectrum, however the superior resolution of TOSCA at energies below 1000  $\text{cm}^{-1}$  is clearly evident. The difference in relative intensity of some of the features is due to the different momentum transfer,  $Q$ , values that are used to produce each INS spectrum. High energy features observed using TOSCA are dominated by modes that scatter at high  $Q$  values, *e.g.* phonon modes, whereas the low energy region is dominated by fundamental modes [14, 19], *e.g.* CH deformations. All of the spectra acquired using the MAPS instrument were processed using only data collected from low angle detector banks, *i.e.* low  $Q$ , which therefore minimises contributions from phonon modes.

The INS spectra for the  $\text{Fe}_2\text{O}_3$  sample after treatment in syngas at 623 K, recorded at 4840  $\text{cm}^{-1}$  and 2017  $\text{cm}^{-1}$ , are presented in Figures 9.5.5 and 9.5.6, respectively. The band observed at 3630  $\text{cm}^{-1}$  is attributed to the  $\nu_{\text{OH}}$  mode of residual hydroxyl groups located on the surface of the magnetite component of the sample. The feature located at 2955  $\text{cm}^{-1}$  is attributed to the  $\nu_{\text{CH}}$  mode of deposited hydrocarbonaceous material. The energy position of this band indicates the presence of aliphatic material, however the broadness of the band, coupled with the low resolution of the spectrometer at this incident energy, means that the presence of olefinic hydrocarbonaceous material cannot be ruled out. The band observed at *ca.* 950  $\text{cm}^{-1}$  is assigned to the in plane deformation of hydroxyl groups ( $\delta_{\text{OH}}$ ) associated with the magnetite component. Finally, the intense band located at *ca.* 600  $\text{cm}^{-1}$  is attributed to a combination of  $A_{1g}$  Fe-O phonon modes associated with the magnetite component [251]. A very weak feature is observed at *ca.* 1465  $\text{cm}^{-1}$ , which could be associated with deformation mode of hydrocarbonaceous species. In particular, the  $\text{CH}_2$

scissors deformation of cycloalkane species are known to occur at this energy [225].

The INS spectra for the catalyst sample that was reduced in H<sub>2</sub> prior to syngas exposure at 623 K, recorded with incident energies of 4840 cm<sup>-1</sup> and 2017 cm<sup>-1</sup>, are presented in Figures 9.5.7 and 9.5.8, respectively. In similarity to the sample that had not been previously reduced prior to syngas exposure (Figures 9.5.5 and 9.5.6), vibrational features are observed at 3630 cm<sup>-1</sup> and 950 cm<sup>-1</sup>, which are respectively assigned to the  $\nu_{\text{OH}}$  and  $\delta_{\text{OH}}$  modes of the magnetite component, albeit with significantly lower intensity. Reduction of the catalyst sample prior to syngas exposure is expected to result in a greater proportion of metallic iron and therefore less magnetite in the post-reaction sample, hence the relatively low intensity of the hydroxyl features in these spectra. A band is also observed at *ca.* 600 cm<sup>-1</sup>, which is assigned to Fe-O phonon modes [250]. As with the hydroxyl bands located at 3630 cm<sup>-1</sup> and 950 cm<sup>-1</sup>, this band is of lower intensity compared with that observed in Figure 9.5.6 due to the lower proportion of magnetite in the sample. Finally, the band located at 2955 cm<sup>-1</sup> indicates the presence of hydrocarbonaceous material of a similar character to that observed for the sample that was not reduced prior to syngas exposure.

Figures 9.5.9 and 9.5.10 present the INS spectra for the catalyst sample exposed to syngas at 723 K, recorded with incident energies of 4840 cm<sup>-1</sup> and 2017 cm<sup>-1</sup>, respectively. In Figure 9.5.9 the spectrum is dominated by a complex band observed in the energy range 2800-3800 cm<sup>-1</sup>, with maxima located at 3035 cm<sup>-1</sup>, 3360 cm<sup>-1</sup>, and 3590 cm<sup>-1</sup>. The features located at 3360 cm<sup>-1</sup> and 3590 cm<sup>-1</sup> are respectively assigned to  $\nu_{\text{OH}}$  stretching modes of bridging and terminal hydroxyl groups associated with the magnetite component. The energy position of the signal located at 3035 cm<sup>-1</sup> indicates the presence of a  $\nu_{\text{CH}}$  stretch associated with an olefinic hydrocarbonaceous residue. However, as with the samples treated in syngas at 623 K, the band is broad and, coupled with the low resolution of the spectrometer at this incident energy, the presence of aliphatic material therefore cannot be discounted. Figure 9.5.10 shows the INS spectrum in the energy range 400-1600 cm<sup>-1</sup> and contains multiple vibrational features. The most intense band is observed at *ca.* 600 cm<sup>-1</sup> and is assigned to the A<sub>1g</sub> mode of Fe<sub>3</sub>O<sub>4</sub>. However, in contrast to the spectra of the catalyst samples exposed to syngas at 623 K, this band is unsymmetrical and may contain a contribution from deformation modes known to occur in this energy region, *i.e.* *cis*-CH wag or skeletal deformation [225], associated with the hydrocarbonaceous overlayer. The band located at *ca.* 950 cm<sup>-1</sup> is assigned to the in-plane deformation ( $\delta_{\text{OH}}$ ) of

hydroxyl groups associated with the magnetite component. The other features observed in this spectrum are assigned to other vibrational modes associated with the hydrocarbonaceous overlayer. The signals located at  $760\text{ cm}^{-1}$  and  $787\text{ cm}^{-1}$  are assigned to out-of-plane CH wag deformations ( $\gamma_{\text{CH}}$ ). The signals at  $1447\text{ cm}^{-1}$  and  $1542\text{ cm}^{-1}$  have been a source of much controversy in the literature [252-254]. However, here, based on the recent work of Albers *et al.* [15], they are tentatively assigned to semi-circle ring deformation modes, possibly coupled with a  $\delta_{\text{CH}}$  mode, associated with perimeter carbons of an extended polycyclic aromatic network [15]. The signal located at  $1380\text{ cm}^{-1}$  is assigned to an in-plane ring deformation and agrees approximately with that observed for naphthalene [255]. Finally, the signal observed at  $1160\text{ cm}^{-1}$  is broadly assigned to an in-plane CH deformation ( $\delta_{\text{CH}}$ ) mode.

The INS spectra for the catalyst that was reduced in  $\text{H}_2$  prior to syngas exposure at 723 K are presented in Figures 9.5.11 and 9.5.12. In Figure 9.5.11 the spectrum is dominated by a band located at  $3035\text{ cm}^{-1}$ . The pre-treatment in hydrogen is deemed to have removed the vast majority of magnetite from the system as there is no intensity observed in the range  $3300\text{-}3600\text{ cm}^{-1}$ , where the  $\nu_{\text{OH}}$  of surface hydroxyl groups would be expected to occur. Figure 9.5.12 presents the spectrum recorded with an incident energy of  $2017\text{ cm}^{-1}$  and is qualitatively very similar to the spectrum of the catalyst exposed to syngas at 723 K without prior reduction in  $\text{H}_2$  (Fig. 9.5.10) with the exception that bands associated with a magnetite component are significantly attenuated, *e.g.* the Fe-O phonon located at  $600\text{ cm}^{-1}$  and the  $\delta_{\text{OH}}$  mode located at *ca.*  $950\text{ cm}^{-1}$ . In similarity to the spectrum of the catalyst treated at 723 K without reduction in  $\text{H}_2$ , bands attributed to CH deformations are observed at  $1160\text{ cm}^{-1}$  and  $1447\text{ cm}^{-1}$  but with a comparatively greater relative intensity. In addition, a relatively intense signal is observed at *ca.*  $865\text{ cm}^{-1}$ , which is tentatively assigned to the CH wag deformation ( $\gamma_{\text{CH}}$ ) mode. It is presumed that this signal was obscured by the  $\delta_{\text{OH}}$  signal in the sample that was not reduced prior to syngas exposure at 723 K. Erley *et al.* [209] observed similar signals for Fe(110) single crystals subjected to syngas at atmospheric pressure. Specifically, they quenched the reaction of syngas over the single crystal when a high methane production rate had been attained and measured the electron energy loss (EELS) spectrum of the sample. Two well-resolved features located at  $3010\text{ cm}^{-1}$  and  $3100\text{ cm}^{-1}$  were observed, which were assigned to the  $\nu_{\text{CH}}$  modes of adsorbed hydrocarbons. Features located at  $870\text{ cm}^{-1}$  and  $1420\text{ cm}^{-1}$ , which were assigned to bending deformation modes, were observed. They also observed a band located at  $1190\text{ cm}^{-1}$  that was tentatively assigned to the possible existence of  $\text{C}_2$  surface species.

Alkyl groups containing multiple  $-\text{[CH}_2\text{]}_n-$  moieties couple in-phase giving rise to intense and predictable INS signals typically located at  $\sim 720\text{ cm}^{-1}$  and  $\sim 1300\text{ cm}^{-1}$ , respectively assigned to  $\text{CH}_2$  rock and  $\text{CH}_2$  twist deformations. Such signals are observed in the INS spectra of hexane [227], heptane [227], octane [227], cyclohexane [256], cyclooctane [256]. No such intense signals are observed in any of the spectra presented here, which, given the energy position of the  $\nu_{\text{CH}}$  band at  $3035\text{ cm}^{-1}$ , supports the proposal that the hydrocarbonaceous layer deposited on these iron catalysts after exposure to syngas at 723 K can be defined by an extended polycyclic aromatic hydrocarbonaceous residue.

An overlaid comparison of the TOSCA spectrum of a sample of the toluene extracted catalyst fines taken from a fluidized bed FTS reactor with the MAPS spectrum of a sample of  $\text{Fe}_2\text{O}_3$  reduced in  $\text{H}_2$  followed by exposure to syngas at 723 K, recorded with an incident neutron energy of  $4840\text{ cm}^{-1}$  and  $2017\text{ cm}^{-1}$ , is presented in Figures 9.5.13 and 9.5.14, respectively. Interestingly, there are a number of vibrational features common to both spectra, despite the very different reaction conditions that each of the samples have been exposed to. For example, the  $\nu_{\text{CH}}$  stretching band, observed in Figure 9.5.13, exhibits reasonable overlap between the two spectra with the exception that the TOSCA spectrum of the catalyst fines sample (red trace) exhibits additional intensity in the aliphatic  $\nu_{\text{CH}}$  region that is not represented in the MAPS spectrum of the syngas treated sample (black trace). In Figure 9.5.14 common features are located at energies of *ca.*  $1450\text{ cm}^{-1}$ , *ca.*  $1200\text{ cm}^{-1}$ , and *ca.*  $850\text{ cm}^{-1}$ , which are assigned to CH deformation modes. In addition, a band located at  $950\text{ cm}^{-1}$ , assigned to the in plane deformation of surface hydroxyl groups ( $\delta_{\text{OH}}$ ) associated with a magnetite component, is also common to both spectra. This indicates that polycyclic aromatic hydrocarbon species that are deposited on an unsupported iron catalyst during syngas exposure at 723 K under atmospheric pressure (a treatment which is often used to activate iron catalysts prior to industrial FTS [156]) are also present in industrial fused iron catalysts that have undergone extended exposure to FTS conditions. Under FTS conditions this polycyclic aromatic species appears to become more abundant and more ordered as indicated by the comparatively well-defined INS spectrum that the post-reaction industrial catalyst fines exhibit on the relatively insensitive TOSCA instrument. This is reasonable and reflects the anticipated greater hydrocarbon retention of the industrial catalyst fines samples.

The INS spectra presented above have revealed insight as to the nature of the hydrocarbonaceous deposits formed on the surface of an unsupported iron-based catalyst subjected to carbon monoxide methanation reactions that has not been previously reported using traditional forms of vibrational spectroscopy. Here, it was possible to make tentative assignments of various vibrational bands that are native to the hydrocarbonaceous overlayer. Previous studies into carbon monoxide methanation at atmospheric pressure have used a combination of Auger electron spectroscopy (AES) and X-ray photoelectron spectroscopy (XPS) to identify several carbonaceous species present on the surface of a Fe(110) single crystal [191]. One of these carbonaceous species was proposed to correspond to a heavily hydrogenated carbidic carbon, referred to as a  $\text{CH}_x$  species, and was suggested to be an important phase in the methanation reaction. The  $\text{CH}_x$  species was proposed to contain mainly CH groups although the presence of  $\text{CH}_2$  and  $\text{CH}_3$  could not be discounted and no further characterization was possible. The INS spectra presented here have shown the strength of the INS technique in aiding the identification of such hydrogenated hydrocarbonaceous overlayers present on real polycrystalline unsupported catalysts.

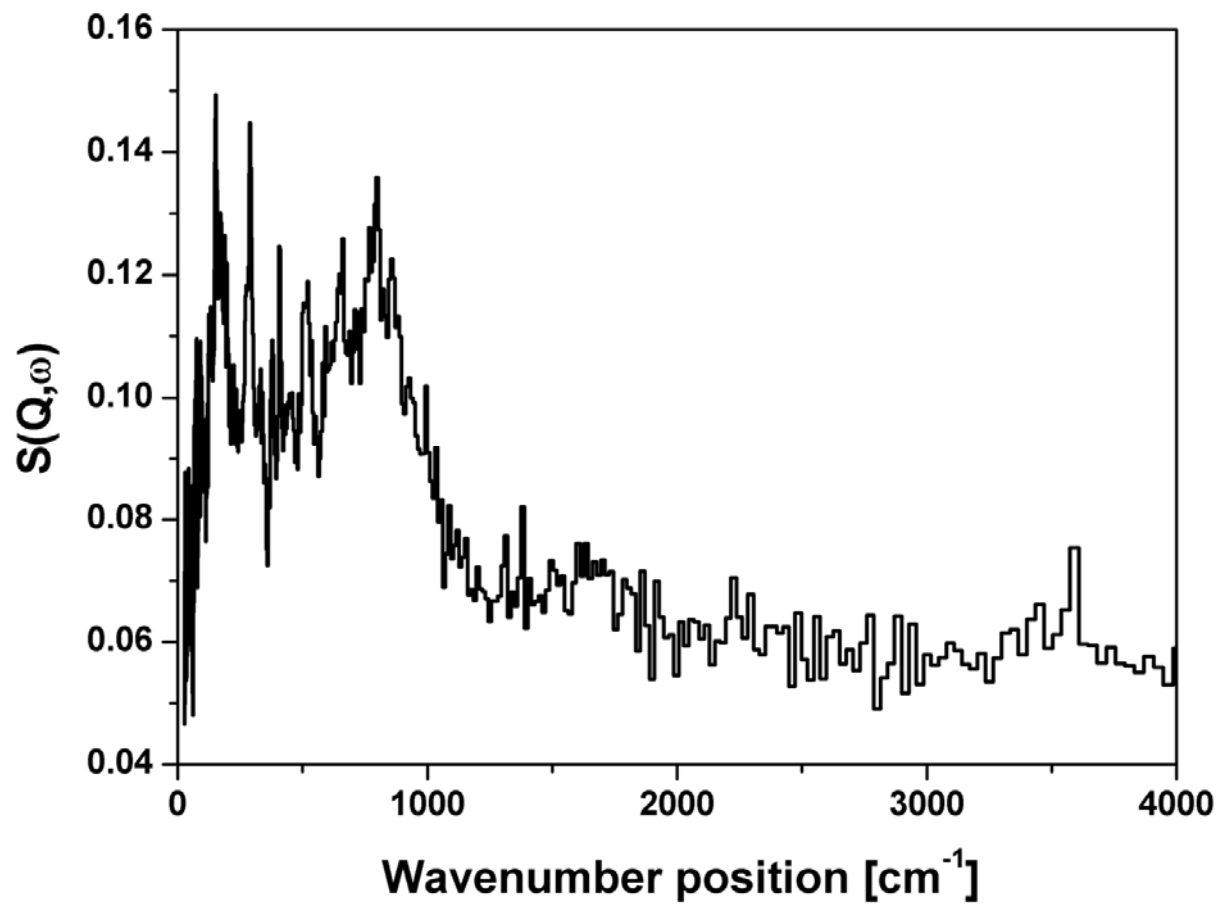


Figure 9.5.1 INS spectrum of the calcined Fe<sub>2</sub>O<sub>3</sub> starting material, as recorded using the TOSCA spectrometer.

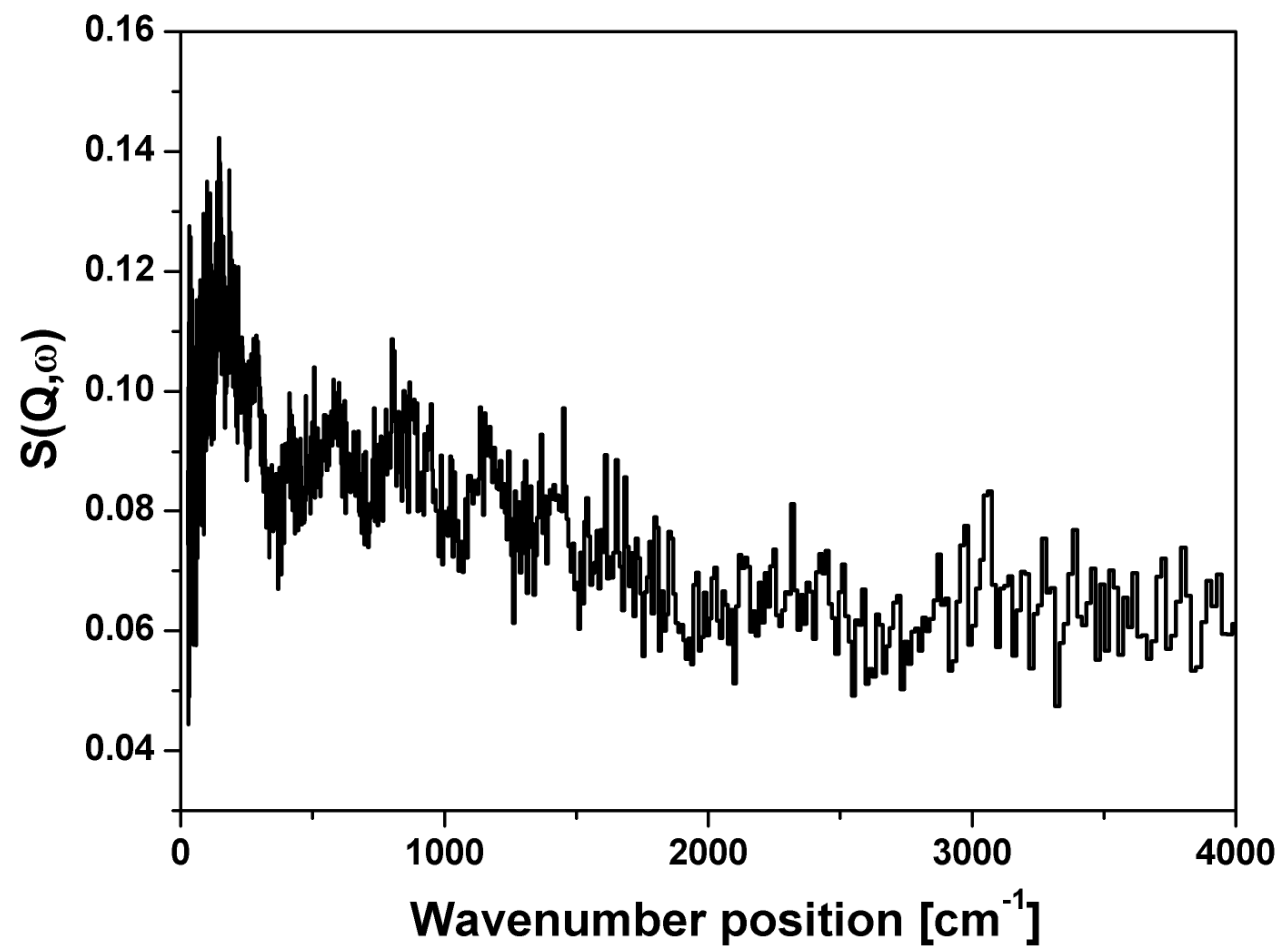


Figure 9.5.2: INS spectrum of catalyst after 6 hours reaction in syngas at 723 K, as recorded using the TOSCA spectrometer.

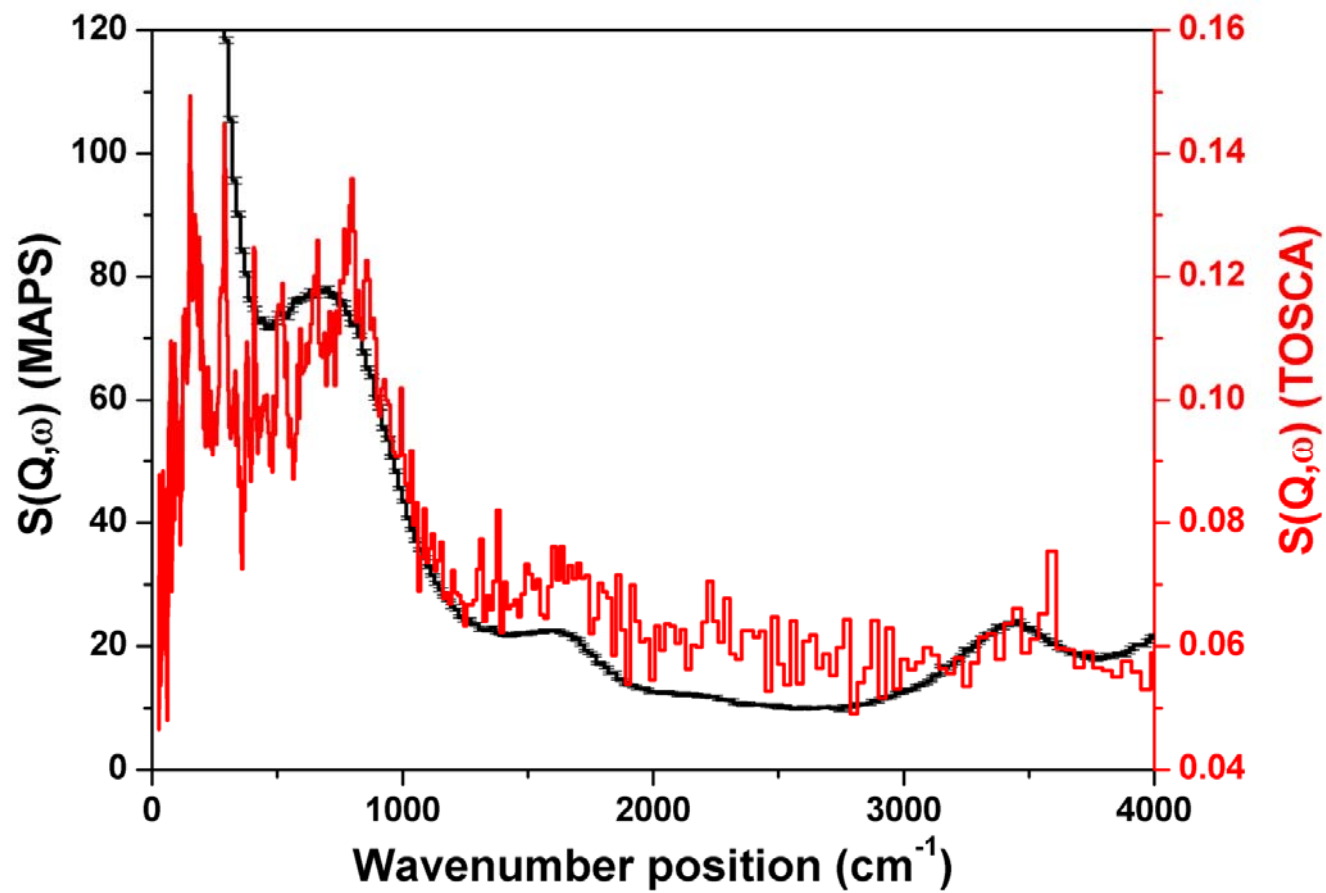


Figure 9.5.3: Comparison of the INS spectrum of the Fe<sub>2</sub>O<sub>3</sub> starting material recorded using the MAPS spectrometer (black trace) and the TOSCA spectrometer (red trace). MAPS spectrum recorded with an incident energy of 4840 cm<sup>-1</sup>.

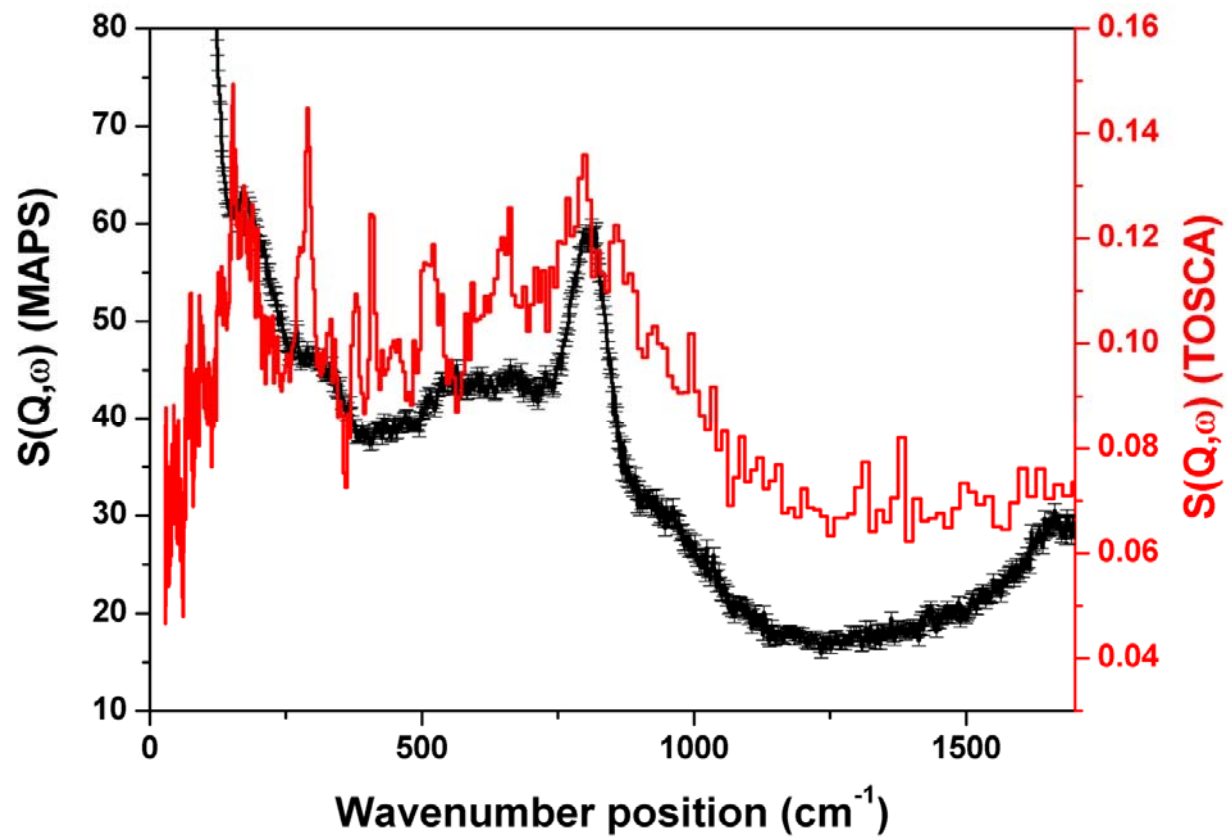


Figure 9.5.4: Comparison of the INS spectrum of the Fe<sub>2</sub>O<sub>3</sub> starting material recorded using the MAPS spectrometer (black trace) and the TOSCA spectrometer (red trace). MAPS spectrum recorded with an incident energy of 2017 cm<sup>-1</sup>.

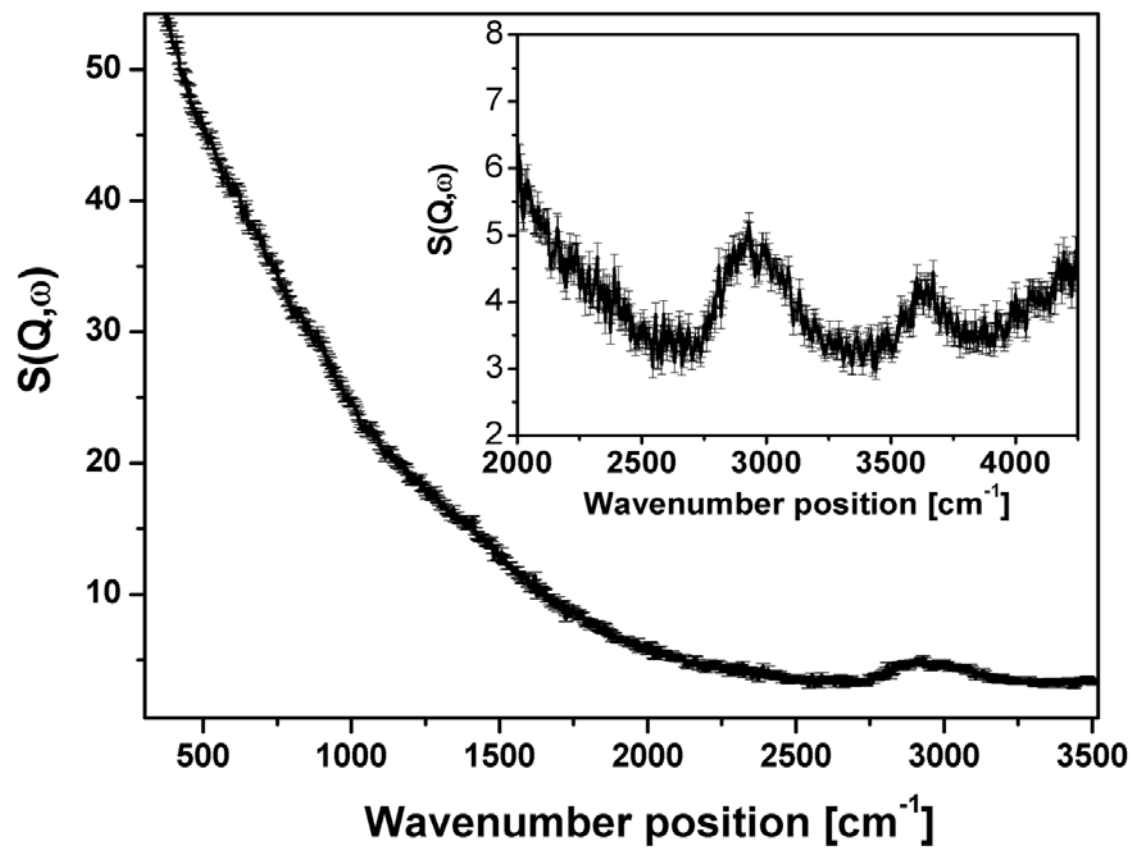


Figure 9.5.5: INS spectrum of catalyst after exposure to syngas at 623 K for a period of 6h. Recorded using the MAPS spectrometer using an incident energy of 4840  $\text{cm}^{-1}$ .

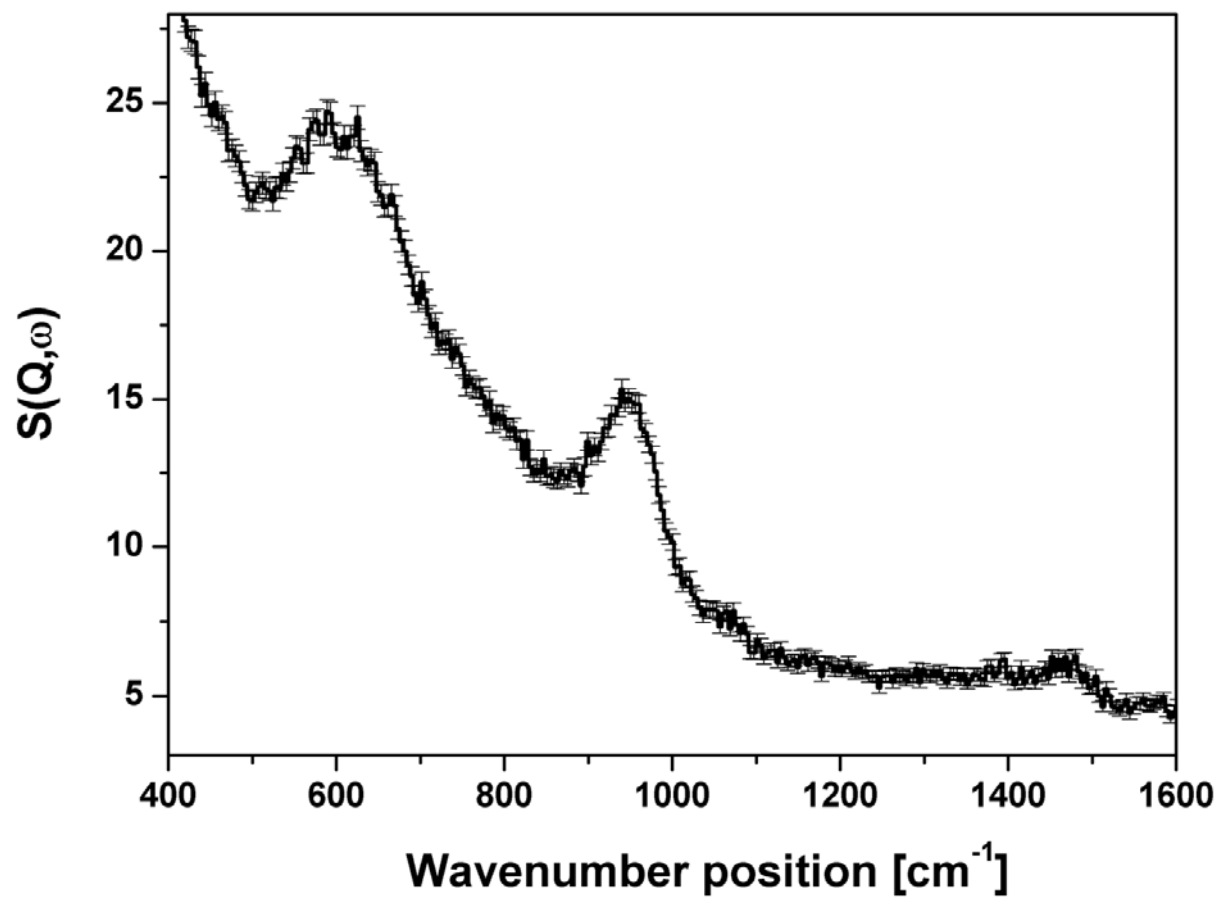


Figure 9.5.6: INS spectrum of catalyst after exposure to syngas at 623 K for a period of 6h. Recorded using the MAPS spectrometer using an incident energy of 2017  $\text{cm}^{-1}$ .

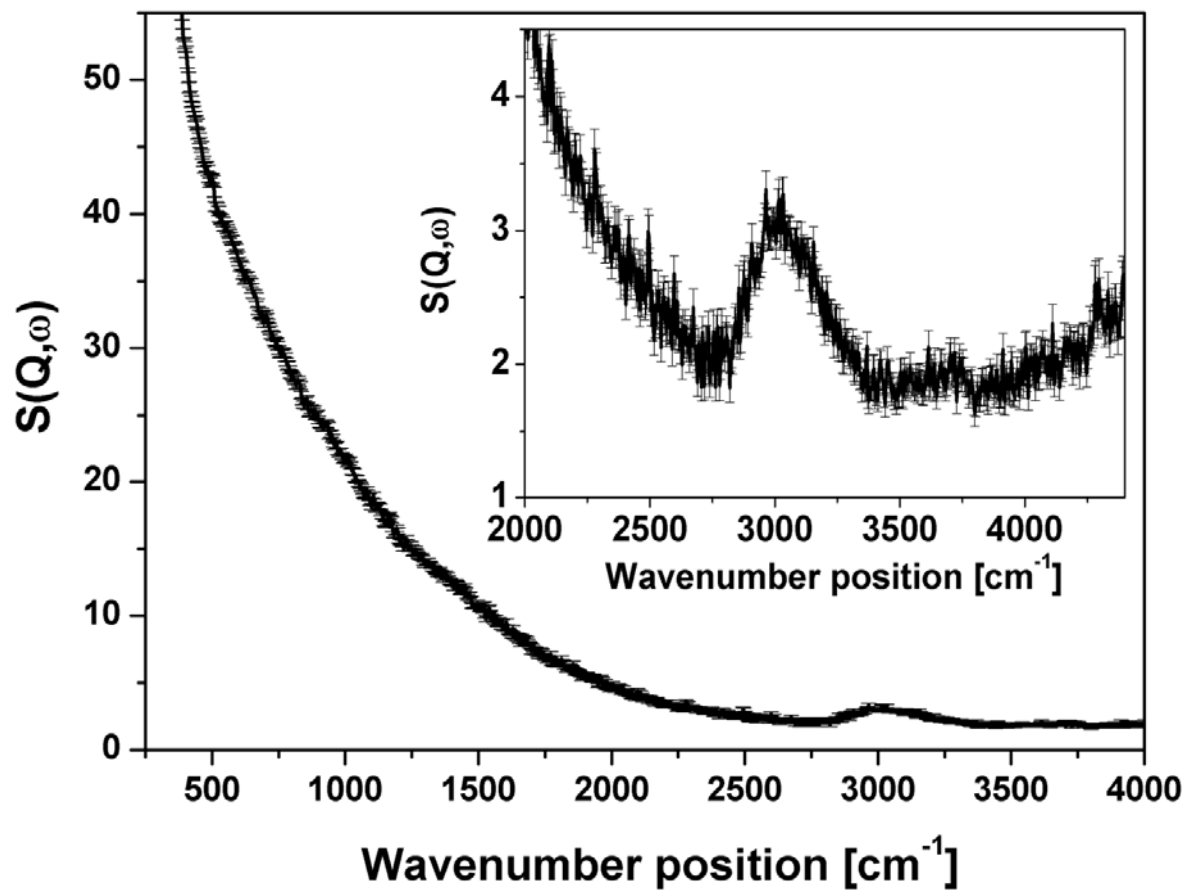


Figure 9.5.7: INS spectrum of catalyst reduced in  $\text{H}_2$  at 773 K followed by exposure to syngas at 623 K for a period of 6h. Recorded using the MAPS spectrometer using an incident energy of  $4840 \text{ cm}^{-1}$ .

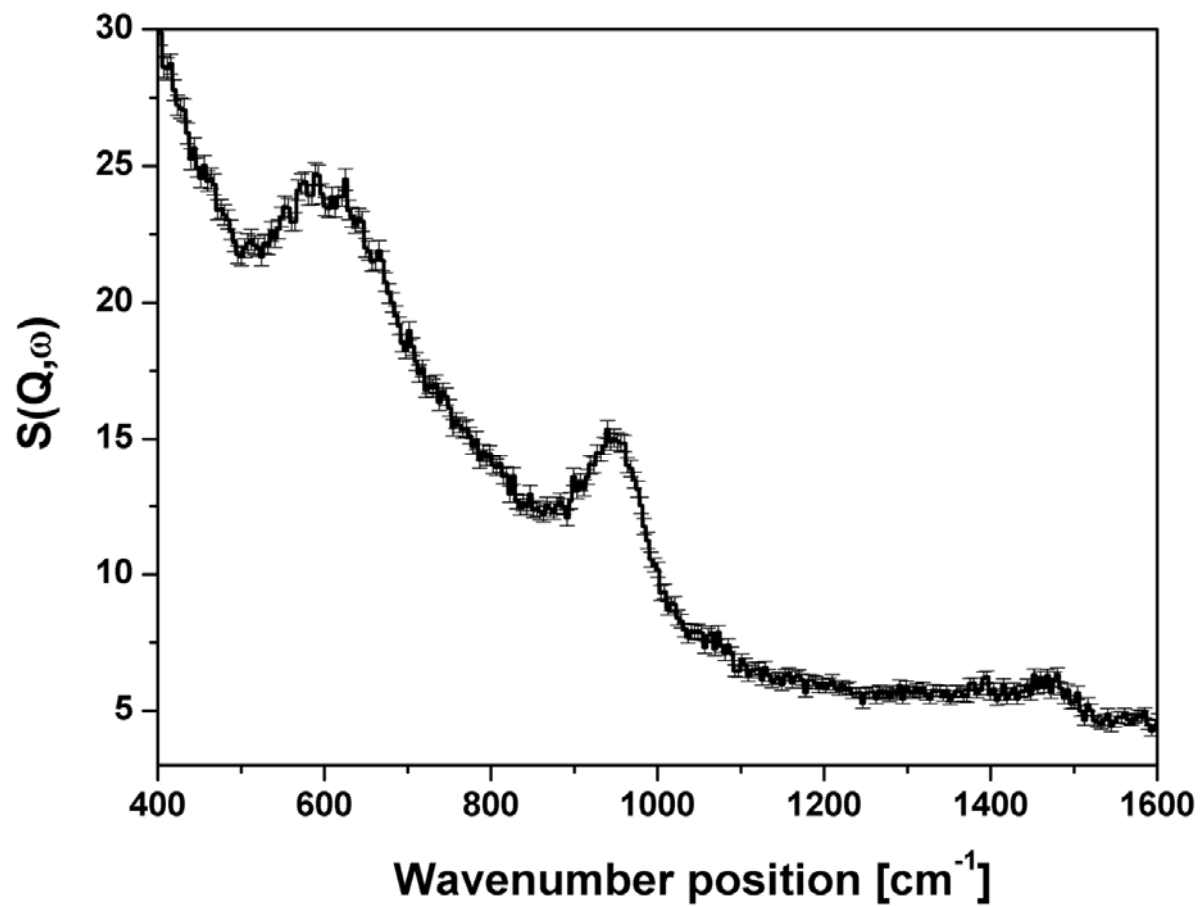


Figure 9.5.8: INS spectrum of catalyst reduced in  $\text{H}_2$  at 773 K followed by exposure to syngas at 623 K for a period of 6h. Recorded using the MAPS spectrometer using an incident energy of  $2017 \text{ cm}^{-1}$ .

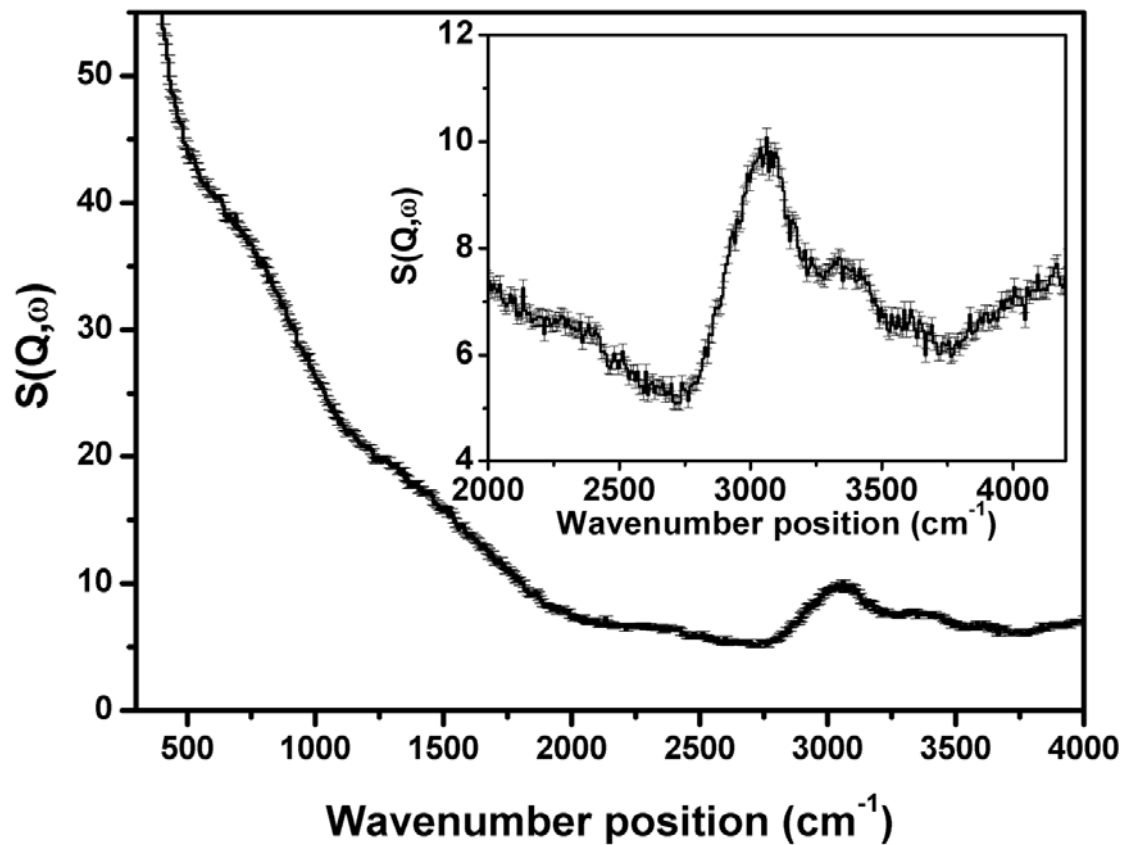


Figure 9.5.9: INS spectrum of catalyst after exposure to syngas at 723 K for a period of 6h. Recorded using the MAPS spectrometer using an incident energy of 4840  $\text{cm}^{-1}$ .

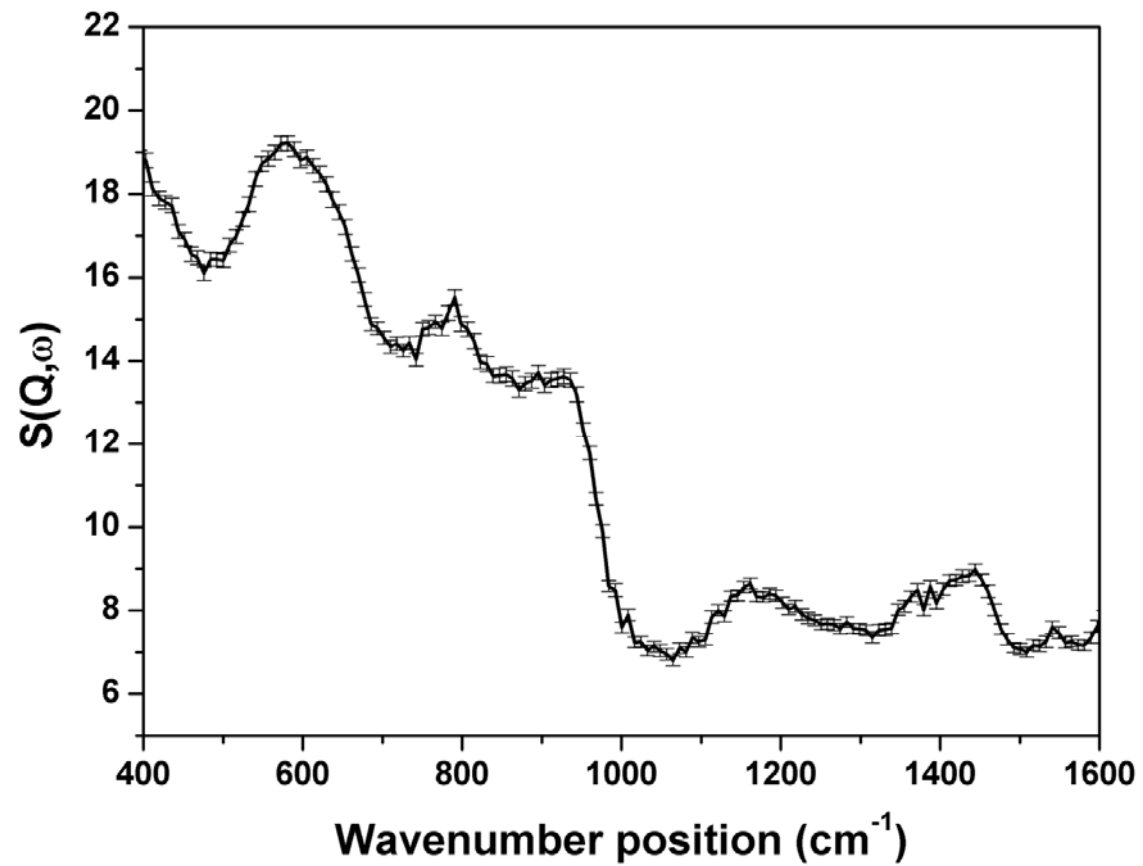


Figure 9.5.10: INS spectrum of catalyst after exposure to syngas at 723 K for a period of 6h. Recorded using the MAPS spectrometer using an incident energy of  $2017 \text{ cm}^{-1}$ .

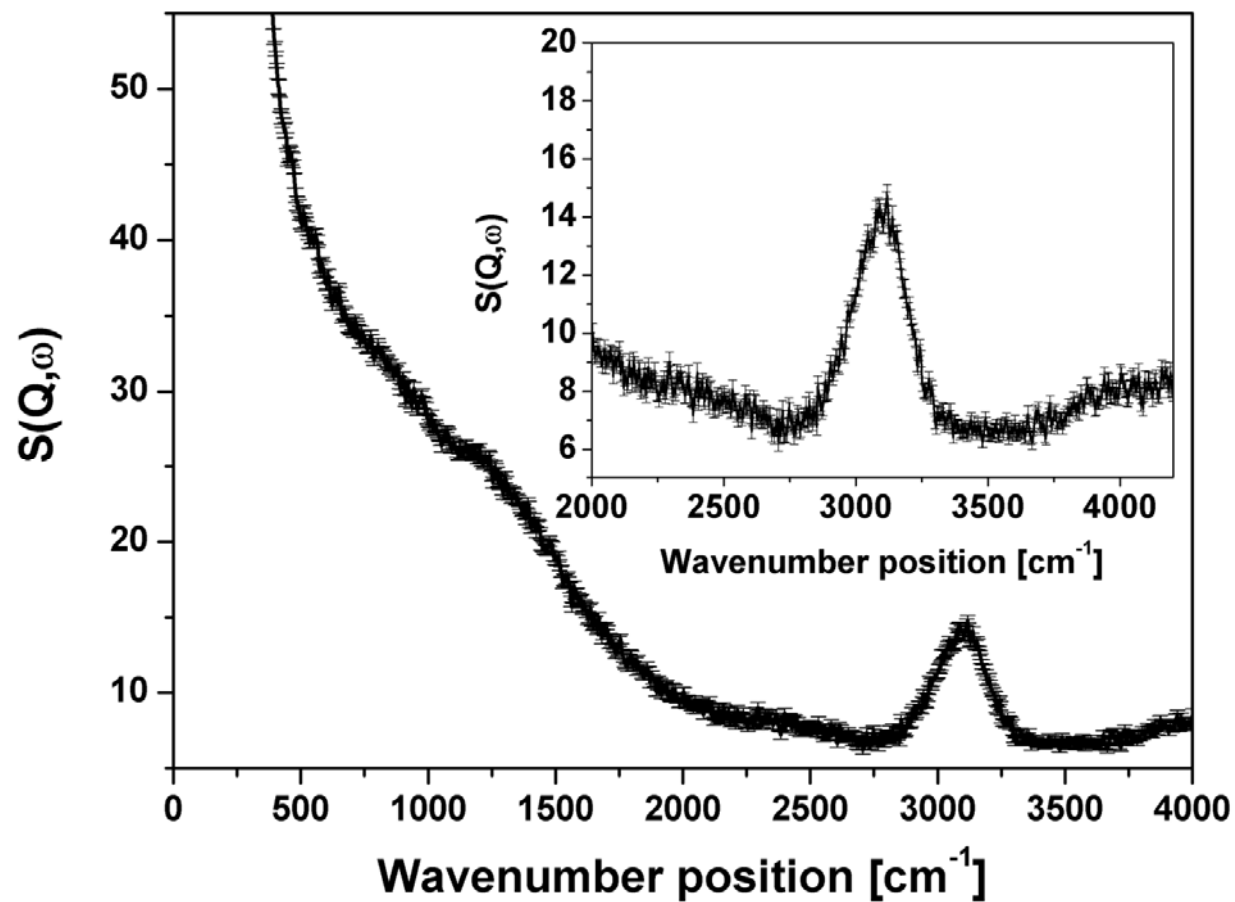


Figure 9.5.11: INS spectrum of catalyst reduced in  $\text{H}_2$  at 773 K followed by exposure to syngas at 723 K for a period of 6h. Recorded using the MAPS spectrometer using an incident energy of  $4840 \text{ cm}^{-1}$ .

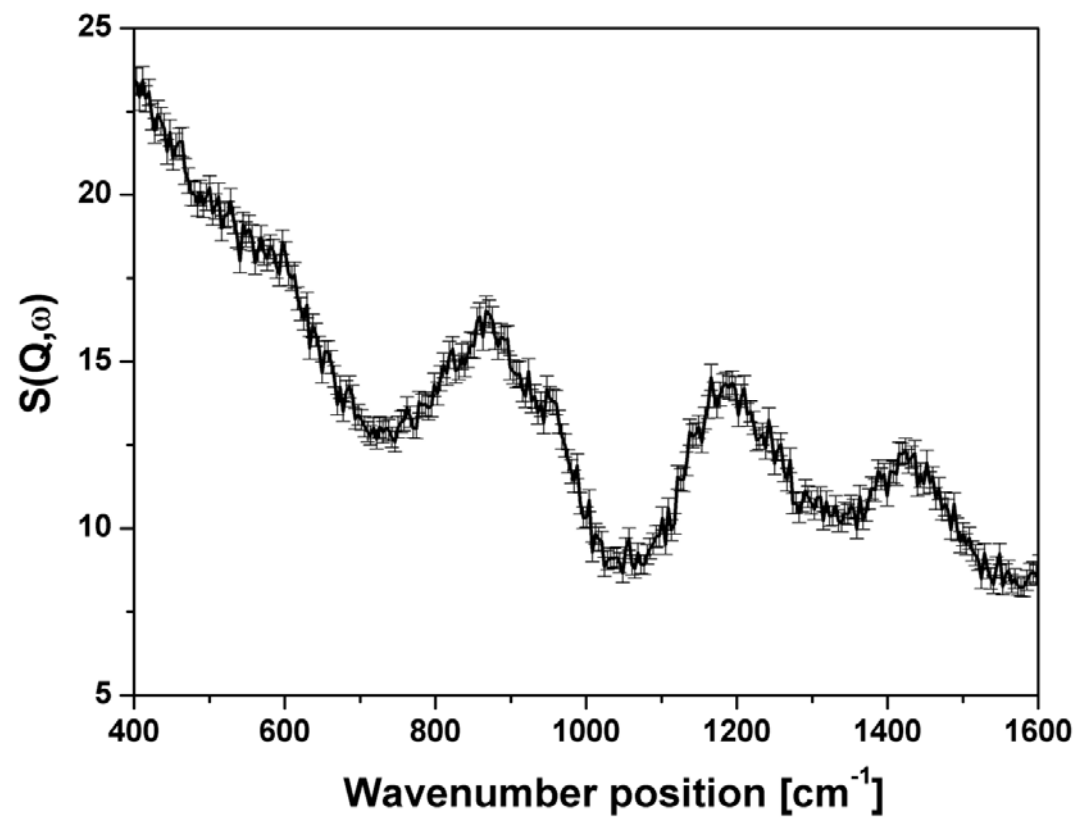


Figure 9.5.12: INS spectrum of catalyst reduced in  $\text{H}_2$  at 773 K followed by exposure to syngas at 723 K for a period of 6h. Recorded using the MAPS spectrometer using an incident energy of  $2017 \text{ cm}^{-1}$ .

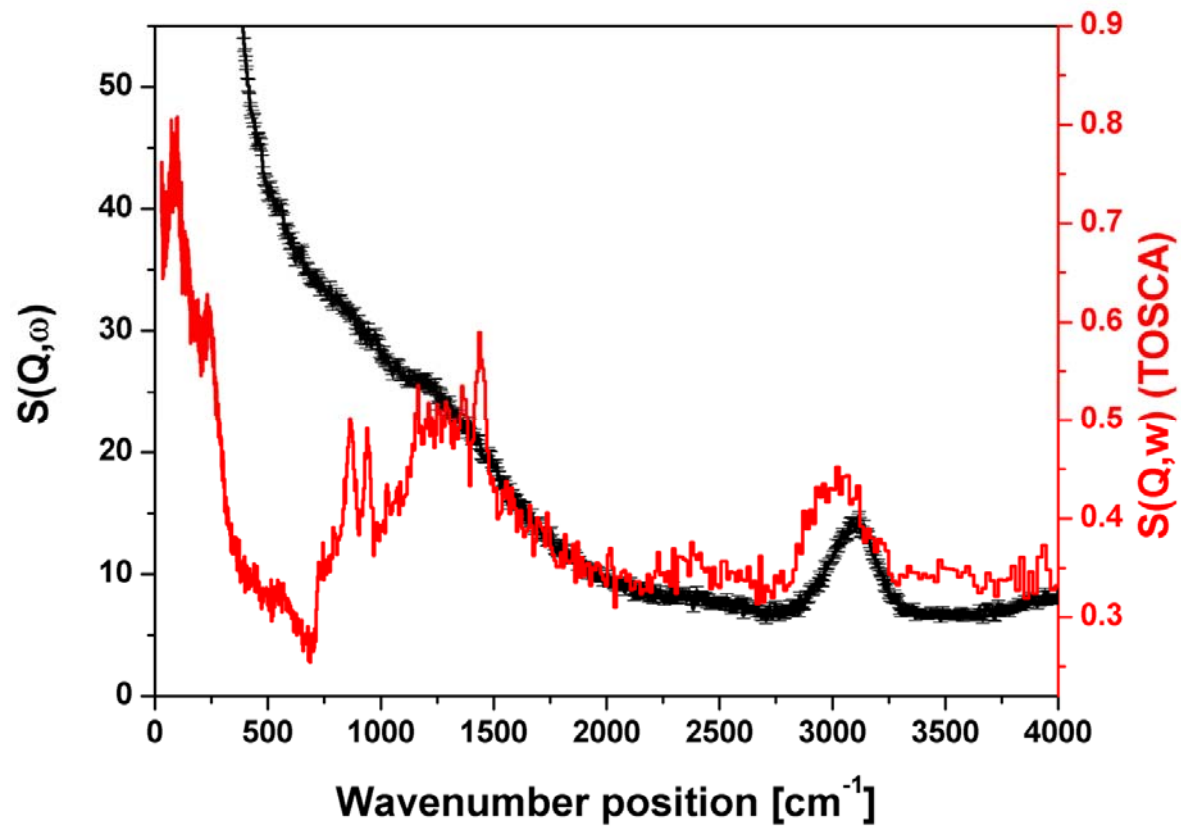


Figure 9.5.13: TOSCA spectrum (red trace) of a sample of toluene extracted catalyst fines removed from a SASOL fluidised bed FTS reactor compared with the MAPS spectrum (black trace), recorded at  $4840\text{ cm}^{-1}$ , of a sample of  $\text{Fe}_2\text{O}_3$  reduced in  $\text{H}_2$  at  $773\text{ K}$  followed by exposure to syngas at  $723\text{ K}$ .

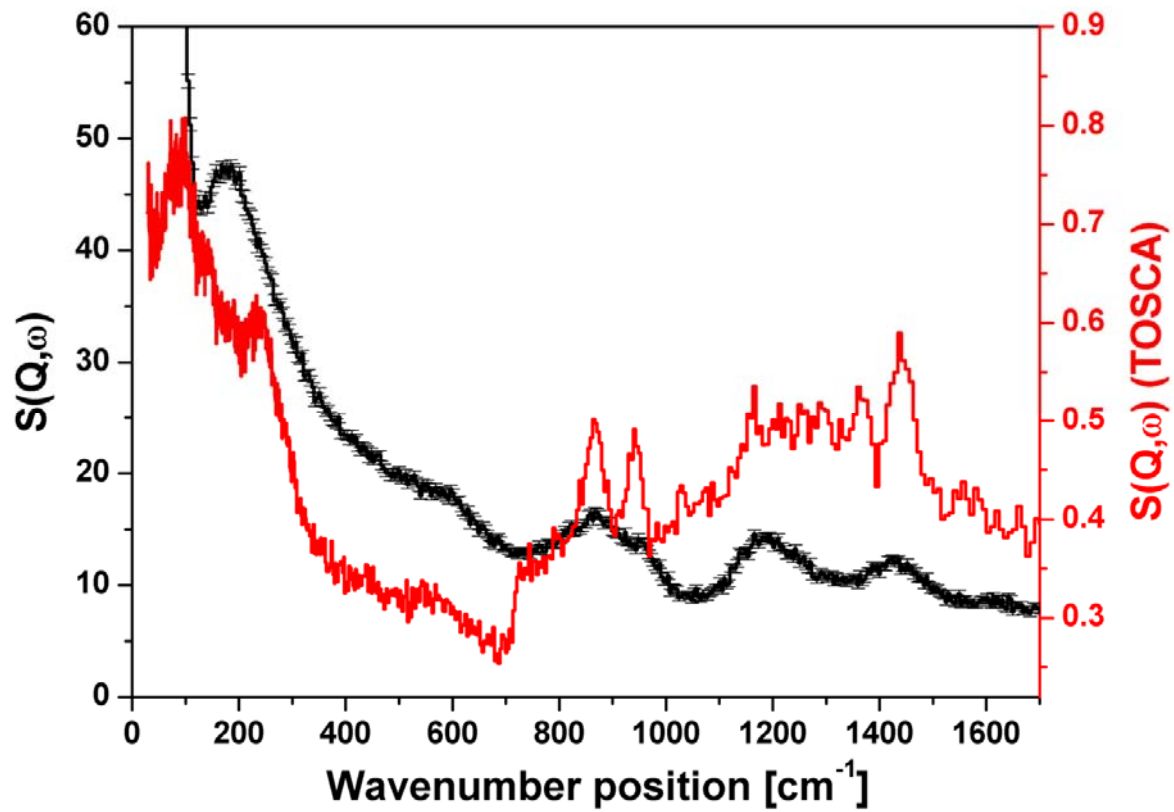


Figure 9.5.14: TOSCA spectrum (red trace) of a sample of toluene extracted catalyst fines removed from a SASOL fluidised bed FTS reactor compared with the MAPS spectrum (black trace), recorded at 4840 cm<sup>-1</sup>, of a sample of Fe<sub>2</sub>O<sub>3</sub> reduced in H<sub>2</sub> at 773 K followed by exposure to syngas at 723 K.

## 9.6 Quantification of hydrocarbonaceous overlayer

One of the benefits of using INS spectroscopy is that it facilitates relatively simple quantification of spectral features due to the fact that the intensity of features is not complicated by electro-optical selection rules or issues such as dipole-dipole coupling inherent in infrared and Raman spectroscopic measurements [14]. Instead, band intensities are dominated simply by the number of oscillators present and the amplitude of motion of those particular oscillations [14, 18]. In principal this means that, within the inherent constraints of modest resolution in the vibrational spectrum ( $50\text{-}100\text{ cm}^{-1}$ ), INS should be able to characterise chemical surface species and also to quantify them. While the characterisation of species present on the surface of heterogeneous catalysts by INS is becoming increasingly prevalent [38, 208, 257-259], the application of INS to measure the concentration of species retained at the catalyst surface has, surprisingly, thus far been sparsely explored [15, 260, 261]. This section describes the application of a simple calibration procedure by which the hydrogen content of a hydrocarbonaceous species on a catalyst surface may be quantified. Parallel temperature programmed oxidation (TPO) measurements are used to determine the total carbon content of each sample. A combination of INS and TPO, applied in this manner, can therefore facilitate the quantification and characterisation of hydrogenous and carbonaceous components contained within the catalyst samples after syngas exposure. In theory this should allow the determination of the global C:H ratio of each post-reaction sample.

### 9.6.1 Hydrogen quantification by INS

For infrared and Raman spectroscopy the intensity of a given vibrational mode is a consequence of the interaction of electromagnetic radiation with the electrons contained within a chemical bond [16]. As the electronic structure for every molecule is unique, the intensities will consequently differ between molecules and the spectrometer must therefore be calibrated for each individual species that is observed. This problem does not occur in INS measurements since the interaction of the neutron is with the atomic nucleus; the electrons are irrelevant. As described previously in Section 1.2, the observed intensity of an INS signal,  $S$ , is a function of both the energy,  $\omega$  ( $\text{cm}^{-1}$ ) and momentum,  $Q$  ( $\text{\AA}$ ), exchanged during the scattering process and is defined by the scattering law (Equation 18):

$$S(Q, \omega_i) \propto (QU_i)^2 \exp(-(QU_{Tot})^2) \sigma \quad (18)$$

Where  $\omega_i$  is the  $i^{\text{th}}$  mode at wavenumber  $\omega$ ,  $U_i$  is the root mean square displacement of the atoms in the mode,  $U_{\text{Tot}}$  is the total root mean square displacement of all the atoms in all the modes, and  $\sigma$  is the inelastic neutron scattering cross section of the atom. Momentum transfer,  $Q$ , is an experimental variable, and the inelastic neutron scattering cross section,  $\sigma$  (barn), is a fundamental property so only the amplitude of motion is a molecular property. If we assume that the C-H stretch can be treated as a harmonic oscillator, then the amplitude of vibration is given by Equation 19:

$$(U_i)^2 = \frac{\hbar^2}{2\mu\omega_i} \quad (19)$$

Where  $\mu$  is the reduced mass of the oscillator. The amplitude of vibration therefore depends only on the transition energy and is independent of the molecular entity. From the above equation it can be seen that the Debye-Waller factor (the exponential term in the scattering law, Equation 10) is dominated by the low energy modes. Since both the hydrocarbonaceous overlayer and a suitable calibrant (see below) will contain many of these, the respective Debye-Waller factor for each will be similar. Thus calibration is transferable between similar species.

Polystyrene ( $[-\text{CH}_2\text{CH}(\text{C}_6\text{H}_5)-]$ ) contains both aliphatic and olefinic C-H moieties and therefore provides a useful resolution test for the instrument. Since the stretching modes of the two different C-H moieties differ in energy only by *ca.*  $200 \text{ cm}^{-1}$ , from Equation 17 it can be seen that the difference in  $U_i$  is only  $\sim 2.5\%$ , which for the measurements presented here is negligible. A high molecular weight variant (29 300) of polystyrene was selected as the large  $n$  mitigates against the effect of end groups and the formula mass can thus be simplified to  $\text{C}_6\text{H}_5\text{C}_2\text{H}_3$ . Figure 9.6.1 shows the INS spectra for a number of different masses of polystyrene each of which is characterised by a broad feature located at  $3000 \text{ cm}^{-1}$ , which is assigned to the  $\nu_{\text{CH}}$  modes of polystyrene. In contrast, the infrared spectrum of the polystyrene calibrant, presented in Figure 9.6.2, contains a number of discrete signals in this energy range, which demonstrates the reduced resolution available with this INS spectrometer used in this configuration compared to infrared spectroscopy. Despite this, the integrated intensity of this single peak represents the number of CH moieties contained within the neutron beam path. Reducing the mass of polystyrene in the beam path resulted in a consequent reduction in the intensity of the feature located at  $3000 \text{ cm}^{-1}$ .

Figure 9.6.3 shows a plot of the integrated intensity for the  $\nu_{\text{CH}}$  feature as a function of number of hydrogen atoms contained in the sample, *i.e.* sample mass, and reveals a linear relationship with a correlation factor of  $R^2 = 0.977$ . The gradient of this line ( $1.398 \times 10^{-19}$  a.u./ $N^{\circ}_{\text{H-atoms}}$ ) gives the response factor for the  $\nu_{\text{CH}}$  mode of CH containing species when measured with the MAPS spectrometer used in this configuration, *i.e.* chopper speed and assembly, and incident energy. The linearity of the response is in agreement with the observations of Albers *et al.* [15], who correlated the integrated area of CH deformation bands with hydrogen content for a number of activated carbon catalyst support materials using the TOSCA spectrometer, and confirms the response to be directly proportional to the number of hydrogen atoms present in the beam. The response factor determined from this calibration procedure can be used to quantify the hydrogen content of CH containing species present in the post-reaction carbon monoxide hydrogenation catalysts.

The integrated intensity of the  $\nu_{\text{CH}}$  band of each of the catalyst samples after syngas exposure was determined by fitting the data to a single Gaussian function using the Origin graphing package [29], as shown in Figures 9.6.4-9.6.7. Based on the response factor taken from the polystyrene calibration curve (Figure 9.6.3), the hydrogen content contained in the hydrocarbonaceous overlayer of the iron catalyst treated in syngas at 623 K is 0.0298% *w/w* ( $2.957 \times 10^{-4}$  moles  $\text{H/g}_{\text{cat}}^{-1}$ ) as seen in Figure 9.6.4. Reducing the catalyst in hydrogen prior to syngas exposure has the effect of modestly reducing this value to 0.0247% *w/w* ( $2.454 \times 10^{-4}$  moles  $\text{H/g}_{\text{cat}}^{-1}$ ) as seen in Figure 9.6.5. In contrast, increasing the temperature at which the catalyst is exposed to syngas results in a vast increase in the integrated intensity of the  $\nu_{\text{CH}}$  band. The catalyst after treatment on syngas at 723 K has hydrogen contained within the hydrocarbonaceous overlayer that accounts for 0.076% ( $7.5547 \times 10^{-4}$  moles  $\text{H/g}_{\text{cat}}^{-1}$ ) of the sample by weight (Figure 9.6.6). Reducing the sample in hydrogen prior to syngas exposure at 723 K appears to encourage the formation of the hydrocarbonaceous overlayer as this sample has hydrogen associated with a hydrocarbonaceous overlayer that accounts for 0.142% of the catalyst sample by weight ( $14.1560 \times 10^{-4}$  moles  $\text{H/g}_{\text{cat}}^{-1}$ ), as seen in Figure 9.6.7. Interestingly, the energy position of the  $\nu_{\text{CH}}$  peak in the spectra of the samples treated in syngas at 623 K ( $2955 \text{ cm}^{-1}$ ) indicates the presence of an aliphatic hydrocarbonaceous species, while for the samples treated in syngas at 723 K the position of the  $\nu_{\text{CH}}$  band ( $3035 \text{ cm}^{-1}$ ) indicates the presence of an olefinic hydrocarbonaceous species. This observation suggests that increasing the temperature at which the sample is treated in syngas not only vastly increases the quantity of the hydrocarbonaceous overlayer deposited on the catalyst surface but also alters the

nature of that deposit.

The hydrogen content of each of the post-reaction catalyst samples is tabulated in Table 9.6.1, below:

<b>Sample treatment</b>	<b>Moles H/g<sub>cat</sub></b>	<b>Hydrogen content (% w/w)</b>	<b>Hydrogen content (ppm)</b>
Syngas 623 K	$2.96 \times 10^{-4}$	0.0298	298
Reduced, syngas 623 K	$2.45 \times 10^{-4}$	0.0247	247
Syngas 723 K	$7.55 \times 10^{-4}$	0.076	760
Reduced, syngas 723 K	$1.42 \times 10^{-3}$	0.142	1420

Table 9.6.1: Hydrogen contents for each of the post-reaction CO hydrogenation catalysts.

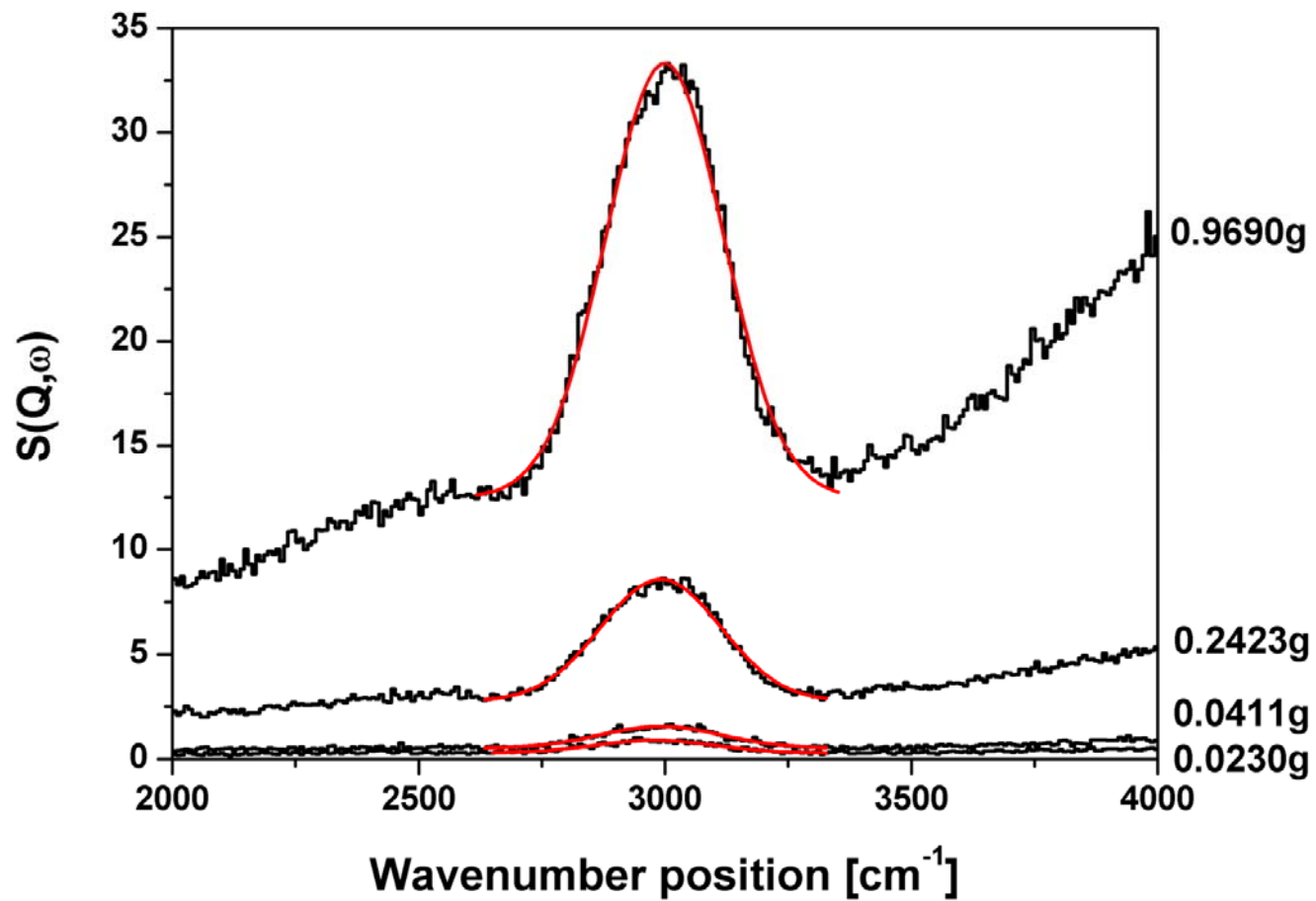


Figure 9.6.1: Stacked plot of INS spectra of various quantities of polystyrene as recorded using the MAPS INS spectrometer. The  $\nu_{\text{CH}}$  features are well described by Gaussian curves, indicated in red.

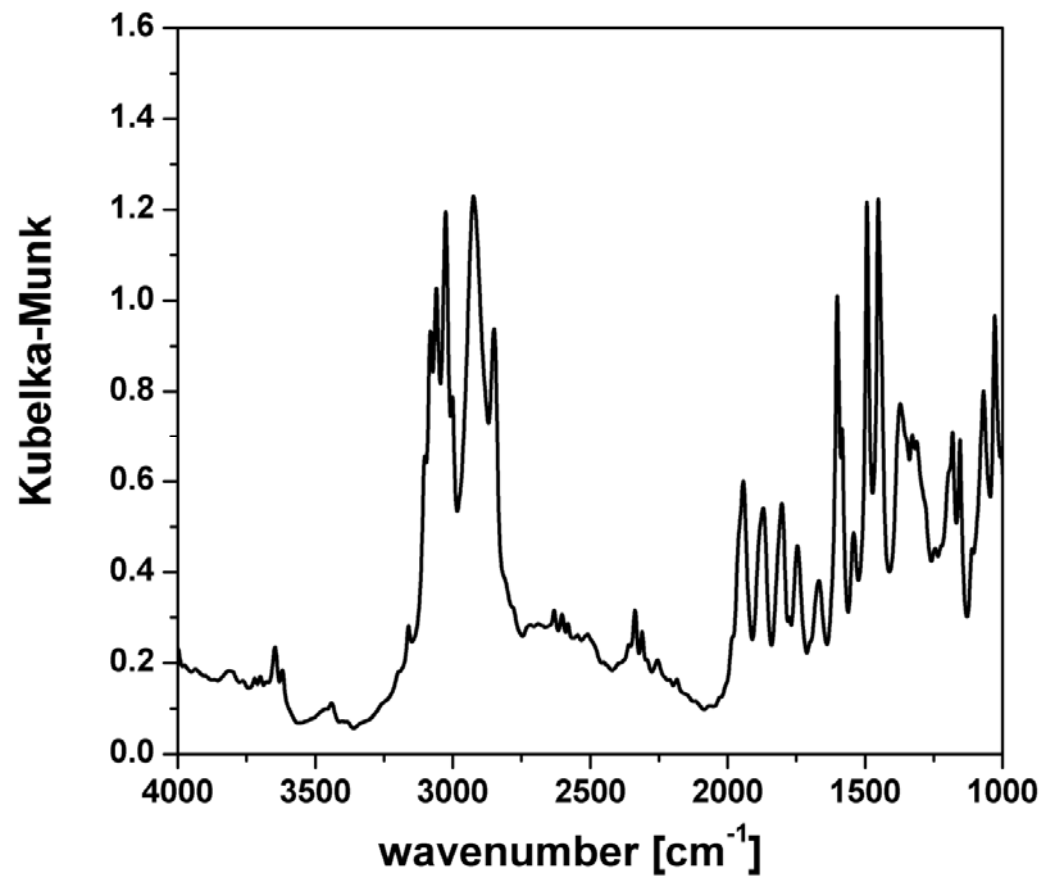


Figure 9.6.2: Diffuse reflectance infrared spectrum of a sample of polystyrene calibrant.

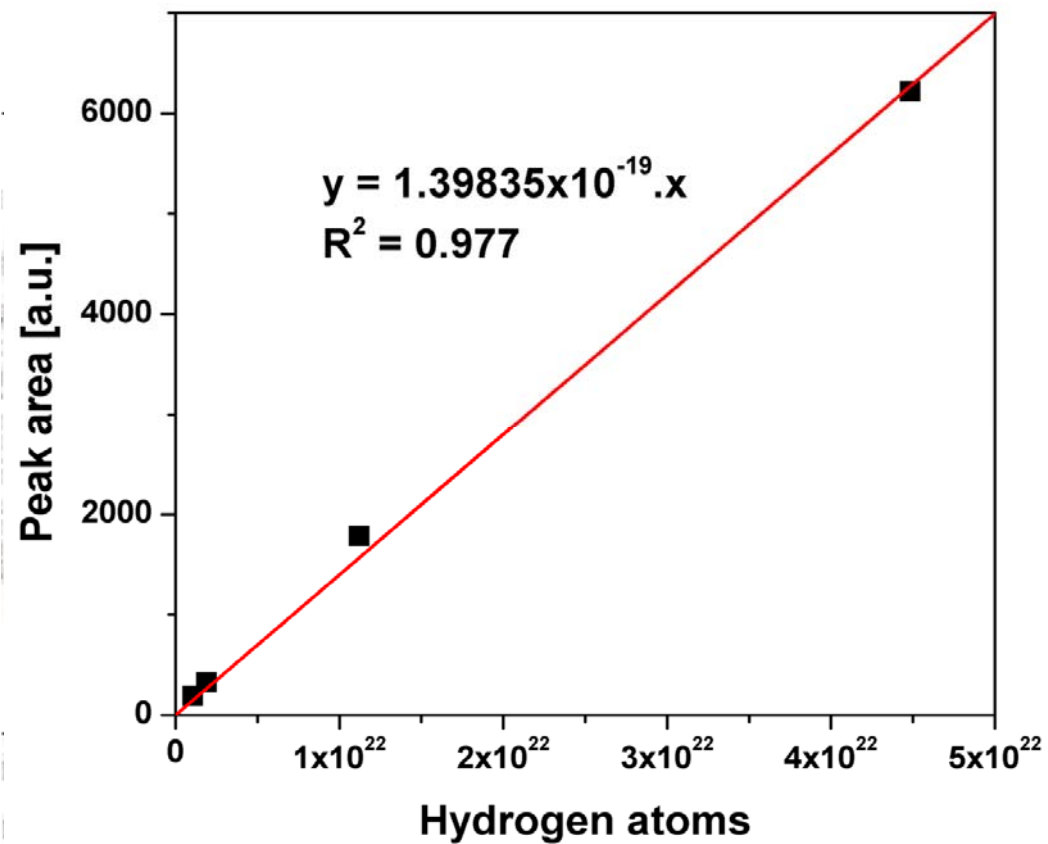


Figure 9.6.3: A plot of integrated band intensity of the  $\nu_{\text{CH}}$  mode of polystyrene as a function of the number of hydrogen atom contained in a sample of a given mass. The straight line represents a linear least squares fit to the data (constrained to the origin), the slope of which defines the sensitivity factor of the MAPS spectrometer operating under the conditions employed here.

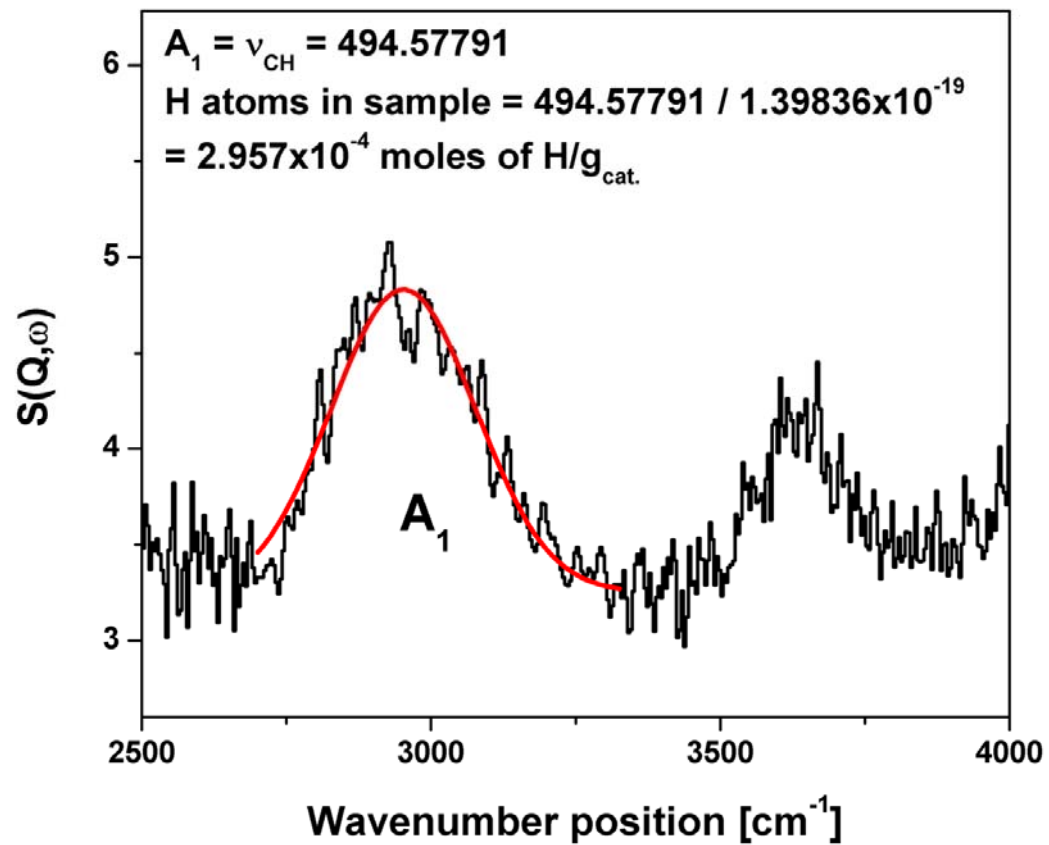


Figure 9.6.4: Integrated intensity of the  $\nu_{\text{CH}}$  band of a post-reaction sample of iron catalyst after exposure to syngas at 623 K for 6 h, as recorded using MAPS.

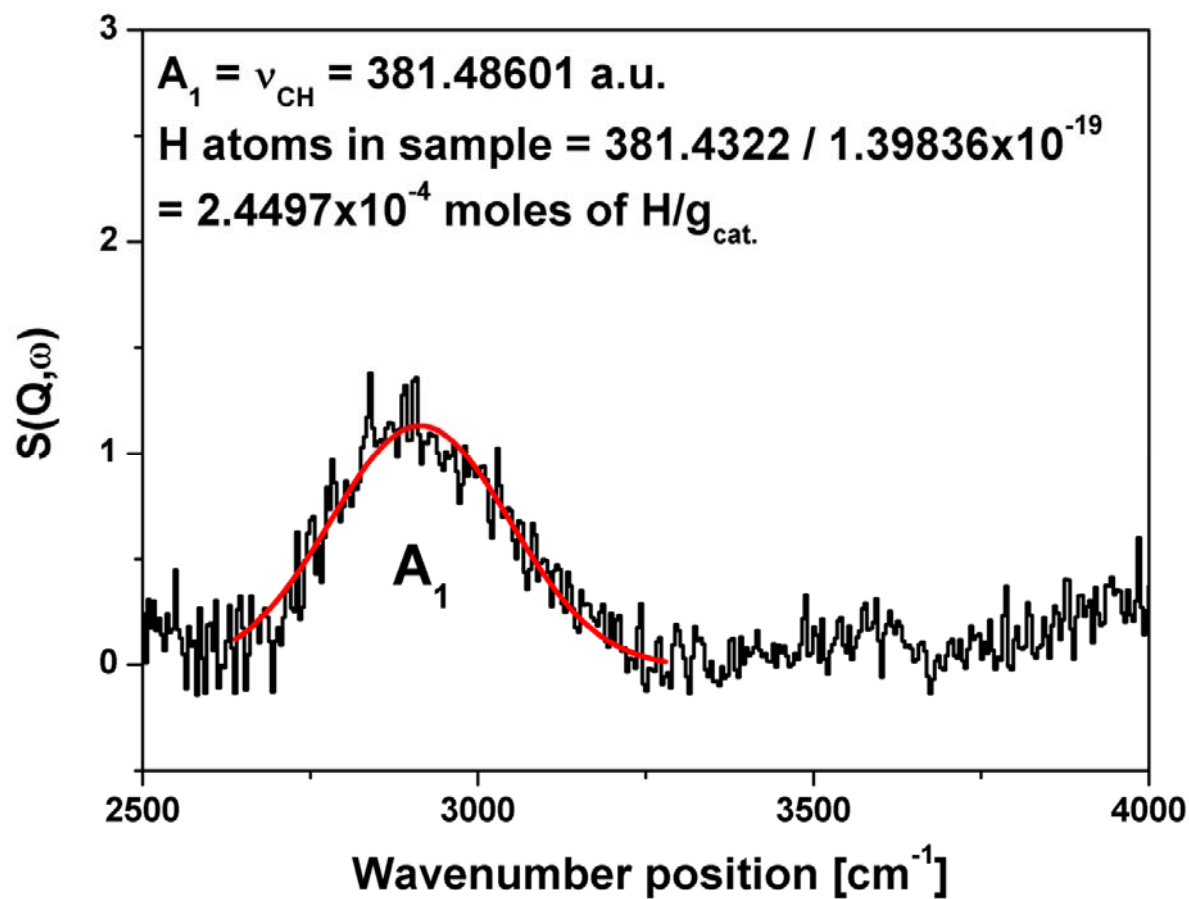


Figure 9.6.5: Integrated intensity of the  $\nu_{\text{CH}}$  band of a post-reaction sample of iron catalyst that was reduced in hydrogen at 773 K followed by exposure to syngas at 623 K for 6 h, as recorded using MAPS.

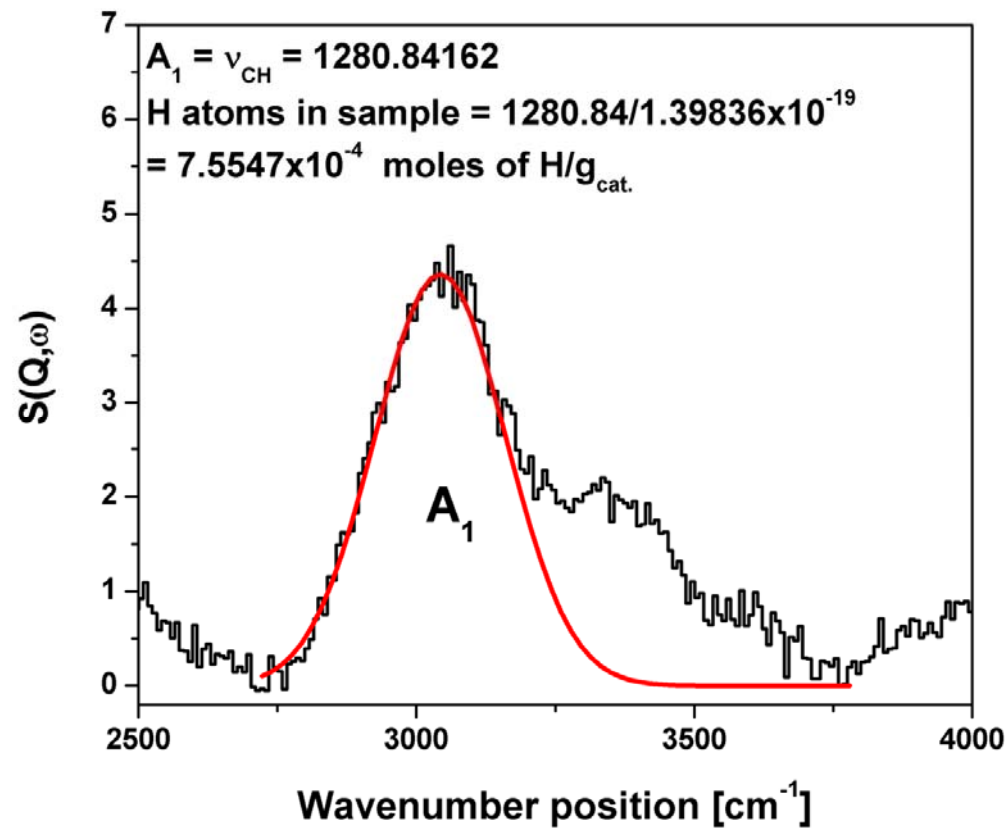


Figure 9.6.6: Integrated intensity of the  $\nu_{\text{CH}}$  band of a post-reaction sample of iron catalyst after exposure to syngas at 723 K for 6 h, as recorded using MAPS.

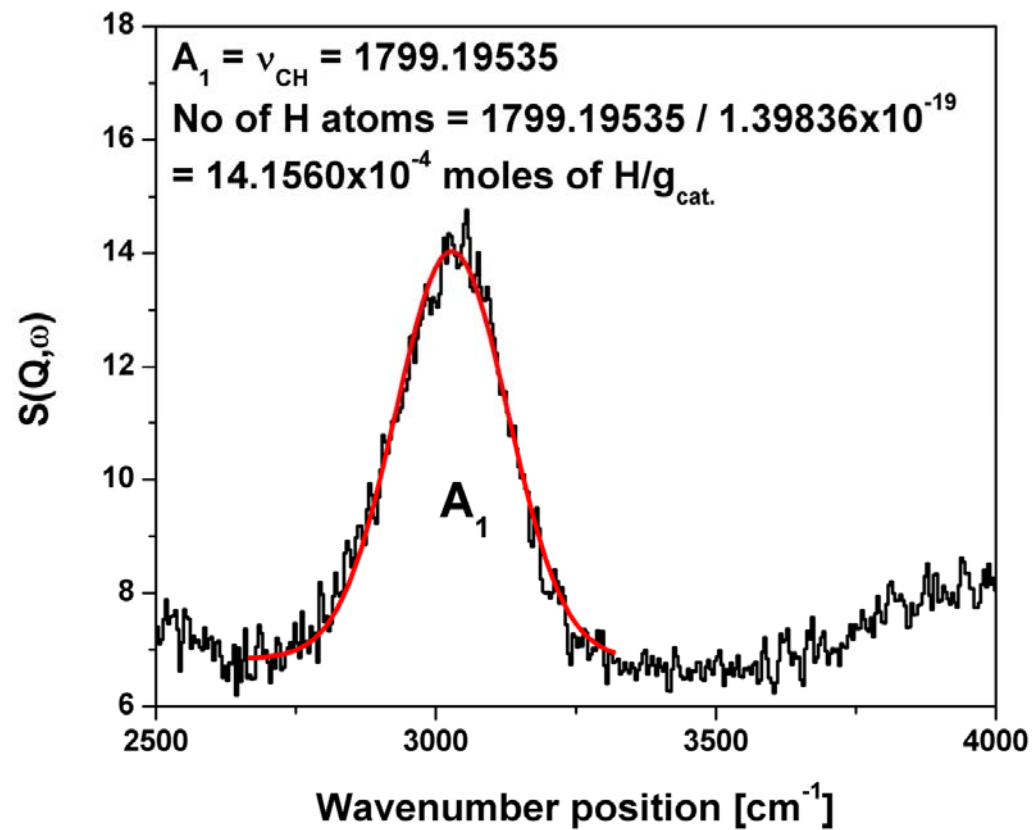


Figure 9.6.7: Integrated intensity of the  $\nu_{\text{CH}}$  band of a post-reaction sample of iron catalyst that was reduced in hydrogen at 773 K followed by exposure to syngas at 723 K for 6 h, as recorded using MAPS.

## 9.7 Temperature programmed oxidation (TPO)

Temperature programmed oxidation (TPO) measurements were used in order to detect and quantify the carbonaceous deposits present in the iron samples after exposure to syngas. Online quadrupolar mass spectrometry presents an ideal method for application of TPO measurements due to the fact that CO<sub>2</sub> evolution can be selectively analyzed by measuring the  $m/z$  44 fragment. Detection and quantification of the oxidation of carbon species contained within each sample was therefore achieved by monitoring the  $m/z$  44 signal, corresponding to CO<sub>2</sub>. Unfortunately, the post-reaction catalyst samples were exposed to air during the transfer from the glovebox to the TPO facility. However, Galuska *et al.* [210] present infrared spectra recorded *in situ* under TPO conditions using dry air, which indicates the exposure to air not to be a problem as a temperature of at least 373 K was found to be required to induce oxidation of carbonaceous deposits present on iron-based catalyst samples after CO hydrogenation. Furthermore, Galuszka *et al.* [210] also presented Mossbauer evidence that heating a spent Fischer-Tropsch catalyst up to 673 K in air is sufficient to oxidize the carbide component of the catalyst. It therefore follows that the TPO profiles presented here represent the oxidation of all surface carbon species including iron carbide(s) and amorphous carbon.

The  $m/z$  44 traces from the TPO profile of each of the post-reaction catalyst samples are presented in Figures 9.8.1-9.8.4. The profiles have been scaled to account for the different masses of sample used in each experiment. The CO<sub>2</sub> evolved during the TPO of each of the post-reaction samples is a result of the oxidation of the various carbonaceous deposits in each sample including: the hydrocarbonaceous overlayer; iron carbide species; and possibly ‘free’ carbon, which has been reported to contribute to deactivation in iron-based FTS catalysts [156], that was not detected by the previously presented XRD, INS or Raman spectroscopy analyses.

As neither of the samples exposed to syngas at 623 K contain any carbide species detectable by XRD, the CO<sub>2</sub> evolved from these samples under TPO conditions is attributed to oxidation of the aliphatic hydrocarbonaceous overlayer implicated in the INS spectra, *i.e.*  $T \leq ca. 700$  K. In contrast, the samples treated in syngas at 723 K, which contain a significant proportion of iron carbide species and olefinic hydrocarbonaceous deposits, evolve CO<sub>2</sub> at temperatures greater than 700 K. The sample exposed to syngas without prior reduction in hydrogen evolved CO<sub>2</sub> up to 800 K, while the sample that had

first been reduced before syngas exposure liberated CO<sub>2</sub> up to *ca.* 950 K. The CO<sub>2</sub> evolution profiles are highly asymmetric and indicate the presence of several types of carbon species. Aside from the greater iron carbide content, the higher temperature of the CO<sub>2</sub> features observed in the TPO of the samples treated at 723 K could be due to the fact that the hydrocarbonaceous deposits of these samples have been shown by INS to be largely composed of an olefinic component, while those of the samples treated at 623 K are aliphatic.

As described in Section 2.6.4, integration of the *m/z* 44 evolution profile allows quantification of the carbon oxidised during the TPO measurement. Using this methodology, the CO<sub>2</sub> evolved in the TPO profiles of each of the post-reaction samples, presented in Figures 9.7.1-9.7.4, was quantified and used to determine the carbon content of each sample. This data are tabulated in Table 9.7.1. The sample treated in syngas at 623 K was found to contain a carbon loading of 0.19% by weight, while the sample that had been reduced prior to syngas exposure at this temperature was found to contain 2.46% carbon by weight. Increasing the temperature at which the samples were exposed to syngas drastically increased the quantity of carbon laid down. For example, the sample treated in syngas at 723 K without prior reduction was found to contain 7.4% carbon by weight, while the sample that was reduced prior to syngas exposure at 723 K contains 23.25% carbon by weight. The greater carbon content of the pre-reduced samples is attributed to the fact that, before exposure to syngas, these samples contain a greater contribution of metallic iron, into which carbon readily dissolves [170], than their non-reduced counterparts. This is indicated by the greater relative intensity of iron carbide features observed in the XRD pattern of the catalyst reduced before syngas exposure at 723 K compared to that of the sample that was reacted at 723 K without prior reduction. Also, the fact that the pre-reduced sample contains a greater quantity of olefinic hydrocarbonaceous deposit, as shown by quantifiable INS measurement, will also contribute to the greater carbon content.

<b>Sample treatment</b>	<b>Moles C/g<sub>cat</sub></b>	<b>Carbon content (% w/w)</b>	<b>Carbon content (ppm)</b>
Syngas 623 K	1.58x10 <sup>-4</sup>	0.19	1900
Reduced, syngas 623 K	0.00205	2.46	24600
Syngas 723 K	0.0061667	7.40	74000
Reduced, syngas 723 K	0.019375	23.25	232500

Table 9.7.1: Carbon contents of iron-based post-reaction CO hydrogenation catalysts.

## 9.8 Determination of the global C:H ratio of post-reaction samples

Having established the quantity of hydrogen associated with the hydrocarbonaceous overlayer by INS (Section 9.6), we can now compare this with the carbon content of each post-reaction catalyst sample as determined by TPO (Section 9.7). Clearly, the hydrogen quantified is only associated with the hydrocarbonaceous overlayer since it was determined using the integrated intensity of the  $\nu_{\text{CH}}$  band, whereas the carbon measured arises from all the carbon sources in each sample, which could include: iron carbides; hydrocarbonaceous overlayer; and possibly ‘free’ carbon. Nevertheless, the combination of these analyses allows the determination of a generalised, global C:H ratio for the post-reaction catalyst samples. Unfortunately, in this case, this methodology does not permit the determination of the C:H ratio of only the hydrocarbonaceous overlayer, which could potentially be a highly diagnostic parameter for the characterisation of the overlayer. However, this methodology could be successfully applied to other systems that do not feature such a range of carbon environments, such as propyne hydrogenation over a supported Pd catalyst [262], where the C:H ratio of the active overlayer could, in principle, be accurately determined. Despite this apparent limitation the global molar C:H ratios for each of the post-reaction catalyst samples are given in Table 9.8.1:

Sample treatment	C:H
Syngas exposure at 623 K, 6h.	0.5:1
Reduced at 773 K, then syngas exposure at 623 K, 6h.	8.4:1
Syngas exposure at 723, 6h.	8.1:1
Reduced at 773 K, then syngas exposure at 723 K, 6h.	13.6:1

Table 9.8.1: Global molar C:H ratios for post-reaction iron catalyst samples.

Both samples exposed to syngas at 623 K contained a similar quantity of hydrogen that was associated with a hydrocarbonaceous overlayer as shown by the similar relative intensity of their associated  $\nu_{\text{CH}}$  bands observed in the INS measurements. The source of the extra carbon carried by the sample that was reduced prior to syngas exposure is therefore attributed to ‘free’ carbon. This statement is based on the fact that the XRD patterns for these samples contained no distinct iron carbide signals. Instead, a broad and weak signal was observed at *ca.* 44°, which was tentatively assigned to metallic iron. It could be the case that this signal was due to a poorly ordered, small quantity of iron

carbide species. Shroff *et al.* [172] have shown by high resolution transmission electron microscopy (HRTEM) that activation of iron oxide in CO at 523 K for 2 h at atmospheric pressure is sufficient to produce iron carbide species, therefore treatment at 623 K should also produce iron carbide species. Poor resolution and signal intensity in the associated XRD patterns means that this cannot be confirmed or denied. However, the fact that an overlayer was detected in the TEM images of these samples (see Section 9.9), and the fact that other authors [172, 185] only observe such overlayers upon iron carbide particles suggests that may actually be present on the samples treated at 623 K presented here. Nevertheless, the source of extra carbon in the pre-reduced sample treated in syngas at 623 K cannot be determined from the data presented here.

The difference in the C:H ratio for the samples exposed to syngas at 723 K is likely to be due to the apparently much greater proportion of iron carbide contained in the sample that was reduced in H<sub>2</sub> prior to syngas exposure, as indicated by the XRD patterns of these samples (Figures 9.3.3 and 9.3.4). The higher C:H ratio could also potentially be due to the presence of graphitic carbon. Fierro *et al.* [158] report graphitic carbon deposits to exhibit a reflection located at *ca.* 20° in the XRD patterns of samples exposed to syngas at 723 K, which is not observed in the XRD patterns presented here. This possibility is also rejected due to the fact that the carbonaceous deposits found on the post-reaction catalyst samples considered here are oxidised at much lower temperatures than graphite (*ca.* 1060 K, Fig. 2.6.2).

Within the confines of the limited resolution available, the MAPS spectra of the CO hydrogenation catalysts compare well with the TOSCA spectra of the SASOL catalyst fines samples, as demonstrated by Figures 9.5.13 and 9.5.14. The TOSCA spectra of the SASOL catalyst fines samples presented in Figures 8.3.1 and 8.3.2 compared well with those simulated for proposed aromatic polycycles presented in Figures 8.4.1 and 8.4.2. However, the stoichiometric C:H ratios for the aromatic polycycles proposed as potential overlayer species is between 1:1-1:1.2, which is quite different to the C:H ratios calculated for the various post-reaction CO hydrogenation catalysts listed in Table 9.8.1. In fact, C:H ratios of the catalysts that were most active in CO hydrogenation are far in excess of the proposed aromatic polycycles. This discrepancy in the observed global C:H ratios for the post-reaction catalysts and the candidate overlayer species is proposed to be due to the partitioning of carbon in the catalyst sample as a number of species including: iron carbide(s); a hydrocarbonaceous overlayer; and, possibly 'free' carbon.

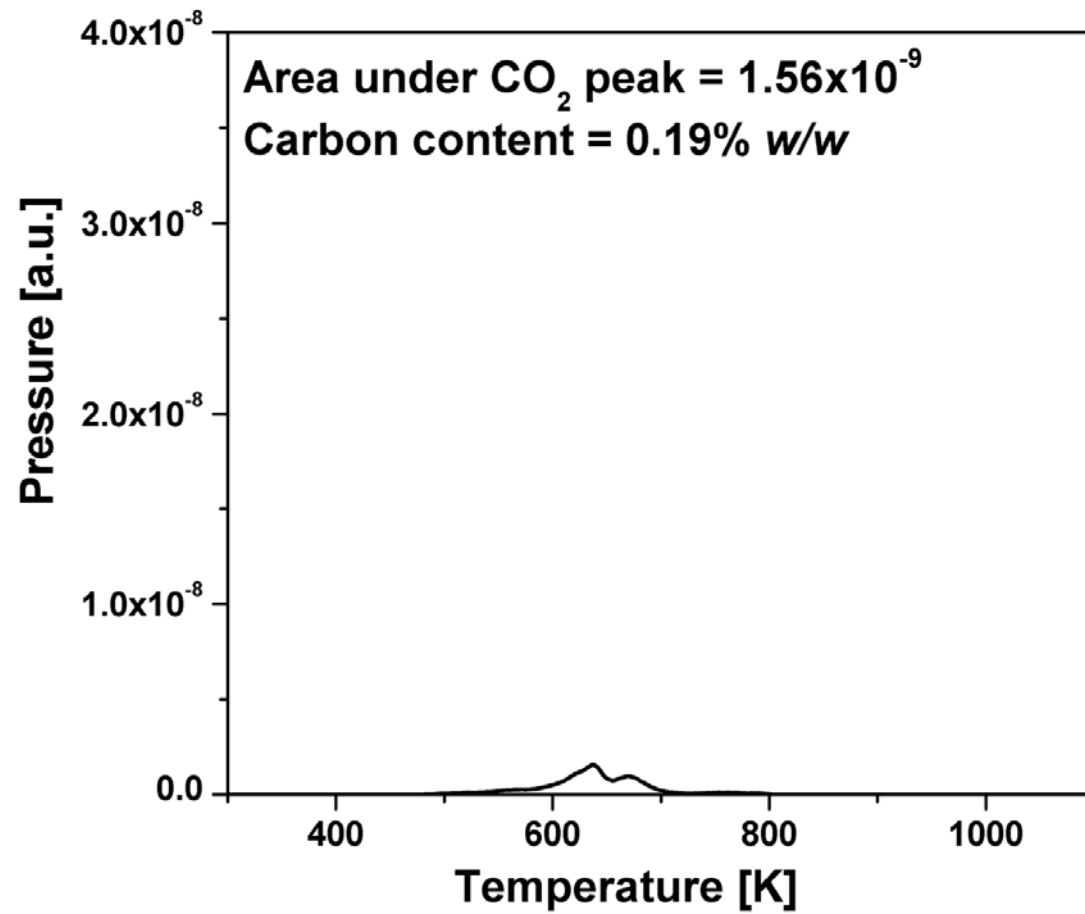


Figure 9.8.1: TPO profile for a sample of the iron catalyst after exposure to syngas at 623 K for 6h.

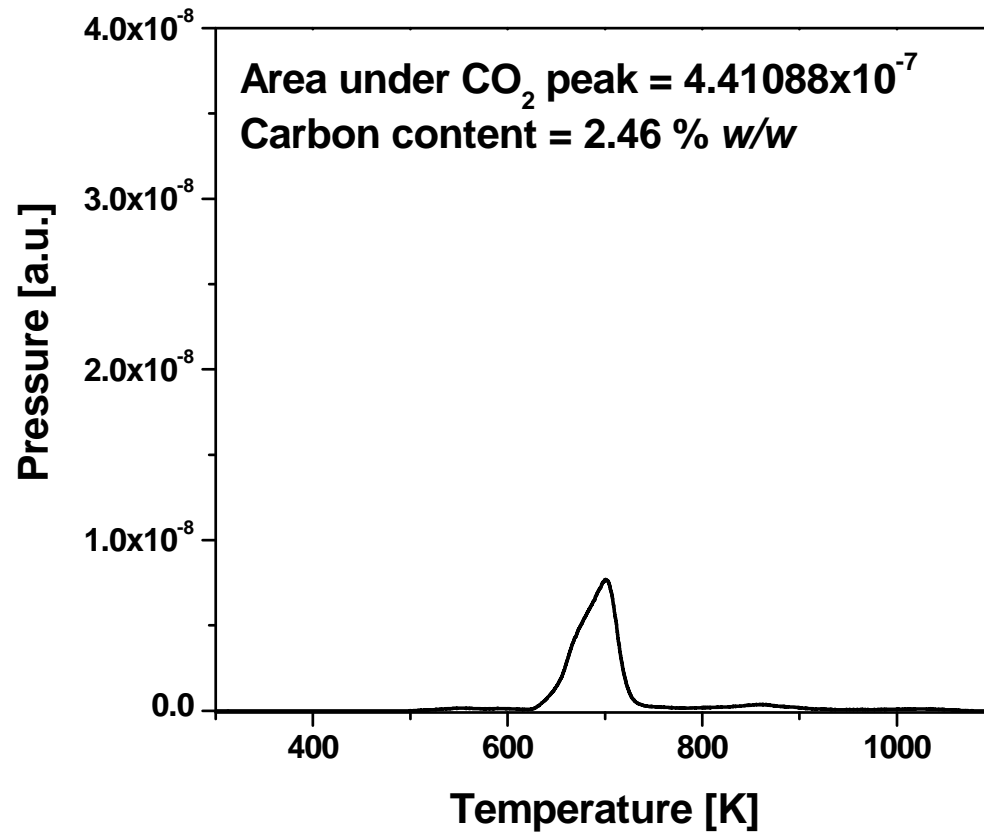


Figure 9.8.2: TPO profile for a sample of the iron catalyst after reduction in H<sub>2</sub> at 773 K followed by exposure to syngas at 623 K for 6h.

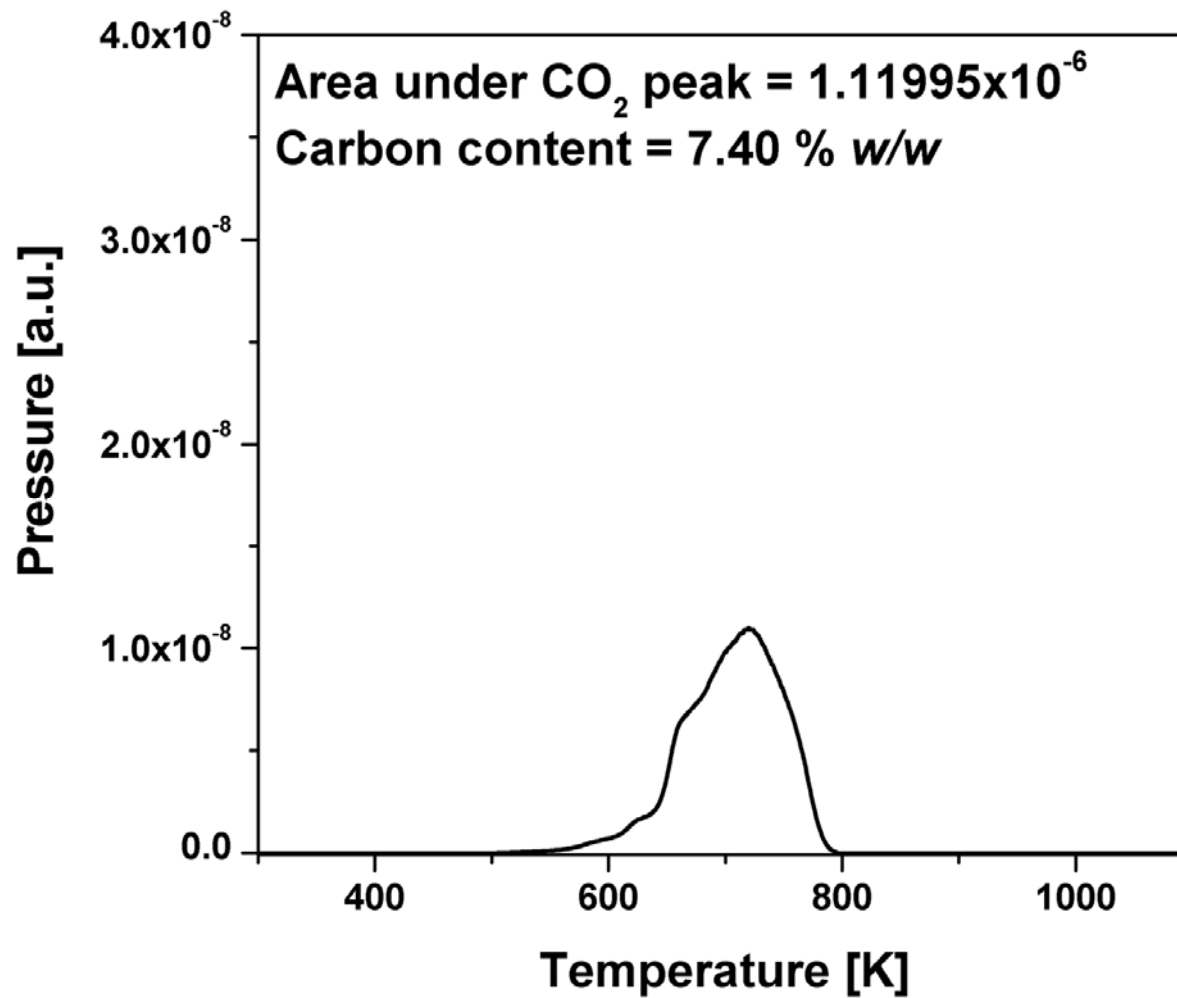


Figure 9.8.3: TPO profile for a sample of the iron catalyst after exposure to syngas at 723 K for 6h.

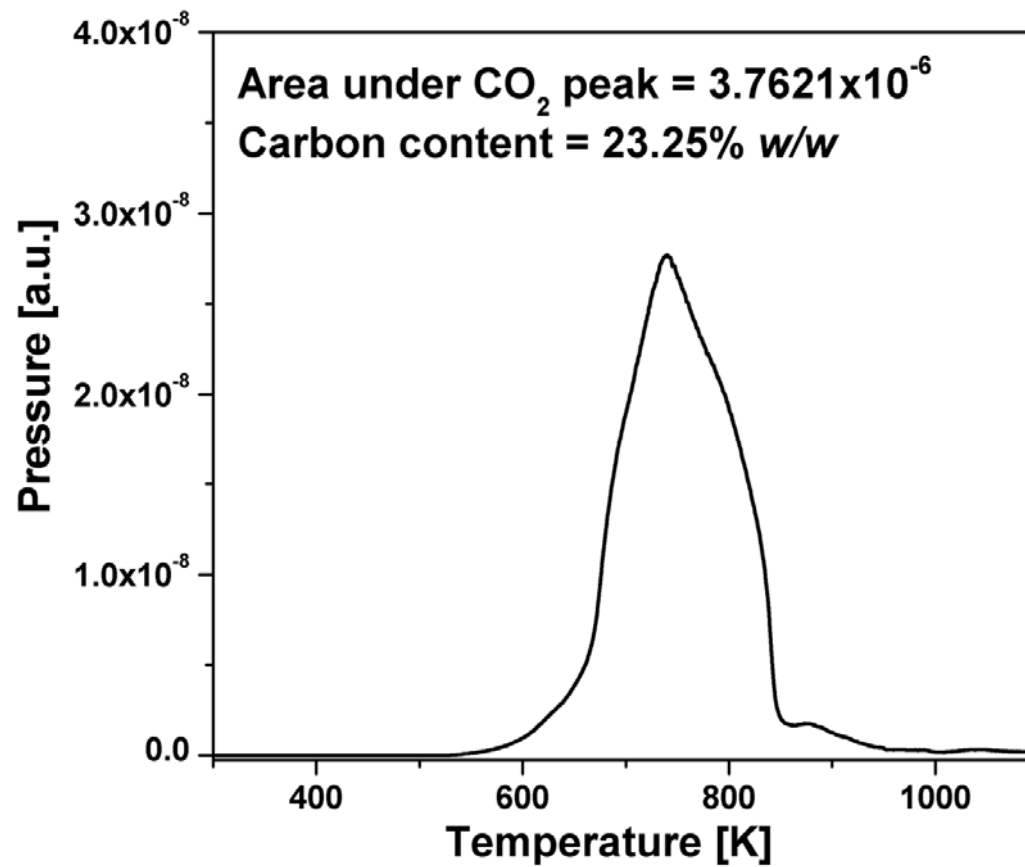


Figure 9.8.4: TPO profile for a sample of the iron catalyst after reduction in H<sub>2</sub> at 773 K followed by exposure to syngas at 723 K for 6h.

## 9.9 Transmission electron microscopy

The microstructure of the post-reaction catalyst samples were studied by transmission electron microscopy (TEM).

TEM images for sample of the catalyst after exposure to syngas at 623 K are presented in Figure 9.9.1. The sample is characterised by a series of particles of apparently random size and shape. Some particles are coated with a distinct overlayer with a thickness of *ca.* 5 nm, which could possibly represent the hydrocarbonaceous overlayer that is observed in the INS spectra and oxidised in the TPO measurements. The bulk of the material is attributed to Fe<sub>3</sub>O<sub>4</sub> as indicated by the associated XRD pattern (Figure 9.3.1). This image compares favourably with that reported by Shroff *et al.* [172] who made similar assignments for a sample of Fe<sub>2</sub>O<sub>3</sub> treated in syngas at 543 K. However, they suggested that the amorphous overlayer was supported on iron carbide particles and not on the underlying magnetite substrate. Interestingly, and in agreement with this investigation, Shroff *et al.* [172] could not detect the carbide phases in powder XRD measurements, but could provide evidence for their presence in the TEM images by *in situ* electron diffraction measurements. TEM images for the catalyst sample that was reduced before being exposed to syngas at 623 K are presented in Figure 9.9.2 and are almost identical to those observed for the catalyst that had not been reduced prior to syngas exposure, with the exception that fewer of the particles appear to present an overlayer.

The TEM images for the catalyst sample that was treated in syngas at 723 K are presented in Figure 9.9.3. These striking images show the catalyst sample to be composed of a series of dense, elliptical inclusions surrounded by an outer layer of *ca.* 5 nm thickness. These ellipses are superimposed upon an abundant, less dense material, assumed to be magnetite given its dominant contribution to the associated XRD pattern of this sample (Figure 9.3.3). Figure 9.9.3(b) shows a high magnification image of one of the elliptical particles. The lattice fringes observed here have a spacing of 2.09 Å, which is consistent with that of iron carbide species as reported by others. While the 2.09 Å fringes, by themselves, do not uniquely identify the carbide phase, it is a combination of the characterization techniques employed in this study that lead us to conclude that the particles observed in Figure 9.9.3 are iron carbide crystallites. Use of *in situ* electron diffraction would have assisted confirmation of this phase, this was not possible due to an insufficiently coherent electron beam.

TEM images of the catalyst sample reduced in H<sub>2</sub> prior to exposure to syngas at 723 K are presented in Figure 9.9.4. Here, the image is characterised by a series of large overlapping particles, attributed to iron carbide, surrounded by an overlayer of *ca.* 5 nm thickness. A high magnification TEM image of the sample, presented in Figure 9.9.4(b) shows the overlayer to be especially thick in some areas of the sample. The apparently high proportion of iron carbide and carbonaceous overlayer is consistent with the TPO, INS, and XRD measurements for this sample, which respectively indicate this sample to have a much higher carbon, hydrocarbon and carbide content than the other samples.

### ***Elemental Mapping***

In order to observe the two dimensional elemental distribution of the post-reaction sample previously reduced in H<sub>2</sub> followed by exposure to syngas at 723 K, energy filtered mapping was carried out. During TEM measurements, elastic and inelastic scattering of the electron beam by the atoms contained within the sample under investigation takes place. The quantity of energy lost in the inelastic scattering process is a function of the atoms native to the sample that are involved in the collision. Thus, by filtering the image so that only energy losses characteristic to a particular element are considered one can observe the contribution of that element to the complete TEM image. In order to construct a map of each element three images are collected from inelastically scattered electrons at, and in front of, the characteristic ionisation energy edge for each element, *e.g.* 700 eV for Fe. The elemental maps presented here are a composite image of one measurement taken at the ionisation edge and two others taken at energies just preceding the edge.

A series of energy filtered images were collected for iron and carbon with respective exposure times of 5s and 8s. A slit width of 35 keV was used throughout. The standard TEM image, *i.e.* taken with zero energy loss, elastically scattered electrons, is presented in Figure 9.9.5(a), while images filtered for iron and carbon are presented in Figures 9.9.5(b) and 9.9.5(c). Collectively, these images confirm that the dense particles observed in the standard TEM image (Figure 9.9.5(a)) contain iron and some carbon, which is consistent with the earlier assignment of these particles to iron carbide, and that the overlayer that surrounds these particles is carbon-rich.

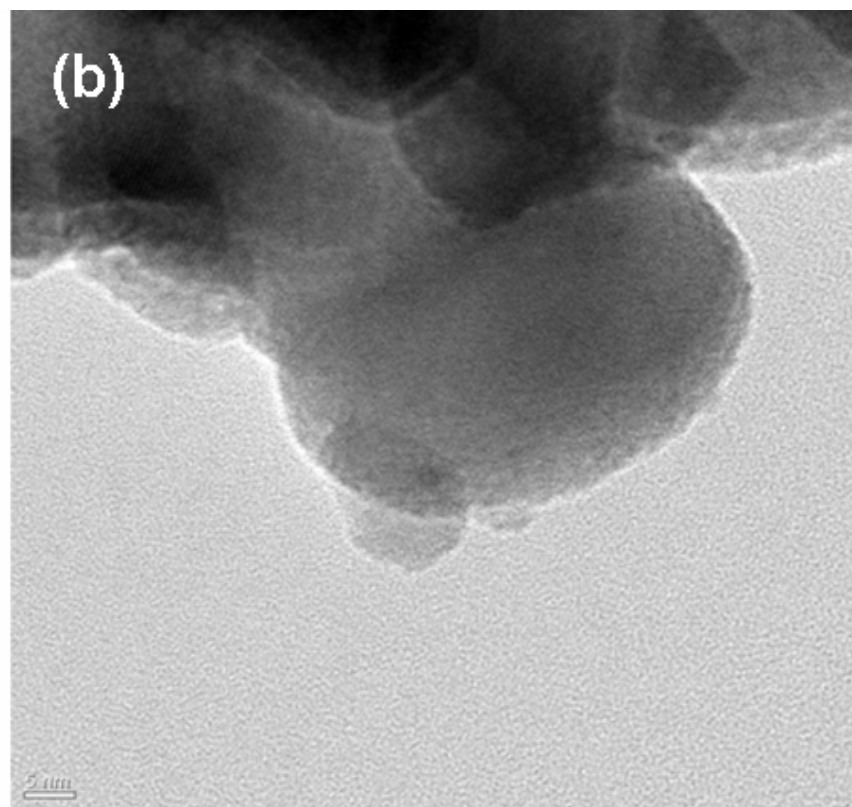
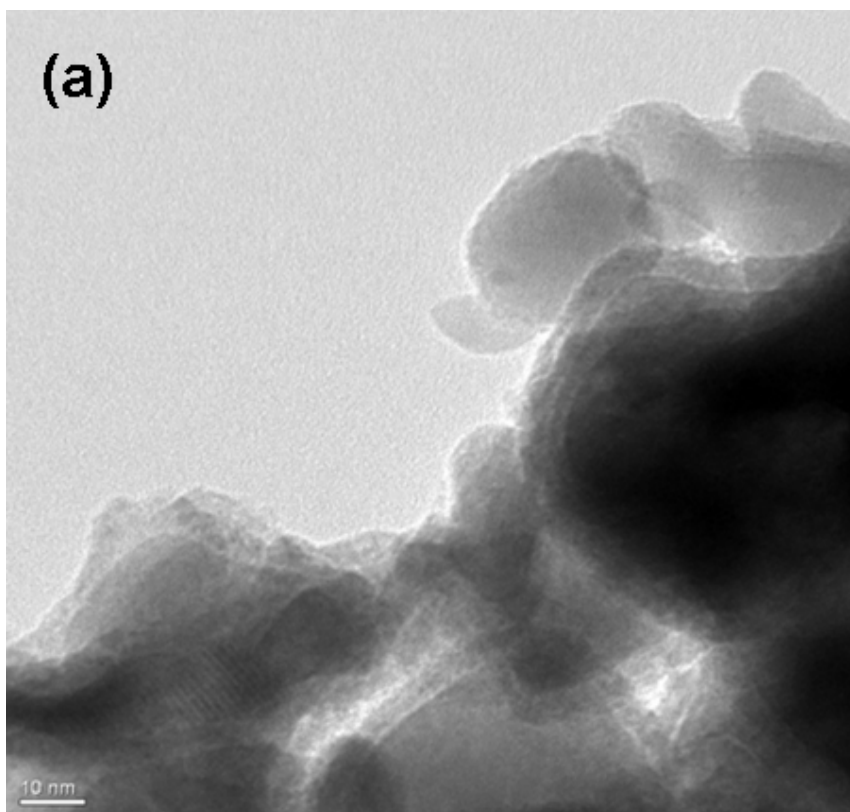


Figure 9.9.1: TEM images of a catalyst sample previously exposed to syngas at 623 K for 6h, recorded at (a) low magnification, and (b) high magnification.

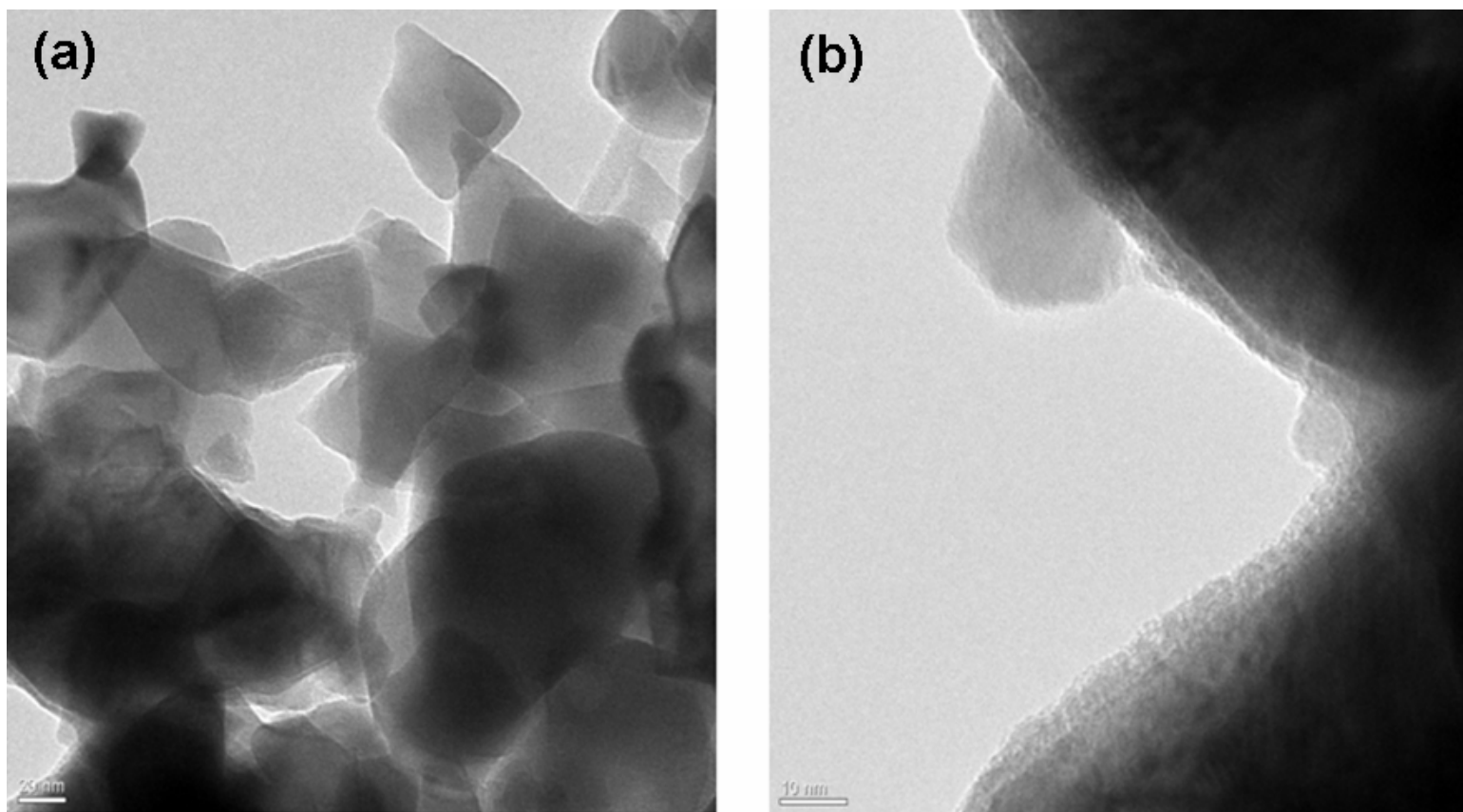


Figure 9.9.2: TEM images of a catalyst sample previously reduced at 773 K followed by syngas exposure at 623 K for 6h, recorded at (a) low magnification, and (b) high magnification.

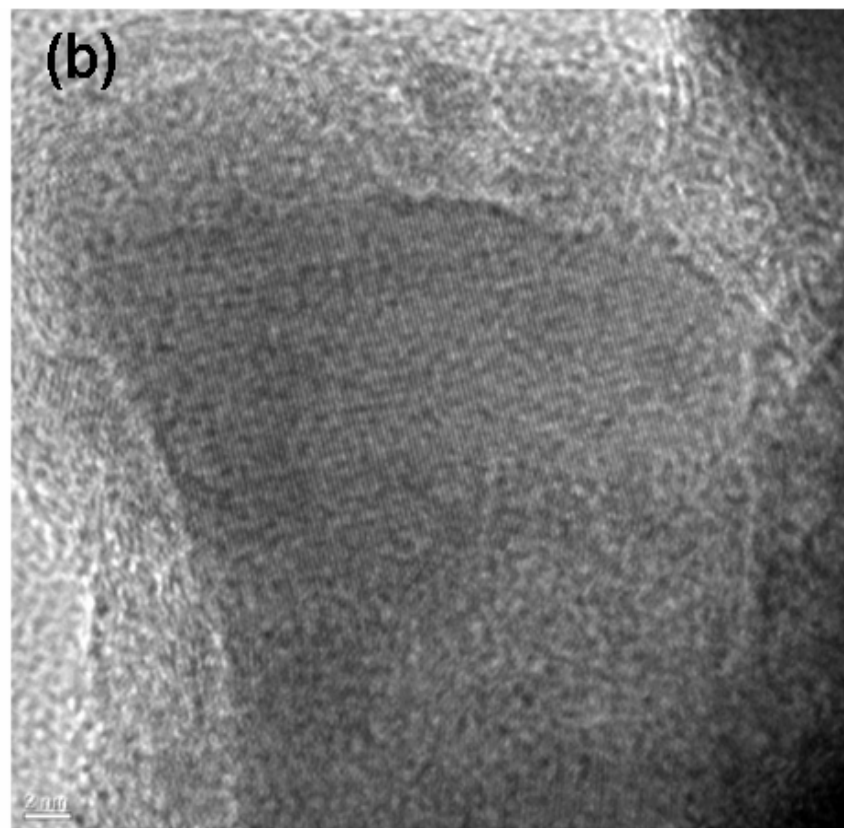
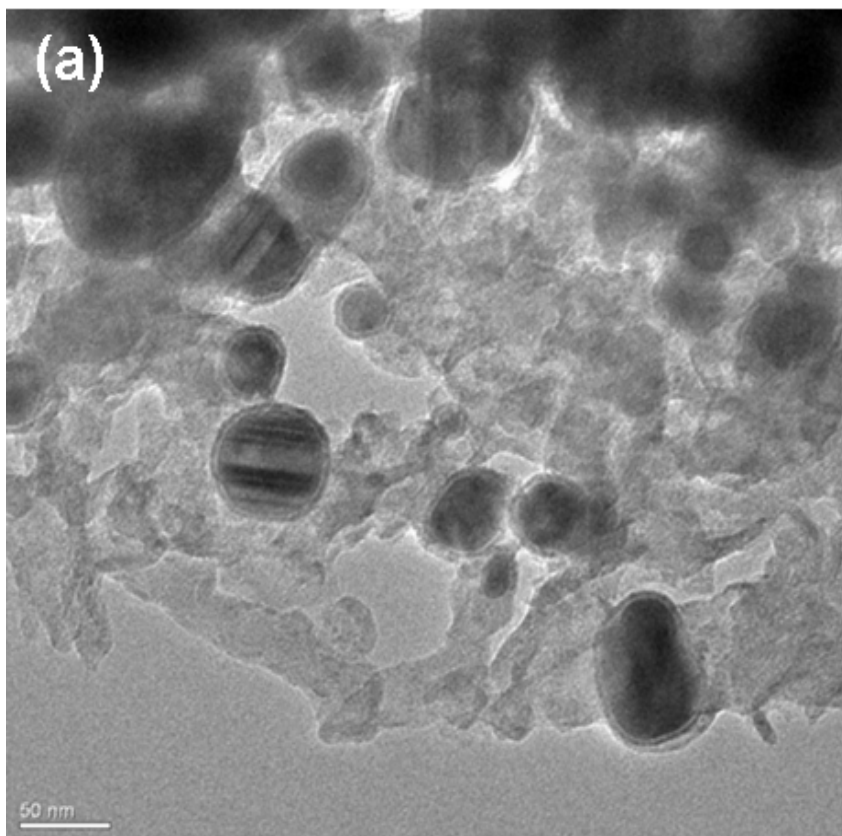


Figure 9.9.3: TEM images of a catalyst sample previously exposed to syngas at 723 K for 6h, recorded at (a) low magnification, and (b) high magnification.

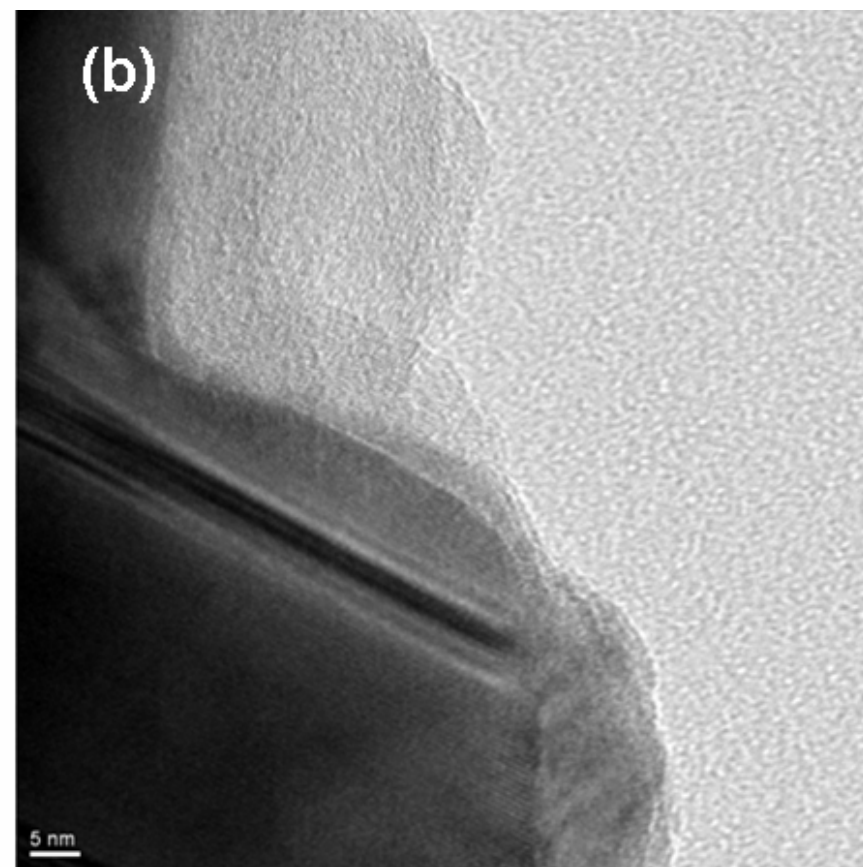
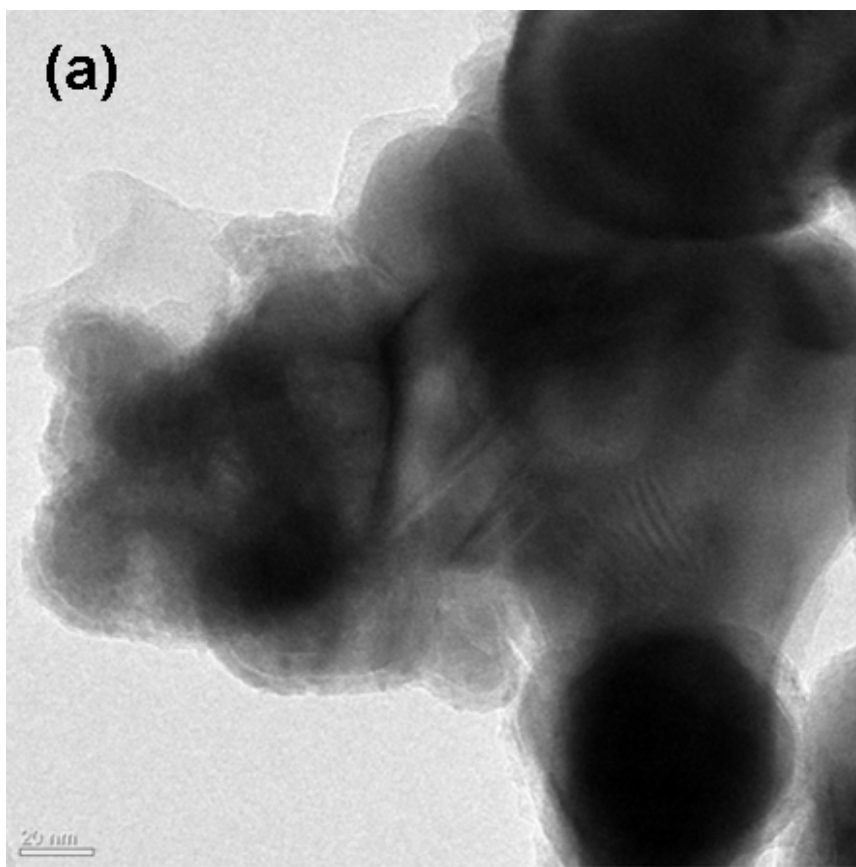


Figure 9.9.4: TEM images of a catalyst sample previously reduced at 773 K followed by syngas exposure at 723 K for 6h, recorded at (a) low magnification, and (b) high magnification.

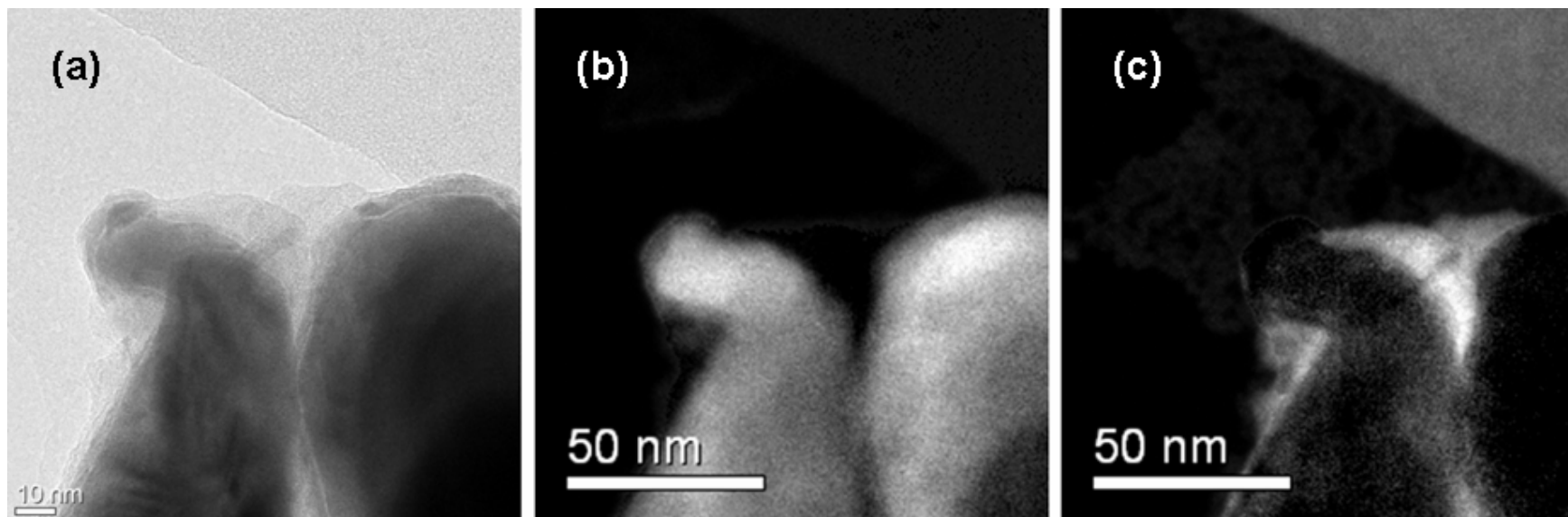


Figure 9.9.5: TEM images of a catalyst sample previously reduced at 773 K followed by syngas exposure at 723 K for 6h. (a) Zero energy loss TEM image of the sample. (b) Image of inelastically scattered electrons corresponding to iron (*e.g.* energy loss = 700 eV). (c) Image of inelastically scattered electrons corresponding to carbon (*e.g.* energy loss = 284 eV).

## 9.10 Conclusions

Temperature programmed reaction studies showed that a temperature greater than 623 K was required to produce a significant quantity of CH<sub>4</sub> detectable by online quadrupole mass spectrometry. XRD measurements showed the samples treated in syngas at 623 K to be almost exclusively composed of Fe<sub>3</sub>O<sub>4</sub>, while treatment in syngas at 723 K led to a significant proportion of iron carbide species, which compare well with database patterns for Hägg carbide,  $\chi$ -Fe<sub>3</sub>C<sub>2</sub>. The sample that had been reduced prior to exposure to syngas contained the greatest relative proportion of iron carbides. Raman spectroscopy showed the sample treated in syngas at 723 K to contain a hydrocarbonaceous component with a low hydrogen content.

Inelastic neutron scattering (INS) spectroscopic measurements were performed using the highly sensitive MAPS instrument, which was calibrated with a number of polystyrene reference standards to reveal a linear response curve that was subsequently used to quantify the hydrogen contained within the hydrocarbonaceous overlayer deposited on each post-reaction catalyst sample. The samples treated at 723 K contained significantly more hydrocarbon than the samples treated at 623 K. The sample reduced in hydrogen prior to syngas exposure at 723 K contained the greatest amount of hydrocarbon of all.

Temperature programmed oxidation (TPO) measurements showed all samples to contain carbon. The samples treated in syngas at 723 K contained vastly more carbon than those treated at 623 K, while reduction of the catalysts prior to syngas exposure also lead to greater carbon laydown. The profiles of the samples, especially those treated at 723 K, revealed a range of carbon environments, which is consistent with the presence of iron carbides and hydrocarbonaceous deposits as evidenced, respectively, by XRD and INS measurements. The TPO profile of the catalysts treated in syngas at 723 K had features located in a similar temperature range to those observed in industrial grade FTS catalysts although the profiles were of a different shape.

Combination of the quantifiable INS and TPO measurements yielded a novel method for the determination of the C:H ratio of a carbonaceous overlayer, however in the case of iron CO hydrogenation catalysts the presence of other carbon containing species, *e.g.* iron carbides, distorts this value.

TEM measurements allowed observation of the microstructure of the catalysts and provided further evidence for iron carbide particles surrounded by a carbonaceous overlayer.

Collectively, the data presented here indicates the presence of  $\text{Fe}_3\text{O}_4$ , an iron carbide species (most likely Hägg carbide,  $\chi\text{-Fe}_5\text{C}_2$ ), and a hydrocarbonaceous overlayer in iron-based catalysts active in the hydrogenation of CO to yield  $\text{CH}_4$ . The presence of an amorphous, purely carbonaceous, component cannot be discounted. Figure 9.10.1 presents a graphical interpretation of the phases observed in the catalyst samples after exposure to syngas at 723 K. The presence of each phase is justified by the various analyses described throughout this chapter. Briefly, there is an underlying magnetite substrate upon which iron carbide crystallites are supported. The iron carbide particles can then support a hydrocarbonaceous overlayer. The role of the hydrocarbonaceous overlayer as either a promoter or poison remains unclear. This hydrocarbonaceous overlayer is the only species where hydrogen and carbon are incorporated and it is possible that a thin layer of this, possibly highly active, polycyclic aromatic hydrocarbon species is intimately associated with the iron carbide which is then surrounded by inactive amorphous carbon. It is this phase where CO hydrogenation activity and FTS activity is proposed to originate. Similar schemes describing the phases present within active iron-based FTS catalyst, where an underlying magnetite substrate supports iron carbide crystallites, which in turn are surrounded by a carbonaceous component, have been reported by both Shroff *et al.* [172, 263] and Dry [166]. The most novel aspect of this investigation is that spectroscopic evidence has been provided that supports the presence of a polycyclic aromatic hydrocarbonaceous residue that has not been previously reported. This observation was made possible by the application of INS spectroscopy, which has not previously been used to study iron based Fischer-Tropsch and CO hydrogenation catalysts.

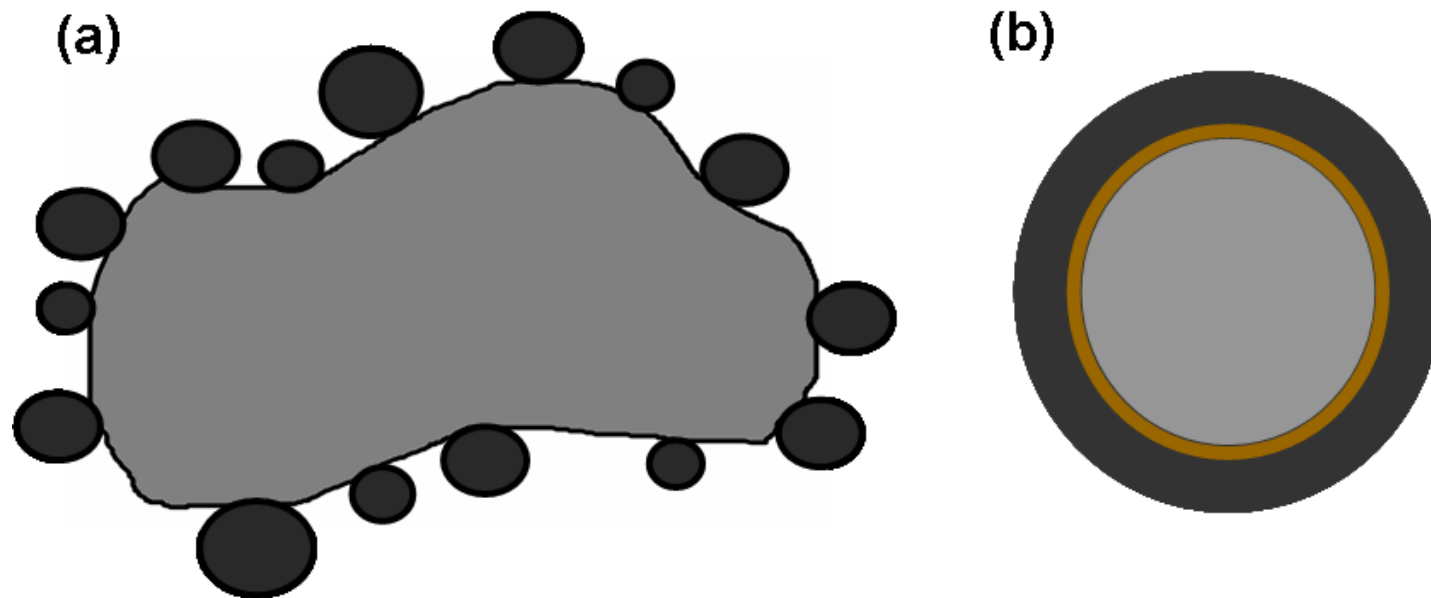


Figure 9.10.1: Graphical representation of the phases present in an iron-based CO hydrogenation catalyst: (a) A magnetite substrate which supports a number of iron carbide crystallites; (b) An expanded view of an iron carbide crystallite. The iron carbide phase in the centre of the particle is surrounded by a thin layer of polycyclic aromatic hydrocarbon (orange), which could be highly active in CO hydrogenation. The hydrocarbonaceous overlayer is surrounded by an amorphous layer of inactive carbon (dark grey).

# 10

## Chapter 10 Summary

## 10.1 Activation of transition alumina catalysts

The examination of an  $\eta$ - $\text{Al}_2\text{O}_3$  catalyst via inelastic neutron scattering (INS) spectroscopy has provided spectroscopic evidence for the processes occurring during thermal activation.

The main conclusions are summarised below:

- INS spectroscopy was used to characterise the thermal activation of an  $\eta$ - $\text{Al}_2\text{O}_3$  catalyst. INS spectroscopy uniquely allowed the observation of both out-of-plane and in-plane hydroxyl deformation modes. In this manner, INS provided spectroscopic evidence for the desorption of both chemisorbed water and surface hydroxyl species upon thermal activation, which is in agreement with the generally accepted activation mechanism for metal oxides described by Kung [54], but has not previously been shown within a single spectroscopic measurement.
- The surface Lewis acidity generated upon exposure of the  $\eta$ - $\text{Al}_2\text{O}_3$  catalyst to the activation conditions described here is sufficient to catalyse the dehydration of methanol to yield dimethyl ether. The surface acidity of the activated catalyst was further characterised by observation of the infrared spectra of chemisorbed pyridine and was found to conform to the surface model proposed by Lundie *et al.* [38].

## 10.2 Modification of surface Lewis acidity of transition alumina catalysts

This section of the investigation considered physical routes to modify the acid site distribution of an  $\eta$ - $\text{Al}_2\text{O}_3$  catalyst, as an alternative to more traditional approach of doping the surface with alkali metal salts. The conclusions drawn from this study are summarised below:

- X-ray diffraction (XRD) measurements have revealed that calcination of an  $\eta$ - $\text{Al}_2\text{O}_3$  catalyst at temperatures  $\geq 1073$  K promotes a progressive phase transformation towards  $\theta$ - $\text{Al}_2\text{O}_3$ . The pore size distribution of a series of differently calcined  $\eta$ - $\text{Al}_2\text{O}_3$  catalysts revealed that the phase transformation proceeded via a displacive merging of the lamellar mesostructure of the material.
- Infrared spectroscopic measurements of adsorbed pyridine showed that the surface Lewis acidity of a  $\eta$ - $\text{Al}_2\text{O}_3$  could indeed be modified by careful calcination of the

catalyst. These measurements revealed the total population of Lewis acid sites to decline on increasing calcination temperature but that so-called *medium-strong* Lewis acid sites were preferentially attenuated in favour of *medium-weak* Lewis sites.

### 10.3A new vibrational probe for Lewis acidity

This section employed a combination of inelastic neutron scattering and periodic *ab initio* calculations to explore the behaviour of the vibrational modes of pyridine adsorbed on an activated alumina surface. The main conclusions are summarised as follows:

- INS spectroscopy revealed a number of low energy modes of pyridine adsorbed on an activated  $\eta$ -Al<sub>2</sub>O<sub>3</sub> catalyst that are otherwise inaccessible via conventional optical spectroscopic techniques, *e.g.* infrared spectroscopy.
- The  $\nu_{6a}$  mode, located at 440 cm<sup>-1</sup> in the spectrum of solid pyridine, was observed to be sensitive to Lewis acidity, exhibiting an unprecedented energy shift of -165 cm<sup>-1</sup> upon adsorption to the Lewis acidic  $\eta$ -Al<sub>2</sub>O<sub>3</sub> substrate.
- Periodic DFT investigations verified this observation and revealed the  $\nu_{6a}$  mode to split into two discrete vibrational states upon adsorption.
- Data from the DFT calculations was used to simulate the INS spectrum of pyridine adsorbed on an  $\alpha$ -Al<sub>2</sub>O<sub>3</sub> (0001) surface, which gave a satisfactory correlation with an experimentally acquired spectrum of pyridine adsorbed on  $\eta$ -Al<sub>2</sub>O<sub>3</sub>, thereby ratifying the validity of the DFT model.

## 10.4 Analysis of a post-reaction fused iron Fischer-Tropsch catalyst

This section investigated the application of INS spectroscopy and other laboratory-based techniques to the characterisation of hydrocarbonaceous species deposited on the surface of a fused iron catalyst after a full industrial cycle in a fluidised bed Fischer-Tropsch synthesis reactor. The main conclusions are summarised below:

- Raman scattering spectroscopic measurements indicate the post-reaction catalyst samples to contain a carbon-rich polyaromatic ring compounds containing  $sp^2$  carbon atoms.
- INS measurements were compliant with the deductions made from the Raman measurements and indicated the carbonaceous overlayer to be composed of a carbonaceous polycyclic aromatic compound that contained a small proportion of aliphatic moieties.
- INS spectra of the catalyst fines compared favourably against simulated INS spectra of candidate partially hydrogenated polyaromatic ring compounds.
- Powder x-ray diffraction (XRD) measurements revealed the catalyst samples to be largely composed of magnetite with contributions from iron carbide species.
- Temperature programmed oxidation (TPO) measurements revealed the catalyst to present a number of largely non-graphitic carbon environments.
- The TPO apparatus was calibrated to allow quantification of carbon, which revealed the catalyst sample to have carbon loading of *ca.* 15% w/w, which compared favourably with parallel CHN microanalysis.

## 10.5 Carbon monoxide hydrogenation over an iron oxide precursor

This section investigated the composition of a precipitated iron oxide catalyst after ambient pressure hydrogenation of carbon monoxide towards methane. The main conclusions drawn from this study are summarised below:

- Temperature programmed reaction studies showed that a temperature greater than 623 K was required to produce a significant quantity of CH<sub>4</sub> detectable by online quadrupolar mass spectrometry.
- XRD measurements showed the samples treated in syngas at 623 K to be almost exclusively composed of Fe<sub>3</sub>O<sub>4</sub>, while treatment in syngas at 723 K led to a significant proportion of iron carbide species. Reduction of samples prior to reaction led to a greater relative proportion of iron carbides.
- Raman spectroscopy showed the sample treated in syngas at 723 K to contain a hydrocarbonaceous component with a low hydrogen content.
- Inelastic neutron scattering (INS) spectroscopic measurements were performed using the sensitive MAPS instrument, which was used to quantify the hydrogen contained within the hydrocarbonaceous overlayer deposited on each post-reaction catalyst sample. The samples treated at 723 K contained significantly more hydrocarbon than the samples treated at 623 K. The sample reduced in hydrogen prior to syngas exposure at 723 K contained the greatest quantity of hydrocarbon.
- Temperature programmed oxidation (TPO) measurements showed all samples to contain carbon. The profiles of the samples revealed a range of carbon environments, consistent with the presence of iron carbides and hydrocarbonaceous species. The TPO profile of the catalysts treated in syngas at 723 K had features located in a similar temperature range to those observed in industrial grade FTS catalysts, although the profiles were somewhat different.
- Combination of the INS and TPO measurements yielded a novel method for the determination of the C:H ratio of a carbonaceous overlayer. However, in the case of

iron CO hydrogenation catalysts the presence of other carbon containing species, *e.g.* iron carbides, distorts this value.

## 10.6 Future work

### 10.6.1 Alumina

The  $-165\text{ cm}^{-1}$  energy shift exhibited by the  $\nu_{6a}$  mode of pyridine upon adsorption to an activated  $\eta\text{-Al}_2\text{O}_3$  catalyst is intriguing. It would be fruitful to repeat these experiments using a series of Lewis acidic substrates to determine whether this effect can be used to quantify the strength of the acidity or can merely be used as an indicator. Likewise, expansion of the *ab initio* investigation to study an alumina substrate that presents a number of Lewis acid sites would also assist this investigation.

### 10.6.2 Iron catalysts

Although the work presented here has improved the current understanding of the hydrocarbonaceous overlayer present on the surface of iron-based catalysts after Fischer-Tropsch synthesis (FTS) and CO hydrogenation, its exact role in the process is still not fully understood. The investigation presented here could be expanded in a number of ways. Mossbauer spectroscopic measurements would reveal the identity of the carbide phases present within the catalyst. Extracting samples from a reactor at various points during the catalyst lifetime and analysing using the techniques described here with additional Mossbauer measurements could help identify the time-dependent changes that occur to the catalyst during FTS. Investigations of the precipitated iron oxide catalyst under FTS conditions using an *in situ* INS cell were initiated but difficulties in the sample handling and cell design prevented the acquisition of useful data. Further work in this area could provide a unique opportunity for the collection of the INS spectrum of an active iron based FTS catalyst without having to undertake intricate sample handling procedures.

# 11

## Chapter 11 References

1. A. Terinin, *Zhur. Fiz. Khim.*, 1940(14), p. 1362.
2. A. Terinin and L. Roev, *Spectrochem. Acta*, 1959(11), p. 946.
3. R. P. Eischens and W.A. Pliskin, *Adv. Catal.*, 1958. **10**, p. 2.
4. N. Sheppard and D.J.C. Yates, *Proc. R. Soc.*, 1956, p. 69.
5. N. Sheppard, *Spectrosc. Eur.*, 1994. **6**, p. 20.
6. J. M. Chalmers and G. Dent, in *Industrial analysis with vibrational spectroscopy*. 1997, Cambridge: Royal Society of Chemistry. 153.
7. P.R. Griffiths, *Chemical Infrared Fourier Transform Spectrometry*. 2nd ed. 2007, New York: Wiley.
8. C. Morterra and G. Magnacca, *Catal. Today*, 1996. **27**, p. 497.
9. P. D. Holmes, G. S. McDougal, I. C. Willcock, and K.C. Waugh, 1991. **9**, p. 15.
10. J. T. Yates and T.E. Madey, in *Vibrational spectroscopy of molecules on surfaces*. 1987, Plenum Press: New York, London.
11. G. Busca, *Catal. Tod.*, 1996. **27**, p. 323.
12. P. Kubelka and F. Munk, *Z. Tech. Physik*, 1931.
13. B.C. Smith, in *Fundamentals of Fourier transform infrared spectroscopy*. 1996, CRC Press: London.
14. P. C. H. Mitchell, S. F. Parker, A. J. Ramirez-Cuesta, and J. Tomkinson, *Vibrational spectroscopy using neutrons*. Series on Neutron Techniques and Applications. Vol. 3. 2005: World Scientific.
15. P.W. Albers, J. Pietsch, J. Krauter, and S.F. Parker, *Phys. Chem. Chem. Phys.*, 2003. **5**(9), p. 194.
16. J.M. Hollas, *Modern Spectroscopy*. 2004, Chichester: J. Wiley.
17. B.S. Hudson, *J. Phys. Chem. A*, 2001. **105**, p. 3949-3960.
18. A.J. Ramirez-Cuesta, *Comp. Phys. Commun.*, 2004. **157**(3), p. 226.
19. S.F. Parker, C.J. Carlile, T. Pike, J. Tomkinson, R.J. Newport, C. Andreani, F.P. Ricci, F. Sacchetti, and M. Zoppi, *Physica B*, 1997. **241**, p. 154.
20. A. D. Taylor, R. C. Ward, W. G. Williams, Y. Endoh, and N. Watanabe, *MARS - A multi-angle rotor spectrometer at the pulsed neutron source ISIS*, in *Proc. ICANS IX, SIN Report 40926*, F. Atchison and W. Fischer, Editors. 1987. p. 535.
21. T. G. Perring, A. D. Taylor, R. Osborn, D. McK. Paul, A. T. Boothroyd, and G. Aeppli, *Proc. ICANS XII, RAL Report 94-025* 1994, p. 1.
22. J. T. McCartney, L. J. E. Hofer, B. Seligman, J. A. Lecky, W. C. Peebles, and R.B. Anderson, *J. Phys. Chem. A*, 1953. **57**(7), p. 730.
23. R. J. O'Brien, L. Xu, R. L Spicer, and B. Davis, *Energy & Fuels*, 1996. **10**, p. 921.
24. L. D. Mansker, Y. Jin, D. B. Bukur, and A. Datye, *Appl. Catal. A.*, 1999. **186**, p. 277.
25. F. J. Perez-Alonso, M. Lopez Granados, M. Ojeda, P. Terreros, S. Rojas, T. Herranz, J. L. G. Fierro, M. Gracia, and J.R. Gancedo, *Chem. Mater.*, 2005. **17**, p. 2329.
26. H. Knozinger and P. Ratnasamy, *Catal. Rev.: Sci. Eng.*, 1978. **17**(1), p. 31.
27. D. Lennon, D. R. Kennedy, G. Webb, and S.D. Jackson, *Stud. Surf. Sci. Catal.*, 1999. **126**, p. 341.
28. D. R. Kennedy, G. Webb, S. D. Jackson, and D. Lennon, *Appl. Catal. A*, 2004. **259**, p. 109.
29. OriginLab, *Origin 6.1*: Northampton.
30. S. Brunauer, P. H. Emmett, and E. Teller, *J. Am. Chem. Soc.*, 1938. **60**, p. 309.
31. E. P. Barrett, L. G. Joyner, and P.P. Halenda, *J. Am. Chem. Soc.*, 1951. **73**, p. 373.
32. C. H. Bartholomew and R.J. Farrauto, *Fundamentals of industrial catalytic processes*. 2006, New Jersey: Wiley.
33. K. Weissermel and H.-J. Arpe, *Industrial Organic Chemistry*. 4th ed. 2003, Weinheim: Wiley-VCH.
34. K. Wefers and C. Misra, *Oxides and hydroxides of aluminium, Alcoa technical*

- report 19. 1987.
35. B.C. Lippens and J.H. de Boer, *Acta Crystallogr.*, 1964. **17**(10), p. 1312-21.
  36. C.N. Satterfield, *Heterogeneous Catalysis in Industrial Practice. 2nd Ed.* 1996. p. 554.
  37. M. Digne, P. Sautet, P. Raybaud, P. Euzen, and H. Toulhoat, *J. Catal.*, 2002. **211**, p. 1.
  38. D. T. Lundie, A.R. McInroy, R. Marshall, J. M. Winfield, P. Jones, C. C. Dudman, S. F. Parker, C. Mitchell, and D. Lennon, *J. Phys. Chem. B*, 2005. **109**, p. 11592.
  39. A.R. McInroy, D.T. Lundie, J.M. Winfield, C.C. Dudman, P. Jones, and D. Lennon, *Appl. Catal. B*, 2007. **70**(1-4), p. 606.
  40. S.I. Ivanov and V.A. Makhlin, *Kinet. Catal.* , 1996. **37**(6), p. 812.
  41. V.A. Makhlin and S.I. Ivanov, *Kinet. Catal.* , 1997. **38**(6), p. 864.
  42. C. J. Mitchell and P. Jones, *Patent: Use of alkali metal-doped  $\gamma$ -alumina as methanol hydrochlorination catalyst, Patent number: 2000-GB2122 2000076658* 2000, Imperial Chemical Industries Plc, UK. p. 18.
  43. W.K. Hall, F.E. Lutinski, and H.R. Gerberich, *J. Catal.*, 1964. **3**, p. 512.
  44. H. Pines and W. Haag, *J. Am. Chem. Soc.*, 1964. **12**, p. 2471.
  45. D.S. MacIver, H.H. Tobin, and R.T. Barth, *J. Catal.*, 1963. **2**.
  46. J.B. Peri, *J. Phys. Chem.*, 1965. **69**, p. 220.
  47. H. Knozinger, *Adv. Catal.*, 1976. **25**, p. 184.
  48. A. Corado, A. Kiss, H. Knozinger, and H.-D. Mueller, *J. Catal.*, 1975. **37**, p. 68.
  49. J. H. de Boer, R. B. Fahim, B. G. Linsen, W.J. Visseren, and W.F.N.M.de Vleeschauwer, *J. Catal.*, 1967. **7**, p. 163.
  50. B. C. Shi and B.H. Davis, *J. Catal.*, 1995. **157**, p. 359.
  51. F.H. van Cauwelaert and W.K. Hall, *Trans. Faraday Soc.*, 1970. **66**(2), p. 454.
  52. K. Sohlberg, S.T. Pantelides, and S.J. Pennycook, *J. Am. Chem. Soc.* , 2001. **123**(1), p. 26.
  53. A. Leonard, P.N. Semaille, and J.J. Fripiat, *Proc. Brit. Ceram. Soc.* , 1969. **13**, p. 103.
  54. H.H. Kung, *Stud. Surf. Sci. Catal.*, 1989. **45**, p. 285.
  55. D.S. MacIver, W.H. Wilmot, and J.M. Bridges, *J. Catal.*, 1964. **3**.
  56. M. Nagao and T. Morimoto, *J. Phys. Chem.*, 2002. **84**(16), p. 2054.
  57. R. L. Burwell Jr, G. L. Haller, K. C. Taylor, J. F. Read, D. D. Eley, H. Pines, and P.B. Weisz, *Adv. Catal.*, 1969. **20**, p. 1.
  58. J.-C. Lavalley and M. Benaissa, *J. Chem. Soc., Chem. Commun.*, 1984. **588**, p. 908.
  59. R. S. Schiffino and R. P. Merrill, *J. Phys. Chem.*, 1993. **97**, p. 6425.
  60. H. Tummes, J. Falbe, and B. Cornils, *West German Patent 1,817,051*. 1972.
  61. R.M. Pearson, *J. Catal.*, 1977. **46**, p. 278.
  62. L. Oliviero, A. Vimont, J.-C. Lavalley, F. Romero Sarria, M. Gaillard, and F. Mauge, *Phys. Chem. Chem. Phys.* , 2005. **7**(8), p. 1861.
  63. J.C. Lavalley, M. Bensitel, J.P. Gallas, J. Lamotte, G. Busca, and V. Lorenzelli, *J. Mol. Struc.*, 1988. **175**, p. 453.
  64. C. Morterra, A. Chiorino, G. Ghiotti, and E. Garrone, *J. Chem Soc. Faraday Trans.*, 1979. **75**, p. 271.
  65. X. Liu and R.E. Truitt, *J. Am. Chem. Soc.* , 1997. **119**(41), p. 9856.
  66. S.E. Tung and E. McIninch, *J. Catal.*, 1964. **3**(3), p. 229.
  67. M. Guisnet, *Stud. Surf. Sci. Catal.*, 1985. **20**(Catal. Acids Bases), p. 283.
  68. M. B. Smith and J. March, *March's Advanced Organic Chemistry - Reactions, Mechanisms, and Structure, 5th ed.* 2001, New York: J. Wiley & sons.
  69. O.F. Kirina, T.V. Antipina, and G.D. Chukin, *Russ. J. Phys. Chem.*, 1973. **47** p. 248.
  70. C. Morterra, G. Cerrato, and G. Meligrana, *Langmuir* 2001. **17**(22), p. 7053.
  71. T. R. Hughes, H. M. White, and R.J. White, *J. Catal.*, 1969. **13**, p. 58.
  72. J. W. Ward and R.C. Hansford, *J. Catal.*, 1969. **13**, p. 154.

73. J. Dewing, G. T. Monks, and B. Youll, *J. Catal.*, 1977. **44**(2), p. 226.
74. J. Shen, R. D. Cortright, Y. Chen, and J.A. Dumesic, *J. Phys. Chem.*, 1994. **98**, p. 8067.
75. Y-F. Shen, S. Suib, M. Deeba, and G.S. Koermer, *J. Catal.*, 1994. **146**, p. 483.
76. H. Schaper, E. B. M. Doesburg, P. H. M. de Korte, and L.L.van Reijen, *Solid State Ionics* 1985. **16**, p. 261.
77. X. Liu, *J. Phys. Chem. C*, 2008. **112**, p. 5066.
78. L. M. Kustov, V.Y. Borovkov, and V.B. Kazanskii, *Russian J. Phys. Chem.* , 1985. **59**, p. 1314.
79. P.A. Korovchenko, R.A. Gazarov, and L.M. Kustov, *Russ. Chem. Bull.* , 1999. **48**(10), p. 1994.
80. H. D. Ruan, R. L. Frost, and J.T. Klopogge, *Appl. Spec.*, 2001. **55**(2), p. 190.
81. J.W. Niemantsverdriet, *Spectroscopy in Catalysis: an introduction*. 3rd ed. 2007, Weinheim: Wiley-VCH.
82. R.M. Pittman and A.T. Bell, *Catal. Lett.*, 1993. **24**, p. 1.
83. P. F. McMillan and R.L. Remmele, *Am. Miner.*, 1986. **71**, p. 772.
84. F.R. Brown, L.E. Makovsky, and K.H. Rhee, *J. Catal.*, 1977. **50**, p. 385.
85. I.E. Wachs, *Catal. Today* 1996. **27**, p. 437.
86. A. R. McInroy, D. T. Lundie, J. M. Winfield, C. C. Dudman, P. Jones, S.F. Parker, and D. Lennon, *Catal. Today*, 2006. **114**, p. 403.
87. H. Benesi, *J. Phys. Chem.*, 1957. **61**, p. 970.
88. H. Benesi, *J. Am. Chem. Soc.* , 1956. **78**, p. 5490.
89. A.N. Webb, *Ind. and Eng. Chem.*, 1957. **49**, p. 261.
90. R.T. Barth and E.V. Ballou, *Anal. Chem.*, 1961. **33**, p. 1081.
91. A.R. McInroy, *Investigation of a new generation of methyl chloride synthesis catalysts*, in *Chemistry*. 2006, University of Glasgow: Glasgow.
92. E.P. Parry, *J. Catal.*, 1963. **2**, p. 371.
93. P.J. Hendra, I.D.M. Turner, E.J. Loader, and M. Stacey, *J. Phys. Chem.*, 1974. **78**(3), p. 300.
94. G. Busca, V. Lorenzelli, G. Ramis, and R.J. Willey, *Langmuir*, 1993. **9**, p. 1492.
95. E. M. Eyring, S.M. Riseman, and F.E. Massoth, in *Catalytic Materials: Relationship between Structure and Reactivity*,. 1984, ACS: Washington. p. 405.
96. A. Stanislaus, M. Absi-Halabia, and K. Al-Dolomaa, *Appl. Catal.*, 1988. **39**, p. 239.
97. F. Eder, M. Stockenhuber, and J.A. Lercher, *Stud. Surf. Sci. Catal.*, 1995. **97**, p. 495.
98. D. T. Chen, S. B. Sharma, I. Filimonov, and J.A. Dumesic, *Catal. Letts.*, 1992. **12**, p. 201.
99. H. Knözinger, *Infrared Spectroscopy for the Characterization of Surface Acidity*, in *Handbook of Heterogeneous Catalysis*, G. Ertl, H. Knözinger, Ferdi Schüth, and J. Weitkamp, Editors. 1997, Wiley: Weinheim.
100. H.A. Benesi, *J. Catal.*, 1973. **28**, p. 176.
101. H. C. Brown, H. I. Schlesinger, and S.Z. Cardon, *J. Am. Chem. Soc.*, 1942. **64**, p. 325.
102. P. A. Jacobs and C.F. Heylen, *J. Catal.* , 1974. **34**, p. 267.
103. D. J. Parillo, R. J. Gorte, and W. E. Farneth, *J. Am. Chem. Soc.*, 1993. **115**, p. 12441.
104. C. H. Kline and J. Turkevich, *J. Chem. Phys.* , 1944. **12**, p. 300.
105. J.B. Peri, in *Catalysis - Science and Technology*, J. R. Anderson and M. Boudart, Editors. 1984, Springer: Berlin. p. 171.
106. A. Iordan, M. I. Zaki, and C. Kappenstein, *J. Chem. Soc. Farady. Trans.*, 1993. **9**, p. 1492.
107. R. Flederow and I.G. Dalla-Lana, *J. Phys. Chem.*, 1980. **84**, p. 2779.

108. M. Arai, S. Nishimaya, S. Tsuruya, and M. Masai, *J. Chem. Soc. Faraday Trans.*, 1996. **92**, p. 2631.
109. M. Haneda, Y. Kintaichi, N. Bion, and H. Hamada, *Appl. Catal. B*, 2003. **46**, p. 473.
110. J. T. Cheng and P.D. Ellis, *J. Phys. Chem.*, 1989. **93**, p. 2549.
111. B. Sakakini, *J. Molec. Struc.*, 1997. **127**, p. 203.
112. K. Jacobi, H. Shi, M. Gruyters, and G. Ertl, *Phys. Rev.*, 1994. **49**, p. 5733.
113. B. Juguin, J.-F. Le Page, and J. Miquel, *US patent: 3 696 167: 3 Oct 1972; Appl. 23 991: 30 Mar. 1970: USA*.
114. K. Tanabe, *Solid Acids and Bases*. 1970, New York Academic Press.
115. W. Daniell, U. Schubert, R. Glockler, A. Meyer, K. Noweck, and H. Knozinger, *Appl. Catal., A: General*, 2000. **196**(2), p. 247.
116. R-S. Zhou and R.L. Snyder, *Acta Cryst. B*, 1991. **47**, p. 617.
117. C. Pecharromán, I. Sobrados, J. E. Iglesias, T. González-Carreño, and J. Sanz, *J. Phys. Chem. B* 1999. **103**, p. 6160.
118. H. Saalfeld, *Neues Jahrh. Mineral. Abh.*, 1960. **95**, p. 1.
119. G. Yamaguchi, Y. I, and W. Chiu, *Bull. Chem. Soc. Jpn*, 1970. **43**, p. 2487.
120. J.S.J. Hargreaves, *Crystal. Rev.*, 2005. **11**, p. 21.
121. D.T. Lundie, *Investigation of a new generation of methyl chloride synthesis catalysts*, in *Chemistry*. 2003, University of Glasgow: Glasgow.
122. G.A. Jeffrey, *An Introduction to Hydrogen Bonding*. 1997, New York, Oxford: Oxford University Press.
123. P. Hoffman and E. Knozinger, *Surf. Sci.*, 1987. **188**, p. 181.
124. W. M. Bowser and W.H. Weinberg, *Surf. Sci.*, 1977. **64**, p. 377.
125. J. Klein and A. Leger, *Phys. Letts.*, 1968. **28A**, p. 134.
126. A. Langseth and R.C. Lord, *Kgl. Danske Vid. Sels. Math.-Fys. Medd.*, 1938. **16**(96), p. 85.
127. F. Partal, M. Fernandez-Gomez, J. J. Lopez-Gonzalez, A. Navarro, and G.J. Kearley, *Chem. Phys.*, 2000. **261**, p. 238.
128. C. Morterra and G. Cerrato, *Langmuir*, 1990. **6**, p. 14.
129. D.J. Shaw, *Introduction to colloid and surface chemistry*. 1992, Oxford: Butterworth-Heinemann. p. 114.
130. J.-F. Lambert and M. Che, *J. Mol. Catal. A*, 2000. **162**, p. 5.
131. A. A. Tsyganenko and V.N. Filimonov, *Spectrosc. Lett.*, 1972. **5**, p. 477.
132. A. A. Tsyganenko and P.P. Mardilovich, *J. Chem. Soc., Faraday Trans.*, 1996. **92**, p. 4843.
133. G. Busca, V. Lorrenzelli, V. Sanchez Escribano, and R. Guidetti, *J. Catal.*, 1991. **131**, p. 167.
134. M. Xu, J. H. Lunsford, D. W. Goodman, and A. Bhattacharyya, *Appl. Catal. A*, 1997. **149**, p. 289.
135. I. Manassen and H. Pines, *Adv. Catal.*, 1966. **16**, p. 49.
136. N. S. Figoli, S. A. Hillar, and J.M. Parera, *J. Catal.*, 1971. **20**, p. 230.
137. J.J. Spivey, *Chem. Eng. Comm.*, 1991. **110**, p. 123.
138. A. R. McInroy, D. T. Lundie, J. M. Winfield, C. C. Dudman, P. Jones, S. F. Parker, J. W. Taylor, and D. Lennon, *Phys. Chem. Chem. Phys.*, 2005. **7**, p. 3093.
139. P. A. Clayborne, T. C. Nelson, and T.C. DeVore., *Appl. Catal. A*, 2004. **257**, p. 225.
140. R. Tleimatmanzalji, D. Bianchi, and G. M. Pajonk, *React. Kinet. Catal. Lett.*, 1993. **51**, p. 29.
141. C. S. John, V. C. Alma, and G.R. Hays, *Appl. Catal.*, 1983. **6**, p. 341.
142. P. Jones and C.C. Dudman, *Personal communication*. 2005.
143. Ineos Chlor Ltd., *Catalyst reference: 25867/19A*.
144. C. Giacovazzo, H. L. Monaco, G. Artioli, D. Viterbo, G. Ferraris, G. Gilli, G. Zanotti, and M. Catti, *Fundamentals of Crystallography*, 1992, Oxford: Oxford

- University Press.
145. D. Lennon, D. T. Iundie, S. D. Jackson, G. J. Kelly, and S.F. Parker, *Langmuir*, 2002. **18**, p. 4667.
  146. M. Bankhead, G. W. Watson, G. J. Hutchings, J. Scott, and D.J. Willock, *Appl. Catal. A*, 2000. **200**(1-2), p. 263.
  147. K. C. Hass, W. F. Schneider, A. Curioni, and W. Andreoni, *J. Phys. Chem. B*, 2000. **104**, p. 5527.
  148. T. M. French and G.A. Somorjai, *J. Phys. Chem.*, 1970. **74**(12), p. 2489.
  149. J. M. Soler, E. Artacho, J. D. Gale, A. Garcia, J. Junquera, P. Ordejon, and D. Sanchez-Portal, *J. Phys.: Condens. Matt.*, 2002. **14**, p. 2745.
  150. C. Ruberto, Y. Yourdshahyan, and B.I. Lundqvist, *Phys. Rev. B.*, 2003. **67**, p. 195412.
  151. M. Riese, Z. Altug, and J. Grotemeyer, *Phys. Chem. Chem. Phys.*, 2006. **8**, p. 4441.
  152. E.K. Gibson, *Amine hydrochloride salts: A problem in polyurethane synthesis*, in *Chemistry. 2007*, University of Glasgow: Glasgow.
  153. M.E. Dry, *Chemtech*, 1982. **12**(12), p. 744.
  154. M. E. S. Hegarty, A. M. O'Connor, and J.R.H. Ross, *Catal. Today*, 1998. **42**(3), p. 225.
  155. M. Asadullaha, S. Itoa, K. Kunimoria, M. Yamadab, and K. Tomishige, *J. Catal.*, 2002. **208**(2), p. 10.
  156. A.P. Steynberg and M.E. Dry, *Stud. Surf. Sci. Catal.*, 2004. **152**, p. 1.
  157. K. Sanderson, *Nature*, 2007. **449**, p. 14.
  158. T. Herranz, S. Rojas, F.J. Pérez-Alonso, M. Ojeda, P. Terreros, and J.L.G. Fierro, *J. Catal.*, 2006. **243**(1), p. 199.
  159. C.D. Frohning and B. Cornils, *Hydrocarb. Proc.*, 1974. **53**, p. 143.
  160. V.U.S. Rao, G.J. Steigel, A.C. Bose, C. G.C., and R.D. Srivastava, *Preprints of papers. American Chemical Society Division of Fuel Chemistry*, 1992. **37**.
  161. R.B. Anderson, *Catalysis*, ed. P.H. Emmett. 1956, New York: Van Nostrand-Reinhold. p. 29.
  162. D.B. Bukur, M. Koranne, X. Lang, K.R.P.M. Rao, and G.P. Huffman, *Appl. Catal. A*, 1995. **126**(1), p. 85.
  163. H. Kolbel and M. Ralek, *Catal. Rev. Sci. Eng.*, 1980. **21**(2), p. 225.
  164. D. B. Bukur, X.S. Lang, and Y.J. Ding, *Appl. Catal. A*, 1999. **186**(1), p. 255.
  165. D.S. Newsome, *Catal. Rev.-Sci. Eng.*, 1980. **21**(2), p. 275.
  166. M.E. Dry, *Catal. Letts.*, 1990. **7**, p. 241.
  167. M.E. Dry, *Appl. Catal. A*, 1996. **138**(2), p. 319.
  168. Y. Leng, Y. Liu, X. Song, and X. Li, *J. Nanosci. Nanotech.*, 2008. **8**(9), p. 4477.
  169. L. Diaz Barriga-Arceo, E. Orozco, V. Garibay-Febles, L. Bucio-Galindo, H. Mendoza León, P. Castillo-Ocampo, and A. Montoya, *J. Phys.: Con. Mat.*, 2004. **16**(22), p. 2273.
  170. J.W. Niemantsverdriet and A.M. van der Kraan, *J. Catal.*, 1981. **72**(2), p. 385.
  171. J.W. Niemantsverdriet, A.M. Van der Kraan, W.L. Van Dijk, and H.S. Van der Baan, *J. Phys. Chem.*, 1980. **84**(25), p. 3363.
  172. M.D. Shroff, D.S. Kalakkad, K.E. Coulter, S.D. Kohler, M.S. Harrington, N.B. Jackson, A.G. Sault, and A.K. Datye, *J. Catal.*, 1995. **156**(2), p. 185.
  173. S. Soled, E. Iglesia, and R.A. Fiato, *Catal. Lett.*, 1990. **7**, p. 271.
  174. W. Ning, N. Koizumi, H. Chang, T. Mochizuki, T. Itoh, and M. Yamada, *Appl. Catal. A*, 2006. **312**, p. 35.
  175. D.B. Bukur, L. Nowicki, and X. Lang, *Energy & Fuels*, 2002. **9**(4), p. 620.
  176. A.J.H.M. Kock, H.M. Fortuin, and J.W. Geus, *J. Catal.*, 1985. **96**(1), p. 261.
  177. D.B. Bukur, K. Okabe, M.P. Rosynek, C.P. Li, D.J. Wang, K.R.P.M. Rao, and G.P. Huffman, *J. Catal.*, 1995. **155**(2), p. 353.
  178. K. Kishi and M.W. Roberts, *J. Chem. Soc., Faraday Trans.*, 1975. **71**, p. 1715.

179. K.Y. Yu, W.E. Spicer, I. Lindau, P. Pianetta, and S.F. Lin, *Surf. Sci.*, 1976. **57**(1), p. 157.
180. C.R. Brundle, *IBM J. Res. Dev.*, 1978. **22**(3), p. 235.
181. T.N. Rhodin and C.F. Brucker, *Solid State Commun.*, 1977. **23**(5), p. 275.
182. R.A. Dictor and A.T. Bell, *J. Catal.*, 1986. **97**(1), p. 121.
183. P.H. Emmett, *Crystallite Phase and Their Relationship to Fischer–Tropsch Catalysis*, 1956, New York: Reinhold.
184. B. Jager and R. Espinoza, *Catal. Today*, 1995. **23**(1), p. 17.
185. D.S. Kalakkad, M.D. Shroff, S. Köhler, N. Jackson, and A.K. Datye, *Appl. Catal. A*, 1995. **133**(2), p. 335.
186. D. Lennon, N. G. Hamilton, P. Webb, and R.P. Tooze, *Progress meeting between SASOL (R.P.T. & P.W.) and Lennon group (D.L. & N.G.H.)*. 2008, SASOL technology UK, St. Andrews.
187. M.E. Dry, *Catalysis—Science and Technology*, in *Catalysis—Science and Technology*, J.R. Anderson, Editor. 1981, Springer-Verlag.: New York.
188. H. N. Pham, L. Nowicki, J. Xu, A. K. Datye, D. B. Bukur, and C. Bartholomew, *Ind. Eng. Chem. Res.*, 2003. **42**(17), p. 4001.
189. T. Herranz, S. Rojas, F.J. Pérez-Alonso, M. Ojeda, P. Terreros, and J.L.G. Fierro, *Appl. Catal. A* 2006. **308**, p. 19.
190. D.L. Trimm, *Catal. Rev. Sci. Eng.*, 1977. **16**(1), p. 155.
191. H.P. Bonzel and H.J. Krebs, *Surf. Sci.*, 1980. **91**(2-3), p. 499.
192. R.W. Joyner and M.W. Roberts, *J. Chem. Soc., Faraday Trans.*, 1974. **70**, p. 1819.
193. W. Erley, H. Ibach, S. Lehwald, and H. Wagner, *Surf. Sci.*, 1979. **83**(2), p. 585.
194. W. Erley and H. Wagner, *Surf. Sci.*, 1978. **74**(2), p. 333.
195. K.J. Singh and H.E. Grenga, *J. Catal.*, 1977. **47**(3), p. 328.
196. J. Benziger and R.J. Madix, *Surf. Sci.*, 1980. **94**(1), p. 119.
197. D. Borthwick, V. Fiorin, S.J. Jenkins, and D.A. King, *Surf. Sci.*, 2008. **602**(13), p. 2325.
198. Y. Jin and A.K. Datye, *J. Catal.*, 2000. **196**(1), p. 8.
199. H. Schulz, *Appl. Catal. A*, 1999. **186**(1-2), p. 3.
200. D.J. Dwyer and J.H. Hardenbergh, *J. Catal.*, 1984. **87**(1), p. 66.
201. C.H. Bartholomew, *Catal. Rev. Sci. Eng.*, 1982. **24**(1), p. 67.
202. C.H. Bartholomew, *Appl. Catal. A Gen.*, 2001. **212**(1-2), p. 17.
203. G.L. Ott, T. Fleisch, and W.N. Delgass, *J. Catal.*, 1980. **65**(2), p. 253.
204. H.J. Krebs, H.P. Bonzel, and G. Gafner, *Surf. Sci.*, 1979. **88**(1), p. 269.
205. D.J. Dwyer and G.A. Somorjai, *J. Catal.*, 1978. **52**(2), p. 291.
206. F. Zaera, *Chem. Rev.*, 1995. **95**, p. 2651.
207. J.L.G. Fierro, *Stud. Surf. Sci. Catal.*, 1990. **57**, p. 67.
208. P. Albers, H. Angert, G. Prescher, K. Seibold, and S.F. Parker, *Chemical Communications*, 1999. **17**, p. 1619.
209. W. Erley, P.H. McBreen, and H. Ibach, *J. Catal.*, 1983. **84**(1), p. 229.
210. J. Galuszka, T. Sang, and J.A. Sawicki, *J. Catal.*, 1992. **136**(1), p. 96.
211. A. Loaiza-Gil, B. Fontal, F. Rueda, J. Mendialdua, and R. Casanova, *Appl. Catal. A*, 1999. **177**(2), p. 193.
212. H.B. Zhang and G.L. Schrader, *J. Catal.*, 1985. **95**(1), p. 325.
213. M. Ding, Y. Yang, B. Wu, J. Xu, C. Zhang, H. Xiang, and Y. Li, *J. Mol. Catal. A*, 2009. **303**(1-2), p. 65.
214. Y. T. Chua and P.C. Stair, *J. Catal.*, 2003. **213**, p. 39.
215. H. Schulz, *Topics in Catalysis*, 2003. **26**(1-4), p. 1.
216. A. Borodzinski and A. Gołębowski, *Langmuir*, 1997. **13**, p. 883.
217. R. Fiedorow, R. Fran'iski, A. Krawczyk, and S. Beszterda, *J. Phys. Chem. Sol.*, 2004. **65**, p. 627.

218. J. F. Shultz, W. K. Hall, B. Seligman, and R.B. Anderson, *J. Am. Chem. Soc.*, 1955. **77**(1), p. 213.
219. G. B. Raupp and W.N. Delgass, *J. Catal.*, 1979. **58**, p. 361.
220. J.B. Butt, *Catal. Letts.*, 1990. **7**, p. 61.
221. C. Li and P.C. Stair, *Catal. Today*, 1997. **33**, p. 353.
222. S. D. Jackson, S. Rugmini, P. C. Stair, and Z. Wu, *Chem. Eng. J.*, 2006. **120**, p. 127.
223. M. A. Pimenta, G. Dresselhaus, M. S. Dresselhaus, L. G. Cancado, A. Jorio, and R. Saito, *Phys. Chem. Chem. Phys.*, 2007. **9**, p. 1276.
224. R. J. Nemanich and S.A. Solin, *Phys. Rev. B*, 1979. **20**(2), p. 392.
225. D. Lin-Vien, N. B. Colthup, W. G. Fately, and J.G. Graselli, *The handbook of infrared and Raman characteristic frequencies of organic molecules*. 1 ed. 1991, Boston: Academic Press. p. 10.
226. J. K. Walters, R. J. Newport, S. F. Parker, and W.S. Howells, *J. Phys.: Condens. Mat.*, 1995. **7**, p. 10059.
227. D. A. Braden, S. F. Parker, J. Tomkinson, and B.S. Hudson, *J. Chem. Phys.*, 1999. **111**, p. 429.
228. M. J. Frisch, G. W. Trucks, H. B. Schlegel, G. E. Scuseria, M. A. Robb, J. R. Cheeseman, J. J. A. Montgomery, T. Vreven, K. N. Kudin, J. C. Burant, J. M. Millam, S. S. Iyengar, J. Tomasi, V. Barone, B. Mennucci, M. Cossi, G. Scalmani, N. Rega, G. A. Petersson, H. Nakatsuji, M. Hada, M. Ehara, K. Toyota, R. Fukuda, J. Hasegawa, M. Ishida, T. Nakajima, Y. Honda, O. Kitao, H. Nakai, M. Klene, X. Li, J. E. Knox, H. P. Hratchian, J. B. Cross, V. Bakken, C. Adamo, J. Jaramillo, R. Gomperts, R. E. Stratmann, O. Yazyev, A. J. Austin, R. Cammi, C. Pomelli, J. W. Ochterski, P. Y. Ayala, K. Morokuma, G. A. Voth, P. Salvador, J. J. Dannenberg, V. G. Zakrzewski, S. Dapprich, A. D. Daniels, M. C. Strain, O. Farkas, D. K. Malick, A. D. Rabuck, K. Raghavachari, J. B. Foresman, J. V. Ortiz, Q. Cui, A. G. Baboul, S. Clifford, J. Cioslowski, B. B. Stefanov, G. Liu, A. Liashenko, P. Piskorz, I. Komaromi, R. L. Martin, D. J. Fox, T. Keith, M. A. Al-Laham, C. Y. Peng, A. Nanayakkara, M. Challacombe, P. M. W. Gill, B. Johnson, W. Chen, M. W. Wong, C. Gonzalez, and J.A. Pople, *Gaussian 03 Revision C.02*. 2004, Gaussian, Inc.: Wallingford CT.
229. J. P. Merrick, D. Moran, and L. Radom, *J. Phys. Chem. A*, 2007. **111**, p. 11683.
230. J. P. Reymond, P. Merideu, and S.J. Teichner, *J. Catal.*, 1982. **75**, p. 39.
231. M.E. Dry, *Catal. Tod.*, 2002. **71**(3-4), p. 227.
232. J. K. Neathery, G. Jacobs, A. Sarkar, and B.H. Davis, *Technical progress report: Separation of Fischer-Tropsch Wax Products from Ultrafine Iron Catalyst Particles*. 2005, The University of Kentucky, Center for Applied Energy Research: Kentucky.
233. D. Gonzalez, O. Altin, S. Eser, and A.B. Garcia, *Mater. Chem. Phys.*, 2007. **101**, p. 137.
234. P. R. Wentreck, B. J. Wood, and H. Wise, *J. Catal.*, 1976. **43**, p. 363.
235. M. Araki and V. Ponec, *J. Catal.*, 1976. **44**, p. 439.
236. A.T. Bell, *Catal. Rev. Sci. Eng.*, 1981. **23**, p. 203.
237. V. Ponec, *Catal. Rev. Sci. Eng.*, 1981. **18**, p. 151.
238. P. Biloen and W.M.H. Sachtler, *Adv. Catal.*, 1981. **30**, p. 165.
239. J. A. Rabo, A. P. Risch, and M.L. Poutsma, *J. Catal.*, 1978. **53**, p. 295.
240. P. Biloen, J. N. Helle, and W.M.H. Sachtler, *J. Catal.*, 1979. **58**, p. 95.
241. A. Kadkhodayan and A. Brenner, *J. Catal.*, 1989. **117**(2), p. 311.
242. E. Kawasaki, J. Sanscrainte, and T.J. Walsh, *A. I. Ch. E. Journal*, 1962. **8**(1), p. 48.
243. I. J. Moon and C.H. Rhee, *Proc of the 1997 TMS Annual Meeting, Feb 9 -13, Orlando, FL, Minerals Metals and Materials Society, Warrendale, PA, USA.*, 1997, p. 649.
244. M. Audier, A. Oberlin, M. Oberlin, M. Coulon, and L. Bonnetain, *Carbon*, 1981.

- 19**, p. 217.
245. K. Mondal, H. Lorethova, E. Hippo, T. Wiltowski, and S.B. Lalvani, *Fuel Proc. Tech.*, 2004. **86**, p. 33.
246. T. Riedel, H. Schulz, G. Schaub, K. W. Jun, J. S. Hwang, and K.W. Lee, *Top. Catal.*, 2003. **26**, p. 41.
247. J. Cheng, P. Hu, P. Ellis, S. French, G. Kelly, and C.M. Lok, *J. Phys. Chem. C*, 2010. **114**, p. 1085.
248. H. Schulz, G. Schaub, M. Claeys, and T. Riedel, *Appl. Catal. A Gen*, 1999. **186**, p. 215.
249. H. D. Babcock and L. L. Herzberg, *Astrophys. J.*, 1948. **108**, p. 167.
250. L.V. Gasparov, D.B. Tanner, D.B. Romero, H. Berger, G. Margaritondo, and L. Forró, *Phys. Rev. B*, 2000. **62**(12), p. 7939.
251. I. Chamritski and G. Burns, *J. Phys. Chem. B*, 2005. **109**(11), p. 4965.
252. J. Galuszka and Y. Amenomiya. in *Proceedings, 9th International Congress on Catalysis*. 1988. Calgary.
253. T. Fukushima, H. Arakawa, and M. Ichikawa, *J. Chem. Soc. Chem. Commun.*, 1985, p. 729.
254. R. P. Underwood and A.T. Bell, *J. Catal.*, 1988. **111**, p. 325.
255. J.M.L. Martin, J. El-Yazal, and J.-P. Francois, *J. Phys. Chem.*, 1996. **100**(38), p. 15358.
256. N. Verdal, J. J. Wilke, and B.S. Hudson, *J. Phys. Chem. A*, 2006. **110**, p. 2639.
257. P. W. Albers and S.F. Parker, *Adv. Catal.*, 2007. **51**, p. 99.
258. G.J. Kearley, *Nucl. Instrum. and Meth. A*, 1995. **354**, p. 53.
259. R. R. Kavanagh, J. J. Rush, R. D. Kelley, and T.J. Udovic, *J. Chem. Phys.*, 1984. **80**, p. 3478.
260. C. Koon, *J. Catal.*, 1989. **120**, p. 484.
261. C. Koon, *J. Catal.*, 1990. **126**, p. 306.
262. R. Marshall, G. Webb, S. D. Jackson, and D. Lennon, *J. Mol. Catal. A*, 2005. **226**, p. 227.
263. M.D. Shroff and A.K. Datye, *Catal. Lett.*, 1996. **37**(1), p. 101.